CONTRIBUTIONS TO NON-UNIFORM LARGE-EDDY SIMULATION FOR VORTEX DOMINATED FLOWS

CONTRIBUTIONS TO NON-UNIFORM LARGE-EDDY SIMULATION FOR VORTEX DOMINATED FLOWS

PROEFSCHRIFT

ter verkrijging van
de graad van doctor aan de Universiteit Twente,
op gezag van de rector magnificus,
prof.dr. W.H.M. Zijm,
volgens het besluit van het College voor Promoties
in het openbaar te verdedigen
op donderdag 5 oktober 2006 om 15.00 uur

door

Fedderik van der Bos

geboren op 13 september 1978
te Joure

Dit proefschrift is goedgekeurd door de promotoren

prof.dr.ir. B.J. Geurts
prof.dr.ir. J.J.W. van der Vegt

"Thesis writing is: second thoughts to the power n."
Free after: J.M. Coetzee, Slow Man (2005).

Voorwoord

Met dit proefschrift komt er een einde aan een periode van vier jaar waarin ik als promovendus werkzaam ben geweest binnen het project "Advanced simulation techniques for vortex dominated flows." Voor mij een leuke en enerverende tijd waar ik met ontzettend veel plezier aan terug zal denken. Dit was echter niet mogelijk geweest zonder een aantal mensen om mij heen, waarvan ik er een aantal wil noemen.

Als eerste is dat mijn dagelijkse begeleider Bernard Geurts. De adequate, maar daarnaast ook zeer ontspannen en persoonlijke manier van begeleiden is mij altijd ontzettend goed bevallen en ik zal daarom ook met veel plezier terug denken aan onze samenwerking. Daarnaast wil ik graag Jaap van der Vegt bedanken. Ten eerste omdat jij mij de kans bood om als promovendus aan de slag te gaan, maar daarnaast ook voor jou rol als tweede begeleider. Een rol die gedurende het project steeds belangrijker is geworden.

Heel veel dank gaat uit ook uit naar mijn medepromovendus binnen het project, Christiaan Klaij. Zonder jou inspanningen, die nodig waren om HEXADAP uit te breiden van de Euler naar de Navier-Stokes vergelijkingen, zouden de resultaten die gepresenteerd worden in het laatste hoofdstuk van dit proefschrift onmogelijk zijn geweest. Maar vooral wil ik je bedanken voor de leuke manier waarop we samen aan dit project hebben gewerkt.

Graag wil ik Nederlands Lucht- en Ruimtevaart instituut (NLR) en het STW bedanken voor de financiering van het project. Binnen de samenwerking met het NLR wil ik vooral Harmen van der Ven bedanken. Ten eerste voor zijn behulpzaamheid met HEXADAP, maar ook voor de zeer betrokken manier waarop hij bezig is geweest gedurende het hele traject.

Voor de goede en ontspannen werksfeer die ik altijd heb beleefd wil ik een flink aantal collega's bedanken. Met name wil ik mijn (ex-)kamergenoten: Kiran, Arek en Milan, en de secretaresses: Mariëlle en Diana bedanken. Maar ook: Alyona, Bert, Chris, Davit, Debby, Mike, Ference, Hadi, Henk, Herman, Janivita, Jaqueline, Joris, Lars, Monica, Natanael, Onno, Pablo, Remco, Sander, Sena, Vijaya en

de afstudeerders, allen bedankt.

In mijn vrije tijd heb ik vele uren doorgebracht bij de volleybalvereniging Harambee. Ik mag terugkijken op een verschikkelijk leuke periode, waarin ik veel opvallende dingen mee heb mogen maken. Alle teamgenoten van Heren 1 (Harem Akbar, Grolsche Katers, Gama (den Griekse insteek) en de Breezersletjes), de dames van de Harambeebies en de vele andere vrienden binnen Harambee, allemaal bedankt.

Als laatste wil ik mijn ouders, Roelant en Karst-jan bedanken voor de rol die ze al mijn hele leven spelen, maar speciaal wil ik ze bedanken voor de getoonde interesse en ondersteuning tijdens de afgelopen jaren.

Fedderik.

Contents

Chapter 1

Introduction

1.1 Turbulent flows

Turbulent flow or, simply, turbulence is associated with the unpredictable, chaotic and highly fluctuating motion observed in air, water and many other gasses and liquids. In day to day life we observe turbulent phenomena when rigorously stirring a cup of tea, in the air we see the white vapor trails formed behind an airplane and we see many different turbulent structures in the flow around a large stone in a fast mountain stream. Numerous other examples of turbulent flow can be given and some are shown in figure 1.1.

Aside to drawing attention by its fascinating appearance, a lot of practical interest exists in turbulent flows. In many flows encountered in industry, weather prediction and aerodynamics, turbulent phenomena are observed. Important examples are the transition to turbulence in pipe flows, the increased drag due to turbulence in flows around airplanes and ships and the use of turbulence to increase mixing in chemical applications [48, 98, 102, 107]. Therefore, intensive research is carried out in order to predict, understand and possibly control turbulence.

In turbulence research one can distinguish three different approaches: the theoretical, the experimental and the numerical approach. These approaches work complementary to each other as each approach has certain limitations in terms of accuracy, resolution and/or the range of flows which can be studied. Theoretical predictions generally provide an accurate description of flows, e.g., in terms of averaged quantities, but are only available for a few turbulent flows [36, 98, 102]. Therefore, for most turbulent flows researchers rely on results acquired by experimental and/or numerical means.

Experimental results are available for many turbulent flows, but are generally lim-

(a)   (b)
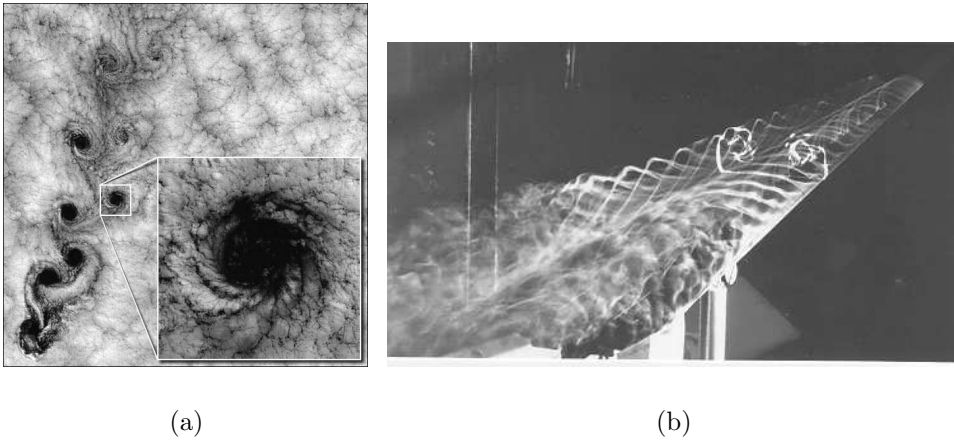
Figure 1.1: Two examples of turbulent flow a) Von Kármán vortices in the clouds around the Galapagos islands (www.earthobservatory.nasa.gov) b) Turbulent vortices in the flow around a delta-wing at $Re_c = 200,000$ [105].

ited in terms of accuracy and resolution. Most measuring techniques only produce data for a small part of the flow domain and often measuring devices are intrusive such that they interfere with the actual flow. Next to these limitations, experiments typically require a huge amount of space, time and money and lack the flexibility of immediately studying the effect of minor changes to a design.

The third approach is the numerical or computational approach. In this approach it is tried to compute the turbulent flow, e.g., using (super)computers [94, 96]. An example of a turbulent flow computed numerically is given in figure 1.2. Numerical simulations have the advantage over experiments that no expensive wind tunnel testing is needed, no scale models have to be produced and information about the flow field is available throughout the domain without the interference of measuring equipment. Moreover, with the developments in computer technology over the past 50 years the possibilities of using numerical methods when investigating turbulent flow have greatly increased.

Simultaneously, this has drawn an increased attention into the development of numerical methods exploiting these improvements in computer speed, computer memory and disk storage. Faster numerical methods have emerged as have methods which can efficiently deal with the complex geometries observed in many flows such as the wing of an airplane up to the swirling blades in a gas turbine. Such type of methods allow more and more complex, turbulent flows to be computed numerically.

The major problem, however, when investigating any turbulent flow by numerical
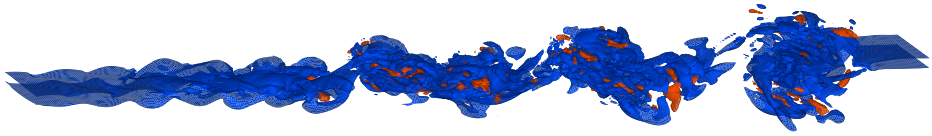
Figure 1.2: Example of numerically simulated turbulent flow: iso-surfaces of the vorticity $\omega_3 = \partial u_2/\partial x_1 - \partial u_1/\partial x_2$ in a spatially evolving mixing layer; blue: $\omega_3 = -0.05$, red: $\omega_3 = 0.05$.

means is that only a limited range of "turbulence" in a flow can be accurately computed. The "turbulence" in a flow is expressed in terms of the so-called Reynolds number, which is given by,

$$Re = \frac{L_\infty U_\infty}{\nu_\infty}. \tag{1.1}$$

Here L_∞, U_∞ and ν_∞ are a reference length, velocity and kinematic viscosity, respectively. These reference variables can be chosen for each specific flow. For the majority of flows a critical Reynolds number exists above which the flow is regarded turbulent. Consequently, by increasing the Reynolds number Re a flow will become turbulent when this critical Reynolds number is reached. The main problem which restricts the range of applicability when investigating turbulent flow by numerical means is that there also exists a critical Reynolds number above which the flow can no longer be accurately computed within an acceptable amount of time given present day computer speed and memory.

This thesis contributes to the research into turbulent flow in complex geometries by numerical means, in which we use a powerful simulation technique for turbulent flow called Large-Eddy Simulation (LES) [48, 91] in combination with a versatile method of discretization called the Discontinuous Galerkin Finite Element Method (DG-FEM) [5, 75, 130]. DG-FEM is a numerical method that is well suited to be used in complex flow geometries. By combining these two methods we expect that complex, turbulent flows at high Reynolds number can be computed by numerical means in the near future.

In the remainder of this introduction we first discuss the typical problems which are encountered when numerically simulating a (complex) turbulent flow and explain the basic idea behind LES. Then the two main aspects on which the research has been focused are introduced: *i)* the use of non-uniform grids and filters in LES [46, 51, 54] and *ii)* the use of LES in combination with a discretization based on DG-FEM [24, 25]. At the end of this introduction an overview is given of all chapters within this thesis.

1.2   Numerical simulation of turbulent flow

In a turbulent flow one can find a broad range of length scales and computing each of these distinct length scales requires a tremendous amount of computer resources. Moreover, the higher the Reynolds number, the broader the range of length scales that is encountered and the more computer resources are needed. To partially alleviate the problem, reduced flow simulation techniques such as LES are used to simulate turbulent flow at high Reynolds number.

The presence of a wide range of distinct length scales can in general directly be observed in a turbulent flow. For example in the flow shown in figure 1.1(a) the diameter of the largest structures observed is on the order of the diameter of the Galapagos islands, approximately 80 km, which are hidden in the lower left corner of this figure. But in the inset of this figure we observe that such a large-scale structure contains many other structures with different, smaller length-scales, which contain even smaller structures, etcetera. The presence of such a broad range of different length-scales is characteristic for a turbulent flow [98, 102].

All the flow-structures within in a turbulent flow can be divided into three different regimes depending on their typical length. These are the large-scale, the intermediate and the viscous or small-scale subrange [98, 102]. The large-scale subrange contains all flow structures with a typical length of approximately L_∞ and larger while the viscous subrange contains the smallest flow-structures present in a turbulent flow with a length-scale of η and smaller. This length-scale η is referred to as the Kolmogorov length-scale. The intermediate subrange contains all flow-structures whose length-scale are in between η and L_∞. The ratio between η and L_∞ for isotropic turbulence is related to the Reynolds number by [98, 102],

$$\frac{L_\infty}{\eta} \ \sim \ Re^{3/4}. \tag{1.2}$$

This relation makes clear that the larger the Reynolds number, the larger is the difference between L_∞ and η and the more length-scales are present in a turbulent flow that need to be computed in a numerical simulation of turbulent flow.

By the work of Richardson (1926) and Kolmogorov (1941) the dynamical behavior of these three different subranges with respect to the kinetic energy is reasonably well understood and has been observed in many different turbulent flows [102]. In a turbulent flow mainly large-scale flow features are affected by external sources such as inflows and outflows, objects in a flow, external forces, etc. Flow features with length-scales in the intermediate and viscous subrange have fairly universal behavior and are largely unaffected by external sources. In the intermediate subrange flow structures are broken up into smaller and smaller structures until these structures are so small that they are dissipated by viscous effects in the viscous
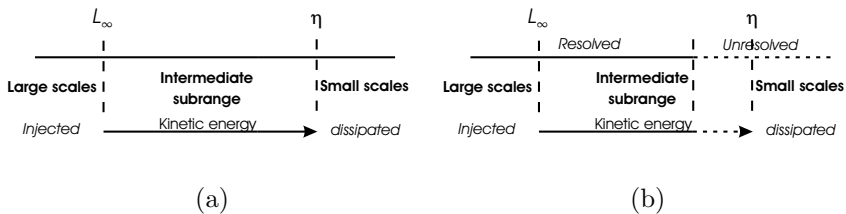
Figure 1.3: a) Spectrum of length-scales encountered in a turbulent flow divided into the large, intermediate and small scale subrange. b) Spectrum of length-scales as they are considered in LES of turbulent flow. In these figure L is the reference length, η is the Kolmogorov length-scale and Δ is the filter-width.

subrange.

Most of the kinetic energy is injected into the flow at the large scales. Then, in the process of flow structures being broken up into smaller structures, this kinetic energy is transported to the smaller scales, but kinetic energy is only dissipated at length-scales below the Kolmogorov length-scale η. In the intermediate subrange, almost no kinetic energy is dissipated, such that on average the kinetic energy is only transported through this range of scales. A sketch of this process is shown in figure 1.3(a).

Expression (1.2) and the sketch shown in figure 1.3(a) provide the background to understand the limitations of numerical simulations of turbulent flow and to motivate the Large-Eddy Simulation technique used in this thesis. More elaborate introductions into the theoretical aspects of turbulent flow, as well as experimental and numerical results which confirm this view, can be found in the many textbooks available (e.g., Nieuwstadt [98] and Pope [102]).

In order to accurately simulate a turbulent flow at high Reynolds number all of the length-scales present in the flow need to be computed. A numerical simulation in which all length-scales, from the largest L_∞ up to the smallest length-scale η, are computed is referred to as a Direct Numerical Simulation (DNS). In such a simulation a grid is used whose typical grid length h is on the order of η, such that the number of grid points N_g needed in a DNS is approximately given by $(L_\infty/h)^3$. Hence the number of grid-points in terms of the Reynolds number Re is approximately given by [98],

$$N_g = \left(\frac{L_\infty}{h}\right)^3 \sim \left(\frac{L_\infty}{\eta}\right)^3 \sim Re^{9/4}. \tag{1.3}$$

This relation reveals that the computational cost of a numerical simulation, in terms of number of grid points needed, scales with $Re^{9/4}$ for three-dimensional, turbulent flow. Therefore, doubling the Reynolds number results in a computation

Turbulent signal u Resolved signal $\overline{u}$ Unresolved part u'
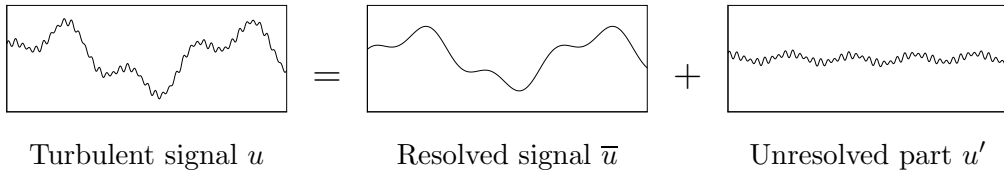
Figure 1.4: Turbulent, filtered and unresolved signal

which is approximately 5 times more grid-points.

To explain the practical consequences of relation (1.3) consider the following example. A well known aerodynamic flow is the flow over a delta-wing, as shown in figure 1.1(b) [63, 105]. Presently the highest Reynolds number reported in literature for such a flow is on the order of 10^4 [55, 63, 75] and such computations take a considerable amount of time, on the order of days up to several weeks. For relevant flow an increase in terms of the Reynolds number of by a factor of 100 [94] is required which results in a computation that would take many years to complete which is far beyond acceptable.

To remedy this problem researchers rely on so called reduced flow simulation techniques when simulating turbulent flow at high Reynolds number. In a reduced flow simulation technique not all turbulent flow features are computed. Only flow scales up to a typical length $\Delta \gg \eta$ are computed and consequently one is allowed to use a considerably coarser grid resulting in a cheaper computation. This process is sketched in figure 1.3(b). As can be seen only the large scales and part of the intermediate subrange are computed. The remainder of the intermediate and the complete viscous subrange are not computed.

Reduced flow simulation techniques generally involve some modeling aspect in order to account for the dynamical effect of the unresolved scales. For example, as shown in figure 1.3(b), the process of transporting kinetic energy through the intermediate subrange is disturbed as only part of the intermediate subrange is computed. A model is needed to restore this process. Over the years a number of reduced flow simulation techniques have been developed amongst which Reynolds Averaged Navier-Stokes (RANS) and Large-Eddy Simulation (LES) are the best known.

1.3   Large Eddy Simulation

In LES flow variables like the velocity $\mathbf{u}$ are divided into a resolved $\overline{\mathbf{u}}$ and an unresolved part $\mathbf{u}' = \mathbf{u} - \overline{\mathbf{u}}$ such that $\mathbf{u} = \overline{\mathbf{u}} + \mathbf{u}'$. The separation into resolved and

unresolved scales is effected by a so-called filter operator $\mathcal{L}$ and the resolved scales are defined as $\overline{\mathbf{u}} = \mathcal{L}(\mathbf{u})$. The resolved scales then contain only those flow features whose typical length-scale is larger than $\Delta \gg \eta$ and this length-scale Δ is referred to as the filter-width. In figure 1.4 an example is given in which a "turbulent" signal is decomposed into a resolved and unresolved part using such a filter. As can be observed after the application of the filter-operator a much smoother signal remains capturing the large scale features of the original turbulent signal.

By only computing length-scales larger than the filter-width Δ, one is allowed to use a grid with a typical grid-length h on the order of $\Delta \gg \eta$. Typical filter-width over grid-ratios $r = \Delta/h$ that are encountered in LES are 1 or 2, such that approximately $(L_\infty/\Delta)^3$ grid-points are needed in an LES. This is considerably lower than the $(L_\infty/\eta)^3$ grid-points needed in a DNS, which is the main virtue of LES [112].

As only the resolved scales are computed different equations are used in LES, compared to DNS. The equations which govern the evolution in time of resolved variables, as the resolved velocity $\overline{\mathbf{u}}(x,t)$, can be arrived at by applying the filter operator $\mathcal{L}$ to the Navier Stokes equations which govern turbulent flow. In the resulting *filtered* Navier-Stokes equations, so-called Sub-Grid-Scale (SGS)-terms are encountered. These SGS-terms represent the dynamic effect of the unresolved flow-scales onto the resolved scales.

SGS-terms are dependent on both resolved $\overline{\mathbf{u}}$ and unresolved variables $\mathbf{u}'$ and the most important of these SGS-terms is the SGS-stress τ_{ij} which is given by,

$$\tau_{ij}(\overline{\mathbf{u}}, \mathbf{u}') \;=\; \overline{u_i u_j} - \overline{u}_i \overline{u}_j \;=\; \overline{\overline{u}_i \overline{u}_j} + \overline{\overline{u}_i u'_j} + \overline{u'_i \overline{u}_j} + \overline{u'_i u'_j} - \overline{u}_i \overline{u}_j, \quad i,j = 1,2,3. \quad (1.4)$$

Here u_i denotes the velocity in the i-th Cartesian direction. It has been observed that the dynamic effects of the unresolved scales onto the resolved scales cannot be neglected in case $\Delta \gg \eta$ [48] and models $m(\overline{\mathbf{u}})$ need to be introduced for these SGS-terms to account for these dynamic effects. These models $m(\overline{\mathbf{u}})$ can only depend on resolved variables as only these are available during computation.

Over the years several models have been developed. Well known examples are the Smagorinsky model [111, 112], the Bardina or scale-similarity model [7], the Clark or gradient model [23] as well as various mixed formulations of these models [141]. LES in which these models have been used already showed considerably improved predictions of important flow features compared to the case in which no model was adopted [141]. For an extensive discussion regarding the many different SGS-models used in LES the reader is referred to Meneveau and Katz [91] or to the textbooks by Geurts [48] and Sagaut [107].

Most of the simulations mentioned above have been carried out on relatively simple flows with simple geometries and have shown the potential of LES. Presently LES

is used in flows as encountered in practical applications. There so-called "complex flows" are encountered: flows with complex geometries, moving and oscillating boundaries, inflows and outflows, etc. The main aim of this thesis is to contribute to the application of LES to such complex flows using a method of discretization which is well suited to be used in complex flows. A number of complications occur when one extends LES to such flows. In this thesis we mainly focus on two types of such complications. These are:

i) The use of non-uniform grids $h(\mathbf{x})$ and non-uniform filter-widths $\Delta(\mathbf{x})$ in LES.

ii) The use of LES in combination with a discretization based on the Discontinuous Galerkin Finite Element Method (DG-FEM).

These two problems make up the main content of this thesis and we will further elaborate upon them next.

1.4   Large Eddy Simulation of complex flows

1.4.1   Non-uniform filter-width and grids in LES

The first main topic in this thesis is related to the fact that in many practical situations the flow is turbulent in a small part of the flow-domain. Therefore one typically encounters a grid with a non-uniform mesh size $h(\mathbf{x})$. An example is given in figure 1.5. The use of a non-uniform grid is beneficial as it allows one to compute turbulent structures in greater detail in those parts of the domain where the flow is turbulent. Flow structures which are in a laminar, i.e. not turbulent, flow regime are then computed at a considerably coarser, thus cheaper, grid resolution. For example in figure 1.5 a fine grid is used only in regions close to turbulent vortical structures depicted in this figure.

Regarding LES, the use of a non-uniform mesh size $h(\mathbf{x})$ preferably involves the use of a non-uniform filter-width, i.e., a filter-width which is dependent on space $\Delta(\mathbf{x})$ [48, 54]. It has already been known for a long time that with the introduction of a non-uniform filter-width $\Delta(\mathbf{x})$ additional SGS-terms are introduced, generally referred to as commutator errors [47, 51, 54]. These commutator errors emerge from the fact that the filtering operations $\overline{\cdot}$ and the differential operations $\partial/\partial x_j$ can no longer be interchanged when a non-uniform filter-width is used. The commutator error for the velocity field u_i is given by,

$$\mathcal{C}_j[u_i](\overline{\mathbf{u}}, \mathbf{u}') \;=\; \overline{\frac{\partial u_i}{\partial x_j}} - \frac{\partial \overline{u}_i}{\partial x_j} \;=\; \overline{\frac{\partial(\overline{u}_i + u_i')}{\partial x_j}} - \frac{\partial \overline{u}_i}{\partial x_j}. \tag{1.5}$$
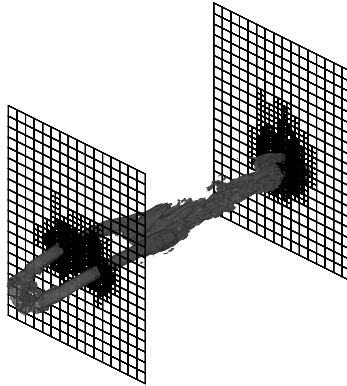
Figure 1.5: Example of a non-uniform grid used in the simulation of complex flows. Shown are the iso-surface of the vorticity magnitude $\boldsymbol{\omega}^2 = 1$ at $t = 30.0$ in a simulation of two counter-rotation vortices (vortex-pair). The two slices give an impression of the grid which is refined around the regions with high vorticity.

The commutator error problem is analyzed in two different ways. The first is based on the following scaling estimate of the commutator error which is arrived at using a straightforward calculation [54, 52, 51, 44],

$$\mathcal{C}_j[u_i] \sim \frac{\partial \Delta}{\partial x_j}\Delta^{N-1}. \tag{1.6}$$

Here N denotes the so-called order of the filter-operator $\mathcal{L}$ which for most filters is equal to 2. Relation (1.6) reveals that the dynamical importance of the commutator error is expected to scale with $i)$ the magnitude of the non-uniformity expressed in terms of the derivative of the filter-width $\partial \Delta/\partial x_j$ and $ii)$ the filter-width Δ^N. In this thesis the results are presented of an *a-priori* analysis using DNS-data [141] which confirm this scaling behavior of the commutator error with both $\partial \Delta/\partial x_j$ and Δ^N. Moreover we compared the size of the commutator error with that of the SGS-stress (1.4) which revealed that the commutator error contributions can be important in case $\partial \Delta/\partial x_j \gg 1$.

Based on the simple scaling relation (1.6) extensive research has been carried out in the past based on so-called higher order filters, i.e. filters with $N > 2$. In principle the commutator error can be made arbitrary small by using an appropriate N-th order filter as $\Delta^N \to 0$ when $N \gg 1$ [44, 54, 122] and $\Delta \ll L_\infty$. The use of higher-order filters in relation to the commutator error problem has, amongst others, been proposed by Ghosal and Moin [54] and over the years a number of realizations of such higher-order filters have been presented in literature. The first realizations of higher-order filters are presented by Van der Ven [131] and Vasilyev *et al.* [133] but were limited to indefinite domains or relatively simple geometries.

Later, N-th order filters have been presented which could in principle be used in arbitrary, possibly non-Cartesian, grids by, for example, Marsden *et al.* [87] and Haselbacher and Vasilyev [64].

Already in an early paper by Geurts *et al.* [51] it was pointed out that not only the commutator error, but all SGS-terms could be made arbitrarily small with the application of a higher order filter. For example for an N-th order filter the SGS-stress scales with $\tau_{ij} \sim \Delta^N$ [44]. In our *a-priori* analysis we verified the scaling behavior with the order of the filter for both the SGS-stress and commutator error which led to the conclusion that the use of higher-order filters does not lead to an independent control of the commutator error.

The second way we discuss the commutator error is by investigating it's Lagrangian nature. This is a novel approach towards the commutator error problem in which it is argued that the effect of the commutator error is highly dependent on the material derivative D_t of the filter-width;

$$D_t\Delta \;=\; \frac{\partial \Delta}{\partial t} + \overline{u}_j \frac{\partial \Delta}{\partial x_j}. \tag{1.7}$$

Consequently commutator error effects are expected only if the flow is directed towards the filter-width non-uniformity. *A priori* analysis using DNS-data was used to investigate this behavior. Specifically we considered the Lagrangian behavior of the commutator error for the transport of kinetic energy and showed that it could be well parameterized in terms of the material derivative of the filter width $D_t\Delta$.

1.4.2 Numerical methods in LES

The use of LES in complex flows in which we encounter non-uniform grids, moving boundaries etc. requires a numerical method which can deal with a non-uniform and deforming grid. Many different numerical methods have been developed over the years and not all numerical methods are well suited to be used for such complex flows. A numerical method which seems well suited to simulate complex flows is DG-FEM. The distinctive aspect of DG-FEM is that higher order accuracy can be achieved while maintaining a very localized stencil [75, 130]. Recently DG-FEM has been applied to the Navier-Stokes equations [5, 8, 16, 75] and already several examples exist in which DG-FEM for the full Navier-Stokes equations is used for complex flows. Klaij *et al.* [75, 130] applied DG-FEM to several aerodynamic flow, including an oscillating wing and the flow over a delta-wing at modest Reynolds number ($Re_c = 40,000$) and Bassi *et al.* [8, 10] applied DG-FEM to turbulent flow in an engine turbine.

It should be pointed out that the method of discretization and the grid employed are an integral part of an LES and can have a considerable influence on the accuracy

of LES. This because when solving the discretized equations one cannot circumvent "discretization effects". These discretization effects typically scale with the grid-length h and only when $h \ll \Delta$ do these discretization errors become negligible in LES. In LES preferably a coarse grid $h \sim \Delta$ is used and consequently the effects due to discretization on the LES results are comparatively large and frequently are on the same order as the errors induced by e.g. the SGS-modeling.

It is well known that modified SGS-terms emerge if the filtering effect of the coarse-grid discretization is incorporated into the large-eddy equations [83, 84, 106]. We will refer to this modified closure problem as the computational turbulent stress tensor [45, 124]. In chapter 5 it will be shown that the computational turbulent stress tensor for compressible flow can be decomposed into of two parts: one part primarily associated with fluctuating density and another part primarily associated with the fluctuating velocity. Using turbulent data at various Mach numbers it will be shown that the effect of the fluctuating density can become considerable at high, supersonic Mach number.

Over the years several studies have been published in which it is tried to understand, predict or illustrate the effect of the coarse-grid discretization and numerical method on the LES-results [42, 46, 53, 92, 93, 101, 140]. Most of the studies into the effect of the discretization in LES mentioned above use either Fourier-spectral [52, 22] or Finite Difference (FD)-methods [42, 62, 92, 93, 140]. Based on these studies some guidelines have been proposed along which for example an acceptable filter-width to grid-ratio $r = \Delta/h$ are suggested. In these studies the results of LES using different filter-width to grid-ratio's are *a-posteriori* compared with the results from a DNS. Recently this approach was further extended by Meyers, Geurts and Baelmans [92, 93] resulting into so-called "accuracy charts". These "accuracy charts" are an illustrative and efficient way to process and compare the results of many different LES using distinct numerical set-ups.

The use of LES in combination with a DG-FEM discretization is fairly new. The first attempts in this direction have been taken in Refs. [25, 103]. DG-FEM is a "projection" based numerical method. An alternative approach, referred to as the Variational Multi-Scale approach to LES (VMS-LES), can be used to formulate the LES equations at the discrete level [24, 69, 70, 71, 127]. The method of discretization becomes an integral part of the LES-technique in VMS-LES. Particularly the use of VMS-LES for compressible flow and the occurrence of commutator errors in VMS-LES will be discussed in this thesis.

Another aspect of DG-FEM which is discussed in this thesis is the "numerical dissipation" [80]. Low order DG-FEM typically possesses considerable "numerical dissipation" which is needed for stability reasons. However, a large numerical contribution to the total dissipation rate of kinetic energy may seriously affects

the effectiveness of a SGS-model. Moreover in some cases it is even suggested to let "the numerical dissipation do the job" and not to incorporate any SGS-modeling [2, 12, 59]. In this thesis we investigate the numerical dissipation using the accuracy charts approach of Meyers *et al.* [92, 93]. It will for example be shown that different constants should be adopted in the SGS-models to gain optimal accuracy depending on the amount of numerical dissipation introduced by the discretization.

1.5 Outline

As stated above the main emphasis in this thesis is on investigating the use of LES in combination with DG-FEM to complex, turbulent flow. Two particular aspects are given special attention. Firstly this is the use of non-uniform grids and filter-widths in LES and, secondly, the use of a discretization based on DG-FEM in LES.

Specifically we will deal with the following topics.

- Results are shown of *a-priori* analysis regarding the scaling estimate of the magnitude of the commutator error (1.6) in terms of the derivative of the filter-width $\partial \Delta / \partial x_j$ and Δ^N.

- We will introduce and evaluate the approximate Lagrangian behavior of the commutator error.

- We will study the computational stress tensor for compressible flow [45].

- The Variational Multi-Scale approach to LES (VMS-LES) will be introduced and we will formulate VMS-LES for compressible flow. Also the occurrence of commutator errors in VMS-LES will be identified.

- Results are shown of an *a-posteriori* investigations using "accuracy charts" in which we illustrate and quantify the effect of numerical dissipation on the SGS-modeling in LES.

In the final chapter we will present results of LES using DG-FEM of the flow over a delta-wing at $Re_c = 100,000$. These simulations allow us to assess the feasibility of LES and DG-FEM for turbulent, aerodynamic flow.

The detailed outline of this thesis is as follows. Chapter 2 introduces the governing equations for turbulent flow. Then, in chapter 3 and 4 the commutator error will be discussed and results are shown of *a-priori*. In the following three chapters the focus will shift to the effect of numerical methods in LES. First in chapter 5 the

effect of a discretization is interpreted as a numerical filter and in particular we will investigate the computational turbulent stress tensor compressible flow. In chapter 6 an LES formulation based on the Variational Multi-Scale approach to LES (VMS-LES) is given suitable for DG-FEM of compressible flow. In chapter 7 the effect of numerical dissipation on the LES SGS-modeling is investigated using a data-base approach. In section 8.1 the main conclusions are drawn. Finally in section 8.2 an outlook is given for the application of LES in combination with DG-FEM. In particular we will discus the feasibility of LES in combination with DG-FEM on locally refined grids. This discussion is based on an early attempt of simulation complex, high Reynolds number flow over a delta-wing using LES and DG-FEM.

Chapter 2

Governing equations

In this chapter we will introduce the equations which govern compressible, turbulent flow (section 2.1), introduce the traditional filtering approach to LES and discuss some popular Sub-Grid-Scale (SGS) models (section 2.2). In section 2.3 we will introduce the DG-FEM discretization for the Navier-Stokes equations supplemented with a Smagorinsky SGS-model.

2.1 Navier Stokes equations for compressible flow

Compressible flow is governed by a set of five equations that together constitute the Navier-Stokes equations. These five equations describe the conservation of mass, momentum and energy and are given by [4, 48, 144],

$$\partial_t \rho + \partial_j \rho u_j = 0, \tag{2.1}$$

$$\partial_t \rho u_i + \partial_j \Big(\rho u_i u_j + \delta_{ij} p - \sigma_{ij} \Big) = 0, \tag{2.2}$$

$$\partial_t E + \partial_j \Big((E + p) u_j - \sigma_{ij} u_i + q_j \Big) = 0. \tag{2.3}$$

Here ρ is the density, u_i the i-th Cartesian velocity component, E the energy density, p the pressure, σ_{ij} the viscous stress tensor and q_j the heat flux. Further, δ_{ij} denotes the Kronecker delta and $\partial_t = \partial/\partial t$ and $\partial_j = \partial/\partial x_j$ are short hand notations for partial differentiation with respect to time and in the j-th Cartesian direction, respectively. Throughout this thesis we use Einstein notation such that summation is implied over repeated indices and vectors can be denoted by $\mathbf{u} = u_i = [u_1, u_2, u_3]$.

In order to close these equations we need to specify constitutive relations for the pressure, viscous stress tensor and the heat flux such that (2.1)-(2.3) can be fully

expressed in terms of the conserved density ρ, momentum ρu_i and energy density E [4, 48, 144]. For the pressure p we use,

$$p = (\gamma - 1)(E - \tfrac{1}{2}\rho u_i u_i), \tag{2.4}$$

where $\gamma = c_p / c_v$ is the ratio between the specific heats at constant volume c_v and at constant pressure c_p. The viscous stress tensor σ_{ij} is given by,

$$\sigma_{ij} = \frac{\mu(T)}{Re} S_{ij}, \quad S_{ij} = \partial_j u_i + \partial_i u_j - \tfrac{2}{3}\delta_{ij}\partial_k u_k, \tag{2.5}$$

where S_{ij} is the rate-of-strain tensor, $\mu(T)$ is the dynamic viscosity and Re is the Reynolds number which for compressible flow is given by,

$$Re = \frac{\rho_\infty L_\infty U_\infty}{\mu_\infty}. \tag{2.6}$$

Here ρ_∞ is the reference density, L_∞ the reference length, U_∞ the reference velocity, μ_∞ the reference viscosity and κ_∞ the reference thermal conductivity. The dynamic viscosity $\mu(T)$ is approximated using Sutherland's law [4, 48, 144],

$$\mu(T) = \frac{1+C}{T+C}T^{3/2}, \tag{2.7}$$

and is related to the kinematic viscosity used in (1.1) by $\mu = \rho\nu$. The temperature T is given by the ideal gas law,

$$T = \gamma M^2 \frac{p}{\rho}, \tag{2.8}$$

where $M = U_\infty / a_\infty$ denotes the Mach number expressing the ratio between the reference velocity U_∞ and reference speed of sound a_∞. Finally the heat flux q_j in the energy equation is given by,

$$q_j = \frac{\mu(T)}{(\gamma - 1)RePrM^2}\partial_j T, \tag{2.9}$$

where $Pr = c_p\mu_\infty / \kappa_\infty$ denotes the Prandtl number expressing the ratio between the reference viscosity μ_∞ and thermal diffusivity constant κ_∞.

These equations have been made dimensionless using a reference length L_∞, density ρ_∞, velocity U_∞, temperature T_∞ and viscosity μ_∞ such that the following dimensionless numbers have emerged: the Mach number M, the Prandtl number Pr and the Reynolds number Re. Throughout this thesis various values for the Prandtl, Mach and Reynolds number are adopted. These are given separately in each chapter. Further, the ratio between the specific heats γ is set to 1.4, while for the constant C in (2.7) the value 0.4 is used which corresponds to air at $276K$.

Filter	Filter kernel $G(s)$	Δ_e
Top-hat	$\begin{cases} 1 & \text{if } -\frac{1}{2} \leq s - \gamma \leq \frac{1}{2}, \\ 0 & \text{otherwise.} \end{cases}$	Δ
Gaussian	$\sqrt{\frac{6}{\pi}}\, e^{-6s^2}$	$\sqrt{\frac{2\pi}{6}}\Delta$
Spectral	$\frac{\sin(k_c s)}{\pi s}$	$\frac{\pi\Delta}{k_c}$

Table 2.1: The filter-kernel $G(s)$ and resulting effective filter-width Δ_e (2.14) for various popular one-dimensional filter operators. The variables Δ, k_c and γ are the externally specified filter-width, cut-off wave number and skewness parameter, respectively.

A short hand notation for equations (2.1)-(2.3) is given by,

$$\partial_t U_\alpha + \partial_j F_{\alpha j}^c(\mathbf{U}) - \partial_j F_{\alpha j}^v(\mathbf{U}, \nabla\mathbf{U}) \;=\; 0, \qquad (2.10)$$

where $U_\alpha = [\rho, \rho u_i, E]$ is the vector of the conserved variables and the 5×3 matrices $F_{\alpha j}^c$ and $F_{\alpha j}^v$ entail the conservative and viscous part of the Navier-Stokes equations, respectively. These two matrices can readily be extracted from (2.1)-(2.3) and are given by,

$$F_{\alpha j}^c(\mathbf{U}) \;=\; \begin{bmatrix} \rho u_j \\ \rho u_i u_j + p\delta_{ij} \\ (E + p)u_j \end{bmatrix}, \quad F_{\alpha j}^v(\mathbf{U}, \nabla\mathbf{U}) \;=\; \begin{bmatrix} 0 \\ \sigma_{ij} \\ \sigma_{ij}u_i - q_j \end{bmatrix}. \qquad (2.11)$$

In this short hand notation we use a particular Einstein notation [145] where Greek indices always imply a range $0, \ldots, 4$, while Latin indices imply the usual range $1, 2, 3$ unless otherwise noted, such that e.g. $U_0 = \rho$, $U_i = \rho u_i$ and $U_4 = E$.

2.2 Non uniformly filtered Navier Stokes equations

In LES a scale separation into resolved and unresolved flow features is considered [48, 107]. This scale separation allows flow variables like the momentum to be decomposed into a resolved $\overline{\rho u_i}$ and an unresolved part $(\rho u_i)'$ such that $\rho u_i = \overline{\rho u_i} + (\rho u_i)'$. The resolved part primarily contains those flow-features with a typical length-scale larger than the filter-width Δ [48]. In LES one aims to arrive at an accurate prediction of the primary flow-features contained in the resolved part.

Traditionally, the resolved part of variables is determined using one dimensional filter operators L. These filters may be used to construct product filters for the relevant three dimensional case. At first we will restrict ourselves to this type of filters. Using such a filter operator L the resolved part of a variable f is defined

as,

$$\overline{f}(x) \;=\; L[f](x) \;=\; \int_{-\infty}^{\infty} \frac{1}{\Delta(x,t)} G\Big(\frac{y-x}{\Delta(x,t)}\Big) f(y)dy. \tag{2.12}$$

Here G is referred to as the filter-kernel and Δ is the externally specified filter-width which we allow to be dependent on space and/or time. A filter operator is required to be normalized such that constant variables remain unchanged after filtering. This implies that the filter-kernel should satisfy,

$$\int_{-\infty}^{\infty} G(s)\, ds \;=\; 1. \tag{2.13}$$

Further a filter is considered 'symmetric' if $G(s) = G(-s)$ and 'skewed' or non-symmetric otherwise. Skewness of a filter is sometimes unavoidable in practical situations and implies a particular 'biasing' of the spatial averaging which, as a result, is no longer fully centered around the point x. For example the top-hat filter as defined in table 2.1 is skewed if $\gamma \neq 0$ and in that case the mid-point of the domain of integration is located at $x + \gamma/2$.

A filter-operator together with the externally specified filter-width Δ define an *effective* filter-width Δ_e. Multiple definitions exist but we adopt the following definition which is based on the L_2-norm of the filter-kernel G/Δ [48, 122, 136],

$$\Delta_e^{-1}(x,t) = \int_{-\infty}^{\infty} \Big\{ \frac{1}{\Delta(x,t)} G\Big(\frac{y-x}{\Delta(x,t)}\Big) \Big\}^2 dy. \tag{2.14}$$

In table 2.1 we have collected some well known filter-kernels G together with their associated effective filter-widths (2.14).

Because we allow the filter-width to be dependent on space and/or time the commutation property between filtering and differentiation no longer holds [51, 52, 54], i.e.

$$\partial_x \overline{f}(x) \neq \overline{\partial_x f}(x). \tag{2.15}$$

This results in a closure term known as the commutator error. In one dimension the commutator error is defined as [52, 122, 123],

$$\mathcal{C}_x(f) \;=\; \overline{\partial_x f} - \partial_x \overline{f} \;=\; [L, \partial_x](f). \tag{2.16}$$

In (2.16) the commutator error $\mathcal{C}_x$ is conveniently written in terms of the commutator-bracket involving the filter operator L and the differential operator ∂_x. In general, the commutator-bracket of two operators, A and B, is defined as,

$$[A, B](f) = A \circ B(f) - B \circ A(f) = A(B(f)) - B(A(f)). \tag{2.17}$$

One dimensional filtering can easily be extended to the relevant three dimensional case by considering product filters [48, 107, 144]. A three dimensional filter-operator $\mathcal{L}$ is then defined as the product of multiple one-dimensional filters, i.e. $\mathcal{L} = L_1 \circ L_2 \circ L_3$, where L_i, together with the filter-width Δ_i and skewness parameter γ_i, constitutes the filter associated with the i-th Cartesian direction. Consequently filtering in three dimensions is defined as [48, 107, 144],

$$\mathcal{L}[f](\mathbf{x}) \;=\; \int_\Omega \mathcal{G}(\mathbf{x}, \mathbf{y}) f(\mathbf{y}) d\mathbf{y}. \tag{2.18}$$

where the three dimensional filter-kernel $\mathcal{G}$ is defined as,

$$\mathcal{G}(\mathbf{x}, \mathbf{y}) \;=\; \prod_{i=1}^{3} \frac{1}{\Delta_i(x,t)} G_i\Big(\frac{y_i - x_i}{\Delta_i(x,t)} \Big). \tag{2.19}$$

Here G_i is the filter-kernel for the filter L_i corresponding to the i-th Cartesian direction.

Traditional filtering is, however, only one of the ways to arrive at a separation into resolved and unresolved scales. Another class of filters considered in this thesis are projective filters. Such filters are typically encountered in case the resolved variables are be expressed in terms of a finite number N_ϕ of basis-functions ϕ_i, $i = 0, \ldots, N_\phi - 1$,

$$\overline{f}(\mathbf{x}) = \sum_{i=0}^{N_\phi - 1} \hat{f}_i \phi_i(\mathbf{x}). \tag{2.20}$$

Here ϕ_i are basis-functions and the constants $\hat{f}_i$ are referred to as the expansion coefficients. These expansion coefficients are generally defined using an L_2-projection such that,

$$\hat{f}_i \;=\; \sum_{i,j=0}^{N_\phi - 1} \mathbb{M}_{ij}^{-1} \int_\Omega f(\mathbf{y}) \phi_j(\mathbf{y})\, d\mathbf{y}, \tag{2.21}$$

and

$$\overline{f}(\mathbf{x}) \;=\; \mathcal{P}[f](\mathbf{x}) \;=\; \sum_{i,j=0}^{N_\phi - 1} \mathbb{M}_{ij}^{-1} \int_\Omega f(\mathbf{y}) \phi_j(\mathbf{y})\, d\mathbf{y}\, \phi_i(\mathbf{x}). \tag{2.22}$$

Here $\mathbb{M}_{ij} = \int_\Omega \phi_i(\mathbf{y}) \phi_j(\mathbf{y})\, d\mathbf{y}$ is the mass-matrix which reduces to a diagonal matrix in case the basis-functions ϕ_i are mutually orthogonal. A special property of the L_2-projection filter, as defined above, is that it can be casted in the form as presented in (2.18). The filter-kernel $\mathcal{G}$ is then given by [135],

$$\mathcal{G}(\mathbf{x}, \mathbf{y}) \;=\; \sum_{i,j} \mathbb{M}_{ij}^{-1} \phi_i(\mathbf{x}) \phi_j(\mathbf{y}). \tag{2.23}$$

Equation		Compressible SGS-terms	Commutator errors
Continuity		-	$\mathcal{C}_t(\rho) + \mathcal{C}_j(\rho u_j)$
Momentum		$\partial_j \overline{\rho}\tau_{ij}$	$\mathcal{C}_t(\rho u_i) + \mathcal{C}_j(\rho u_i u_j)$
		-	$\mathcal{C}_i(p)$
		$-\partial_j(\overline{\sigma}_{ij} - \breve{\sigma}_{ij})$	$-\mathcal{C}_j(\sigma_{ij})$
Energy	α_1	-	$-\frac{1}{2}\widetilde{u}_i\widetilde{u}_i\{\mathcal{C}_t(\rho) + \mathcal{C}_j(\rho u_j)\}$
	α_2	$\widetilde{u}_i\partial_j\overline{\rho}\tau_{ij}$	$\widetilde{u}_i\{\mathcal{C}_t(\rho u_i) + \mathcal{C}_i(p)$
			$\qquad + \mathcal{C}_j(\rho u_i u_j)\}$
	α_3	$(\partial_j\overline{pu_j} - \partial_j\overline{p}\widetilde{u}_j)/(\gamma-1)$	$\{C_t(p) + \mathcal{C}_j(pu_j)\}/(\gamma-1)$
	α_4	$\overline{p\partial_j u_j} - \overline{p}\partial_j\widetilde{u}_j$	-
	α_5	$-\{(\overline{\sigma_{ij}\partial_j u_j} - \overline{\sigma}_{ij}\partial_j\widetilde{u}_i)$	$-\widetilde{u}_i\mathcal{C}_j(\sigma_{ij})$
		$\qquad + \partial_j(\widetilde{u}_i\overline{\sigma}_{ij} - \widetilde{u}_i\breve{\sigma}_{ij})\}$	
	α_6	$\partial_j\overline{q}_j - \partial_j\breve{q}_j$	$\mathcal{C}_j(q_j)$

Table 2.2: SGS-terms in compressible flow for non-uniformly filtered Navier-Stokes equations. The SGS-terms identified in the intermediate column are those that are encountered when a commuting filter operator is used [144, 141] while those SGS-terms which solely emerge when a non-commuting filter operator is used are gathered in the final column.

The main distinction between general integral filters and projection filters is that projection filters satisfy the projection property, such that $\mathcal{L} \circ \mathcal{L}(f) = \mathcal{L}(f)$. In order to distinguish between non-projective and projective filters we will frequently denote projection filters with $\mathcal{P}$, see (2.22). Of the filters presented in table 2.1 only the spectral cut-off filter is projective which stems from the fact that the spectral cut-off filter is retrieved if in (2.23) (one-dimensional) Fourier-spectral basis-functions $e^{\imath kx}$, $k = -k_c, \ldots, k_c$, are used with k_c the cut-off wave-number.

The application of a non-uniform three-dimensional filter to the Navier-Stokes equations (2.1)-(2.3) yields the complete, unclosed large-eddy equations. These may be expressed as [99, 141, 144],

$$\partial_t\overline{\rho} + \partial_j\overline{\rho}\widetilde{u}_j = -\mathcal{C}_t(\rho) - \mathcal{C}_j(\rho u_j), \tag{2.24}$$

$$\partial_t\overline{\rho}\widetilde{u}_i + \partial_j(\overline{\rho}\widetilde{u}_i\widetilde{u}_j + \delta_{ij}\overline{p} - \breve{\sigma}_{ij}) = -\mathcal{C}_t(\rho u_i) - \mathcal{C}_j(\rho u_i u_j) - \partial_j\overline{\rho}\tau_{ij}$$
$$-\mathcal{C}_i(p) + \mathcal{C}_j(\sigma_{ij}) + \partial_j(\overline{\sigma}_{ij} - \breve{\sigma}_{ij}), \tag{2.25}$$

$$\partial_t\breve{E} + \partial_j\Big(\big(\breve{E} + \overline{p}\big)\widetilde{u}_j - \breve{\sigma}_{ij}\widetilde{u}_i + \breve{q}_j\Big) = \alpha_1 + \alpha_2 + \alpha_3 + \alpha_4 + \alpha_5 + \alpha_6, \tag{2.26}$$

where $\overline{\rho}$, $\overline{\rho u_i}$ and $\overline{p}$ are the filtered variables, $\widetilde{u}_i$ is the Favre-filtered velocity [31,

32, 33],

$$\widetilde{u}_i = \frac{\overline{\rho u_i}}{\overline{\rho}}, \tag{2.27}$$

$\mathcal{C}_t$ is the commutator error in time [37], which for a field f is defined as,

$$\mathcal{C}_t(f) \ = \ \overline{\partial_t f} - \partial_t \overline{f} \ = \ [\mathcal{L}, \partial_t]\,(f), \tag{2.28}$$

and $\mathcal{C}_j$ is the three dimensional commutator error defined as,

$$\mathcal{C}_j(f) \ = \ \overline{\partial_j f} - \partial_j \overline{f} \ = \ [\mathcal{L}, \partial_j]\,(f). \tag{2.29}$$

Further $\breve{E}$, $\breve{\sigma}_{ij}$ and $\breve{q}_j$ are the energy density, viscous stress tensor and heat flux evaluated using resolved variables such that, e.g.,

$$\breve{E} \ = \ \frac{\overline{p}}{\gamma - 1} + \tfrac{1}{2}\overline{\rho}\widetilde{u}_k\widetilde{u}_k. \tag{2.30}$$

In (2.24)-(2.26) a number of closure terms can be identified and these are collected on the right hand sides of these equations as well as in table 2.2. We distinguish between two groups of SGS-terms. The first group consists of those SGS-terms which emerge when a commuting filter operator is used (compressible SGS-terms [141, 144]). The second group of SGS-terms consists of those SGS-terms which are encountered when the commutation property between filtering and differentiation does not apply (commutator errors).

The group of SGS-terms which emerge when a commuting filter is used is extensively discussed in [141, 144]. The most important SGS-term of this group is the SGS-stress which for compressible flow is given by,

$$\overline{\rho}\tau_{ij} \ = \ \overline{\rho}\big(\widetilde{u_i u_j} - \widetilde{u}_i\widetilde{u}_j\big) \ = \ \overline{\rho u_i u_j} - \frac{\overline{\rho u_i}\,\overline{\rho u_j}}{\overline{\rho}}. \tag{2.31}$$

At sufficiently low Mach number only modeling of the SGS-stress $\overline{\rho}\tau_{ij}$ is required [137, 141, 144] and we will discuss some models m_{ij} for the SGS-stress momentarily.

The representation of the filtered compressible flow equations as given in (2.24) - (2.26) is based on the filtered quantities $[\overline{\rho}, \overline{\rho u_i}, \overline{p}]$. Other, closely related, formulations have been considered as well, leading to the same LES template but with slightly different definitions of some of the closure terms [88, 99, 137]. For example one can also consider $[\overline{\rho}, \overline{\rho u_i}, \overline{E}]$ as filtered variables and introduce an alternative filtered pressure $\breve{p}$ instead. Alternative expressions for the energy equation have also been put forward in [95, 30]. However, in each of these formulations, the dominant closure term, which involves the turbulent stress tensor τ_{ij}, appears in exactly the same manner.

All SGS-terms in the second group of SGS-terms are related to the commutator error in time $\mathcal{C}_t$ or the three dimensional commutator error $\mathcal{C}_j$. Compared to the SGS-stress, commutator errors have not extensively been studied. The commutator errors will be discussed in chapters 3 and 4. Modeling approaches for the commutator errors are introduced and discussed at the end of chapter 4.

Before proceeding with the introduction of SGS-models for the SGS-stress tensor $\overline{\rho}\tau_{ij}$ a short comment should be made regarding the denomination Sub-*Grid*-Scale terms [21, 60, 62, 146]. Formally all the SGS-terms as discussed above should be regarded as Sub-*Filter*-Scale (SFS) terms as only the effect of the non-uniform filter applied to the equations is incorporated. However, throughout we will stick with the traditional denomination SGS and only mention this particular subtlety here.

Many SGS-models for the SGS-stress have been developed over the years. A thorough review and comparison can be found in publications by Vreman *et al.* [141, 144], Geurts [48] and Meneveau and Katz [91]. Of the wide array of SGS-models for the SGS-stress only one is actually used in this thesis: the Smagorinsky model [111, 112]. For compressible flow this model is given by,

$$m_{ij}^{\text{Smag}} = -\mu_e \widetilde{S}_{ij}, \quad \text{with } \mu_e = \overline{\rho}(c_s \Delta)^2 |\widetilde{S}|, \tag{2.32}$$

where $\widetilde{S}_{ij} = \partial_j \widetilde{u}_i + \partial_i \widetilde{u}_j - \frac{2}{3}\delta_{ij}\partial_k \widetilde{u}_k$ is the rate-of-strain tensor based on the Favre-filtered velocity, μ_e the eddy-viscosity in which c_s is the Smagorinsky constant, $\Delta = (\Delta_1 \Delta_2 \Delta_3)^{1/3}$ and $|\widetilde{S}|^2 = \frac{1}{2}\widetilde{S}_{ij}\widetilde{S}_{ij}$ is the rate of strain magnitude. The Smagorinsky model shows low correlation with the actual SGS-stress compared to other SGS-models in *a-priori* tests and is often found to be too dissipative [82, 137, 144]. This problem is largely remedied with the use of a Smagorinsky constant that is dependent on time and or space, e.g., using of a dynamical procedure [39, 40].

Two other well known SGS-models are the Bardina or similarity model and gradient model. These are introduced below and in chapter 4 two similar models for the commutator error will be introduced. The Bardina or similarity model is given by [7],

$$m_{ij}^{\text{sim}} = \overline{\rho}\big(\widetilde{\widetilde{u}_i \widetilde{u}_j} - \widetilde{\widetilde{u}}_i \widetilde{\widetilde{u}}_j\big). \tag{2.33}$$

This model is based on a similarity assumption between scales close to the cut-off wave-number $\sim \Delta^{-1}$ and the unresolved scales. The similarity model correlates much better with the SGS-stress in *a-priori* testing than the Smagorinsky SGS-model, but in practice it is found to dissipate not enough kinetic energy at low resolution [144]. Therefore it is often supplemented with a Smagorinsky SGS-model to form a mixed model [141, 144].

Because of the additional filtering of resolved variables required for the Bardina model this model is quite expensive. Therefore the gradient model [23] was put

forward which is arrived at after a Taylor expansion of (2.33) and is given by,

$$m_{ij}^{\text{gradient}} = \tfrac{1}{12}\overline{\rho}\Delta^2 \frac{\partial \widetilde{u}_i}{\partial x_k}\frac{\partial \widetilde{u}_j}{\partial x_k} \qquad (2.34)$$

This model correlates well with the SGS-stress, but also tends to underestimate the dissipation of kinetic energy.

2.3 DG-FEM discretization

In this section the DG-FEM discretization for the Navier-Stokes equations supplemented with a Smagorinsky SGS-model is given. The actual discretization resembles the DG-FEM formulation introduced in Refs. [73, 75]. Only the necessary aspects required for this thesis will be given and the reader is frequently referred to these references for additional details. Results of simulations based on this discretization will be presented in chapters 7 and 8.

DG-FEM has been introduced in the 1970s and has proven their potential for convective Euler equations, see [129, 130]. The main advantage of DG-FEM compared to other methods of discretization such as finite difference or finite volume methods is that higher order accuracy can be achieved while maintaining a discretization which is as local as possible. This later aspect implies that within the "DG-FEM philosophy" only communication with the neighboring element is allowed. This has considerable advantages for e.g. parallization.

Only recently DG-FEM formulations have received considerable attention for elliptic equations [5, 6] and subsequently for the Navier-Stokes equations [8, 9, 75]. In this section we will give a DG-FEM discretization for the Navier-Stokes equations including the Smagorinsky SGS-model. This discretization is largely based on the formulations presented in [8, 75]. However, with the introduction of a Smagorinsky SGS-model the equations become non-linear with respect to the gradient tensor $\partial_j U_\alpha$ [18, 19]. Compared to DG-FEM formulations for the Navier-Stokes equations which are linear with respect to $\partial_j U_\alpha$ this requires some additional assumptions in order to keep the discretization "as local as possible" which will be pointed out.

We present the discretization using the short hand notation introduced at the end of section 2.1. Including the Smagorinsky SGS-model the equations read as,

$$\partial_t U_\alpha + \partial_j F_{\alpha j}^c(\mathbf{U}) - \partial_j F_{\alpha j}^v(\mathbf{U}, \nabla\mathbf{U}) + \partial_j M_{\alpha j}(\mathbf{U}, \nabla\mathbf{U}) = 0, \qquad (2.35)$$

where 5×3 matrix $M_{\alpha j}$ constitutes the SGS-model. For the Smagorinsky model

$M_{\alpha j}$ is expressed as,

$$M_{\alpha j}(\mathbf{U}, \nabla\mathbf{U}) \;=\; -\,\mu_e \begin{bmatrix} 0 \\ S_{ij} \\ 0 \end{bmatrix}, \tag{2.36}$$

where μ_e is the eddy-viscosity as defined in (2.32).

The remainder of this section is divided into two parts. In the first part the polynomial basis-functions, the solution spaces and some necessary notation is introduced (section 2.3.1). After this we proceed with the introduction of the actual discretization (section 2.3.2).

2.3.1   DG-FEM basis-functions and solution spaces

In a DG-FEM the domain Ω is divided into N_K open elements $K \subset \Omega$ with a typical length-scale h. The resulting tessellation $\mathcal{T}_h$ is given by,

$$\mathcal{T}_h \;=\; \left\{ K \subset \mathbb{R}^3 \,\middle|\, K_i \cap K_j = \emptyset \text{ if } i \neq j, \; \bigcup_{i=1}^{N_K} K_i = \Omega \right\}. \tag{2.37}$$

The union of all shared element faces $S = \partial K_L \cap \partial K_R$ is denoted by,

$$\Gamma = \left\{ S \neq \emptyset \,\middle|\, S = \partial K_L \cap \partial K_R, \; K_L, K_R \in \mathcal{T}_h \right\}, \tag{2.38}$$

while the union of boundary faces $S = \partial K \cap \partial \Omega$ is denoted by,

$$\Gamma^{\text{bound}} = \left\{ S \neq \emptyset \,\middle|\, S = \partial K \cap \partial \Omega, \; K \in \mathcal{T}_h \right\}. \tag{2.39}$$

Over each element K we next introduce basis-functions which span the local polynomial space $P_p(K)$ of maximal polynomial order p. The resulting computational solution space is given by,

$$\mathcal{U}_h \;:=\; \left\{ U_\alpha \in [L^2(\Omega)]^5 \,\middle|\, U_\alpha|_K \in [P_p(K)]^5 \; \forall K \in \mathcal{T}_h \right\}. \tag{2.40}$$

Next we present a particular construction of these basis-functions for which we follow [130].

First we define N_p reference polynomials $\{\hat{\phi}_i\}_{i=0}^{N_p-1}$ over a reference element $\hat{K} = [-1,1]^3$. The polynomials $\{\hat{\phi}_i\}_{i=0}^{N_p}$ are constructed such that they span the local polynomial space $P_p(\hat{K})$ and are defined as,

$$P_p(\hat{K}) \;=\; \{\hat{\phi}_i(\boldsymbol{\xi})\}_{i=0}^{N_p-1} \;=\; \left\{ g_i(\xi_1)g_j(\xi_2)g_k(\xi_3) \,\middle|\, 0 \leq i + j + k \leq p \right\} \tag{2.41}$$
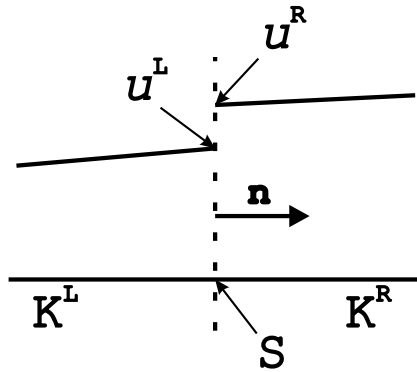
Figure 2.1: Local Riemann problem at an interface $S = \partial K_L \cap \partial K_R$. As a convention we assume that $\mathbf{n} = \mathbf{n}^L$.

where g_i, $i = 0 \ldots p$, are one-dimensional Legendre polynomials which are given by [1],

$$g_0(\xi) = 1, \quad g_1(\xi) = \xi, \quad g_2(\xi) = \xi^2 - \tfrac{1}{3}, \quad \ldots \ . \tag{2.42}$$

Then, for example,

$$
\begin{aligned}
\hat{\phi}_0(\boldsymbol{\xi}) &= g_0(\xi_1)g_0(\xi_2)g_0(\xi_3) = 1, \\
\hat{\phi}_1(\boldsymbol{\xi}) &= g_1(\xi_1)g_0(\xi_2)g_0(\xi_3) = \xi_1, \\
&\ \ \vdots \qquad \vdots \\
\hat{\phi}_4(\boldsymbol{\xi}) &= g_2(\xi_1)g_0(\xi_2)g_0(\xi_3) = (\xi_1^2 - \tfrac{1}{3}), \\
\hat{\phi}_5(\boldsymbol{\xi}) &= g_1(\xi_1)g_1(\xi_2)g_0(\xi_3) = (\xi_1^2 - \tfrac{1}{3})\xi_2, \\
&\ \ \vdots \qquad \vdots \\
\hat{\phi}_{N_p-1}(\boldsymbol{\xi}) &= g_p(\xi_1)g_p(\xi_2)g_p(\xi_3).
\end{aligned}
$$

The polynomial basis-functions for an arbitrary element $K \in \mathcal{T}_h$ are defined using a mapping $G_K : \hat{K} \to K$ from the reference element $\hat{K} = [-1, 1]^3$ to element K. The polynomial basis-functions for this element K are then defined as,

$$\phi_i^K(\mathbf{x}) = \hat{\phi}_i(G_K^{-1}(\mathbf{x})), \quad i = 0, \ldots, N_p - 1. \tag{2.43}$$

For the DG-FEM discretization of elliptic equations there is a need to introduce the "gradient" solution space Σ_h. This space is closely related to the solution space $\mathcal{U}_h$ and is defined as,

$$\Sigma_h := \left\{ Z_{\alpha j} \in [L^2(\Omega)]^{5 \times 3} \,\middle|\, Z_{\alpha j}|_K \in [P_p(K)]^{5 \times 3} \ \forall K \in \mathcal{T}_h \right\}. \tag{2.44}$$

Here $P_p(K)$ is the same polynomial space as used in the definition of $\mathcal{U}_h$ such that for all $U_\alpha \in \mathcal{U}_h$, $\partial_j^h U_\alpha \in \Sigma_h$. The operator $\partial_j^h = \partial_j|_K$, $K \in \mathcal{T}_h$ denotes the element-wise or broken differential operator [27].

Finally we introduce the usual jump and averaging operators $[\![\cdot]\!]_j$ and $\{\!\{\cdot\}\!\}$. For $U_\alpha \in \mathcal{U}_h$ at a face $S = \partial K_L \cap \partial K_R$ (see figure 2.1) these are defined as,

$$[\![U_\alpha]\!]_j = U_\alpha^L n_j^L + U_\alpha^R n_j^R, \quad \{\!\{U_\alpha\}\!\} = \tfrac{1}{2}(U_\alpha^L + U_\alpha^R). \tag{2.45}$$

Here $\mathbf{n}^L$ and $\mathbf{n}^R = -\mathbf{n}^L$ are the outward pointing normals with respect to K_L and K_R, respectively, $U_\alpha^L(y) = \lim_{\varepsilon \downarrow 0} U_\alpha(\mathbf{y} - \varepsilon \mathbf{n}^L)$ and $U_\alpha^R(y) = \lim_{\varepsilon \downarrow 0} U_\alpha(\mathbf{y} - \varepsilon \mathbf{n}^R)$. For $Z_{\alpha j} \in \Sigma_h$ we introduce,

$$[\![Z_{\alpha j}]\!]_j = Z_{\alpha j}^L n_j^L + Z_{\alpha j}^R n_j^R, \quad \{\!\{Z_{\alpha j}\}\!\} = \tfrac{1}{2}(Z_{\alpha j}^L + Z_{\alpha j}^R). \tag{2.46}$$

After having introduced the necessary notation we now proceed with the actual discretization of (2.35).

2.3.2   DG-FEM discretization of the Navier-Stokes equations with a Smagorinsky model

In order to discretize (2.35) we introduce the auxiliary variable $\theta_{\alpha j} \in \Sigma_h$. Then the second order PDE (2.35) can be rewritten into a system of two first order PDEs [8, 9, 75],

$$0 = \partial_t U_\alpha + \partial_j F_{\alpha j}^c(\mathbf{U}) - \partial_j \mathbb{F}_{\alpha j}^v(\mathbf{U}, \theta), \tag{2.47}$$

$$\theta_{\alpha j} = \partial_j U_\alpha. \tag{2.48}$$

Here we have merged the matrices $F_{\alpha j}^v$ and $M_{\alpha j}$ into the matrix $\mathbb{F}_{\alpha j}^v$:

$$\mathbb{F}_{\alpha j}^v(\mathbf{U}, \nabla\mathbf{U}) = F_{\alpha j}^v(\mathbf{U}, \nabla\mathbf{U}) + M_{\alpha j}(\mathbf{U}, \nabla\mathbf{U}) = \begin{bmatrix} 0 \\ (\mu(T) + \mu_e)S_{ij} \\ \sigma_{ij}u_i - q_j \end{bmatrix}. \tag{2.49}$$

Then, after multiplying equation (2.47) and (2.48) with arbitrary test-functions $W_\alpha \in \mathcal{U}_h$ and $Z_{\alpha j} \in \Sigma_h$, respectively, integrating over the individual elements $K \in \mathcal{T}$ and finally summing over all these elements, we arrive at,

$$0 = \sum_{K \in \mathcal{T}_h} \int_K W_\alpha \Big(\partial_t U_\alpha + \partial_j F_{\alpha j}^c(\mathbf{U}) - \partial_j \mathbb{F}_{\alpha j}^v(\mathbf{U}, \theta) \Big) \, d\mathbf{x}, \tag{2.50}$$

$$\sum_{K \in \mathcal{T}_h} \int_K Z_{\alpha j} \theta_{\alpha j} \, d\mathbf{x} = \sum_{K \in \mathcal{T}_h} \int_K Z_{\alpha j} \partial_j U_\alpha \, d\mathbf{x}. \tag{2.51}$$

After some manipulations these equations become (see [8, 9, 75] for details),

$$
\begin{aligned}
0 \;=\; & \sum_{K \in \mathcal{T}_h} \int_K W_\alpha \partial_t U_\alpha \, d\mathbf{x} \\
& - \sum_{K \in \mathcal{T}_h} \int_K \partial_j W_\alpha \Big(F^c_{\alpha j}(\mathbf{U}) - \mathbb{F}^v_{\alpha j}(\mathbf{U}, \theta) \Big) d\mathbf{x} \\
& + \int_\Gamma [\![W_\alpha]\!]_j \{\!\{ \widehat{F}^c_{\alpha j}(\mathbf{U}^L, \mathbf{U}^R) - \widehat{\mathbb{F}}^v_{\alpha j}(\mathbf{U}^L, \mathbf{U}^R, \theta^L, \theta^R) \}\!\} \\
& \qquad + \{\!\{ W_\alpha \}\!\} [\![\widehat{F}^h_{\alpha j}(\mathbf{U}^L, \mathbf{U}^R) - \widehat{\mathbb{F}}^v_{\alpha j}(\mathbf{U}^L, \mathbf{U}^R, \theta^L, \theta^R)]\!]_j \, d\mathbf{x}, \quad (2.52)
\end{aligned}
$$

$$
\begin{aligned}
\sum_{K \in \mathcal{T}_h} \int_K Z_{\alpha j} \theta_{\alpha j} \, d\mathbf{x} \;=\; & \sum_{K \in \mathcal{T}_h} \int_K Z_{\alpha j} \partial_j U_\alpha \, d\mathbf{x} \\
& + \int_\Gamma [\![Z_{\alpha j}]\!]_j \{\!\{ \widehat{U}_\alpha(\mathbf{U}^L, \mathbf{U}^R) - U_\alpha \}\!\} \\
& \qquad + \{\!\{ Z_{\alpha j} \}\!\} [\![\widehat{U}_\alpha(\mathbf{U}^L, \mathbf{U}^R) - U_\alpha]\!]_j \, d\mathbf{x}, \quad (2.53)
\end{aligned}
$$

where $\widehat{F}^c_{\alpha j}$, $\widehat{\mathbb{F}}^v_{\alpha j}$ and $\widehat{U}_{\alpha j}$ are the convective, viscous and auxiliary numerical flux, respectively. These fluxes are dependent on the left and right states of $\mathbf{U}$ and θ at an interface $S \in \Gamma$ and are introduced to deal with the multi-valued solutions at the element faces S. For the actual choice of these fluxes we follow [8, 75] and their definitions are given next. In the presentation we restrict ourselves to the case of periodic boundary conditions when all element faces can be treated as interior faces and $\Gamma^{\text{bound}} = \emptyset$. The extension to other types of boundary conditions can be found in [73, 75].

Auxiliary flux

The numerical flux $\widehat{U}_\alpha$ in the auxiliary equation (2.53) is given by $\widehat{U}_\alpha = \{\!\{ U_\alpha \}\!\}$ [8, 75], such that (2.53) becomes,

$$
\sum_{K \in \mathcal{T}_h} \int_K Z_{\alpha j} \theta_{\alpha j} \, d\mathbf{x} \;=\; \sum_{K \in \mathcal{T}_h} \int_K Z_{\alpha j} \partial_j U_\alpha \, d\mathbf{x} - \int_\Gamma \{\!\{ Z_{\alpha j} \}\!\} [\![U_\alpha]\!]_j \, d\mathbf{x}. \quad (2.54)
$$

This expression is simplified by introducing the global lifting operator $R_{\alpha j} \in \Sigma_h$ [6, 9, 73, 75],

$$
\sum_{K \in \mathcal{T}_h} \int_K Z_{\alpha j} R_{\alpha j}(\mathbf{U}) \, d\mathbf{x} \;=\; \int_\Gamma \{\!\{ Z_{\alpha j} \}\!\} [\![U_\alpha]\!]_j \, d\mathbf{x}, \quad \forall Z_{\alpha j} \in \Sigma_h, \quad (2.55)
$$

and provides the following definition for a gradient of state $\theta_{\alpha j} = \partial^h_j U_\alpha - R_{\alpha j}(\mathbf{U})$ [103].

Viscous Flux

As numerical flux for the viscous part a central flux in combination with a stabilization term is used [8, 9, 15, 19, 75],

$$\widehat{\mathbb{F}}_{\alpha j}^{v}(\mathbf{U}^{L}, \mathbf{U}^{R}, \theta^{L}, \theta^{R}) \;=\; \{\!\{\mathbb{F}_{\alpha j}^{v}(\mathbf{U}, \theta) - \eta_{v} A_{\alpha j \beta k}(\mathbf{U}) R_{\beta k}^{S}(\mathbf{U})\}\!\}. \tag{2.56}$$

The constant in the stabilization term $\eta_v > 0$ is known as the Brezzi constant, $A_{\alpha j \beta k}(\mathbf{U})$ is the homogeneity tensor, which well be discussed momentarily, and $R_{\beta k}^{S}(\mathbf{U}) \in \Sigma_h$, $S \in \Gamma$, is the local lifting operator which is defined as,

$$\sum_{K \in \mathcal{T}_h} \int_K Z_{\beta k} R_{\beta k}^{S}(\mathbf{U}) \, d\mathbf{x} \;=\; \int_S \{\!\{Z_{\beta k}\}\!\} [\![U_\beta]\!]_k \, d\mathbf{x}, \quad \forall Z_{\beta k} \in \Sigma_h, S \subset \Gamma. \tag{2.57}$$

One can readily verify that the global and local lifting operator are related to each other through $R_{\alpha j} = \sum_{S \in \Gamma} R_{\alpha j}^{S}$.

We choose to define the homogeneity tensor $A_{\alpha j \beta k}$ as,

$$A_{\alpha j \beta k}(\mathbf{U}) = \frac{\partial F_{\alpha j}^{v}(\mathbf{U}, Z)}{\partial Z_{\beta k}} + \mu_e \, \delta_{\alpha i} \frac{\partial S_{ij}(\mathbf{U}, Z)}{\partial Z_{\beta k}}, \tag{2.58}$$

and is constructed under the assumption that the eddy-viscosity coefficient μ_e is constant element-wise. For the Navier-Stokes equations, which are linear with respect to the gradient tensor $\partial_j U_\alpha$, the homogeneity tensor is defined as [75]:

$$\tilde{A}_{\alpha j \beta k}(\mathbf{U}) \;=\; \frac{\partial F_{\alpha j}^{v}(\mathbf{U}, Z)}{\partial Z_{\beta k}}. \tag{2.59}$$

and one may use that $\tilde{A}_{\alpha j \beta k}(\mathbf{U}) \, \partial_k U_\beta = F_{\alpha j}^{v}(\mathbf{U}, Z)$. This property is essential in order to maintain the strict locality of the method [75, 128]. Now with the introduction of the Smagorinsky model the equation are non-linear with respect to the gradient tensor $\partial_j U_\alpha$ and $A_{\alpha j \beta k}(\mathbf{U}) \, \partial_k U_\beta \approx \mathbb{F}_{\alpha j}^{v}(\mathbf{U}, Z)$.

Convective fluxes

For the convective fluxes we consider both the HLLC flux and Lax-Friedrich's flux. Lax-Friedrich's flux is given by,

$$\widehat{F}_{\alpha j}^{c}(\mathbf{U}^{L}, \mathbf{U}^{R}) \;=\; \{\!\{F_{\alpha j}^{c}(\mathbf{U})\}\!\} + \tfrac{1}{2}\lambda [\![U_\alpha]\!]_j. \tag{2.60}$$

Here λ is the maximum of the Euler flux Jacobian $J_{\alpha\beta} = \partial F_{\alpha j}^{c}(\mathbf{U}) n_j / \partial U_\beta$ and is given by,

$$\lambda = \max(|\hat{u}^{L}|, |\hat{u}^{L} \pm a^{L}|, |\hat{u}^{R}|, |\hat{u}^{R} \pm a^{R}|), \tag{2.61}$$
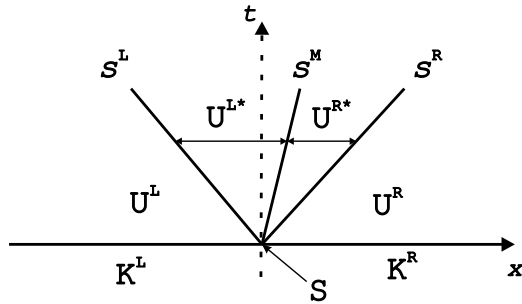
Figure 2.2: Illustration of the HLLC flux [11]. The terms s^L, s^R and s^M are the shock-speeds corresponding to the two acoustic and one contact wave, respectively, in the solution of the Riemann problem, $\mathbf{U}^L$ and $\mathbf{U}^R$ are the left and right states, while $\mathbf{U}^{L*}$ and $\mathbf{U}^{R*}$ are the left and right intermediate states (2.66).

where $\hat{u}^L = \mathbf{u}^L \cdot \mathbf{n}$, $\hat{u}^R = \mathbf{u}^R \cdot \mathbf{n}$ and $a = \sqrt{\gamma p / \rho}$ the speed of sound. Lax-Friedrich's flux can be seen as a generalization of the well known upwind-flux [80].

For the HLLC-flux the discontinuity at the element interface (see figure 2.1) is interpreted as a local Riemann problem [80, 121]. However, instead of solving the full local Riemann problem the HLLC-flux only solves this problem approximately, hence the HLLC-flux is often termed an approximate Riemann solver [11, 80, 121].

The complete HLLC-flux can be written as [130],

$$
\widehat{F}^c_{\alpha j}(\mathbf{U}^L, \mathbf{U}^R) = \{\!\{F^c_{\alpha j}\}\!\} - \Big\{ (|s^L| - |s^M|) U^{L*}_\alpha n^L_j + (|s^R| - |s^M|) U^{R*}_\alpha n^R_j
$$
$$
+ |s^L| U^L_\alpha n^L_j + |s^R| U^R_\alpha n^R_j \Big\}. \tag{2.62}
$$

where s^L and s^R are the shock-speeds of the two acoustic waves and s^M the shock-speed of the contact wave in the solution of the Riemann problem for the Euler equations [11, 121]. These are given by,

$$
s^L = \min(\hat{u}^L - a^L, \hat{u}^R - a^R), \tag{2.63}
$$
$$
s^R = \max(\hat{u}^L + a^L, \hat{u}^R + a^R), \tag{2.64}
$$
$$
s^M = \frac{\rho^R \hat{u}^R (s^R - \hat{u}^R) - \rho^L \hat{u}^L (s^L - \hat{u}^L) + p^L - p^R}{\rho^R (s^R - \hat{u}^R) - \rho^L (s^L - \hat{u}^L)}. \tag{2.65}
$$

such that $s^L < s^M < s^R$. The two intermediate states $\mathbf{U}^{L*}$ and $\mathbf{U}^{R*}$ are defined according to Batten [11, 130] such that $\mathbf{U}^{L*}$ is given by,

$$
\mathbf{U}^{L*} = \frac{s^L - \hat{u}^L}{s^L - s^M} \mathbf{U}^L + \frac{1}{s^L - s^M} \begin{bmatrix} 0 \\ (p^* - p^L)n_i \\ p^* s^M - p^L \hat{u}^L \end{bmatrix}, \tag{2.66}
$$

The right intermediate state $\mathbf{U}^{R*}$ is arrived at by replacing all subscripts L with R in (2.66). Finally the intermediate pressure p^* is constructed such that $p^* = p^{R*} = p^{L*}$ and is given by,

$$p^{L*} = \rho^L(s^L - \hat{u}^L)(s^M - \hat{u}^L) + p^L. \tag{2.67}$$

In fact, the HLLC-flux is constructed such that, based on the wave speeds s^L, s^R and s^M, the HLLC-flux uses either $\mathbf{U}^L$, $\mathbf{U}^R$ or one of the intermediate states $\mathbf{U}^{L*}$ or $\mathbf{U}^{R*}$ to compute the flux [11], i.e. $\widehat{F}^c_{\alpha j}(\mathbf{U}^L, \mathbf{U}^R) = F^c_{\alpha j}(\mathbf{U}^{\mathrm{HLLC}})$, where

$$\mathbf{U}^{\mathrm{HLLC}} = \begin{cases} \mathbf{U}^L & \text{if} \quad s^L > 0, \\ \mathbf{U}^{L*} & \text{if} \quad s^L \leq 0 < s^M, \\ \mathbf{U}^{R*} & \text{if} \quad s^M \leq 0 \leq s^R, \\ \mathbf{U}^R & \text{if} \quad s^R < 0. \end{cases} \tag{2.68}$$

For example in case $s^L < 0$ and $0 < s^M < s^R$ (see figure 2.2) the HLLC-flux adopts the left intermediate state $\mathbf{U}^{L*}$ [11, 121].

Discrete Navier-Stokes operator

After the introduction of the numerical fluxes $\hat{F}^c$, $\hat{\mathbb{F}}^v$ and $\hat{U}$ we can now proceed with the construction of the discrete Navier-Stokes operator $B_h^{\mathrm{DG}}(\mathbf{W}, \mathbf{U})$. Therefore we next insert the gradient of state $\theta = \nabla^h \mathbf{U} - R$ into (2.52),

$$\begin{aligned} 0 = & \sum_{K \in \mathcal{T}_h} \int_K W_\alpha \partial_t U_\alpha \, d\mathbf{x} \\ & - \sum_{K \in \mathcal{T}_h} \int_K \partial_j W_\alpha \Big(F^c_{\alpha j}(\mathbf{U}) - \mathbb{F}^v_{\alpha j}(\mathbf{U}, \nabla^h \mathbf{U} - R) \Big) \, d\mathbf{x} \\ & + \int_\Gamma [\![W_\alpha]\!]_j \{\!\!\{ \widehat{F}^c_{\alpha j}(\mathbf{U}^L, \mathbf{U}^R) \\ & \qquad - \widehat{\mathbb{F}}^v_{\alpha j}(\mathbf{U}^L, \mathbf{U}^R, \nabla^h \mathbf{U}^L - R^L, \nabla^h \mathbf{U}^R - R^R) \}\!\!\} \, d\mathbf{x}, \quad (2.69) \end{aligned}$$

where we have used that by construction $\widehat{F}^c_{\alpha j}$ and $\widehat{F}^v_{\alpha j}$ are single-valued at the element interfaces, hence $[\![\widehat{F}^c_{\alpha j}(\mathbf{U})]\!]_j$ and $[\![\widehat{\mathbb{F}}^v_{\alpha j}]\!]_j$ are zero.

The problem now lies in the terms $\mathbb{F}^v_{\alpha j}(\mathbf{U}, \nabla^h \mathbf{U} - R(\mathbf{U}))$. In the case without the Smagorinsky model, we could use $F^v_{\alpha j}(\mathbf{U}, \nabla^h \mathbf{U} - R(\mathbf{U})) = F^v_{\alpha j}(\mathbf{U}, \nabla^h \mathbf{U}) - \tilde{A}_{\alpha j \beta k}(\mathbf{U}) R_{\beta k}(\mathbf{U})$, with $\tilde{A}_{\alpha j \beta k}(\mathbf{U})$ as defined in (2.59). Here we can only assume that

$$\mathbb{F}^v_{\alpha j}(\mathbf{U}, \nabla^h \mathbf{U} - R(\mathbf{U})) \approx \mathbb{F}^v_{\alpha j}(\mathbf{U}, \nabla^h \mathbf{U}) - A_{\alpha j \beta k}(\mathbf{U}) R_{\beta k}(\mathbf{U}), \tag{2.70}$$

where the homogeneity tensor $A_{\alpha j \beta k}$ is defined according to (2.58). However, the use of an approximation similar to (2.70) is required to maintain the strict locality of the method.

Therefore, upon inserting (2.56) and the approximation (2.70) into (2.69), the discretization will be based on,

$$
\begin{aligned}
0 = & \sum_{K \in \mathcal{T}_h} \int_K W_\alpha \partial_t U_\alpha \, d\mathbf{x} \\
& - \sum_{K \in \mathcal{T}_h} \int_K \partial_j W_\alpha \Big(F^c_{\alpha j}(\mathbf{U}) - \mathbb{F}^v_{\alpha j}(\mathbf{U}, \nabla \mathbf{U}) + A_{\alpha j \beta k}(\mathbf{U}) R_{\beta k}(\mathbf{U}) \Big) \, d\mathbf{x} \\
& + \int_\Gamma [\![W_\alpha]\!]_j \{\!\{ \widehat{F}^c_{\alpha j}(\mathbf{U}) - \mathbb{F}^v_{\alpha j}(\mathbf{U}, \nabla \mathbf{U}) \\
& \qquad\qquad\qquad + A_{\alpha j \beta k}(\mathbf{U}) R_{\beta k}(\mathbf{U}) + \eta_v A_{\alpha j \beta k} R^S_{\beta k}(\mathbf{U}) \}\!\} \, d\mathbf{x}.
\end{aligned} \tag{2.71}
$$

After some reshuffling and using the definition of the global lifting operator (2.55) this expression may be written as,

$$
\begin{aligned}
0 = & \sum_{K \in \mathcal{T}_h} \int_K W_\alpha \partial_t U_\alpha \, d\mathbf{x} - \sum_{K \in \mathcal{T}_h} \int_K \partial_j W_\alpha \Big(F^c_{\alpha j}(\mathbf{U}) - \mathbb{F}^v_{\alpha j}(\mathbf{U}, \nabla \mathbf{U}) \Big) \, d\mathbf{x} \\
& + \int_\Gamma [\![W_\alpha]\!]_j \{\!\{ \widehat{F}^c_{\alpha j}(\mathbf{U}) \}\!\} - \{\!\{ \partial^h_j W_\alpha A_{\alpha j \beta k}(\mathbf{U}) \}\!\} [\![U_\beta]\!]_k \\
& \qquad\qquad\qquad\qquad - [\![W_\alpha]\!]_j \{\!\{ \mathbb{F}^v_{\alpha j}(\mathbf{U}, \nabla \mathbf{U}) \}\!\} \, d\mathbf{x} \\
& + \sum_{K \in \mathcal{T}_h} \int_K R_{\alpha j}(\mathbf{W}) A_{\alpha j \beta k} R_{\beta k}(\mathbf{U}) \, d\mathbf{x} \\
& + \eta_v \sum_{S \in \Gamma} \sum_{K \in \mathcal{T}_h} \int_K R^S_{\alpha j}(\mathbf{W}) A_{\alpha j \beta k} R^S_{\beta k}(\mathbf{U}) \, d\mathbf{x}.
\end{aligned} \tag{2.72}
$$

As a final step the following approximation is used which allows us to completely express the discretization in terms of the local lifting operator [28],

$$
\begin{aligned}
& \sum_{K \in \mathcal{T}_h} \int_K R_{\alpha j}(\mathbf{W}) A_{\alpha j \beta k} R_{\beta k}(\mathbf{U}) \, d\mathbf{x} \\
& \qquad \cong \; n_f \sum_{S \in \Gamma} \sum_{K \in \mathcal{T}_h} \int_K R^S_{\alpha j}(\mathbf{W}) A_{\alpha j \beta k} R^S_{\beta k}(\mathbf{U}) \, d\mathbf{x}.
\end{aligned} \tag{2.73}
$$

Here n_f denotes the number of faces connected to an element. This last step is required in order to achieve the strict locality. The full discrete Navier-Stokes

operator is now given by,

$$
\begin{aligned}
B_h^{\mathrm{DG}}(\mathbf{W}, \mathbf{U}) \;=\; & \sum_{K \in \mathcal{T}_h} \int_K W_\alpha \partial_t U_\alpha \, d\mathbf{x} \\
& - \sum_{K \in \mathcal{T}_h} \int_K \partial_j W_\alpha \Big(F_{\alpha j}^c(\mathbf{U}) - \mathbb{F}_{\alpha j}^v(\mathbf{U}, \nabla \mathbf{U}) \Big) \, d\mathbf{x} \\
& + \int_\Gamma [\![W_\alpha]\!]_j \{\!\{ \widehat{F}_{\alpha j}^c(\mathbf{U}) \}\!\} - \{\!\{ \partial_j^h W_\alpha A_{\alpha j \beta k}(\mathbf{U}) \}\!\} \, [\![U_\beta]\!]_k \\
& \hspace{4em} - [\![W_\alpha]\!]_j \{\!\{ \mathbb{F}_{\alpha j}^v(\mathbf{U}, \nabla \mathbf{U}) \}\!\} \, d\mathbf{x} \\
& + (\eta_v + n_f) \sum_{S \in \Gamma} \sum_{K \in \mathcal{T}_h} \int_K R_{\alpha j}^S(\mathbf{W}) A_{\alpha j \beta k} R_{\beta k}^S(\mathbf{U}) \, d\mathbf{x}. \quad (2.74)
\end{aligned}
$$

In the final steps towards discretizing the equations we observe that the discrete solution $\mathbf{U}^* \in \mathcal{U}_h$ should satisfy,

$$
0 \;=\; B(\mathbf{W}, \mathbf{U}^*), \quad \forall \mathbf{W} \in \mathcal{U}_h. \tag{2.75}
$$

In order to determine this solution, next $\mathbf{U}$ as well as the test-functions $\mathbf{W}$ are expressed in terms of basis-functions such that for each element we approximate $\mathbf{U}$ and $\mathbf{W}$ as.

$$
U_\alpha(\mathbf{x}, t) = \sum_{i=0}^{N_p-1} \hat{U}_{\alpha i}^K(t) \phi_i^K(\mathbf{x}), \quad W_\alpha(\mathbf{x}, t) = \sum_{i=0}^{N_p-1} \hat{W}_{\alpha i}^K(t) \phi_i^K(\mathbf{x}), \tag{2.76}
$$

Here $\hat{U}_{\alpha i}^K(t)$ and $\hat{W}_{\alpha i}^K(t)$ are the expansion coefficients for $\mathbf{U}$ and $\mathbf{W}$, respectively, at time t.

Upon inserting the approximations for $\mathbf{U}$ and $\mathbf{W}$ into (2.75) and using the fact that we may choose the test-function arbitrary, the following system of equations is arrived at for each element $K \in \mathcal{T}$,

$$
0 \;=\; \mathbb{M}_{ij}(K) \Big(\partial_t \hat{U}_{\alpha j}^K(t) \Big) + L_{\alpha i}^K(\hat{\mathbf{U}}(t)), \quad i = 0, \ldots, N_p - 1. \tag{2.77}
$$

Here $\mathbb{M}_{ij}(K) = \int_K \phi_i^K(\mathbf{x}) \phi_j^K(\mathbf{x}) \, d\mathbf{x}$ is the local mass-matrix, $\hat{\mathbf{U}}(t)$ denotes the vector of expansion coefficients at time t and $L_{\alpha i}^K(\hat{U}(t))$ are the residuals. These

residuals $L_{\alpha i}^K$ are given by,

$$
\begin{aligned}
L_{\alpha i}^K(\hat{\mathbf{U}}(t)) \;=\; & -\int_\Omega \partial_j \phi_i^K \Big(F_{\alpha j}^c(\mathbf{U}) - \mathbb{F}_{\alpha j}^v(\mathbf{U}, \nabla\mathbf{U}) \Big)\, d\mathbf{x} \\
& + \int_{\partial K} [\![\phi_i^K]\!]_j \{\!\{\widehat{F}_{\alpha j}^c(\mathbf{U})\}\!\} - \{\!\{\partial_j^h \phi_i^K A_{\alpha j \beta k}(\mathbf{U})\}\!\} \, [\![U_\beta]\!]_k \\
& \qquad\qquad\qquad - [\![\phi_i^K]\!]_j \{\!\{\mathbb{F}_{\alpha j}^v(\mathbf{U}, \nabla\mathbf{U})\}\!\}\, d\mathbf{x} \\
& + (\eta_v + n_f) \sum_{S \in \partial K} \int_S [\![\phi_i^K]\!]_j \{\!\{A_{\alpha j \beta k} R_{\beta k}^S(\mathbf{U})\}\!\} \, d\mathbf{x}, \qquad (2.78)
\end{aligned}
$$

where in the last term use was made of the definition of the local lifting operator.

In chapters 7 and 8 results of simulations based on this discretization are given. For the time-stepping, in chapter 7 explicit Runge-Kutta time-stepping is used, while in chapter 8 use is made of the fully implicit Space-Time DG-FEM (STDG-FEM) method [73, 75, 130]. In STDG-FEM the equations are directly solved in four dimensions, three spatial dimensions and one in time. Details concerning the time stepping will be given in chapters 7 and 8, respectively. Finally we note that for full details, e.g., on how to compute the local lifting operator $R_{\beta k}^S(\mathbf{U})$ or the treatment of boundary conditions other then periodic boundary conditions the reader is referred to [73, 75, 130].

Chapter 3

Commutator errors in the filtering approach to LES

In this chapter[1] the commutator error is analyzed based on the simple scaling relation (1.6) already given in Chapter 1. First in section 3.1 we further discuss non-uniform filtering and the commutator error problem. Then in section 3.2 the dominant scaling behavior is determined not only for the commutator error $\mathcal{C}_j$, but also for the SGS-stress τ_{ij}. In section 3.3 results of an *a-priori* analysis are shown confirming this scaling behavior and finally in section 3.4 the main results are summarized.

3.1 Introduction

LES holds promise to become a relevant engineering simulation strategy, applicable to flows of realistic complexity. However, in order to efficiently extend the LES capabilities to turbulent flows in complex geometries it is required to allow for spatially non-uniform grids and filters [50, 54]. These filters are characterized by a filter-width which is an explicit function of spatial coordinates[2] $\Delta(\mathbf{x})$. The filter-width should be reduced, i.e., one locally resolves more scales of the flow, in the 'turbulent' parts of the flow-domain. Likewise, in regions with comparably quiescent flow the filter-width can be chosen larger without notably affecting the accuracy of the simulation.

The introduction of a spatially non-uniform filter-width complicates the devel-

---

[1]This chapter is largely based on Van der Bos and Geurts [122].
[2]and possibly also of time [37], however, this is not included in the present chapter.

opment of the corresponding large-eddy approach since additional closure terms emerge that may or may not require explicit modeling. These terms are generally referred to as commutator-error subgrid terms or simply commutator-errors and originate from the fact that non-uniform filtering and differentiation do not commute [50, 54, 52, 38], i.e.,

$$\overline{\frac{\partial u}{\partial x}} \neq \frac{\partial \overline{u}}{\partial x}. \tag{3.1}$$

These commutator-errors have been considered before in literature (e.g., [47, 54, 52, 72, 131, 133]) concentrating on their proper definition, the relation with the explicit filter that was used and the role of specialized higher-order filters in connection to the magnitude of these terms. In this and the following chapter we extend this work in a number of ways.

In this chapter a detailed investigation of the commutator-errors, their effects on the flow and an estimation of their actual magnitude, using direct numerical simulation data of a turbulent mixing flow, will be considered. This is an essential prerequisite before non-uniform filtering with significant gradients in the filter-width can be applied in actual LES. In this chapter we present results of analysis and *a priori* data-base evaluation and incorporate regular second order filters, such as the symmetric top-hat and Gaussian filters, as well as high order filters [26, 131, 133] and filters with an a-symmetric (skewed) support [51] into the investigation.

A first impression of the magnitude and scaling of the commutator-errors can be obtained through investigating Taylor expansions of the relevant terms. The present analysis extends earlier work by Ghosal and Moin [54] who considered symmetric filters. In this chapter also skewed filters are considered which significantly alters the findings, as the skewness of a filter implies a decrease of the order of the filter which leads to an increase in size of the commutator-error [51]. Conversely, an increase in the order of a filter results in a formal decrease of the size of the commutator-error and has led to the development of higher order filters. Higher order filters have originally been proposed in the context of LES in [51] and constructed in a specific framework in [47, 131]. These filters have recently regained interest [60, 64, 87, 133] and appear to resolve the issue of explicitly modeling commutator-errors in LES. Specifically, the use of a suitable higher order filter can render the commutator-errors arbitrarily small. However, the use of higher order filters also leads to a formally equally strong decrease of the contributions of the turbulent SGS-flux $\partial_j \tau_{ij}$ in view of the identical dominant scaling behavior with Δ and its derivatives [47, 51]. Hence, it is not possible to obtain a separate control over the commutator-errors compared to the turbulent SGS-flux merely by adopting a suitable class of filters. In fact, other measures need to be taken to influence the size of the commutator-errors relative to the traditional subgrid terms, as will be indicated in this chapter.

The analytical estimates will be complemented by *a priori* evaluations based on DNS-data of a turbulent mixing flow [141]. This allows to compare the actual magnitude of all commutator-errors and subgrid terms on specific LES grids and for selected filter-width variations. The effect of skewness and of filter-order on the SGS-flux and the commutator-errors will be considered. These results establish the actual scaling of the commutator-errors and SGS-fluxes, confirming the Taylor expansion estimates. The *a priori* comparisons help to globally identify conditions such that explicit commutator-error modeling is required. In particular, if the filter-width variations $|\partial_j \Delta|$ become too large, the commutator-errors need to be separately parameterized with appropriate subgrid models. We will propose some explicit commutator-error models and compare their properties with basic properties of the exact commutator-errors at the end of chapter 4.

In order to simplify the analysis in this and the following chapter the isothermal incompressible Navier-Stokes equations rather than the compressible Navier-Stokes equations (2.1)-(2.3) are used. Compared to the compressible Navier-Stokes equations, the isothermal incompressible Navier-Stokes equations assume a constant density, $\rho \equiv \rho_\infty$, and a kinematic viscosity, $\nu = \mu/\rho$, independent of temperature [65, 100] and are given,

$$\partial_j u_j = 0, \tag{3.2}$$

$$\partial_t u_i + \partial_j \left(u_i u_j + \delta_{ij} p - \frac{1}{Re} \partial_j u_i \right) = 0. \tag{3.3}$$

Here the Reynolds number Re is defined according to (1.1).

If we apply a non-uniform filter operator over these equations we find,

$$\partial_j \overline{u}_j = -\mathcal{C}_j(u_j), \tag{3.4}$$

$$\partial_t \overline{u}_i + \partial_j \left(\overline{u}_i \overline{u}_j + \delta_{ij} \overline{p} - \frac{1}{Re} \partial_j \overline{u}_i \right) = -\mathcal{C}_t(u_i) - \partial_j \tau_{ij} - \mathcal{C}_j(u_i u_j)$$

$$-\mathcal{C}_i(p) + \frac{1}{Re} [C_j(\partial_j u_i) + \partial_j C_j(u_i)]. \tag{3.5}$$

Here $\overline{u}_i$ and $\overline{p}$ are the filtered variables and a number of SGS-terms can be identified on the right-hand-sides of these equations. Most of the SGS-terms are commutator errors and only one SGS-term due to non-linear interaction of the resolved variables is encountered: the SGS-stress τ_{ij}. In the incompressible limit the SGS-stress simplifies to $\tau_{ij} = \overline{u_i u_j} - \overline{u}_i \overline{u}_j$ which can be readily verified upon inserting $\rho \equiv \rho_\infty$ in (2.31).

The organization of this chapter is as follows. The dependence of the size of the commutator-error on the order of the filter will be established in section 3.2 and compared with the magnitude of the divergence of the turbulent stress-tensor. In section 3.3 results of an *a priori* analysis of the commutator-error will be presented.

In particular, we will introduce, quantify and compare several measures for the magnitude of the commutator-errors and the SGS-fluxes. The *a priori* analysis will focus on effects derived from the order and skewness of the filter. Finally, in section 3.4 we summarize our findings.

3.2   Dominant scaling behavior of sub-grid-scale terms

In this section we first determine the dominant scaling of the commutator errors for various general filters. We comment on the effect of skewness and afterwards consider the use of higher order filters. Subsequently, we determine the dominant scaling behavior of the turbulent stress contributions. It will be shown that both types of SGS-terms can be reduced arbitrarily by raising the order of the filter to a sufficiently high value. In fact, both subgrid contributions display identical leading-order scaling with the non-uniform filter-width and its derivatives. Consequently, for non-uniform filter-widths both contributions may require explicit modeling. In case the filter-width is constant, only the turbulent stress contributions remain. Hence, commutator errors can only be avoided independently by properly controlling the gradients in Δ. It is not possible to reduce the commutator errors separately by merely adhering to specialized higher order filters as claimed by a number of researchers [52, 54, 133].

Dominant scaling behavior of the commutator error

To determine the order of magnitude of the commutator errors one may explicitly evaluate $\partial_x \overline{f}(x)$ in one spatial dimension (see also Refs. [38, 50, 54]). After some calculations the following expression for the commutator error is obtained,

$$
\begin{aligned}
\mathcal{C}_x(f)(x) \;=\; & -\Delta'(x) \int_{\frac{x_0-x}{\Delta(x)}}^{\frac{x_1-x}{\Delta(x)}} s G(s) f'(x+\Delta(x)s)\, ds \\
& + \frac{1}{\Delta(x)}\left[1+(y-x_0)\frac{\Delta'(x)}{\Delta(x)}\right] G\left(\frac{y-x}{\Delta(x)}\right) f(y)\Bigg|_{y=x_0}^{x_1}, \quad (3.6)
\end{aligned}
$$

where x_0 and x_1 and the boundaries of the domain. As noted most explicitly in [38], the commutator error consists of two parts; an interior part and a boundary term. The latter term arises since principally filtering can not be extended beyond the boundaries of the flow-domain [29]. For common filters such as the top-hat and Gaussian filter this contribution is zero or negligible if x is sufficiently separated from the boundary. The interior contribution to the commutator error arises directly from the non-uniform filter-width, as expressed by the leading Δ'-factor.

In the remainder of this chapter we will restrict ourselves to the interior term of the commutator error and consider $x_0 \to -\infty$ and $x_1 \to \infty$. This is appropriate for the inhomogeneous turbulent mixing layer flow studied here.

The scaling of the interior term of the commutator error with filter-width can be inferred from Taylor expansion, provided the solution is sufficiently smooth. If one introduces the coordinate transformation $s = (y - x)/\Delta(x)$ in (2.12) one obtains after some calculation,

$$
\mathcal{C}_x(f)(x)
$$

$$
= -\Delta'(x) \int_{-\infty}^{\infty} s G(s) f'(x + \Delta(x)s) \, ds, \tag{3.7}
$$

$$
= -\Delta'(x) \int_{-\infty}^{\infty} s G(s) \left[f'(x) + s\Delta(x) f''(x) + \frac{1}{2} s^2 \Delta^2(x) f'''(x) + \cdots \right] ds, \tag{3.8}
$$

$$
= -\sum_{r=1}^{\infty} \frac{1}{(r-1)!} \Delta' \Delta^{r-1} M_r \frac{\partial^r f}{\partial x^r}, \tag{3.9}
$$

where M_r denotes the r-th moment of the filter, defined as:

$$
M_r = \int_{-\infty}^{\infty} s^r G(s) \, ds. \tag{3.10}
$$

Since we consider normalized filters the zero-th moment $M_0 = 1$. In the sequel of this chapter we restrict to filters for which all moments M_r with $r > 0$ exist. It should be remarked that the spectral cut-off filter does not satisfy this condition; in particular, for the spectral cut-off filter the even order moments beyond second order do not exist. We hence exclude the spectral cut-off filter from the discussion. In this section we will for convenience also assume that the solutions have continuous derivatives of all orders and convergent Taylor expansions.

The smoothing properties of general filters can be characterized to some degree by the effect of filtering on polynomials. For convenience in what follows we formalize this and introduce an N-th order filter by requiring,

$$
M_r = \delta_{r0} \quad \text{for} \quad r = 0, \ldots, N-1, \tag{3.11}
$$

where δ_{ij} denotes the Kronecker delta. Such N-th order filters leave polynomials of degree $N - 1$ invariant. In terms of (3.11) the symmetric top-hat filter and the Gaussian filter are second order filters, while the a-symmetric top-hat filter, when $\gamma \neq 0$, is formally only first order, i.e., only normalized. This illustrates that non-zero skewness decreases the order of the corresponding symmetric filter.

For symmetric filters the lowest order contribution in (3.9) may arise at $r = 2$ and the commutator error is of order $O(\Delta'\Delta)$. This estimate for the commutator error

applies to common second order filter such as the symmetric top-hat or Gaussian filters and has been derived before in literature [38, 47, 54]. Next, we turn to skewed filters. In this case the odd moments M_{2r-1} are nonzero and the lowest order contribution to the commutator error may arise at $r = 1$. Thus, skewness formally reduces the order of the filter and increases the scaling of the commutator error to $O(\Delta')$.

One has to realize that, although filters can be strictly a-symmetric, it is well possible that the lowest order contributions to the commutator error remain very small. Effects of skewness on the commutator error become apparent only in case the lowest order odd moments M_{2r-1} become sufficiently large. For example, the filters considered in [54] are strictly skewed filters in physical space. However, in illustrations found in this reference the odd moments were negligible compared to the even moments M_{2r} and overall the filters approximately corresponded to symmetric filters. For the skewed top-hat filter considered in this and the following chapter the first and second moment are given by $M_1 = \gamma$ and $M_2 = \frac{1}{12} + \gamma^2$. Hence, effects of skewness are expected to become relevant if the shift γ is large enough. As an indication $|M_1| \approx M_2$ for $1/10 \leq |\gamma| \leq 1/2$.

Filters for which $N > 2$ are referred to as higher order filters. Higher-order filters may be constructed in different ways, see Refs. [47, 51, 131, 133]. Typically such higher-order filters are formulated in terms of the externally specified filter-width Δ. It is important to notice that if one keeps Δ fixed in this class of filters then the effective filter-width at order N, denoted by $\Delta_e(N)$, can be shown to decrease (rapidly) with increasing N. The interpretation is appealing in order to emphasize that at fixed Δ the filtering becomes less and less effective with increasing N and, for the filters considered by us, approaches the identity operator in the limit. In fact, the limiting identity operator leaves all modes invariant which corresponds to its Fourier-transform being equal to unity for all wave-numbers. Correspondingly, the effective filter-width as defined in (2.14) is zero, in line with the limiting behavior of $\Delta_e(N)$ mentioned above.

The expression for the commutator error as given in (3.9) suggests the possibility of directly controlling its magnitude by considering higher order filters as introduced above. By requiring that certain moments M_r identically vanish, the leading order contribution to the commutator error can be controlled explicitly. Specific high-order filters serving this purpose were first proposed in [131]. In view of (3.9) all N-th order filters have the property that the implied commutator error reduces to $O(\Delta'\Delta^{N-1})$. This would allow to neglect the commutator error contributions from the filtered LES equations, simply by turning to an appropriate higher order of filtering. However, the dominant scaling behavior of the commutator error is of no consequence by itself. Rather, one has to incorporate the dominant scaling of the divergence of the turbulent stress-tensor as well, before anything more definite

can be established. We turn to this next.

Dominant scaling behavior of the SGS-stress

In order to establish the dominant scaling of the turbulent stress contributions we proceed analogous to the above derivation for the commutator error. The one-dimensional SGS-stress tensor is given by $\tau = \overline{u^2} - \overline{u}^2$ for which one readily obtains,

$$
\begin{aligned}
\tau(x) &= \int_{-\infty}^{\infty} G(s)u^2(x + \Delta(x)s)\, ds \\
&\qquad - \left\{ \int_{-\infty}^{\infty} G(s)u(x + \Delta(x)s)\, ds \right\}^2, \tag{3.12} \\
&= \int_{-\infty}^{\infty} G(s)\Big(\sum_{r=0}^{\infty} \frac{1}{r!}\Delta^r s^r \partial_x^r u^2 \Big)\, ds \\
&\qquad - \left\{ \int_{-\infty}^{\infty} G(s)\Big(\sum_{r=0}^{\infty} \frac{1}{r!}\Delta^r s^r \partial_x^r u \Big)\, ds \right\}^2, \tag{3.13}
\end{aligned}
$$

in which we used expressions for $\overline{u^2}$ and $\overline{u}$ arrived at by a Taylor series expansion similar to (3.8) (see also [17, 51]). This expression can be simplified to,

$$
\begin{aligned}
\tau(x) &= \sum_{r=0}^{\infty} \frac{M_r}{r!}\Delta^r \partial_x^r u^2 - \sum_{r=0}^{\infty} \left(\frac{M_r}{r!} \right)^2 \Delta^{2r}(\partial_x^r u)^2 \\
&\qquad - 2\sum_{q=0}^{\infty}\sum_{r=q+1}^{\infty} \frac{M_q\, M_r}{q!\, r!}\Delta^{q+r}\, \partial_x^q u\, \partial_x^r u. \tag{3.14}
\end{aligned}
$$

For an N-th order filter the scaling behavior of the turbulent stress tensor displays characteristic dominant terms. These can be inferred from (3.14) as:

$$
\tau(x) = \frac{M_N}{N!}\left(\partial_x^N u^2 - 2u\, \partial_x^N u \right)\Delta^N + O(\Delta^{N+1}). \tag{3.15}
$$

From (3.15) we observe that $\tau \sim \Delta^N$ for general N-th order filters, in case $N \geq 2$. Consequently, the relevant flux $\partial_x \tau$ scales with terms of $O(\Delta^N)$ as well as terms of $O(\Delta'\Delta^{N-1})$. We observe that the dominant formal scaling behavior is identical to that established above for the commutator error. In the special case $N = 1$, the first term in (3.15) is identically zero in view of the property $\partial_x u^2 = 2u\partial_x u$. For these filters the SGS-stress is thus unaffected by a non-zero first moment M_1 and, although $N = 1$ the turbulent stress tensor scales as $O(\Delta^2)$. This is formally one order in Δ smaller than the corresponding commutator error at $N = 1$.

Although the use of higher order filters allows additional control over the size of the commutator error and SGS-stress, the dominant scaling of both the commutator error as well as the divergence of the turbulent stress tensor with Δ and its derivatives is formally identical if $N \geq 2$. For $N = 1$ we even observe that the commutator error is formally larger than the SGS-flux. Judging from these order of magnitude estimates, this suggests that if in a certain flow the turbulent stress contributions require explicit modeling, one should also consider incorporating explicit modeling for the commutator errors. It appears to make little sense to model one of the subgrid terms and ignore the other class of subgrid contributions which are formally of equal order of magnitude.

The order of magnitude estimates provide only a fairly rough indication of the dynamic importance of the individual subgrid contributions. In fact, rather than controlling the size of the commutator errors by increasing the order of the filter as suggested before in literature, the control of the spatial variations in Δ appears to allow another method of separately influencing the size of the SGS-flux relative to that of the commutator errors. If Δ' can be kept sufficiently small, it is conceivable that the terms with the lowest order scaling in Δ have a (very) small 'pre-factor' which can even imply that only the next order terms, i.e., the turbulent stress related contributions only, require explicit treatment. In order to quantify these aspects we turn to an *a priori* analysis of the various subgrid terms in the next section and determine the actual size of the commutator errors and turbulent stress contributions in developed turbulent mixing.

3.3   A priori analysis of commutator errors in turbulent mixing flow

In this section, data of DNS of turbulent flow in a temporal mixing layer will be used to quantify the magnitude of commutator errors and SGS-fluxes for a variety of filter-width non-uniformities and filter specifications. In particular, for skewed as well as higher order filters the size of the closure terms will be determined and specific trends will be interpreted in view of the analysis presented in the previous section. We first describe the DNS, then introduce some measures with which the closure terms will be quantified and finally present *a priori* results which establish the magnitude of the terms in relation to, e.g., filter-width, skewness and order of the filter.

Description of DNS and filter-widths

For the *a priori* analysis of the commutator errors we consider turbulent flow in a temporal mixing layer. We evaluate data presented in [141]. The governing equa-
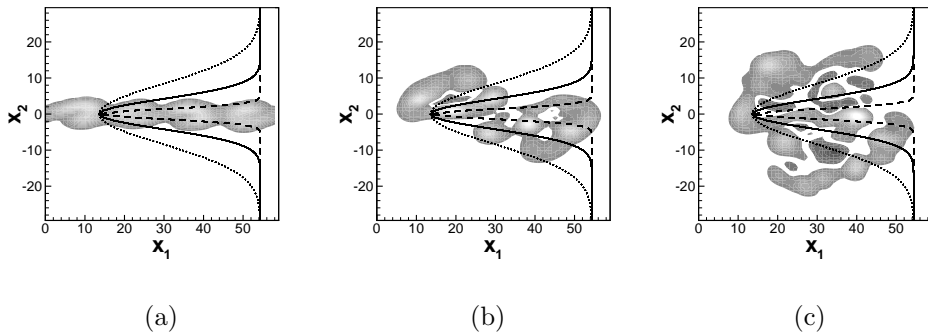
Figure 3.1: Contours of the spanwise vorticity of the temporal mixing layer at a) $t = 20$, b) $t = 50$ and c) $t = 80$. Superimposed on these figures are the non-uniform filter-width variations Δ_2 as a function of x_2 for the case $\alpha = 3/4$ and $\beta = 5$ (dotted), $\beta = 10$ (solid) and $\beta = 30$ (dashed).

tions are solved in a cubic geometry of side ℓ which is set equal to four times the wavelength of the most unstable mode according to linear stability theory. Periodic boundary conditions are imposed in the streamwise (x_1) and spanwise (x_3) direction, while in the normal (x_2) direction the boundaries are free-slip walls. The initial condition is formed by mean profiles corresponding to constant pressure, $u_1 = \tanh(x_2)$ for the streamwise velocity component and $u_2 = u_3 = 0$. Superimposed on the mean profile are two- and three-dimensional perturbation modes obtained from linear stability theory. The DNS data were obtained at a spatial resolution of 192^3 grid-cells, employing a fourth order accurate spatial discretization scheme in combination with explicit Runge-Kutta time-stepping. A full description may be found in [141].

The filter-widths that will be considered are kept constant in the x_1 and x_3 directions while in the x_2 direction we allow for significant variations in Δ. Specifically, the filter-width is reduced considerably near the centerline where the flow is most unsteady and displays rapid, large-amplitude variations. We parameterize the filter-width variations by the following two-parameter family:

$$\Delta_1 = \Delta_3 = \Delta_r, \qquad \Delta_2(x_2) = \Delta_r(1 - \alpha e^{-(\beta x_2/\ell)^2}). \qquad (3.16)$$

The reference filter-width Δ_r is taken equal to $\ell/16$, corresponding to the evaluation of LES described in [141]. In the definition of the non-uniform filter-width $\Delta_2(x_2)$, the parameter α controls the ratio between the minimal filter-width and Δ_r, i.e., α measures the 'depth' of the filter-width modulation. In addition, the parameter β controls the width of the region of the flow-domain in which the filter-width varies significantly. The maximal value of α considered here is $\alpha = 3/4$ which corresponds to a minimal filter-width $\Delta_{\min} = \Delta_r/4 = \ell/64$ which is equal to three grid-cells in the DNS grid. In figure 3.1 different non-uniform filter-width variations are

shown alongside snapshots of the evolving flow. By varying α and β and specific properties of the filter such as skewness and order, a systematic assessment of the commutator errors can be made.

Measures for the closure terms

To quantify the dynamic effects of the closure terms we concentrate on the decomposition of the non-uniformly filtered convective flux. This decomposition follows from the application of a non-uniform filter operator $\mathcal{L}$ to the convective terms in the momentum equations, i.e.,

$$\overline{\partial_j(u_i u_j)} = \partial_j(\overline{u}_i \overline{u}_j) + \partial_j \tau_{ij} + \mathcal{C}_j[u_i u_j], \qquad (3.17)$$

where we distinguish a mean, SGS-flux and commutator error contribution on the right-hand side of (3.17) respectively. Since the filter-width is considered non-uniform only in the x_2-direction the commutator error $\mathcal{C}_j(u_i u_j)$ reduces to $\mathcal{C}_2(u_i u_2)$.

To quantify the magnitude of the various fluxes in (3.17) the L_2-norm is considered, which for a field f is defined as,

$$\|f\|^2 = \frac{1}{|\Omega|} \int_\Omega f(\mathbf{x})^2 \, d\mathbf{x}. \qquad (3.18)$$

The domain of integration Ω can coincide with the entire flow-domain ℓ^3 and $d\mathbf{x} = dx_1 dx_2 dx_3$, but for some quantities we will restrict the integration to the homogeneous directions x_1 and x_3 and adapt Ω accordingly. This allows to identify the variation of the field f in the normal direction.

Next to the L_2-norm of the individual contributions in (3.17) we also consider the dissipation rate for the resolved kinetic energy,

$$\varepsilon = -\partial_t \overline{E} = -\partial_t \left(\int_\Omega \tfrac{1}{2} \overline{u}_i \overline{u}_i \, d\mathbf{x} \right). \qquad (3.19)$$

Using the non-uniformly filtered momentum equation for incompressible flow (3.5) one obtains,

$$\varepsilon = \int_\Omega \left\{ -\overline{u}_i \partial_j(\overline{u}_i \overline{u}_j) - \overline{u}_i \partial_i \overline{p} + \frac{1}{Re} \overline{u}_i \partial_{jj} \overline{u}_i - \overline{u}_i \partial_j \tau_{ij} \right. $$
$$\left. -\overline{u}_i \mathcal{C}_j(u_i u_j) - \overline{u}_i \mathcal{C}_i(p) + \frac{1}{Re} \overline{u}_i \Big[\mathcal{C}_j(\partial_j u_i) + \partial_j \mathcal{C}_j(u_i) \Big] \right\} d\mathbf{x}. \quad (3.20)$$

The total contribution arising from the nonlinear convective flux involves, next to the turbulent stress terms, the 'basic mean' contribution $\overline{u}_i \partial_j(\overline{u}_i \overline{u}_j)$ and the

'basic commutator error' term $\overline{u}_i \mathcal{C}_j(u_i u_j)$. Combined, these may be written in a convenient form as,

$$
\begin{aligned}
\overline{u}_i \partial_j(\overline{u}_i \overline{u}_j) &+ \overline{u}_i \mathcal{C}_j(u_i u_j) \\
&= \left(\overline{u}_i \partial_j(\overline{u}_i \overline{u}_j) - \tfrac{1}{2}\overline{u}_i \overline{u}_i \partial_j \overline{u}_j \right) + \left(\overline{u}_i \mathcal{C}_j(u_i u_j) - \tfrac{1}{2}\overline{u}_i \overline{u}_i \mathcal{C}_j(u_j) \right), \\
&= \tfrac{1}{2}\partial_j(\overline{u}_i \overline{u}_i \overline{u}_j) + \left(\overline{u}_i \mathcal{C}_j(u_i u_j) - \tfrac{1}{2}\overline{u}_i \overline{u}_i \mathcal{C}_j(u_j) \right),
\end{aligned}
\tag{3.21}
$$

where use was made of the non-uniformly filtered continuity equation (3.4): $\partial_j \overline{u}_j = -\mathcal{C}_j(u_j)$. This decomposition of the convective flux contribution incorporates the non-solenoidal features of the non-uniformly filtered velocity-field [141, 122]. Formally, it is analogous to the formulation that is commonly used for compressible flow; in the latter case

$$
\varepsilon = -\partial_t \left(\int_\Omega \tfrac{1}{2}\overline{\rho} \widetilde{u}_i \widetilde{u}_i \, d\mathbf{x} \right),
\tag{3.22}
$$

where $\widetilde{u}_i$ denotes the Favre-filtered velocity (2.27). In the compressible case the velocity is non-solenoidal for physical reasons whereas here $\partial_j \overline{u}_j \neq 0$ due to non-uniformity of the filter. Following this convention, we may express ε as

$$
\varepsilon = \varepsilon_{\text{mean}} + \varepsilon_{\text{p}} + \varepsilon_{\text{visc}} + \varepsilon_{\text{SGS}} + \varepsilon_{\text{CE}},
\tag{3.23}
$$

where we identified different contributions defined as follows:

$$
\varepsilon_{\text{mean}} = \int_\Omega \overline{u}_i \, \partial_j \overline{u}_i \overline{u}_j - \tfrac{1}{2}\overline{u}_i \overline{u}_i \, \partial_j \overline{u}_j \, d\mathbf{x} = \int_\Omega \tfrac{1}{2}\partial_j(\overline{u}_i \overline{u}_i \overline{u}_j) \, d\mathbf{x},
\tag{3.24}
$$

$$
\varepsilon_{\text{p}} = \int_\Omega \overline{u}_i \, \partial_i p \, d\mathbf{x},
\tag{3.25}
$$

$$
\varepsilon_{\text{visc}} = -\frac{1}{Re} \int_\Omega \overline{u}_i \, \partial_j \partial_j \overline{u}_i \, d\mathbf{x},
\tag{3.26}
$$

$$
\varepsilon_{\text{SGS}} = \int_\Omega \overline{u}_i \, \partial_j \tau_{ij} \, d\mathbf{x},
\tag{3.27}
$$

$$
\varepsilon_{\text{CE}} = \int_\Omega \overline{u}_i \, \mathcal{C}_j(u_i u_j) - \tfrac{1}{2}\overline{u}_i \overline{u}_i \, \mathcal{C}_j(u_j) \, d\mathbf{x}.
\tag{3.28}
$$

These individual terms denote the mean convective contribution, the pressure contribution, the viscous dissipation, the SGS-contribution and the effect of the commutator error, respectively. The contribution due to the pressure, ε_{p}, was shown to be negligible at the low Mach number ($M = 0.2$) considered in the DNS [141]. In case Ω is the entire domain (ℓ^3) the mean dissipation $\varepsilon_{\text{mean}}$ is zero in view of the boundary conditions. As mentioned above, by restricting the integration domain to the homogeneous x_1 and x_3 directions, the definitions (3.23)-(3.28) reduce to local dissipation – or transport terms.
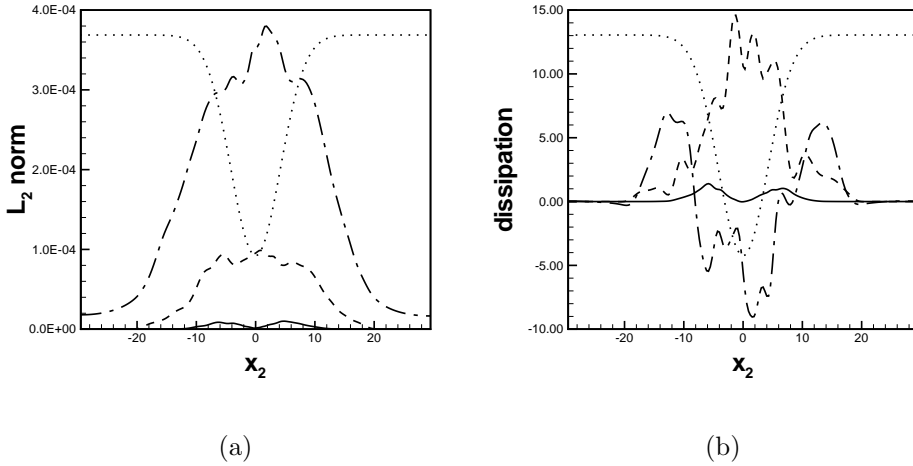
(a)   (b)

Figure 3.2: (a) L_2-norms of the decomposition (3.17) in the streamwise direction and (b) contributions to the resolved kinetic energy dissipation of the mean convective flux (dash-dotted), SGS-flux $\partial_j \tau_{ij}$ (dashed) and commutator error (solid). We use $\alpha = 3/4$, $\beta = 10$ and consider the field at $t = 60$. The variations of the filter-width as function of x_2 are depicted by the dotted line.

The evaluation of the various closure terms and diagnostics from the DNS-data employs different filters and filter-widths. Moreover, different numerical methods may be adopted in the post-processing of the data. The basic methods adopted in this chapter are formally second order accurate. For the numerical integration the trapezoidal rule has been applied. If data are required at locations not contained in the DNS-grid, linear interpolation is used to obtain approximate values. Finally, derivatives are approximated using second order central finite differences with mesh-spacing $\Delta_r/4$ which is equal to the minimal filter-width incorporated. Next to the basic combination of second order methods we also repeated part of the analysis using fourth order accurate methods. We observed small changes in specific results. However, turning to such higher-order methods does not lead to alterations in the conclusions that may be drawn. Therefore, in the sequel we will only present results obtained using the second order methods.

After these preparations we next present the results of the *a priori* analysis, concentrating on the decomposition (3.17) and the kinetic energy dissipation rate (3.23). First, we turn to symmetric second order filters and consider different non-uniform filter-widths to provide a point of reference. Then we consider effects of skewness in combination with the top-hat filter. Finally, we introduce a class of high-order filters, based on the Gaussian filter, and explicitly calculate the size of the SGS-fluxes and the commutator errors for increasing filter-order.

Magnitude of commutator errors for second order symmetric filters

In figure 3.2 results are shown in case the symmetric top-hat filter is applied to the field at $t = 60$ and the non-uniform filter-width is determined by $\alpha = 3/4$ and $\beta = 10$. For the L_2-norms only the results from the field in the streamwise direction, i.e., originating from $\partial_j(u_1 u_j)$, are shown. The L_2-norms corresponding to $\partial_j(u_2 u_j)$ and $\partial_j(u_3 u_j)$ display similar behavior and are not shown. The graphs in figure 3.2(a) indicate that the L_2-norm of the commutator error is about an order of magnitude smaller than the SGS-flux $\partial_j \tau_{ij}$ for this specific case. The SGS-flux itself is again one order of magnitude smaller than the mean convective flux $\partial_j(\overline{u}_1 \overline{u}_j)$. The latter finding is consistent with previous observations made for this flow [137].

Regarding the contributions in figure 3.2(b) the SGS-flux represents almost all the dissipation of resolved kinetic energy. In addition, the net positive and negative contributions originating from the mean convective flux are seen to approximately cancel, confirming that $\varepsilon_{\mathrm{mean}} = 0$ if integrated over the entire flow-domain. Finally, the contribution from the commutator error is found to be positive and therefore a dissipative term in this case. The location of maximum local contribution to the commutator error dissipation coincides approximately with the location where Δ' is maximal, consistent with the basic analysis in the previous section. The local contribution to the SGS-dissipation $\varepsilon_{\mathrm{SGS}}$ is maximal near the centerline of the flow. Similarly to the L_2-norm, the maximum contribution to the commutator error dissipation $\varepsilon_{\mathrm{CE}}$ is about an order of magnitude smaller than the maximum of SGS-contribution.

To further classify the type of contributions to the dynamics of the resolved kinetic energy we next distinguish the explicit sources of dissipation and production. The positive ε^+ and negative contributions ε^- for the SGS-flux are defined as:

$$\varepsilon_{\mathrm{SGS}}^+(x_2) = \int_\Omega \max(0, \overline{u}_i\, \partial_j \tau_{ij})\, dx_1 dx_3, \qquad (3.29)$$

$$\varepsilon_{\mathrm{SGS}}^-(x_2) = \int_\Omega \min(0, \overline{u}_i\, \partial_j \tau_{ij})\, dx_1 dx_3. \qquad (3.30)$$

Likewise, we can formulate $\varepsilon_{\mathrm{CE}}^+$ and $\varepsilon_{\mathrm{CE}}^-$ for the commutator error. Production ε^- is often associated with "backscatter" in literature. In figure 3.3 the production and dissipation corresponding to the SGS-fluxes and commutator errors are shown. In both cases the dissipation is larger than the production, resulting in a net dissipation as already shown in figure 3.2(b). The ratio between the total production and total dissipation, defined as the integral over x_2 of $\varepsilon^\pm(x_2)$, is observed to be about the same for the SGS-fluxes and the commutator errors.

Next we compare different non-uniform filter-widths $\Delta_2(x_2)$. In view of (3.9),

<div align="center">(a)   (b)</div>
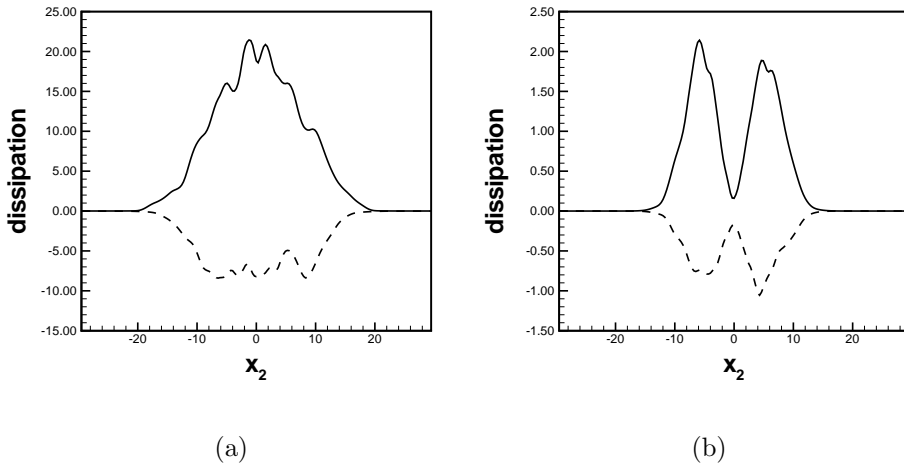
Figure 3.3: The explicit dissipation (solid) and production (dashed) contributions to the resolved kinetic energy dissipation due to (a) the SGS-flux and (b) the commutator error.

<div align="center">(a)   (b)</div>
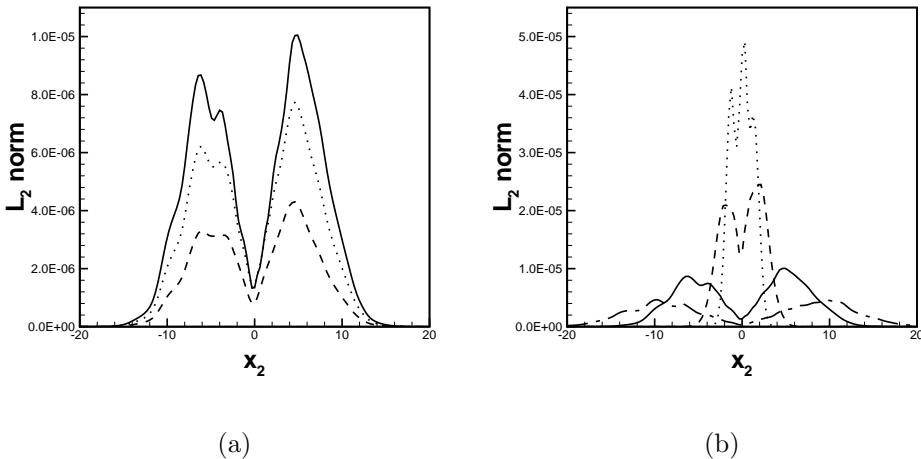
Figure 3.4: The L_2-norm of the commutator error in the streamwise direction at $t = 60$: (a) $\alpha = 1/4$ (dashed), $1/2$ (dotted) and $3/4$ (solid) with β fixed to 10; (b) α fixed to $3/4$ and $\beta = 5$ (dash-dotted), 10 (solid), 30 (dashed) and 60 (dotted).

the second order top-hat filter should give rise to a commutator error that scales with $\Delta\Delta'$. The influence of Δ' on the commutator errors can be controlled by varying the parameters α and β. In figure 3.4 the L_2-norms are shown for different combinations of α and β. An increase in either α or β corresponds to an increase in Δ'. Correspondingly, the larger and spatially more localized variations in the filter-width lead to considerable increases in the commutator errors. This may readily be inferred from figures 3.4(a) and 3.4(b).

In complex turbulent flows one may wonder which strategy of spatially varying Δ is best. On the one hand one may select a fairly gradual transition between a region of large/small filter-width to a nearby region of small/large filter-width. One may think of a case as represented by $\beta = 5$ in figure 3.4(b). Then, Δ' is small and so is the commutator error; no explicit modeling of this contribution appears to be required. This seems to be the most favorable strategy, but one has to realize that it is also computationally the most expensive. A gradual transition requires a wide transition-region which may be wasteful in terms of number of grid-points. On the other hand, if a relatively sharp transition is considered, e.g., illustrated by $\beta = 60$, the derivative Δ' may become sufficiently large to lead to a commutator error which may no longer be neglected. In fact, the commutator error can locally become as important as the SGS-fluxes and correspondingly the commutator error should be explicitly modeled. Depending on whether or not adequate models for the commutator error contributions can be formulated, one may be tempted to adopt the 'safer' more expensive option or the more efficient option which requires a commutator error model.

We next proceed by considering the effect of skewness of the filter and subsequently turn to higher order filters. In the latter case we will explicitly compare the magnitude of the commutator errors with that of the SGS-fluxes for increasing order of filtering.

Skewness and commutator errors

An efficient implementation of non-uniform filters gives rise to skewed filters in a very natural way. Consider filtering at a grid-location x_i. In one dimension this can be obtained by integrating over the interval $[x_{i-m}, x_{i+n}]$ where m and n are suitable integers. Even if the filter corresponds to a 'symmetric' choice of points around x_i, i.e., $m = n$, the non-uniformity of the grid in physical space will imply a-symmetry and non-zero skewness. Skewed filters are virtually unavoidable close to solid walls while in other flow-regions skewness arises quite naturally from grid-non-uniformities, if one uses this grid-based implementation. Strictly speaking, grid and filter-width non-uniformities do not have to correspond directly to each other and non-uniform filters can also be defined on uniform grids, as is considered
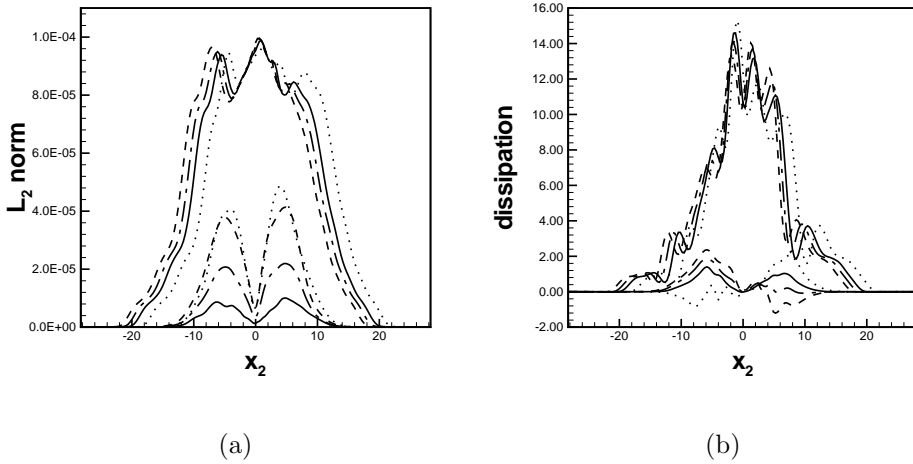
(a)   (b)

Figure 3.5: (a) L_2-norms of the SGS-fluxes and commutator errors in the stream-wise direction and (b) contributions to the resolved kinetic energy dissipation at $t = 60$ for the a-symmetric top-hat filter in case $\gamma = 0$ (solid), $\gamma = 0.25$ (dash-dotted), $\gamma = 0.50$ (dashed) and $\gamma = -0.50$ (dotted). The upper set of curves correspond to the SGS-fluxes, the lower set of curves denote the effect of the commutator errors.

here. Either way, this sketch illustrates that typical filters in complex flow domains are likely to be skewed and effects of skewness deserve to be studied in detail.

In the previous section it has been shown that skewness of a filter can have a considerable effect on the size of the commutator error. Skewness implies a decrease of the order of the filter compared to the associated symmetric case. For filters that are second order at zero skewness, nonzero skewness leads to a commutator error of order $O(\Delta')$. Here, we will explicitly calculate the size of the commutator errors for the skewed top-hat filter as defined in table 2.1 with $\gamma \neq 0$. For simplicity, we consider the case of constant skewness, which is adequate to illustrate the main effects.

In figure 3.5 the L_2-norm and local energy transport $\varepsilon(x_2)$ of the commutator error and the SGS-fluxes are shown as function of the shift-parameter γ. From the series expansion of the SGS-stress it was concluded that this term was not affected by a non-zero first moment. In figure 3.5(a) we observe indeed that the size of the SGS-flux is largely unaffected by the value of the shift $\gamma = M_1$. This is in sharp contrast with the L_2-norm of the commutator error for which a significant increase is observed with increasing $|\gamma|$ as predicted by the analytical estimates obtained in the previous section.

Additional illustrations of skewness in relation to the commutator error can be observed in figure 3.5(b), where the local contributions $\varepsilon_{\mathrm{SGS}}(x_2)$ and $\varepsilon_{\mathrm{CE}}(x_2)$ are shown. The SGS contributions are quite unaffected by the skewness of the filter, while the commutator error effect increases with $|\gamma|$. In case skewed filters are applied the commutator error contribution to the resolved kinetic energy dissipation looses its symmetry across the centerline at $x_2 = 0$. The resulting commutator error effect can even change sign, either above or below the centerline depending on γ, which indicates that not only the size but also the dynamical consequences of the commutator error may depend considerably on the skewness. In the following chapter it will be shown that symmetric filters give rise to dissipative effects and non-zero skewness is associated with additional dispersive contributions [123, 125].

Finally, we observe that in certain regions of the flow-domain the effects of the SGS-fluxes and the commutator errors are of comparable magnitude in case the skewness is sufficiently large. So, unlike most cases involving symmetric second order filters, strongly skewed lower order filters imply that one can no longer ignore the explicit inclusion of commutator errors in the subgrid modeling.

In the following paragraphs higher order filters will be considered and the decrease of the commutator error with increasing filter-order will be compared with that of the SGS-fluxes. First the construction of a specific class of higher order filters will be described. Estimates for the commutator error and SGS-fluxes will subsequently be discussed.

Construction of higher order filters

In literature various classes of higher order filters have been proposed. Vasilyev *et al.* [133] constructed a class of filters, which was later extended to complex geometries by Marsden *et al.* [87] and by Haselbacher and Vasilyev [64]. These filters are based on a non-uniform grid to achieve non-uniform filtering. In our application here, we would prefer to be able to adopt a wide range of different non-uniform filter-widths without having to change the grid each time, i.e., achieve a level of independence between filter-width and grid non-uniformities. To arrive at such a formulation the so-called Daubechies construction is used [26].

The construction of Daubechies filters relies on a wavelet-type transformation of a general base filter $G_0(s)$. We require that all moments M_r, $r \geq 0$ of the base-filter $G_0(s)$ exist and that the base-filter is properly normalized, i.e., $M_0 = 1$. The desired higher order filter-kernel $G_N(s)$ is expressed as,

$$G_N(s) = \sum_{j=0}^{n-1} d_j G_0\left(\frac{s}{j+1}\right), \tag{3.31}$$

N	$\{d_j\}$	Δ_e
2	$\{1\}$	1.023Δ
4	$\{\frac{4}{3}, -\frac{1}{6}\}$	0.805Δ
6	$\{\frac{3}{2}, -\frac{3}{10}, \frac{1}{30}\}$	0.740Δ
8	$\{\frac{8}{5}, -\frac{2}{5}, \frac{8}{105}, -\frac{1}{140}\}$	0.710Δ

Table 3.1: Resulting coefficients $\{d_j\}$ for several lower order filters. The effective filter-width Δ_e corresponds to higher order filters using a Gaussian filter as base-filter.

where d_j are appropriate constants, which will be determined next taking (3.11) into account. We notice that the filter-kernel G_N has a much wider support compared to the original base-filter since s is divided by $j + 1$.

We selected the Gaussian filter as base-filter and restrict ourselves here to symmetric filters. By definition the higher order filter-kernel inherits the symmetry properties of the base-filter and the odd moment M_{2r+1} of G_N are zero. We define $n = N/2$ in (3.31). The requirements for higher-order filters (3.11) give rise to the following system of equations for the unknown coefficients $\{d_j\}$:

$$\delta_{i0} = \int s^{2i} \sum_{j=0}^{n-1} d_j G_0 \left(\frac{s}{j+1}\right) ds = M_{2i} \sum_{j=0}^{n-1} d_j (j+1)^{2i+1}, \qquad (3.32)$$

for $i = 0, \ldots, n-1$ and M_{2i} are the moments of the base-filter. For second-order base filters $M_{2i} \neq 0$ and by definition $M_0 \equiv 1$. Hence (3.32) can be multiplied by M_{2i}^{-1} and an $n \times n$ linear system $\mathbf{Ad} = \mathbf{b}$ for $\mathbf{d} = [d_0, d_1, \ldots, d_{n-1}]$ results where $\mathbf{A}$ and $\mathbf{b}$ are defined as,

$$\mathrm{A}_{ij} = (j+1)^{2i+1}, \qquad b_i = \delta_{i0}, \qquad i, j = 0, \ldots, n-1. \qquad (3.33)$$

It can be shown that the matrix A is invertible. For various n explicit construction of the higher order filters can be obtained and in table 3.1 resulting coefficients are given for several higher order filters as well as the resulting effective filter-width Δ_e (2.14). The previously mentioned decrease of the effective filter-width $\Delta_e(N)$ with increasing order can clearly be observed.

The moments M_{2i} depend on the specific choice for the base-filter. However, the coefficients $\{d_j\}$ follow from $\mathbf{Ad} = \mathbf{b}$ from which these moments have been removed; consequently the coefficients $\{d_j\}$ are independent of the specific choice of the symmetric base-filter. This construction can also be developed for a-symmetric filters in which case $\mathrm{A}_{ij} = (j+1)^{i+1}$ and $n = N$. In figure 3.6 some resulting higher order filters $G_N(s)$ as well as their Fourier-transform $H_N(\omega)$ are depicted. In figure
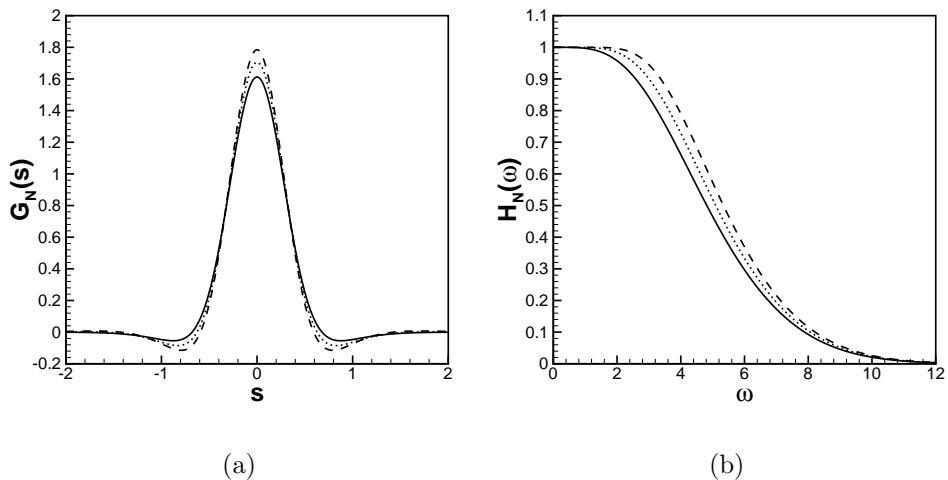
Figure 3.6: a) Filter kernel G_N and b) Fourier transform H_N of several higher order filters using a Gaussian base filter: 2nd order (solid), 4th order (dotted) and 8th order (dashed).

3.6(b) we see that with increasing order more and more modes are quite unaffected by the filter confirming the reasoning put forward on page 52 that filtering becomes less and less effective with increasing order. In figure 3.6(a) we observe that as the desired filter-order is increased the filter-kernel is seen to develop characteristic changes of sign which imply that the realizability conditions for the turbulent stress tensor are no longer maintained [142].

For the evaluation of the DNS-data the integrals are numerically approximated using the trapezoidal rule and the discrete filter can be formulated as,

$$\overline{u}_i = \sum_{j=-n_-}^{n_+} w_{ij} u_{i+j}, \tag{3.34}$$

where the filter-weights w_{ij} are given by,

$$w_{ij} = \frac{x_{j+1} - x_{j-1}}{2} \frac{1}{\Delta(x_i)} G_N\left(\frac{x_j - x_i}{\Delta(x_i)}\right). \tag{3.35}$$

In this approach the numbers n_- and n_+ should be chosen fairly large in order for the moments M_r, $r = 1, \ldots, N - 1$ to be accurately captured. We selected $n_- = n_+ = 96$, i.e., integrate over all points available in the DNS-data [141, 144]. The discrete moments

$$M_r \approx \sum_{j=-n_-}^{n_+} w_{ij} \left(\frac{x_{i+j} - x_i}{\Delta_i}\right)^r, \tag{3.36}$$

(a)   (b)
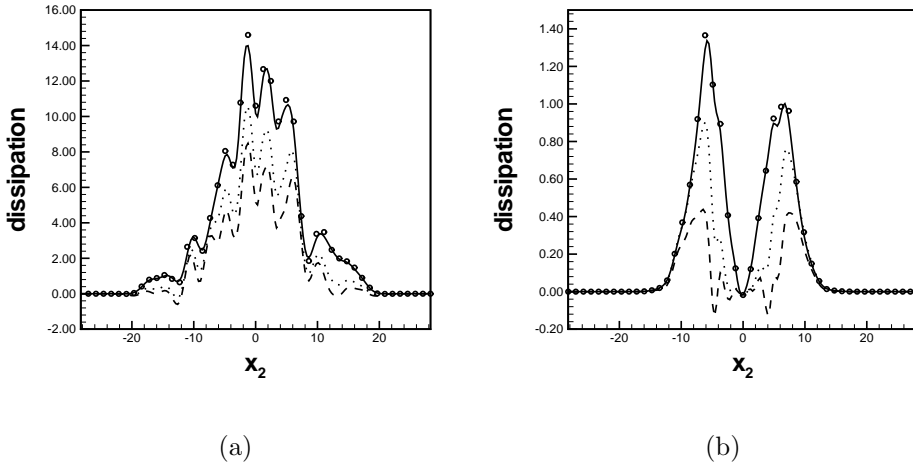
Figure 3.7: Contribution to the dissipation of the resolved kinetic energy caused by (a) the SGS-flux and (b) by the commutator error at $t = 60$ for higher order filters; second order Gaussian (solid), fourth order (dotted) and sixth order (dashed). Also depicted are the results obtained with the second order top-hat filter (circles).

were found to be smaller than 10^{-5}, for all moments $r = 1, \ldots, N-1$, up to $N = 8$ for the cases considered. Hence, up to eighth order filtering is achieved in this way.

Magnitude of SGS-fluxes and commutator errors as function of filter-order

In section 3.2 it was shown that an N-th order filter gives rise to a commutator error which scales with $O(\Delta'\Delta^{N-1})$. Also, for $N \geq 2$ the SGS-stress τ_{ij} scales with $O(\Delta^N)$, which leads to a SGS-flux $\partial_j \tau_{ij}$ with contributions of $O(\Delta^N)$ and $O(\Delta'\Delta^{N-1})$. Hence, in regions where Δ' is sufficiently large, both SGS-flux and commutator error display identical dominant scaling in Δ controlled by the order of the filter. Consequently, both contributions may require explicit subgrid modeling in such regions. To further illustrate this, we will next extend the dominant scaling analysis with the calculation of the actual size of the SGS-flux and commutator errors in turbulent mixing. We will use the symmetric high order Daubechies filters with non-uniform filter-widths constructed above.

In figure 3.7 the local contributions $\varepsilon_{\mathrm{SGS}}$ and $\varepsilon_{\mathrm{CE}}$ are shown for several higher

order filters. First, we compared the Gaussian filter with the symmetric top-hat filter. These two second order filters are shown to yield only minor differences, confirming findings in [142]. In figure 3.7 the strong reduction of the contribution of both the SGS-flux and the commutator error with increasing filter-order can be observed. Roughly speaking the maximal local SGS-flux contribution decreases by about 30% for every increase of the filter-order by two. The size of the commutator error contribution is seen to be reduced slightly more rapidly with increasing order of the filter. When N changes from two to four the maximum commutator error contribution decrease by about 35% and by an additional 50% when N is increased to six. We hence clearly observe that both the SGS-flux and commutator error contributions reduce in a fairly comparable way with increasing order of filtering. The specific implementation of the higher order filters used here may induce some inaccuracy in the evaluation of the higher order cases. This does not permit a further quantitative evaluation of the observed behavior. However, the general trends are sufficiently strong to illustrate the predicted decrease of *both* contributions as N increases, which was the central point of this analysis.

The use of higher order filters not only influences the dominant scaling of the subgrid terms but it may also affect the construction of acceptable subgrid models. It is not necessarily true that SGS-models which are accurate in combination with ordinary second order filters work equally well for higher order filters. For example, the standard Smagorinsky model [111, 91] contains an explicit scaling with Δ^2 which also carries over to the popular dynamic model [40]. In addition, the well known gradient or Clark model is explicitly based on filters with a non-zero second moment [141, 23]. In case higher-order filters are adopted to try to reduce the explicit influence of the commutator error, it appears unavoidable that one should also incorporate corresponding changes in the basic model-assumption for the SGS-stresses, e.g., correct the model to comply with the theoretical scaling. Similarity models such as Bardina's model [7] or Leray's model [43] do not require such an explicit alteration; the proper dominant scaling is already contained in the definition of these models.

The analysis in this and the previous section has indicated that skewness of a filter, which is often unavoidable, can have a strong influence on the size of the commutator error relative to the SGS-flux. Moreover, sufficiently rapid variations in the local filter-width may induce local situations in which the commutator error is no longer negligible compared to the SGS-fluxes. Finally, the use of higher order filters does not offer an independent control over the size of either type of subgrid terms. Hence, in various situations or for the sake of retaining appropriate efficiency in LES of complex flows, one has to resort to explicitly developing specific

models for the commutator error. We will present an analysis of commutator error models in the next chapter.

3.4   Concluding remarks and discussion

In this chapter we presented results of research into the commutator error in LES by investigating it scaling with the gradient of the filter-width and the order of the filter. The commutator error arises in case a filter with non-uniform filter-width is applied to the Navier-Stokes equations. The dynamic consequences of the commutator error received comparably little attention in literature. However, for the application of LES to practical situations in which complex flow phenomena are present in a complex flow domain, the use of a filter-width which depends on space and/or time is considered very advantageous [54]. An investigation of the associated commutator error is a pre-requisite before filters with non-uniform filter-width can be applied with confidence.

For incompressible flow the main commutator error arises from filtering the convective flux $\partial_j(u_i u_j)$. It can be expressed as:

$$\mathcal{C}_j(u_i u_j) \;=\; \overline{\partial_j u_i u_j} - \partial_j \overline{u_i u_j}, \tag{3.37}$$

and should be directly compared with the SGS-fluxes $\partial_j \tau_{ij}$ involving the turbulent stress tensor τ_{ij}. Using Taylor expansions the influence on the commutator error arising from the filter-width Δ, its spatial derivative $\partial_j \Delta$ or the order of the filter, has been established. For general N-th order filters the commutator error was shown to scale with $\Delta' \Delta^{N-1}$. For common filters such as the symmetric top-hat and Gaussian filters this implies a scaling with $\Delta' \Delta$. The scaling even reduces to $O(\Delta')$ for first order filters which arise from skewed versions of popular second order filters. From a similar analysis the SGS-stress tensor τ_{ij} scales with $O(\Delta^N)$ in case $N \geq 2$ and with $O(\Delta^2)$ for $N = 1$. This yields an SGS-flux $\partial_j \tau_{ij}$ that scales with a formally dominant contribution of $O(\Delta' \Delta^{N-1})$ and sub-dominant term of $O(\Delta^N)$. In case $|\partial_j \Delta|$ is sufficiently large this scaling analysis indicates that both the commutator error and the SGS-flux behave in the same way. In fact, this analysis suggests that the use of higher order filters does not allow an *independent* control over the commutator error compared to the SGS-flux, as was hinted at before [131, 133]. Moreover, for skewed filters, additionally with sharp variations in filter-width the explicit modeling of both closure terms appears unavoidable.

Using DNS-data of the temporal mixing layer [141] the magnitude of the commutator error and the SGS-flux was explicitly calculated in order to complement the dominant scaling analysis. The use of turbulent flow data allowed for a quantitative comparison between the dynamical importance of the commutator error

and the SGS-stress. The effect of skewness of the filter on the commutator error showed to be considerable in certain cases, consistent with the observation that the order of a filter is reduced by one if the kernel is skewed. For the commonly adopted top-hat and Gaussian filters this is especially important because the SGS-stress is unaffected by a non-zero first moment M_1. The *a priori* analysis reveals that strongly skewed filters induce a commutator error which becomes locally as important as the SGS-stress and thus both closure terms would require explicit modeling. Likewise, the commutator error requires explicit modeling in case $|\partial_j \Delta|$ becomes sufficiently large. Finally, the influence of the order of the filter on the magnitude of the closure terms was determined and the global trends were found to be in line with the scaling analysis.

Since very little developments have been made in the explicit modeling of commutator errors, it is natural to consider under what conditions these terms can safely be neglected. Unlike suggestions made in literature that this can be achieved by adhering to higher order filters, an *independent* control over the size of the commutator errors compared to the SGS-fluxes is obtained only by properly restricting spatial variations of the filter-width. Keeping the gradient of the filter-width small presents itself as a favorable strategy for avoiding the commutator error. Unfortunately, with this option one remains quite close to the uniform filter-width situation and this does not offer a flexible and computationally effective adaptation to complex flows in complex domains.

Chapter 4

Lagrangian dynamics of commutator errors

In this chapter[1] we will introduce and discuss the approximate Lagrangian behavior of the commutator error. After a short introduction, in section 4.2 the dynamics of the resolved kinetic energy is introduced and leads to the Lagrangian interpretation of the dynamics of the commutator error. *A priori* testing of this dynamical behavior in terms of the transport of kinetic energy is presented in section 4.3. Section 4.4 is devoted to the analysis and testing of several models for the commutator error $\mathcal{C}_j(u_i u_j)$ including a model based on the Lagrangian interpretation. Finally the results are summarized in section 4.5.

4.1 Introduction

In recent years the demand has become stronger for LES to be extended to realistic flow situations as encountered, e.g., in industry, aerodynamics and local weather prediction. To efficiently extend the capabilities of LES to such complex flow situations we require the filter-width to become non-uniform, dependent on space and/or time. With the introduction of a non-uniform filter additional closure terms emerge generally referred to as commutator-errors (2.29) [54, 51, 122, 47, 52]. Compared to the SGS-stress τ_{ij}, the commutator-error received little attention in

---

[1]This chapter is largely based on Van der Bos and Geurts [123].

literature. However, as shown in the previous chapter, the commutator-error can become dynamically important in case the local variations in the filter-width are strong enough.

In this chapter an explicit Lagrangian interpretation of the dynamics of commutator-errors is provided which directly suggests a corresponding model for the commutator error. We examine the effect of commutator-errors on the transport of resolved kinetic energy. It will be shown that the commutator-error can be associated with the apparent local creation and destruction of resolved flow-features in case the filter-width is decreased or increased along a flow-path respectively. As a consequence, the amount of kinetic energy which is locally resolved varies when filter-width variations are encountered along a flow-path. The Lagrangian interpretation suggests to model the commutator-error in terms of the material derivative of the filter-width. This model may capture both spatial as well as temporal variations in the filter-width. We will formulate the explicit Lagrangian commutator-error model and test it against other Commutator-Error-models (CE-models) that are based on similarity assumptions instead (section 4.4) [51, 122, 47].

The type of non-uniform filter in the definition of the commutator-error explicitly affects the type of dynamic contributions of these terms. We will investigate both the commonly used symmetric filters as well as skewed filters. Symmetry or skewness of a filter is associated with the filter-kernel being an even function or not. The use of skewed filters is sometimes unavoidable, e.g., when the local filter-width is defined in terms of a fixed number of grid-intervals. This implies smaller filter-width in case the grid is locally refined, but also implies skewness of the filter. As shown in the previous chapter the dynamic effect of the commutator-error becomes significantly larger when skewed filters are used. In this chapter both the dispersive and dissipative effects associated with filter-skewness [54, 51, 133] will be included explicitly in the Lagrangian modeling. *A priori* testing of these models using simulation data of turbulent mixing establishes that explicitly accounting for skewness is essential in order to maintain acceptable accuracy.

The organization of this chapter is as follows. In section 4.2 we consider the dynamic effect of a non-uniform filter-width on the evolution of the resolved kinetic energy. We propose, in addition, a new explicit parameterization for the transport of resolved kinetic energy. In section 4.3 we describe the *a priori* testing of this model for the transport of resolved kinetic energy. Section 4.4 contains the results of *a priori* testing of the proposed Lagrangian model for the commutator-error $\mathcal{C}_j(u_i u_j)$ as arises in the momentum equations against CE-models based on simi-

larity assumptions. Finally, in section 4.5 some concluding remarks are collected.

4.2 Resolved kinetic energy dynamics: consequences of non-uniform filtering for dissipation and dispersion

In this section we concentrate on the local transport of resolved kinetic energy for incompressible flow. First, we derive the transport equation for resolved kinetic energy in case the filter is spatially non-uniform. Then, through a 'Lagrangian' interpretation of the non-uniform filtering, the importance of skewness and of spatial variation of the filter-width is identified (subsection 4.2.1). Finally, using a single-mode analysis, the explicit dissipative and dispersive contributions of the commutator error are illustrated. Combined with the Lagrangian interpretation of the commutator errors, this points toward a proposition for the explicit modeling of these effects (subsection 4.2.2). The analysis of the kinetic energy dynamics in actual direct numerical simulation of developed turbulent mixing is postponed until section 4.3.

To characterize the various contributions to the evolution of resolved kinetic energy, we focus on the local transport denoted by $\psi = -\partial_t(\frac{1}{2}\overline{u}_i\overline{u}_i)$. The local transport of resolved kinetic energy is related to the dissipation rate of kinetic energy ε introduced in (3.19) by $\varepsilon = \int_\Omega \psi\,d\mathbf{x}$. Hence the variable ψ truly captures the local effects of the various terms. Starting from the filtered momentum equation (3.5) and taking the inner product with $\overline{u}_i$ one can obtain an expression for the transport of resolved kinetic energy [123],

$$
\begin{aligned}
\psi &= -\overline{u}_i\partial_j(\overline{u}_i\overline{u}_j) - \overline{u}_i\partial_i\overline{p} + \frac{1}{Re}\overline{u}_i\partial_{jj}\overline{u}_i - \overline{u}_i\partial_j\tau_{ij} \\
&\quad -\overline{u}_i\mathcal{C}_j(u_iu_j) - \overline{u}_i\mathcal{C}_i(p) + \frac{1}{Re}\overline{u}_i\Big[\mathcal{C}_j(\partial_ju_i) - \partial_j\mathcal{C}_j(u_i)\Big].
\end{aligned}
\tag{4.1}
$$

Analogous to (3.23) we may then decompose ψ as,

$$
\psi = \psi_{\text{mean}} + \psi_{\text{p}} + \psi_{\text{visc}} + \psi_{\text{SGS}} + \psi_{\text{CE}}.
\tag{4.2}
$$

Here we identify the individual contributions associated with the mean velocity-field, pressure, viscous stresses, SGS-stress and the 'combined commutator error'

respectively. These contributions are defined explicitly as (compare with (3.25)-(3.28)),

$$\psi_{\mathrm{mean}} = \overline{u}_i \left[\partial_j(\overline{u}_i\overline{u}_j) - \tfrac{1}{2}\,\overline{u}_i\partial_j\overline{u}_j \right] = \tfrac{1}{2}\partial_j(\overline{u}_i\overline{u}_i\overline{u}_j), \tag{4.3}$$

$$\psi_{\mathrm{p}} = \overline{u}_i\,\partial_i\overline{p}, \tag{4.4}$$

$$\psi_{\mathrm{visc}} = -\frac{1}{Re}\overline{u}_i\,\partial_{jj}\overline{u}_i, \tag{4.5}$$

$$\psi_{\mathrm{SGS}} = \overline{u}_i\,\partial_j\tau_{ij}, \tag{4.6}$$

$$\psi_{\mathrm{CE}} = \overline{u}_i\left[\mathcal{C}_j(u_iu_j) - \tfrac{1}{2}\overline{u}_i\mathcal{C}_j(u_j)\right]. \tag{4.7}$$

As already discussed on page 56 the additional terms in ψ_{mean} and ψ_{CE} are due to the "compressibility" $\partial_j\overline{u}_j = -\mathcal{C}_j(u_j)$ that is introduced with the use of a non-uniform filter. Regarding the transport of kinetic energy governed by the commutator error ψ_{CE} we will concentrate on the contributions associated with the convective flux. Hence, terms involving $\mathcal{C}_i(p)$ and $Re^{-1}[\mathcal{C}_j(\partial_j u_i) - \partial_j\mathcal{C}_j(u_i)]$ are not included in the discussion.

4.2.1   Interpretation of non-uniform filtering

In this subsection we first illustrate the application of a non-uniform filter in one spatial dimension. In particular, we concentrate on sine-waves and focus on the local quality of resolution in relation to the wavenumber of the signal and the local filter-width. Moreover, skewness is included and shown to affect the phase of the filtered signal. Subsequently, a Lagrangian interpretation of non-uniform filtering is formulated which characterizes the situation in three spatial dimensions. This provides a basis for explicit modeling of the corresponding commutator error dynamics that will be considered momentarily.

The application of a filter effectively removes flow-features that vary sufficiently rapidly on the scale of the local filter-width. The appropriate parameter to quantify this for symmetric filters is $k\Delta(x)$ where k denotes the wavenumber of the signal. In figure 4.1 we illustrate the effect of abruptly varying Δ from one value in the first half of the domain to another value in the second half. For illustration purposes, if the sine-wave is reduced in amplitude by about 50% or more, we will refer to it as 'subgrid' while it is considered 'resolved' otherwise. For the non-uniform top-hat filter considered in this example this rough identification implies that if $k\Delta(x) \lesssim 1/2$ then the corresponding signal may be considered locally resolved. Specifically in this example, we notice that, e.g., the $k = 2$ mode can be considered resolved throughout the domain while the mode at $k = 12$ clearly is subgrid everywhere. The interesting modes are in between, e.g., at $k = 6$, which may be considered *subgrid* in part of the domain and *resolved* in other parts of the domain.
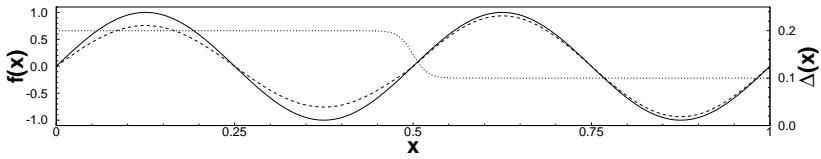
(a)
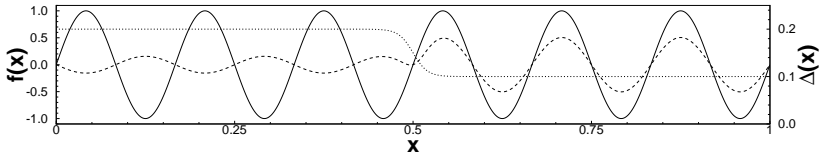
(b)
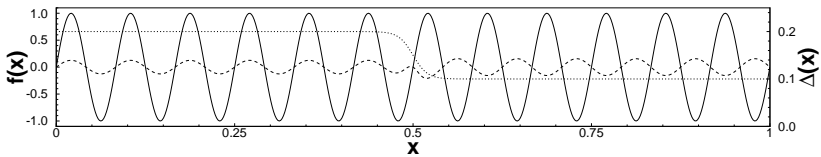
(c)

Figure 4.1: Filtered (dashed) and unfiltered (solid) sine-waves $f(x) = \sin(2\pi kx)$ with (a) $k = 2$, (b) $k = 6$ and (c) $k = 12$ in the domain $[0, 1]$. The filter-width $\Delta(x)$ (dotted) is non-uniform and specified as $\Delta(x) = 1/5$ for $x < 1/2$ and $\Delta(x) = 1/10$ for $x > 1/2$ with a short transition region around $x = 1/2$.

We may associate the actual effect of a non-uniform filter with the transition from 'resolved' to 'subgrid' for specific modes. Before this transition from 'resolved' to 'subgrid' is used to clarify the dynamic behavior of the commutator error $\mathcal{C}_j$ first the particular effect due to filter-skewness is illustrated.

Effect of skewness

The effect of skewness of a filter can most readily be illustrated by applying the skewed top-hat filter introduced in table 2.1 to a single sine-wave $u = \sin(2\pi kx)$. Direct evaluation of the filter yields the filtered velocity given by:

$$\overline{u}(x) = A(k\Delta)\sin(2\pi k(x + \Delta(x)\gamma)), \tag{4.8}$$

(a)

(b)
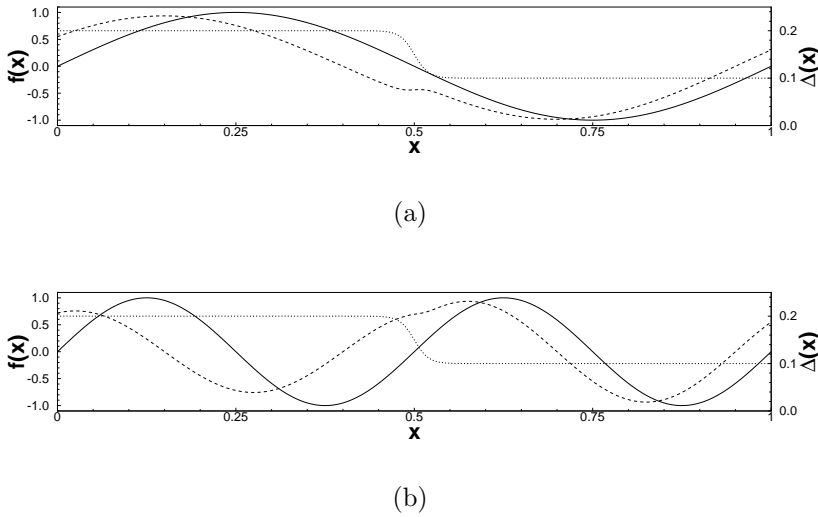
Figure 4.2: Filtered (dashed) and unfiltered (solid) sine-waves $f(x) = \sin(2\pi kx)$ with (a) $k = 1$ and (b) $k = 2$ in the domain $[0, 1]$. The filter is maximally skewed with $\gamma = \frac{1}{2}$ and the filter-width $\Delta(x)$ (dotted) is non-uniform and specified as $\Delta(x) = 1/5$ for $x < 1/2$ and $\Delta(x) = 1/10$ for $x > 1/2$ with a short transition region around $x = 1/2$.

where the damping factor A depends on $k\Delta$ as,

$$A(k\Delta) = \frac{\sin(\pi k\Delta)}{\pi k\Delta}. \tag{4.9}$$

We observe that the amplitude reduction for the skewed top-hat filter is not influenced by explicit skewness. Instead, the effect of explicit filter-skewness (i.e., $\gamma \neq 0$) is clearly recognized by a local phase-shift. This implies that the filtered signal is either lagging or leading the original wave depending on $\Delta\gamma$. In figure 4.2 we illustrate the case in which $\gamma = \frac{1}{2}$. This clearly illustrates that the phase-shift by which the filtered wave lags behind the unfiltered signal is reduced from $\gamma/5$ to $\gamma/10$ when passing the non-uniformity from left to right. Hence, the reduction of filter-width in the direction of the wave propagation implies next to an increase in amplitude of the resolved wave also a reduction of phase-shift when $\gamma \neq 0$. This illustrates clearly both dispersive and dissipative effects arising from non-uniform, skewed filtering which was already recognized in [51, 133].

We will next extend the interpretation of commutator errors to three spatial dimensions.
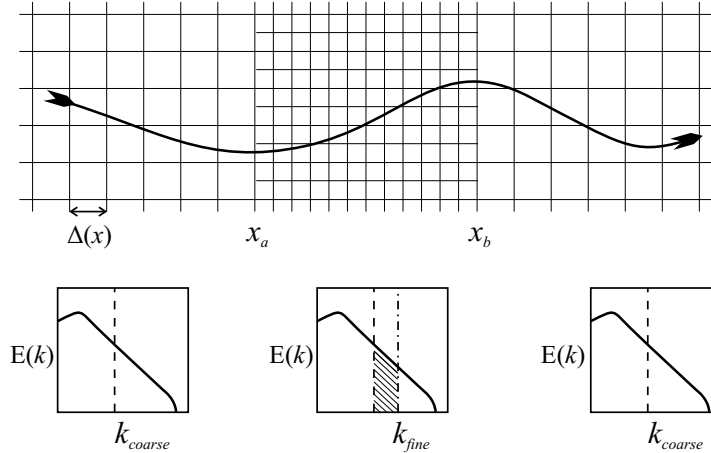
Figure 4.3: An illustration of filter-width variations which induce commutator errors that represent the apparent creation and destruction of scales associated with variations in the local resolution of the flow. An increased local resolution in the direction of the flow, corresponds to an apparent creation of small-scale flow-structures while a reduced resolution may be associated with the annihilation of the corresponding flow-structures.

Lagrangian interpretation of commutator errors

In figure 4.3 a non-uniform grid is sketched which can resolve different ranges of wave-numbers depending on the location in the grid. If we consider a particular flow-path as indicated then for $x < x_a$ all scales up to k_{coarse} may be resolved while for $x_a < x < x_b$ the filter-width is decreased such that scales in the range $[k_{\text{coarse}}, k_{\text{fine}})$ also become available as resolved scales.

The local effect corresponding to a decrease of the filter-width can be interpreted as an effective production of resolved kinetic energy. Similarly, if the non-uniform filter-width is increased, this should result in a decrease of resolved kinetic energy, e.g., contributing to an effective dissipation. Correspondingly, the commutator errors can be associated with the apparent local creation/destruction of turbulent flow scales if the filter-width is decreased/increased along a flow-path. Hence, the contributions arising from the commutator error are directly linked to the magnitude and sign of changes in the filter-width in the direction of the local flow-path. Large variations in Δ do not necessarily imply large commutator error contributions in an actual simulation; only if these changes occur in the direction of the local flow can commutator error dynamics become essential. This suggests a

direct modeling in terms of the material derivative of Δ which contains the central contribution $u_j \partial_j \Delta$, expressing exactly this observation.

4.2.2 Single-mode analysis of commutator error dynamics

In this subsection we will consider the effect of non-uniform, skewed filtering and specify in some detail the commutator error associated with individual Fourier-modes in a solution. This will further specify the connection with the material derivative of the filter-width, argued in the previous subsection.

In the single-mode analysis of the commutator error we assume that $u = \exp(\imath kx)$. Application of the skewed top-hat filter yields

$$\overline{u} \;=\; A(\frac{k\Delta}{2})e^{\imath k(x+\Delta\gamma)} \;=\; A(\frac{k\Delta}{2})u(x+\Delta\gamma), \tag{4.10}$$

with damping function A given by (4.9). The modified wave-number k', as introduced by Ghosal and Moin [54], may be used in quantifying the commutator error. Specifically, k' is defined through $\partial_x \overline{u} \;=\; \imath k' \overline{u}$. For symmetric filters the commutator error may be shown to be diffusive [54]. In the following, we will derive the modified wave-number corresponding to skewed filters and show that both diffusive and dispersive contributions arise in that case [133].

From (4.10) one can easily derive that

$$\partial_x \overline{u} \;=\; \partial_x\Big(A(\frac{k\Delta}{2})u(x+\Delta\gamma)\Big) \;=\; F\Big(\frac{k\Delta}{2}\Big)\frac{k\Delta'}{2}\overline{u} + \imath(1+\Delta'\gamma)k\overline{u}, \tag{4.11}$$

where, for the skewed top-hat filter, the function F is given by

$$F\Big(\frac{k\Delta}{2}\Big) \;=\; -\Big(\frac{2}{k\Delta} - \cot\Big(\frac{k\Delta}{2}\Big)\Big). \tag{4.12}$$

Correspondingly, using the definition of the modified wave-number k', we find

$$k' = -\imath F\Big(\frac{k\Delta}{2}\Big)\frac{k\Delta'}{2} + (1+\Delta'\gamma)k. \tag{4.13}$$

This expression of the modified wave-number k' contains the expression found in Ref. [54], as well as a dispersive contribution $\gamma\Delta'$ which is encountered for non-zero skewness $\gamma \neq 0$ [133]. We will next derive the single-mode expression for $\overline{u}\,\mathcal{C}_x(u^2)$ and make the connection with the material derivative of Δ more explicitly. Extended to three dimensions $\overline{u}\,\mathcal{C}_x(u^2)$ is closely related to $\overline{u}_i\mathcal{C}_j(u_iu_j)$ which is the main contributor to the transport of resolved kinetic energy by the commutator error ψ_{CE}.

The single-mode expression for the commutator error of the convective flux $\mathcal{C}_x(u^2)$ is given by,

$$
\begin{aligned}
\mathcal{C}_x(u^2) &= \overline{\partial_x e^{2\imath kx}} - \partial_x \overline{e^{2\imath kx}} = \overline{\partial_x e^{2\imath kx}} - \partial_x \left(A(k\Delta) e^{2\imath k(x+\Delta\gamma)} \right) \\
&= 2\imath k \overline{e^{2\imath kx}} - 2\imath k(1 + \Delta'\gamma)\overline{e^{\imath 2kx}} + F(k\Delta)\overline{e^{2\imath k(x+\Delta\gamma)}}.
\end{aligned}
\tag{4.14}
$$

This may be rewritten as,

$$
\mathcal{C}_x(u^2) = -\Delta'\gamma\overline{\partial_x u^2} + \frac{\Delta'}{\Delta}F(k\Delta)\overline{u^2},
\tag{4.15}
$$

such that $\overline{u}\mathcal{C}_x(u^2)$ is given by,

$$
\overline{u}\mathcal{C}_x(u^2) = \overline{u}\left(-\gamma\overline{\partial_x u^2} + F(k\Delta)\frac{\overline{u^2}}{\Delta} \right)\Delta'
\tag{4.16}
$$

In (4.16) we recognize two distinct contributions which we will discuss next.

The interpretation of the commutator error given in the previous subsection suggests to parameterize ψ_{CE} in terms of the material derivative of $\Delta_j(\mathbf{x})$ along a flow-path, i.e., $D_t\Delta_j = \partial_t\Delta_j + \overline{u}_k\partial_k\Delta_j = \overline{u}_k\partial_k\Delta_j$ in case Δ_j does not explicitly depend on time t. By defining L_∞ and T_∞ as characteristic length and time-scales, one can readily verify that $D_t\Delta_j$ has dimension $L_\infty T_\infty^{-1}$, whereas the dimension of ψ_{CE} equals $(L_\infty T_\infty^{-1})^3 L_\infty^{-1}$. Accounting for the proper physical dimension the following specific parameterization for ψ_{CE} is evident:

$$
\psi_{\mathrm{CE}} \sim \frac{|\overline{\mathbf{u}}|^2}{\Delta_j}\,\overline{u}_k\partial_k\Delta_j \equiv \xi_0,
\tag{4.17}
$$

where $|\overline{\mathbf{u}}|^2 = \overline{u}_i\overline{u}_i$. The front factor $F(k\Delta)$ in (4.16) further quantifies this contribution and shows that this term is small in case $k\Delta \ll 1$, as is to be expected for all subgrid contributions. In the sequel, we will use the notation ξ_0 to represent this part of the commutator error. Expression (4.17) includes the material derivative of $\ln(\Delta_j)$ which is a measure of the relevance of the commutator error relative to the turbulent stresses [47]. Inspection of (4.16) indicates that skewness provides an additional contribution $\sim \overline{\partial_x u^2}\, D_t\Delta$ which has a similar interpretation as a ratio between the square of a characteristic velocity and a length scale multiplied by the material derivative of the filter-width.

An explicit parameterization for the commutator error contribution can be obtained by observing that $\overline{u^2}/\Delta = \overline{u}^2/\Delta + O(\Delta)$ and $\overline{\partial_x u^2} = \partial_x\overline{u}^2 + O(\Delta')$ when $\gamma \neq 0$. Guided by (4.16) the following model for the transport of resolved kinetic energy is proposed:

$$
\psi_{\mathrm{CE}} \approx \xi \equiv c_0\xi_0 - c_1\xi_1,
\tag{4.18}
$$

with c_0 and c_1 constants to which we return momentarily, and ξ_1 given by

$$\xi_1 \;=\; \gamma_j \frac{\partial |\overline{\mathbf{u}}|^2}{\partial x_j} \frac{D\Delta_j}{Dt}. \tag{4.19}$$

In the next section we will consider the kinetic energy dynamics associated with general non-uniform, skewed filters, applied to turbulent mixing and use statistical analysis to verify (4.18).

4.3   Commutator-error energy dynamics in turbulent mixing

In this section we will first describe the statistical evaluation method with which we will quantify the agreement between the actual ψ_{CE} and its explicit Lagrangian modeling hypothesis (4.18). This will be collected in subsection 4.3.1. Subsequently, we will present results for the kinetic energy dynamics obtained from evaluating the non-uniformly filtered direct numerical simulation database which was already introduced in subsection 3.3. In the presentation of these results we distinguish between symmetric and skewed filters. In subsection 4.3.2 we turn to symmetric filters in which case ξ reduces to ξ_0. Subsequently in subsection 4.3.3 we will extend the testing to skewed filters and focus on the effectiveness of the proposed additional contribution ξ_1. The consequences of the Lagrangian modeling hypothesis for the direct representation of the commutator errors as arise on flux-level in the momentum equations form a separate issue that will be presented in section 4.4.

4.3.1   Temporal mixing layer and statistical evaluation method

In order to assess the Lagrangian modeling hypothesis for the commutator error energy dissipation rate ψ_{CE} we will use turbulent flow in a temporal mixing layer at Reynolds number $Re = 50$. The details of this particular DNS as well as the filter-width have already been given in subsection 3.3. By correlating ψ_{CE} with the proposed model, we may illustrate the quality of the Lagrangian hypothesis, both for symmetric as well as for skewed filters.

The filter-widths Δ_i are defined in a similar way as in the previous chapter, i.e. the filter-widths in the homogeneous x_1 and x_3 directions are constant, while the filter-width associated with the x_2-direction is non-uniform and clustered near the centerline (see equation (3.16)). However the parameter α which controls the 'depth' of the filter-width modulation is kept fixed to $\alpha = 3/4$. Again the

filtered quantities needed in the evaluation of the kinetic energy dynamics are obtained using the composite trapezoidal rule applied to the top-hat filter. The required spatial derivatives are approximated using second order accurate central finite differencing with grid-spacing $\Delta_r/4$.

To test the kinetic energy parameterization expressed in (4.18) we will interpret ψ_{CE} and ξ as stochastic variables and quantify their main features using a statistical analysis. Since the filter is non-uniform in the x_2-direction only, the model ξ reduces to,

$$\xi = \left(c_0 \frac{\overline{u_i}\overline{u_i}}{\Delta_2} - c_1\,\gamma_2\partial_2\overline{u_i}\overline{u_i} \right) \overline{u}_2\Delta_2'. \tag{4.20}$$

In order to assess the quality of the Lagrangian model we will focus on the correlation between ψ_{CE} and ξ. Moreover, we determine the Probability Density Function (PDF) $P(\xi, \psi_{\mathrm{CE}})$ using a standard binning procedure for these two quantities which expresses their connections in further detail. We will consider results of this evaluation both for symmetric as well as skewed filters.

4.3.2 Correlation and PDF of energy dynamics model for symmetric filters

In this subsection we test the modeling of ψ_{CE} for symmetric filters in which case ξ reduces to ξ_0. In subsection 4.3.3 we will extend the testing to skewed filters and focus on the effectiveness of the proposed additional contribution ξ_1.

The correlation between ψ_{CE} and ξ for symmetric filters at different filter-width non-uniformities was studied. Quite low correlation was observed in the initial, laminar and transitional stages in cases where the filter-width is only mildly non-uniform but over quite an extended region, e.g., corresponding to $\beta = 5$ or $\beta = 10$. This low correlation is associated with the fact that either $\Delta_2' \approx 0$ in the region around the centerline, or, initially, $\overline{u}_2 \approx 0$ in large parts of the domain (see figure 3.1(a)). Consequently, the model in (4.20) is virtually zero in these phases of the flow development. However, once the mixing layer has evolved also away from the centerline into the parts of the domain where Δ_2' is significant, a comparably high correlation of about 0.6 is observed.

More detail regarding the quality of (4.18) can be inferred from the PDF $P(\xi, \psi_{\mathrm{CE}})$. For the calculation of the PDF a binning procedure [126] has been used in terms of the quantities ξ^* and ψ_{CE}^* which are given by ξ and ψ_{CE} normalized by their root-mean square values, i.e.,

$$\xi^* = \frac{\xi}{\langle \xi^2 \rangle^{\frac{1}{2}}}, \qquad \psi_{\mathrm{CE}}^* = \frac{\psi_{\mathrm{CE}}}{\langle \psi_{\mathrm{CE}}^2 \rangle^{\frac{1}{2}}}. \tag{4.21}$$
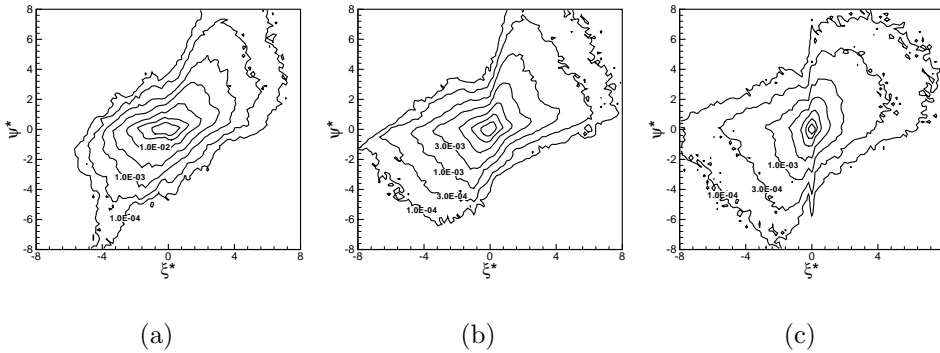
Figure 4.4: The PDF $P(\xi, \psi_{\mathrm{CE}})$ for the flow at $t = 60$, with non-uniform filter-widths corresponding to $\alpha = 3/4$ and a) $\beta = 5$, b) $\beta = 10$ and c) $\beta = 30$.

In figure 4.4 we observe that the PDF's are localized around the origin since either $\overline{u}_2$ or Δ'_2 is small in large parts of the domain; observe the contour-levels used in the figure. More importantly, we observe that contours of the PDF's are mainly located in the first and third quadrant which underlines the quality of the hypothesis formulated in (4.18). The predominance of contour-lines in the first and third quadrants indicates that whenever $|\psi^*_{\mathrm{CE}}|$ is large, so is $|\xi^*|$, and that in addition the signs correlate very well. These aspects are certainly required in order for the modeling hypothesis to be accurate.

The PDF's can be used to obtain one-dimensional conditional averages which further quantify the effectiveness of the model ξ. As an example, it is expected that 'events' in which $\psi^*_{\mathrm{CE}} > 0$ will correspond closely with locations where $\xi > 0$ and vice versa. This relation may be illustrated by considering what we will refer to as the positivity correlation:

$$\Psi^+(a) \;\; = \;\; \langle \psi_{\mathrm{CE}} > 0 \,|\, \xi = a \rangle. \tag{4.22}$$

The function Ψ^+ denotes the expectation that the dissipation is positive given the value of ξ. It is expected that $\Psi^+(a) \to 1$ for $a > 0$ and $\Psi^+(a) \to 0$ for $a < 0$, i.e., the commutator error dissipation is positive whenever the modeled term is and vice versa. In fact, there should be a sharp 'cross-over' from $\Psi^+ \approx 0$ to $\Psi^+ \approx 1$ as a changes sign, to indicate that the Lagrangian modeling hypothesis is accurate. Closely related is the conditional expectation of ψ_{CE} as a function of a,

$$\mathcal{E}(a) = \langle \psi^*_{\mathrm{CE}} \,|\, \xi = a \rangle. \tag{4.23}$$

Close correlation of ψ_{CE} and ξ would imply an approximately linear dependence of $\mathcal{E}$ as function of a.

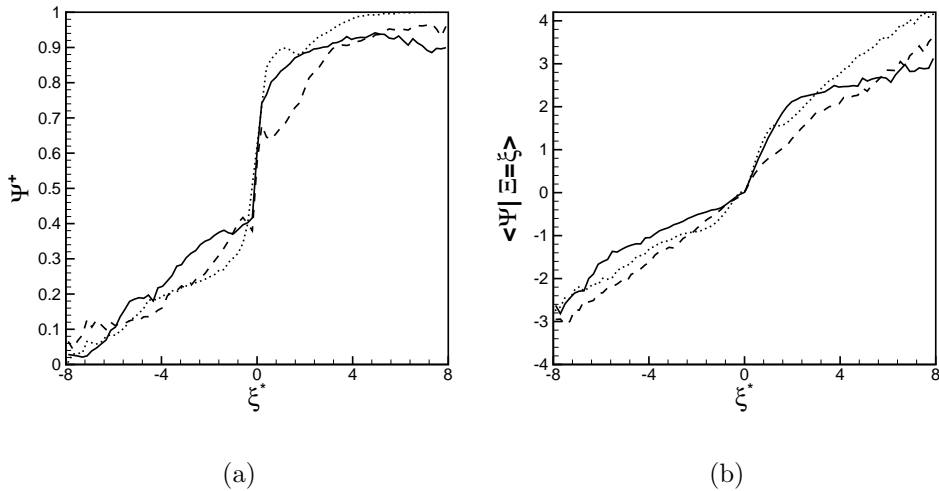(a)   (b)

Figure 4.5: The stochastic variables a) $\Psi^+(\xi)$ and b) $\mathcal{E}(\xi)$ in case $\alpha = 3/4$, $\beta = 10$ and $t = 40$ (dotted), $t = 60$ (solid) and $t = 80$ (dashed).

In figure 4.5 we plotted Ψ^+ and $\mathcal{E}$ for the characteristic case $\alpha = 3/4$ and $\beta = 10$ at various stages in the development of the flow. In figure 4.5(a) the expected behavior of Ψ^+ is indeed observed, including the sharp transition around $\xi^* = 0$. In figure 4.5(b) an almost linear relation between $\mathcal{E}$ and ξ is observed, which further establishes the quality of the new parameterization for symmetric filters.

4.3.3   Correlation and PDF of energy dynamics model for skewed filters

Next, we turn to skewed filtering in the definition of the commutator errors. First, we establish that the originally proposed parameterization (4.17) is no longer adequate for non-zero skewness and that the dispersive part ξ_1 needs to be included. Next, we will study the effect of varying the relative importance of the dissipative (ξ_0) and the dispersive (ξ_1) contributions in the Lagrangian model, for various values of the filter skewness.

In figure 4.6 we display Ψ^+ for several values of the skewness parameter γ and a characteristic turbulent field obtained at $t = 60.0$. In this figure the sharp crossover around $\xi = 0$ is still present, but the size of the 'jump' becomes smaller as skewness increases. The desired behavior in which that $\Psi^+(\xi) \to 0$ for $\xi < 0$ and $\Psi^+(\xi) \to 1$ for $\xi > 0$ is not so clear for $\gamma \neq 0$. For example, for $\gamma = \frac{1}{2}$, $\Psi^+(\xi)$ tends to 0.45 for $\xi < 0$ and to 0.65 for $\xi > 0$. The correlation-coefficient was found to drop to approximately 0.15 in cases of maximal skewness $\gamma = \pm\frac{1}{2}$.
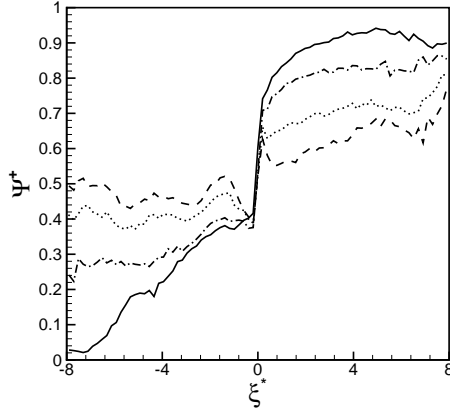
Figure 4.6: The positivity correlation $\Psi^+(\xi)$ between ψ_{CE} and the dissipative model ξ_0 at $t = 60.0$ in case $\alpha = 3/4$ and $\beta = 10$ for the symmetric case $\gamma = 0$ (solid) and various values of the skewness: $\gamma = \frac{1}{10}$ (dash-dot), $\gamma = \frac{1}{4}$ (dotted) and $\gamma = \frac{1}{2}$ (dashed).
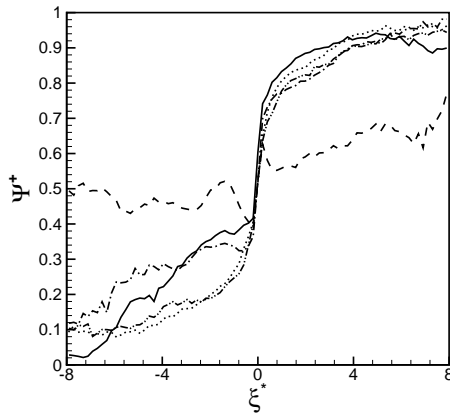
Figure 4.7: The positivity correlation $\Psi^+(\xi)$ between ψ_{CE} and the full Lagrangian model $\xi = c_0\xi_0 - c_1\xi_1$ in case the filter-width is given by $\alpha = 3/4$ and $\beta = 10.0$ at $t = 60.0$ and skewness $\gamma = \frac{1}{2}$ with various values of the ratio c_1/c_0, $c_1/c_0 = 0$ (dashed), $c_1/c_0 = 5$ (dash-dot), $c_1/c_0 = 30$ (dotted) and $c_1/c_0 = \infty$ (dash-dotdot). For comparison also the symmetric result is given (solid).

The failure of ξ_0 to cover all aspects of ψ_{CE} suggests the need to include the explicit dispersive contributions due to ξ_1 in case the filter is skewed. Hence, we next extend the testing to the full parameterization (4.18) where $\xi = c_0\xi_0 - c_1\xi_0$ with parameters c_0 and c_1. In figure 4.7 we show Ψ^+ for various values of c_1/c_0 at skewness $\gamma = \frac{1}{2}$. The expected behavior of Ψ^+ is similarly recovered by incorporating ξ_1 into the model, and compares well with that obtained in the symmetric filter case.

The dependence of correlation and Ψ^+ on the ratio c_1/c_0 naturally leads to the

(a)   (b)

Figure 4.8: The correlation between ψ_{CE} and ξ as a function of the ratio between c_1 and c_0. a) $\gamma = \frac{1}{2}$ at various moments in time, $t = 40.0$ (dashed), $t = 50.0$ (dotted), $t = 60.0$ (solid) and $t = 70.0$ (dash-dot). b) $t = 60.0$ and $\gamma = \frac{1}{2}$ (solid), $\gamma = \frac{1}{4}$ (dashed), $\gamma = \frac{1}{10}$ (dotted), $\gamma = \frac{1}{20}$ (dash-dot), $\gamma = \frac{1}{100}$ (dash-dotdot) and $\gamma = \frac{1}{1000}$ (long dash).
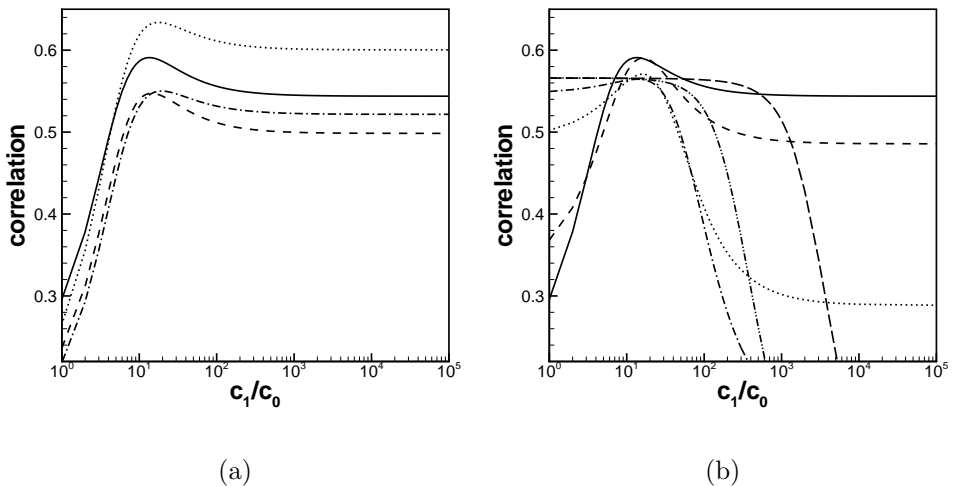
question what ratio is optimal. In figure 4.8(a) the correlation is shown as a function of c_1/c_0 at various moments in time for $\gamma = \frac{1}{2}$. We notice that the correlation has a peak near $c_1/c_0 \approx 13$. Moreover, this 'optimal' value for c_1/c_0 is quite independent of the skewness parameter γ as shown in figure 4.8(b). The limiting cases corresponding to $c_1/c_0 = 0$ or $c_1/c_0 = \infty$, i.e., when c_1 or c_0 is zero, correspond to the individual correlation of the diffusive- ξ_0 and the dispersive-part ξ_1 respectively. Consequently these limiting cases indicate whether for a given skewness either dissipation or dispersion is dominant. Clearly, when $\gamma \approx 0$ and the behavior of the commutator error is diffusive a high correlation is observed when $c_1 = 0$, while the correlation is zero when $c_0 = 0$. If the skewness increases then dispersion becomes more and more important. Moreover, already for $\gamma = \frac{1}{4}$ the individual correlation for the dispersive part ξ_1 is higher than that for the diffusive part ξ_0 and the dynamical behavior of the commutator error is dominated by dispersion rather than diffusion.

More global information can be gathered from figure 4.9. In this figure contours of the correlation between ψ_{CE} and ξ are shown as a function of c_1/c_0 as well as the skewness γ. The graphs shown in figure 4.8(b) are horizontal intersections of figure 4.9 for a given skewness γ. As can been seen in this figure in a small band around $\gamma = 0$ dispersive effects are absent as the highest correlation is observed for $c_1 = 0$. For $|\gamma| > \frac{1}{10}$ the relative importance of dispersion increases considerably
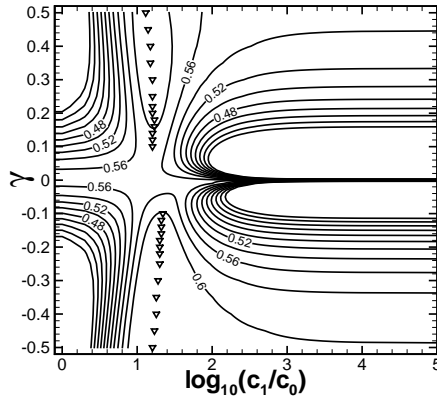
Figure 4.9: Contour plot of the correlation between ψ_{CE} and ξ as a function of the ratio between c_1 and c_0 and the skewness γ when $t = 60$, $\alpha = 0.75$ and $\beta = 10$. The contours-increment is 0.02. The ∇-symbols indicate the location of maximum correlation for a given skewness.

with increasing skewness. In this regime where dispersive effects are important the tendency of the correlation to peak at a constant value of the ratio c_1/c_0 is also observed. This tendency was already observed in figure 4.8(b) and is in figure 4.9 depicted by the ∇-symbols. For a given skewness these symbols indicate the peak correlation. For this particular snapshot of the flow and typical filter-width layout the location of the maximum correlation is observed when $c_1/c_0 \approx 13$. Other snapshots and other filter-width lay-outs indicate that the optimal ratio should be somewhere between 10 and 30.

In this section we have shown that the parameterization (4.18) can capture the dominant dissipative and dispersive aspects of the local transport of resolved kinetic energy arising from the commutator error. The results generally show high correlation between ψ_{CE} and ξ for both symmetric and skewed filters. In the next section we will hence consider the corresponding subgrid model for the commutator error $\mathcal{C}_j(u_i u_j)$. Moreover, we will compare the resulting model with other explicit commutator error models (CE-models) arising from general similarity assumptions.

4.4   Explicit modeling of the commutator error

In this section we first formulate explicit models for the commutator errors. Subsequently, results of *a priori* testing will be discussed, where special attention will be given to the quality of the proposed models in case skewed filters are applied.

4.4.1 Similarity and Lagrangian type commutator error models

In this subsection three models $\mathcal{M}_i$ for the commutator error $\mathcal{C}_j(u_i u_j)$ will be introduced. The first two models are based on similarity assumptions [47] and resemble the similarity and gradient model for the SGS-stress τ_{ij} introduced in section 2.2. The third model is based on the Lagrangian interpretation of the commutator error.

The similarity CE-model extends the Bardina or similarity model for the SGS-stress (2.33) [7]. In fact, for any SGS-term similarity type models can be formulated and involve the evaluation of the SGS-term using resolved variables. Consequently, the similarity model corresponding to the commutator error for the convective fluxes in the momentum equation may be defined as:

$$\mathcal{M}_i^{\text{sim}} \;=\; \overline{\partial_j(\overline{u_i}\overline{u_j})} - \partial_j\overline{\overline{u_i}\overline{u_j}}. \tag{4.24}$$

The similarity model for the commutator error contains a number of additional explicit applications of the filter-operator. These are computationally expensive and an alternative can be obtained using Taylor expansions. This gives rise to the gradient CE-model. It shows close resemblance to the gradient SGS-model (2.34) [23], except that here also the first order contribution is incorporated in order to accommodate skewed filters. The derivation of the gradient CE-model proceeds analogous to the derivation of (3.9) and results in:

$$\mathcal{M}_i^{\text{gradient}} = -\sum_{k=1}^{3} \left\{ M_{k1}(\partial_j\Delta_k)\partial_k\overline{u_i}\overline{u_j} + M_{k2}\Delta_k(\partial_j\Delta_k)\partial_k^2\overline{u_i}\overline{u_j} \right\}. \tag{4.25}$$

Here M_{kr} is the r-th moment of the filter applied in the k-th direction. The first and second moments of the filter make this model sensitive to the actual filter that was adopted. For the *a priori* testing of these models the (skewed) top-hat filter will be used, for which we obtained $M_{k1} = \gamma_k$ and $M_{k2} = \frac{1}{12} + \gamma_k^2$ and γ_k is the skewness parameter for the x_k-direction.

The third model $\mathcal{M}_i$ that will be introduced is based on the Lagrangian behavior of commutator errors. In line with the Lagrangian model (4.18) for the transport of resolved kinetic energy and the physical dimension of the commutator error flux the following Lagrangian CE-model is proposed for the case Δ_j does not depend explicitly on t:

$$\mathcal{M}_i^{\text{Lag}} \;=\; \left\{ d_0\frac{\overline{u_i}}{\Delta_j} - d_1\gamma_j\,\partial_j\overline{u_i} \right\}D_t\Delta_j \;;\;\; D_t\Delta_j = \overline{u_k}\partial_k\Delta_j. \tag{4.26}$$

Here d_0 and d_1 are appropriate (dynamic) constants. This model represents the Lagrangian interpretation discussed above in section 4.2.1 and includes separate contributions associated with the skewness of the filter.

Model	time										
	0	10	20	30	40	50	60	70	80	90	100
Sim	0.99	0.94	0.93	0.95	0.95	0.95	0.94	0.92	0.93	0.93	0.94
Grad	0.61	0.53	0.63	0.76	0.78	0.74	0.75	0.75	0.74	0.80	0.80
Lag	0.49	0.54	0.59	0.56	0.48	0.45	0.40	0.37	0.38	0.43	0.46

Table 4.1: Correlation between $\mathcal{M}_1$ and the actual commutator error $\mathcal{C}_j(u_1 u_j)$ determined from the DNS-fields at different moments in time. In this symmetric case $\gamma = 0$ and the filter-width is specified by $\alpha = 0.75$ and $\beta = 10.0$.

Further analogies between the SGS-fluxes $\partial_j \tau_{ij}$ and the commutator errors may be exploited to extend existing SGS-models to CE-models. For example, generalized similarity models may involve (approximate) inversion [41, 118], or regularization principles such as Leray's formulation [43]. Moreover, the commutator error formally obeys Germano's identity [39] which may be formulated as follows. If a test-filter $\mathcal{L}_{\mathrm{tf}}$ is introduced next to $\mathcal{L}$ then the following identity may be verified:

$$[\mathcal{L}_{\mathrm{tf}} \circ \mathcal{L}, \partial_j] (\mathbf{u}) = [\mathcal{L}_{\mathrm{tf}}, \partial_j] \circ \mathcal{L}(\mathbf{u}) + \mathcal{L}_{\mathrm{tf}} \circ [\mathcal{L}, \partial_j] (\mathbf{u}). \tag{4.27}$$

This identity represents Leibniz's rule for the commutator error bracket (2.17) and may allow the dynamic determination of possible additional parameters in assumed basic CE-models, similar to dynamic modeling approaches which were found successful for the SGS-stress [40].

In the remainder of this section we will consider results of *a priori* testing of the explicit CE-models introduced above.

4.4.2 A priori testing of CE-models

Symmetric filters

In table 4.1 the correlation between the exact and the various modeled commutator error representations is given in case symmetric filters are applied. The similarity CE-model shows a very high correlation of about 0.94, while the gradient models shows a correlation of 0.77. The Lagrangian CE-model performs rather poorly as far as correlation is concerned with a correlation around 0.44. The high correlation of the similarity type models is reminiscent of the situation that arises when modeling the turbulent stress tensor, especially at relatively modest filter-widths.

The L_2-norm (3.18) of the commutator error flux over planes at constant x_2 provides a clear profile with which the actual dynamic contribution of these terms and their proposed models can directly be compared. In figure 4.10 the resulting L_2-profiles for $\mathcal{C}_j(u_1 u_j)$ and $\mathcal{M}_1$ are shown. The similarity and gradient CE-model tend to respectively under- or over-predict the L_2-profile, but their shape is gen-
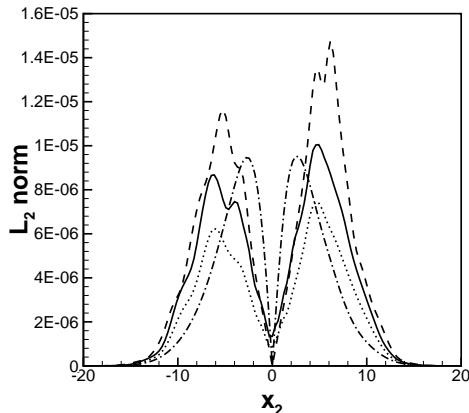
Figure 4.10: The L_2-norm of $\mathcal{C}_j(u_1 u_j)$ and $\mathcal{M}_1$ as a function of the normal x_2-direction for the symmetric case: exact (solid), similarity (dotted), gradient (dashed), Lagrangian with $d_0 = 0.05$ (dash-dot).

erally in good agreement with the exact L_2-profile of $\mathcal{C}_j(u_1 u_j)$. The latter corresponds of course with the high values for the correlation coefficients observed in table 4.1. For example the location of the maxima above and below the centerline are predicted well with these models. The Lagrangian model tends to position these maxima slightly too close to the centerline. By selecting, e.g., $d_0 = 0.05$ the magnitude of these extrema may be predicted accurately using the Lagrangian model. Since the commutator error also satisfies the Germano identity, there is a natural option to determine the model coefficients using the dynamic procedure. This can further improve the correspondence between $\mathcal{C}_j(u_i u_j)$ and the Lagrangian model, without the need to introduce ad hoc parameters. Introducing an extra amplitude parameter in one of the similarity models will lead to a loss of Galilean invariance of these models [67] and is less appealing.

Skewed filters

For the skewed filter case the correlation results are collected in table 4.2 in case the skewness parameter $\gamma = 1/2$. In this table various ratios d_1/d_0 are considered for the Lagrangian model. At this skewness an optimal ratio appears $d_1/d_0 \approx 20$ at which value the highest correlation is obtained. This correlation is considerably higher than observed for the Lagrangian-model in the symmetric case and is similar to the correlation of the similarity and gradient CE-model.

In figure 4.11 the L_2-profile is shown for the various models. For the Lagrangian model the realizations are shown with $d_0 = 0.05$ and d_1 either 0.8 or 1.0, corresponding to $d_1/d_0 \approx 20$. Consistent with the observed improved correlation in

Model	$\frac{d_1}{d_0}$	time										
		0	10	20	30	40	50	60	70	80	90	100
Sim		0.58	0.63	0.65	0.67	0.65	0.63	0.59	0.63	0.67	0.69	0.68
Grad		0.78	0.79	0.74	0.73	0.72	0.69	0.57	0.53	0.50	0.49	0.45
Lag	0	0.28	0.31	0.23	0.14	0.08	0.07	0.04	0.07	0.06	0.04	0.05
	1	0.34	0.43	0.41	0.34	0.28	0.25	0.21	0.20	0.17	0.15	0.16
	2	0.38	0.52	0.53	0.51	0.44	0.40	0.35	0.31	0.26	0.25	0.24
	10	0.48	0.68	0.74	0.77	0.73	0.69	0.62	0.57	0.60	0.48	0.43
	20	0.48	0.68	0.73	0.77	0.74	0.70	0.64	0.58	0.51	0.49	0.44
	30	0.48	0.67	0.73	0.76	0.74	0.70	0.64	0.58	0.51	0.49	0.44
	∞	0.46	0.65	0.71	0.74	0.72	0.69	0.63	0.58	0.50	0.49	0.44

Table 4.2: Correlation between $\mathcal{M}_1$ with the real commutator error $\mathcal{C}_j(u_1 u_j)$ determined from the DNS-fields at different moments in time. The skewness is given by $\gamma = \frac{1}{2}$ and the filter-width by $\alpha = 0.75$ and $\beta = 10.0$.

(a)   (b)
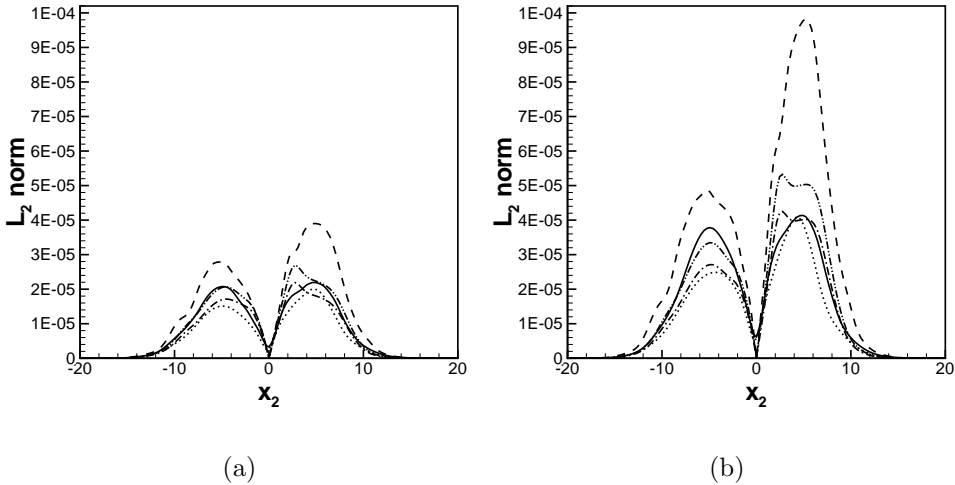
Figure 4.11: The L_2-norm of $\mathcal{C}_j(u_1 u_j)$ as a function of the normal x_2-direction as predicted by the commutator error models with skewness given by a) $\gamma = 1/4$ and b) $\gamma = 1/2$ and the filter-width by $\alpha = 0.75$ and $\beta = 10$: exact (solid), similarity (dotted), Clark (dashed), Lagrangian model with $d_0 = 0.05$ and $d_1 = 0.8$ (dash-dot) and Lagrangian model with $d_0 = 0.05$ and $d_1 = 1.0$ (dash-dotdot)

table 4.2 the Lagrangian model corresponds much closer to the actual commutator error in the skewed case, producing approximately similar agreement as the other two models. For example, the peaks above and below the centerline are predicted well by the Lagrangian model in this case.

4.5 Concluding remarks

In this chapter the effects of the commutator error has been studied on the dynamics of the resolved kinetic energy and in relation to the momentum equation. It was argued that the commutator error can be associated with the apparent local creation or destruction of resolved turbulent flow scales. In turn, this leads to a local increase or decrease in resolved kinetic energy, depending on the variations in the filter-width Δ.

In the Lagrangian interpretation, the effect of a non-uniform filter-width on the resolved kinetic energy can be captured in terms of the material derivative of the filter-width $D_t\Delta = \partial_t\Delta + \overline{u}_i\partial_i\Delta$. Correspondingly, the local transport of kinetic energy by the commutator error, ψ_{CE}, was modeled by,

$$\psi_{\text{CE}} \approx \xi = \Big(c_0\frac{|\mathbf{u}|^2}{\Delta_j} - c_1\gamma\frac{\partial|\mathbf{u}|^2}{\partial x_j}\Big)\frac{D\Delta_j}{Dt}, \tag{4.28}$$

where γ denotes the skewness of the filter. Skewness has been explicitly incorporated since the commutator error exhibits both diffusive and dispersive behavior in case skewed filters are applied. In terms of (4.28) the $-c_1\gamma\partial_j|\mathbf{u}|^2$-part accounts for this dispersive effect. The other term in (4.28) represents the contributions associated with strictly symmetric filters.

The Lagrangian modeling (4.28) has been tested *a priori* using DNS-data of a temporal mixing layer. The results indicated the accuracy of the proposed model for the transport of resolved kinetic energy by the commutator error. The commutator error dispersion is found to be considerable in case $|\gamma| \gtrsim \frac{1}{10}$. These additional effects could be successfully captured by the dispersive part in (4.28). The optimal ratio between the constants c_1 and c_0 is in the range $10 - 30$.

The Lagrangian context also suggests an explicit model for the convective flux commutator $\mathcal{C}_j(u_iu_j)$. We performed an *a priori* testing of this new model and compared it to other CE-models based on similarity and gradient formulations [122]. The results showed that the Lagrangian commutator error model correlates less well in case symmetric filters are applied. For the skewed case the Lagrangian CE-model correlates roughly comparably to the other two models. The similarity and gradient models are well known for their high levels of correlation. This indicates that the spatial structure of the commutator error is better captured by one of these two models than by the Lagrangian model. However, the similarity and gradient models are known to fail to represent important aspects of the subfilter dynamics. In particular, too many small scales are generated in simulations using the similarity model while the gradient model may be responsible for inducing instabilities in the large-eddy simulation. By construction, the new Lagrangian model does properly capture the underlying dynamics of the commutator error.

However *a-posteriori* testing of these models in simulations adopting a non-uniform grid and filter-width is required to provide decisive answers.

Chapter 5

Computational turbulent stress tensor for compressible flow

With the application of a spatial filter operator to the Navier-Stokes equations scales smaller than the filter-width Δ are removed. This motivates the use of a grid-spacing h on the order of the filter-width Δ. However, such a coarse grid also induces its own filtering effect as small scale flow features which cannot be captured by the grid are removed from the simulation. In this chapter[1] the filtering effect of the coarse grid discretization is incorporated into the analysis. This results into a modified closure problem to which we will refer to as the computational stress tensor. Particularly, we will investigate the computational stress tensor as it occurs in compressible flow. First in section 5.1 the general computational stress tensor is introduced and illustrated using the inviscid Burgers equations. The computational stress tensor for compressible flow will be given in section 5.2. It will be shown that this computational stress tensor can be decomposed into two parts, one part primarily associated with the fluctuating density ρ' and one part primarily associated with the fluctuating velocity u''. This decomposition is further investigated in section 5.3 and an approach towards modeling the fluctuating density is introduced. Finally in section 5.4 the results are summarized.

5.1 Computational turbulent stress tensor

The spatial filtering of the nonlinear terms in the Navier-Stokes equations gives rise to closure problems. Specifically, these SGS-terms represent the dynamic effects of the filtered-out small scales on the evolution of the retained larger length-scales.

---

[1]This chapter is largely based on Van der Bos and Geurts [124].

These dynamic effects should be modeled in terms of the resolved flow only in order to close the system of filtered equations. Commonly, one considers this closure problem as defined purely with reference to the spatial filtering. Considerable effort has been put into construction, testing and tuning of such SGS-models over the past years, see, e.g., [48, 91]. However, the next step in the formulation of LES of a turbulent flow involves the introduction of the numerical method and hence also the introduction of a new length-scale h which characterizes the (local) grid spacing. This discretization step induces a second element of possible flow filtering which translates into additional contributions to the dynamics of the resolved scales. In this chapter we consider these combined filtering effects in detail and focus on the closure of the 'computational turbulent stress tensor' which entails the filtering effect of both the basic spatial LES-filter as well as that induced by the spatial discretization. Specifically, we extend existing literature [83, 84, 106] on this topic to compressible flows. In the sequel we will frequently refer to the basic spatial LES-filter as the *formal* filter, while filtering effects due to the spatial discretization will be referred to as part of the *numerical* filter [115].

With the application of the formal filter, scales smaller than the filter-width Δ are effectively removed from the solution. This motivates the use of a grid-spacing h on the order Δ instead of having to resolve the Kolmogorov dissipation length-scale $\eta \ll \Delta$, as would be required for DNS. In general it is unclear what subgrid resolutions $r = \Delta/h$ are acceptable from the point of view of numerical reliability of the simulations. However, in LES-practice feasibility constraints frequently lead to a subgrid resolution r as low as 1 or 2 [22, 42, 140]. In such cases the smallest retained flow-features are only marginally resolved and one may anticipate a significant effect from the numerical discretization at large Δ [92, 93]. Hence, even though the numerical filtering component can be controlled in principle by choosing r sufficiently large, virtually all LES studies reported in literature contain dynamic contributions arising from the coarseness of the discretization. For incompressible flow the numerical contamination was investigated earlier in terms of the induced numerical filter [83, 84, 106].

The closure effects arising from the numerical filter are in most cases of practical LES not negligible as the subgrid resolution r is quite low [21, 62, 146]. Therefore, the numerical filtering should be fully included into the analysis and modeling of the LES equations. This advocates considering the closure problem at the level of the actual computational model, i.e., after the spatial discretization has been incorporated. Such an approach differs markedly from addressing the closure problem in terms of the turbulent stresses as arise on the PDE-level of filtered Navier-Stokes equations. The most important aspects of this 'computational turbulent stress' closure problem can be readily appreciated in terms of the one-dimensional inviscid Burgers equation. This will be sketched next to provide a background against

which the extensions toward three-dimensional compressible flow will be developed in the rest of this chapter.

If we apply a formal filter $\overline{(\cdot)}$ to the inviscid Burgers equation we may write the result as,

$$\partial_t \overline{u} + \tfrac{1}{2}\partial_x \overline{u^2} \;=\; \partial_t \overline{u} + \tfrac{1}{2}\partial_x \overline{u}^2 + \tfrac{1}{2}\partial_x \tau = 0, \tag{5.1}$$

where $\tau = \overline{u^2} - \overline{u}^2$ is the 'turbulent' or 'SGS' stress, t denotes time, x is the spatial coordinate, u is the velocity and an over-bar indicates the formal filter. The term sub-grid scale (SGS) is commonly used in LES literature to refer to what are actually sub-filter-width scales [21]. These stresses describe the dynamical effect of the small scales on the resolved scales and need to be replaced by a so-called subgrid model $m(\overline{u})$ in order to close the equation. Subsequently, the closed filtered Burgers equation can be discretized in terms of a discrete derivative operator δ_x.

Compared to the standard LES framework, the order of the modeling and discretization steps may also be reverted. Instead of first introducing the turbulent stress tensor τ and then discretising the filtered equation, we can also start from the discrete convective flux $\delta_x(\overline{u}^2)$ that is directly available in the computational model and group the remainder into the extended closure problem. To further clarify the corresponding closure problem we express the discrete derivative operator as $\delta_x f = \partial_x \widehat{f}$ where $\widehat{f}$ denotes the numerically induced filter [106]. Restricting ourselves to this representation, we may write in full detail,

$$
\begin{aligned}
\partial_t \overline{u} + \tfrac{1}{2}\partial_x \overline{u^2} \;&=\; \partial_t \overline{u} + \tfrac{1}{2}\delta_x \overline{u}^2 + \tfrac{1}{2}\left(\partial_x \overline{u^2} - \delta_x \overline{u}^2\right)\\
&=\; \partial_t \overline{u} + \tfrac{1}{2}\partial_x \widehat{\overline{u}^2} + \tfrac{1}{2}\partial_x(\overline{u^2} - \widehat{\overline{u}^2})\\
&=\; \partial_t \overline{u} + \tfrac{1}{2}\partial_x \widehat{\overline{u}^2} + \tfrac{1}{2}\partial_x \xi = 0,
\end{aligned}
\tag{5.2}
$$

in which we introduced $\xi = \overline{u^2} - \widehat{\overline{u}^2}$ to denote the *computational turbulent stress tensor*. This tensor constitutes the full closure problem in the *modified equation* and includes the contributions due to the spatial discretization [45].

The difference between the computational turbulent stress ξ and the SGS-stress τ is given by,

$$\xi \;=\; \overline{u^2} - \overline{u}^2 + \overline{u}^2 - \widehat{\overline{u}^2} \;=\; \tau + \mathcal{H}(\overline{u}^2), \tag{5.3}$$

and can be expressed in terms of the high-pass filter associated with the numerical filter $\mathcal{H}(f) = f - \widehat{f}$. This high-pass filter is extensively discussed for a range of discretizations in [45]. For a given discretization method the difference between ξ and τ depends on the subgrid resolution which characterizes the strength of the numerical filtering. If the subgrid resolution r is sufficiently large, the numerical filter operator $\widehat{(\cdot)}$ reduces to the identity operator on all length-scales relevant to

τ. This implies that $\xi \to \tau$, and consequently (5.2) reduces to (5.1) as was to be expected.

However, in practical LES settings the grid spacing is chosen such that $h \lesssim \Delta$ and the numerical filter component in the full closure problem needs to be explicitly accounted for. Often, the numerical filter $\widehat{(\cdot)}$ is not explicitly known. In this chapter we will focus attention on the characteristic case in which the numerical filter is taken the same as the basic LES filter such that $\xi = (\overline{u^2} - \overline{u}^2)/2$. Such a situation can arise in different ways. For example, we may start with the top-hat filter with filter-width $\Delta = 2h$ as basic LES filter. This filter is identical to the induced filter associated with second order central finite differencing. Conversely, more general finite difference and finite volume discretizations each induce 'their' specific associated spatial filter, which might also be adopted as basic LES filter [45]. In either of these cases the numerically induced filter would be identical to the basic LES filter. In this chapter we will restrict primarily to the top-hat filter and consider typically a filter-width over grid ratio $\Delta/h = 2$. The effect of this second order filter compares closely with the effect of other second order filters, such as the Gaussian filter [48, 142]. In this approximate sense one may interchange different second order filters if this would facilitate a specific analysis. Extensions to general numerical filtering only constitute technical complications and will not be developed explicitly here.

This sequence of steps to arrive at a computational LES model has been applied to the incompressible Navier-Stokes equations previously by Rogallo and Moin [106] and Lund and Kaltenbach [84, 83]. The resulting SGS-terms were analyzed, e.g., by Carati *et al.* [21, 146], Gullbrand and Chow [62] and by De Stefano and Vasilyev [115]. In this chapter we will extend this literature and analyze the large-eddy equations for the compressible Navier-Stokes equations. We will distinguish two parts in the computational stress tensor ξ_{ij} for compressible flow. The first contribution corresponds mainly to turbulent stresses arising from variations in *velocity* while the other part is influenced more by variations in *density*. This decomposition of the computational turbulent stress tensor motivates the introduction of separate models for each of these dynamic effects. Especially in case compressibility effects are large, e.g., at high Mach numbers, one may expect significant contributions from density variations and it can be beneficial to introduce dedicated subgrid models for each of these contributions. Results of an *a priori* investigation using DNS of turbulent mixing at various Mach numbers will be used to quantify the individual contributions. At sufficiently high (supersonic) Mach numbers the dynamical effect of density variations are found to require explicit modeling. A new set of density variation models based on approximate deconvolution is proposed along lines set out in [116].

The organization of this chapter is as follows. In section 5.2 both the formal and nu-

merical filter are introduced in detail and applied to the compressible Navier-Stokes equations. In section 5.3 the magnitudes of the density and velocity variation parts are investigated using a DNS-database of turbulent mixing at various Mach numbers. The deconvolution modeling of the density-variations at high Mach number is also presented. Concluding remarks are collected in section 5.4.

5.2   Computational turbulent stress tensor for compressible flow

In this section we will first introduce the computational turbulent stress tensor ξ_{ij} for the Navier-Stokes equations which govern compressible flow (subsection 5.2.1). This discussion follows that of the inviscid Burgers equation considered earlier in the introduction. The computational turbulent stress tensor ξ_{ij} is subsequently rewritten in terms of a velocity and a density variation part (subsection 5.2.2).

5.2.1   Spatial discretization and numerical filter

The application of the formal filter implies that the LES solution is contained in flow-features with length-scales larger than the filter-width Δ. This motivates the use of a grid spacing h on the order of Δ. As sketched in the introduction, the ratio Δ/h in actual simulations is not very large in view of practical computing restrictions. Correspondingly, the spatial discretization may have a considerable additional filtering effect [92]. This advocates the evaluation of the filtered equations on the level of the computational model. Hence, a shift of attention toward the computational turbulent stress tensor ξ_{ij} is implied, which will be introduced in detail next.

The formal filtering of the nonlinear convective terms in the momentum equation $\partial_j \rho u_i u_j$ leads to a contribution $\partial_j(\overline{\rho u_i u_j})$ which is commonly rewritten as (2.26),

$$\partial_j(\overline{\rho u_i u_j}) \; = \; \partial_j \overline{\rho} \widetilde{u}_i \widetilde{u}_j + \partial_j \overline{\rho} \tau_{ij}. \tag{5.4}$$

where τ_{ij} is the SGS-stress (2.31). However, within the computational system that arises after the spatial discretization one has direct access only to $\delta_j(\overline{\rho} \widetilde{u}_i \widetilde{u}_j)$. Here, we denote the numerical approximation of the partial differential operator ∂_j by the discrete derivative operator δ_j. This distinction suggests a decomposition in which,

$$\partial_j(\overline{\rho u_i u_j}) = \delta_j(\overline{\rho} \widetilde{u}_i \widetilde{u}_j) + \left[\partial_j(\overline{\rho u_i u_j}) - \delta_j(\overline{\rho} \widetilde{u}_i \widetilde{u}_j) \right]. \tag{5.5}$$

The closure problem between square brackets is a combination of the formal closure problem on the PDE-level and a numerical component. The latter can be specified

in more detail for a large class of spatial discretization methods. In fact, the discrete derivative operator δ_j, associated with finite volume, finite difference or finite element methods, contributes directly to the spatial filtering. A simple example is the second-order central finite differencing method [106]. This discretization induces a top-hat filter with a filter-width equal to twice the grid-spacing h. In detail,

$$\delta_x\Big(f(x,t)\Big) \;=\; \frac{f(x+h,t)-f(x-h,t)}{2h} \;=\; \partial_x\Big(\int_{x-h}^{x+h}\frac{f(s,t)}{2h}\,ds\Big). \qquad (5.6)$$

This example motivates the following general definition of the implied numerical filter $\widehat{(\cdot)}$: $\delta_x f \;=\; \partial_x \widehat{f}$ (see also [45] for further discussion). Assuming the same implied numerical filter for each of the coordinate directions [83], we may rewrite the filtered convective term as,

$$\partial_j(\overline{\rho u_i u_j}) = \delta_j(\widehat{\overline{\rho}\widetilde{u}_i\widetilde{u}_j}) + \partial_j(\overline{\rho u_i u_j} - \widehat{\overline{\rho}\widetilde{u}_i\widetilde{u}_j}) = \partial_j(\widehat{\overline{\rho}\widetilde{u}_i\widetilde{u}_j}) + \partial_j\xi_{ij}, \qquad (5.7)$$

where the computational turbulent stress tensor is given by,

$$\xi_{ij} \;=\; \overline{\rho u_i u_j} - \widehat{\overline{\rho}\widetilde{u}_i\widetilde{u}_j}. \qquad (5.8)$$

The decomposition (5.7) contains contributions from the filtered mean flux vector $\widehat{\overline{\rho}\widetilde{u}_i\widetilde{u}_j}$ next to the divergence of the computational turbulent stress tensor.

The subgrid resolution $r = \Delta/h$ may be used to roughly classify the 'strength' of the induced numerical filtering. In case the smallest retained scales are only marginally resolved ($r \approx 1-2$) the induced numerical filtering $\widehat{(\cdot)}$ may be expected to be dynamically important and lead to significant differences between τ_{ij} and ξ_{ij}. In case the smallest retained scales are properly captured by the spatial discretization ($r \geq 4-6$ [42]) the approximately grid-independent LES solution is obtained. This corresponds to an induced numerical filter operator $\widehat{(\cdot)} \approx Id$ where Id denotes the identity operator. In this case $\xi_{ij} \approx \tau_{ij}$. Commonly, in present-day LES the subgrid resolution is not chosen much larger than $r \approx 1-2$ [22, 92, 42, 140] and consequently one needs to include the numerical filtering component in the full closure problem (5.7) if the filter-width is sufficiently large. In order to connect most directly to this current LES practice, we primarily adhere to $\Delta/h = 2$.

The induced numerical filter is determined by the combination of the discretization method, the subgrid resolution and the computational grid. In LES a wide variety of numerical discretization methods and grids is employed. Each such combination induces its own numerical filter that should be analyzed in individual cases. A characteristic setting that will be used in the sequel is $\widehat{(\cdot)} = \overline{(\cdot)}$, i.e., the induced numerical filter is identified with the formal filter. Consequently, ξ_{ij} is given by

$$\xi_{ij} \;=\; \overline{\rho u_i u_j} - \overline{\overline{\rho}\widetilde{u}_i\widetilde{u}_j}. \qquad (5.9)$$

This setting would correspond, e.g., to $\Delta = 2h$ and second order finite differencing as sketched in (5.6). Other combinations yield different induced numerical filters [45] which can be investigated along similar lines as adopted in this chapter. Such extensions primarily constitute technical complications in the analysis and will not be elaborated upon here.

We next consider the contributions to the computational turbulent stress tensor ξ_{ij} as defined in (5.9) in more detail.

5.2.2   Computational turbulent stress tensor in compressible flow

In this subsection we propose a decomposition of the computational turbulent stress tensor $\xi_{ij} = \overline{\rho u_i u_j} - \overline{\rho \widetilde{u}_i \widetilde{u}_j}$ which accounts quite directly for the separate effects of velocity and density variations. The effects of compressibility in ξ_{ij} may be split off as follows:

$$
\begin{aligned}
\xi_{ij} = \overline{\rho u_i u_j} - \overline{\rho \widetilde{u}_i \widetilde{u}_j} &= \overline{\rho} \, \widetilde{u_i u_j} - \overline{\rho \widetilde{u}_i \widetilde{u}_j} \\
&= \overline{\rho} \, \widetilde{u_i u_j} - \overline{\rho} \, \widetilde{\widetilde{u}_i \widetilde{u}_j} + \overline{\rho} \, \widetilde{\widetilde{u}_i \widetilde{u}_j} - \overline{\rho \widetilde{u}_i \widetilde{u}_j} \\
&= \overline{\rho} \Big\{ \widetilde{u_i u_j} - \widetilde{\widetilde{u}_i \widetilde{u}_j} \Big\} + \Big(\overline{\rho \widetilde{u}_i \widetilde{u}_j} - \overline{\rho \widetilde{u}_i \widetilde{u}_j} \Big) \\
&= \overline{\rho} \eta_{ij} + \overline{\rho' \widetilde{u}_i \widetilde{u}_j}
\end{aligned}
\tag{5.10}
$$

where we introduced the tensor $\eta_{ij} = \widetilde{u_i u_j} - \widetilde{\widetilde{u}_i \widetilde{u}_j}$ to represent contributions from small scales in the velocity, defined with reference to the Favre filter. The final expression for the computational stress tensor in (5.10) motivates the introduction of the following two stresses: $\xi_{ij}^{\mathrm{vel}} = \overline{\rho} \, \eta_{ij}$ and $\xi_{ij}^{\mathrm{dens}} = \overline{\rho' \widetilde{u}_i \widetilde{u}_j}$, such that,

$$
\xi_{ij} = \xi_{ij}^{\mathrm{vel}} + \xi_{ij}^{\mathrm{dens}}.
\tag{5.11}
$$

Expression (5.11) splits ξ_{ij} into a part that is associated primarily with variations in the velocity (ξ_{ij}^{vel}) and a part that characterizes variations in density (ξ_{ij}^{dens}). Upon putting $u_i = \widetilde{u}_i + u_i''$, the velocity variation part ξ_{ij}^{vel} may be expressed as,

$$
\xi_{ij}^{\mathrm{vel}} = \overline{\rho} \Big(\widetilde{\widetilde{u}_i u_j''} + \widetilde{u_i'' \widetilde{u}_j} + \widetilde{u_i'' u_j''} \Big).
\tag{5.12}
$$

In this expression only small-scale variations in velocity are encountered directly. Variations in ρ only influence the Favre averaging itself and their effect on ξ_{ij}^{vel} is only 'indirect'. The interpretation of ξ_{ij}^{dens} as the density variation part is straightforward as only ρ' is encountered directly in ξ_{ij}^{dens}. Clearly in the incompressible limit this term is zero and at very low Mach number ξ_{ij}^{dens} may be expected to be negligibly small. Significant effects of ξ_{ij}^{dens} are expected only at sufficiently high

Mach number. In these circumstances explicit models for ρ' should be considered in relation to the closure of ξ_{ij}. We return to this in the next section.

The decomposition of ξ_{ij} may be further motivated by comparison with the incompressible numerical stress tensor as studied in [83, 115, 21, 146, 62, 61]. The incompressible numerical stress tensor ξ_{ij}^{inc} may be expressed as

$$\xi_{ij}^{\mathrm{inc}} = \overline{u_i u_j} - \overline{u_i}\,\overline{u_j} \tag{5.13}$$

This tensor only contains contributions from small-scale features in the turbulent velocity. Upon formally replacing the bar filter by the associated Favre filter we may directly make the identification with η_{ij} in (5.10), which further substantiates the interpretation of ξ_{ij}^{vel}.

In the next section we will study ξ_{ij} in more detail, compare the magnitude of ξ_{ij}^{dens} and ξ_{ij}^{vel} at various Mach numbers and introduce an explicit model for the density variations.

5.3   Computational turbulent stress: density and velocity variations

In this section we compare the magnitude of ξ_{ij}^{dens} and ξ_{ij}^{vel} using DNS-data of a temporal mixing layer at various Mach numbers. We establish a strong increase of ξ_{ij}^{dens} with increasing compressibility effects. This indicates under what flow conditions both ξ_{ij}^{vel} and ξ_{ij}^{dens} need to be modeled, and hence also when it is adequate to only address ξ_{ij}^{vel}.

The available DNS database contains turbulent flow data of a temporal mixing layer at subsonic Mach numbers $M = 0.2$, $M = 0.6$ and at a supersonic value $M = 1.2$ in a computational box $\Omega = [0, \ell_1] \times [-\frac{1}{2}\ell_2, \frac{1}{2}\ell_2] \times [0, \ell_3]$. The box-length in the vertical direction is $\ell_2 = 59$. This is kept the same for all Mach numbers considered, while ℓ_1 and ℓ_3 are sufficiently large to accommodate at least four periods of the most unstable mode as predicted by linear stability theory [139]. Specifically, we adopted $\ell_1 = \ell_3 = 59$ and 68 for the $M = 0.2$ and $M = 0.6$ case, respectively. In the $M = 1.2$ case the most unstable mode is three-dimensional and $\ell_1 = 39.9$ and $\ell_3 = 22.1$ [143]. Periodic boundary conditions are imposed in the streamwise (x_1) and spanwise (x_3) directions and free-slip walls are adopted in the vertical (x_2) direction. The initial condition for the streamwise velocity is formed by a tanh-profile in the vertical direction on which perturbation modes based on linear stability theory have been added. This leads to rapid transition to strongly three-dimensional turbulence that is used here to assess the dependence

of the computational turbulent stress tensor on the Mach number. In each of the simulations the turbulent regime is characterized by many small-scale components which are much smaller than ℓ_1 and ℓ_3. Correspondingly, the size of the domain in the homogeneous directions is certainly large enough throughout the simulations to neglect possible effects arising from the use of periodic boundary conditions. For further details concerning the DNS-data we refer to [141, 143].

The Reynolds number Re based on the upper-stream velocity and half the initial vorticity thickness is set to 50 when $M = 0.2$ and $M = 0.6$ while $Re = 100$ when $M = 1.2$. The higher Reynolds number at $M = 1.2$ was adopted to speed-up the transition process to turbulence [143]. The simulations at $Re = 50$ and $M = 0.2$, 0.6 use a resolution of 192^3 grid-points, while $320 \times 513 \times 192$ grid-points were used for the simulation at $Re = 100$ and $M = 1.2$. Explicit, four-stage, second order, compact storage Runge-Kutta time-stepping is combined with a fourth order accurate finite volume discretization for the subsonic flows while a hybrid method composed of the third-order accurate MUSCL shock-capturing scheme in combination with fourth order central discretization was used in the supersonic case [138, 48]. The filter-width $\Delta = \ell_2/16$ and the top-hat filter was used to process individual snapshots of the numerical solutions contained in the database. We separately verified that the use of a Gaussian filter instead of the top-hat filter leads to similar conclusions regarding the computational turbulent stress tensor and its dependence on M. In fact, both the top-hat and the Gaussian filter are second order filters and the Fourier-transform $\widehat{G}$ of the kernels of these filters can be written as $\widehat{G}(k\Delta) = 1 - (k\Delta)^2/24 + \ldots$ if $|k\Delta| \ll 1$, where k is the wavenumber of a Fourier-mode (further details may be found in [49]). The similarity between these two filters underlines the fact that virtually identical results were obtained for all quantities investigated in this chapter, when either of these operators was adopted. Similar observations were made in [142].

In order to quantify the magnitude of ξ_{ij}^{dens} and ξ_{ij}^{vel}, the 'planar' L_2-measure as a function of the vertical coordinate is considered. For a general field f this is given by,

$$L_2^{\mathrm{pl}}(f)(x_2, t) \;=\; \left(\frac{1}{\ell_1 \ell_3} \int_0^{\ell_3} \int_0^{\ell_1} f^2(\mathbf{x}, t) \, dx_1 dx_3 \right)^{1/2} \tag{5.14}$$

We investigate turbulent flow at various Mach numbers. Since the turbulent mixing layer develops at different rates for the different Mach numbers it is more insightful to compare flow solutions with approximately the same momentum thickness. For the self-similarly developing temporal mixing layer the momentum thickness $\delta(t)$ is a strictly increasing function of time t [141] given by

$$\delta(t) \;=\; \tfrac{1}{4} \int_{-\frac{1}{2}\ell_2}^{\frac{1}{2}\ell_2} \langle \overline{\rho} \rangle_{13} \left(1 - \frac{\langle \overline{\rho} \widetilde{u}_1 \rangle_{13}}{\langle \overline{\rho} \rangle_{13}} \right) \left(1 + \frac{\langle \overline{\rho} \widetilde{u}_1 \rangle_{13}}{\langle \overline{\rho} \rangle_{13}} \right) dx_2, \tag{5.15}$$

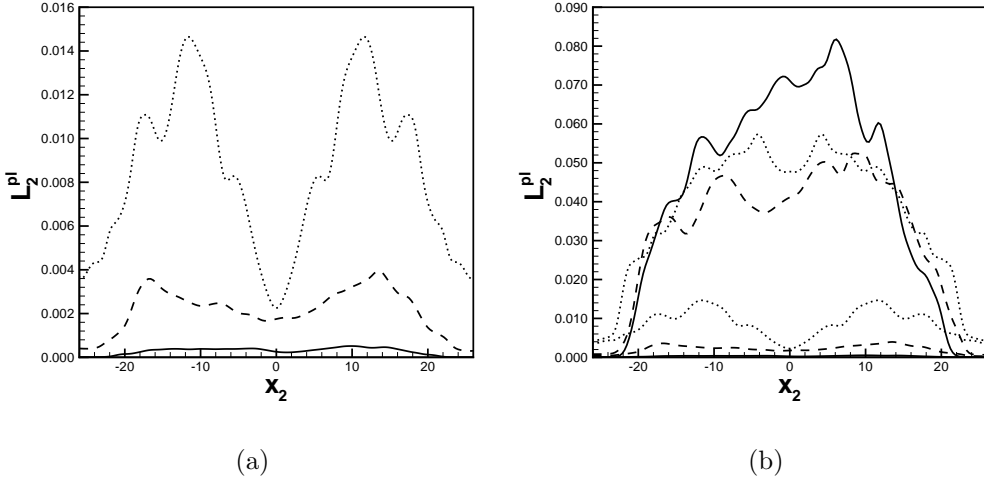(a)   (b)

Figure 5.1: The planar L_2-norm L_2^{pl} as a function of the vertical coordinate at instants in the developed turbulent regime when $\delta \approx 5$, which corresponds to $t = 70.0$, $t = 90.0$ and $t = 195.0$ for $M = 0.2$, $M = 0.6$ and $M = 1.2$ respectively. Lines are shown solid ($M = 0.2$), dashed ($M = 0.6$) and dotted ($M = 1.2$): (a) the density variation part ξ_{11}^{dens} only and (b) both the density ξ_{11}^{dens} (lower set of curves) and the velocity variation part ξ_{11}^{vel} (upper set of curves).

where $\langle \cdot \rangle_{13}$ denotes averaging over the homogeneous x_1- and x_3-directions. The momentum thickness is a large-scale flow-property that is quite independent of the adopted subgrid resolution [42]. The use of $\delta(t)$ instead of t is quite instrumental in comparing the results at very different Mach numbers. If a further systematic scaling of time could be formulated that would collapse the different curves for the momentum-thickness onto a single Mach-independent curve, then this could further support the interpretation of the findings. Presently, there is no such scaling known in literature. In the turbulent regime, the growth-rate of the momentum-thickness is a decreasing function of M, but its specific dependence on Mach number is quite complicated and still a topic of ongoing research [143].

The dependence of $L_2^{\text{pl}}(\xi_{11}^{\text{dens}})$ on x_2 at different Mach numbers is shown in figure 5.1(a). We focus on the characteristic 11-component and compare solutions in the developed turbulent regime at different times t, selected such that $\delta \approx 5$. Close to the incompressible limit as $M = 0.2$, the density variation part of the computational turbulent stress is quite negligible. With increasing Mach number the magnitude of $L_2^{\text{pl}}(\xi_{11}^{\text{dens}})$ strongly increases. In figure 5.1(b) the magnitude of $L_2^{\text{pl}}(\xi_{11}^{\text{dens}})$ is compared with $L_2^{\text{pl}}(\xi_{11}^{\text{vel}})$. In both subsonic cases $M = 0.2$ and $M = 0.6$ the magnitude of the density variation part is much smaller than the
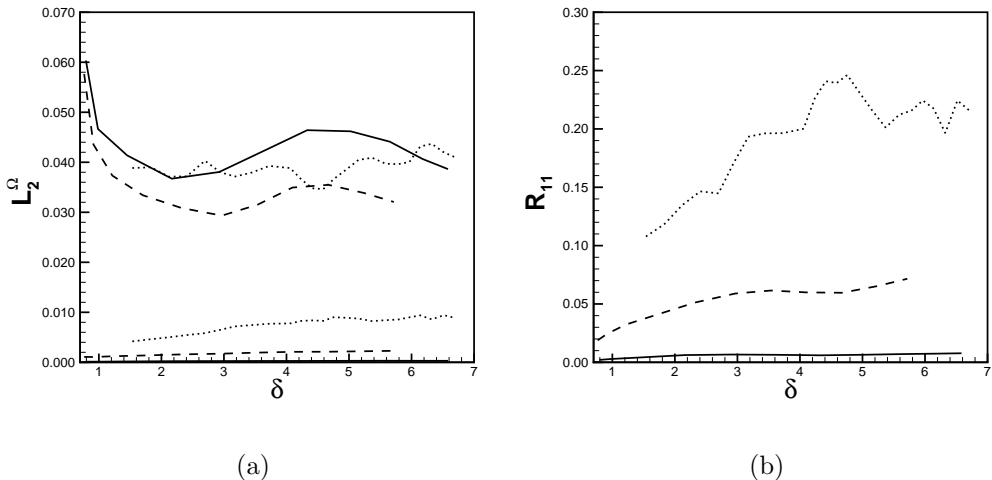
(a) (b)

Figure 5.2: In (a) L_2^Ω is plotted as function of the momentum thickness δ: velocity variation part (upper set of curves) and density variation part (lower set of curves). In (b) their ratio R_{11} as a function of the momentum thickness is displayed. The corresponding Mach numbers are $M = 0.2$ (solid), $M = 0.6$ (dashed) and $M = 1.2$ (dotted).

contributions due to velocity variations. However, in the supersonic case $M = 1.2$ the density variation part is seen to represent a fraction of ξ_{11} of about 20 % as may be quantified, e.g., by comparing the peak values of L_2^{pl}.

To further illustrate the relative importance of the two contributions to ξ_{ij} we consider the evolution of the full L_2-norm of ξ_{ij}^{dens} and ξ_{ij}^{vel}. The three-dimensional L_2-norm is given by,

$$L_2^\Omega(f)(t) = \left(\frac{1}{\ell_1 \ell_2 \ell_3} \int_\Omega f^2(\mathbf{x}, t) \, d\mathbf{x} \right)^{1/2}. \tag{5.16}$$

In figure 5.2(a) we collected $L_2^\Omega(\xi_{11}^{\mathrm{dens}})$ and $L_2^\Omega(\xi_{11}^{\mathrm{vel}})$ as a function of the momentum thickness. The time-dependence of L_2^Ω is illustrated in figure 5.2 and displays an initial decrease of the velocity variation part in the transitional stage, followed by quite large but gradual variations around 0.04 in the turbulent regime. The density variation part displays a gradual increase as the flow develops from the laminar initial condition to the turbulent state and settles around an M dependent value during the self-similar stages of the development. At low Mach numbers the values of L_2^Ω due to density variations are small during the entire development of the flow. However, in the supersonic case the norm of ξ_{11}^{dens} becomes approximately 20% of the norm of ξ_{11}^{vel}. Overall, the variations in $L_2^\Omega(\xi_{11}^{\mathrm{vel}})$ with Mach number

are comparably small; compressibility effects appear most pronounced in ξ_{11}^{dens}. Similar trends can be observed in relation to other components of ξ_{ij}. The relative importance of ξ_{ij}^{dens} and ξ_{ij}^{vel} may be quantified more precisely in terms of the ratio,

$$R_{ij}(t) \;=\; \frac{L_2^{\Omega}(\xi_{ij}^{\text{dens}})(t)}{L_2^{\Omega}(\xi_{ij}^{\text{vel}})(t)}. \tag{5.17}$$

The dependence of R_{11} as a function of the momentum thickness is shown in figure 5.2(b). For each of the cases considered, this ratio is seen to vary quite gradually around a Mach-dependent turbulent value as $\delta \gtrsim 3$. During these developed turbulent stages R_{11} is approximately 1% as $M = 0.2$, 6% as $M = 0.6$ and varies between 20% and 25% as $M = 1.2$. The ratios corresponding to the other components $R_{12}, \ldots, R_{33}$ (not shown) reveal similar behavior, albeit that some components saturate at lower levels of about 10% at $M = 1.2$.

Summarizing, the planar and three-dimensional L_2-norms quantify the expected dependence of ξ_{ij}^{dens} on the Mach number and establish a corresponding degree of independence of ξ_{ij}^{vel}. Additionally, the magnitude of the density variation part in the computational turbulent stress tensor is small in the subsonic regime but can be considerable at sufficiently high Mach numbers. In the latter case the relative magnitude can go up to $\approx 20 - 25\%$.

Next we turn to explicit modeling of the density variation part ξ_{ij}^{dens}.

Explicit modeling of density variations.

In the definition of $\xi_{ij}^{\text{dens}} = \overline{\rho' \widetilde{u}_i \widetilde{u}_j}$ two filtered ($\widetilde{u}_i$ and $\widetilde{u}_j$) and one small-scale contribution ρ' arise. To close this contribution to the large-eddy equations, we consider how well the density variations may be approximated by $\rho^{\star} - \overline{\rho}$. Here $\rho^{\star} \approx \rho$ is an approximation of the unfiltered density such that $\xi_{ij}^{\text{dens}} \approx \overline{(\rho^{\star} - \overline{\rho}) \widetilde{u}_i \widetilde{u}_j}$. Over the past years several so-called inverse filtering techniques have been proposed which can be used to approximate unfiltered variables [41]. A successful inverse filtering technique is the approximate deconvolution method (ADM) [116, 118, 117] that will be considered in more detail next in relation to approximating ρ'.

ADM is based on truncation of the geometric series expansion of the formal inverse of a filter operator. If we denote the filter by the operator $\mathcal{L}$ and its (formal) inverse by $\mathcal{L}^{-1}$ then the unfiltered density is formally given by,

$$\rho = \mathcal{L}^{-1}(\overline{\rho}) = \left(Id - (Id - \mathcal{L}) \right)^{-1}(\overline{\rho}) = \sum_{k=0}^{\infty} (Id - \mathcal{L})^k (\overline{\rho}) \approx Q_N(\overline{\rho}), \tag{5.18}$$

where the N-th order approximate inversion operator Q_N is obtained from the first N terms in the formal series expansion. This series converges to $\mathcal{L}^{-1}$ as $N \to \infty$,

provided $|1 - \widehat{G}(k)| < 1$, where $\widehat{G}$ denotes the Fourier transform of the filter-kernel [116]. Since $\hat{G}(0) = 1$, this implies that $\hat{G}(k)$ has to be strictly positive in wave-number space. This condition is satisfied, e.g., by a Gaussian or Helmholtz filter [48], but not by the top-hat or the spectral cut-off filter. Still, for finite N the operator Q_N is well defined and may be interpreted to provide the approximate inverse modeling of the density.

For a number of values of the truncation parameter N we may obtain explicit approximations for the reconstructed density $\rho_N^\star$ and the corresponding small-scale variability $\rho_N' = \rho_N^\star - \overline{\rho}$. In detail we obtain

$$\rho_0^\star = \overline{\rho} \quad ; \quad \rho_0' = 0 \tag{5.19}$$
$$\rho_1^\star = 2\overline{\rho} - \overline{\overline{\rho}} \quad ; \quad \rho_1' = \overline{\rho} - \overline{\overline{\rho}} \tag{5.20}$$
$$\rho_2^\star = 3\overline{\rho} - 3\overline{\overline{\rho}} + \overline{\overline{\overline{\rho}}} \quad ; \quad \rho_2' = 2\overline{\rho} - 3\overline{\overline{\rho}} + \overline{\overline{\overline{\rho}}} \tag{5.21}$$

The N-th order approximation for ξ_{ij}^{dens} is then simply given by $\overline{\rho_N' \widetilde{u}_i \widetilde{u}_j}$. Repeated application of the filter $\mathcal{L}$ is required in order to arrive at an efficient implementation of ADM. To get an insight in the accuracy and effectiveness of the ADM modeling of the small-scales in the density an *a priori* test at supersonic Mach number is considered next.

The DNS data corresponding to the supersonic turbulent mixing layer at $M = 1.2$ were first filtered using a Gaussian filter with filter-width $\Delta = \ell_2/16$. In order to resemble the situation in actual LES the filtered data were subsequently projected onto a coarsened grid. Specifically, we applied a coarsening by a factor of 16 in each coordinate direction, compared to the grid used for the DNS and the adopted coarse grid contains $20 \times 32 \times 12$ grid cells. This corresponds to a subgrid resolution $r = 2$. Other resolutions such as $40 \times 64 \times 24$ were also investigated, either at the same subgrid-resolution or at a higher value $r = 4$. The accuracy of the N-th order ADM-approximations is investigated by the L_2-error normalized by the filtered density,

$$E_N^{\mathrm{pl}} = \frac{L_2^{\mathrm{pl}}(\rho_N^\star - \rho)}{L_2^{\mathrm{pl}}(\overline{\rho})} \quad \text{and} \quad E_N^{\Omega} = \frac{L_2^{\Omega}(\rho_N^\star - \rho)}{L_2^{\Omega}(\overline{\rho})}. \tag{5.22}$$

In figure 5.3(a) the error E_N^{pl} is shown as a function of the vertical direction for the same snapshot used in figure 5.1. The corresponding L_2-norm E_N^{Ω} as function of the momentum-thickness is contained in figure 5.3(b). The decrease of E_N^{pl} and E_N^{Ω} with increasing N is clearly illustrated. For $N = 1 - 3$ the error reduces quite quickly, while for $N > 3$ only small additional improvements are observed. In total, about a factor of two reduction in the error-levels can be obtained with the ADM procedure, in this case. We also studied the application of ADM at increased
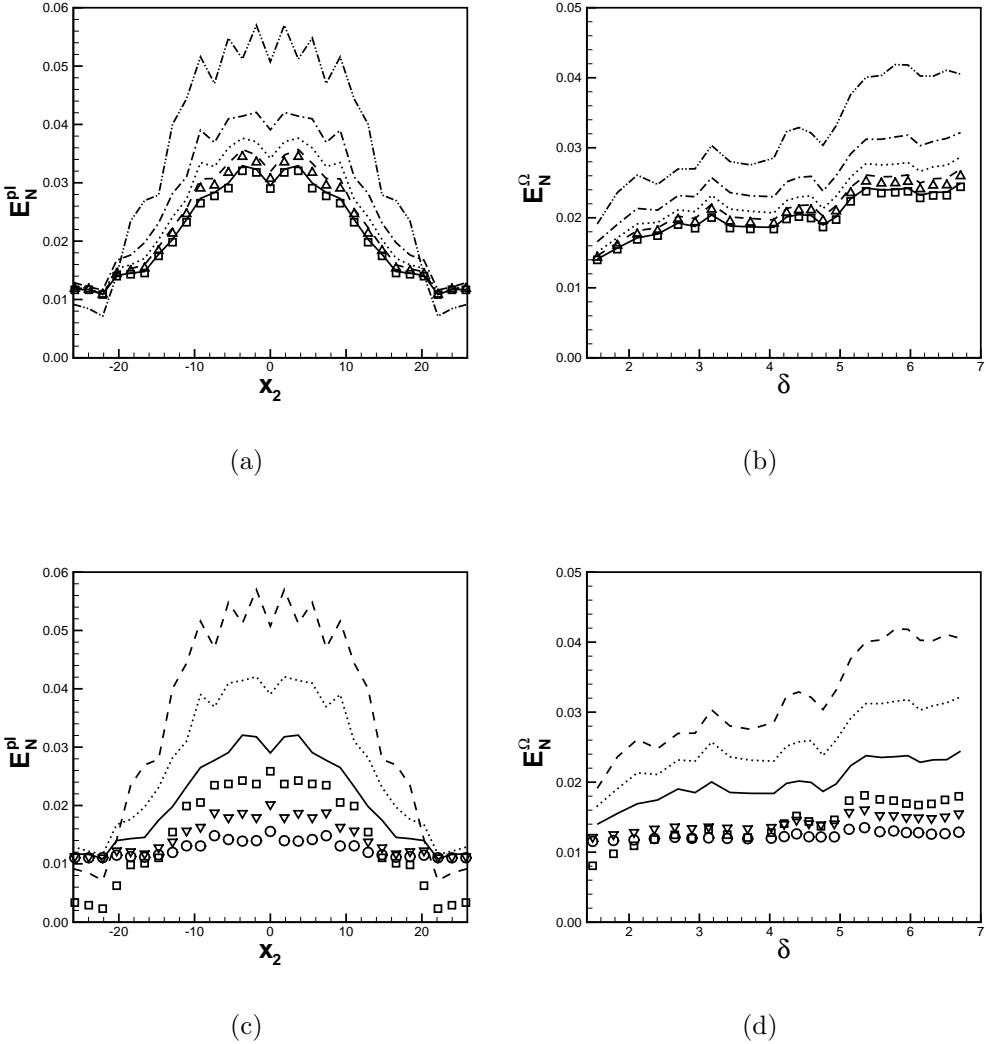
(a)   (b)

(c)   (d)

Figure 5.3: L_2-measures of the relative error in the approximated density $\rho_N^\star$ as a function of a) vertical direction for the field when $\delta \approx 5$, and b) momentum thickness. Use was made of N-th order ADM in combination with a Gaussian filter: $N = 0$ (dash-dotdot), $N = 1$ (dash-dot), $N = 2$ (dotted), $N = 3$ (dashed), $N = 4$ ($\triangle$), $N = 6$ (solid), $N = 8$ ($\square$). In c) and d) results are compared using a sub-grid resolution $\Delta/h = 2$ and a spatial resolution of $20 \times 32 \times 12$ (lines) and $40 \times 64 \times 24$ (symbols), $N = 0$ (dashed/$\square$), $N = 1$ (dotted/$\triangledown$) and $N = 8$ (solid/$\circ$).

subgrid resolution. At a resolution of $40 \times 64 \times 24$ using $\Delta = \ell_2/16$, i.e., $r = 4$, the reduction in the error-level proceeds also at higher N and reaches a factor of about 3.5 at $N = 8$. The residual non-zero values for the error at high N are associated with the additional projection of $\overline{\rho}$ onto the coarser LES grid. At fixed $r = 2$, the ADM-approximation of the density variations becomes more accurate at higher spatial resolution. This arises since in this case the filter-width Δ decreases with increasing resolution and the approximate inversion of order N is accurate over a wider range of length-scales. The improvements can be observed in figure 5.3(c) and 5.3(d), where we compare the errors E_N^{pl} and E_N^{Ω} at resolutions $20 \times 32 \times 12$ and $40 \times 64 \times 24$, respectively, with $r = 2$. Again, we observe that the error is reduced by about a factor of two in these cases when N is increased, but since the 'start-level' of the error at $N = 0$ is lower at higher resolution, also the results at higher N become more accurate. These illustrations indicate the possibilities for an accurate reconstruction of ρ arising from ADM already at a modest value of $N = 3$ for low subgrid resolution $\Delta/h = 2$.

5.4   Concluding remarks

In this chapter we investigated the computational turbulent stress tensor for compressible flow. The computational turbulent stress tensor is the main SGS-term in the discretized LES equations. In view of the small filter-width to grid ratio $r = \Delta/h$ that is typically used in LES, the dynamic consequences of both formal and induced numerical spatial filtering need to be incorporated in the analysis and, ultimately, in the SGS modeling.

In case the induced numerical filter $\widehat{(\cdot)}$ is identified with the formal filter $\overline{(\cdot)}$, the computational turbulent stress tensor for three-dimensional compressible flow may be written as

$$\xi_{ij} \;=\; \overline{\rho u_i u_j} - \overline{\overline{\rho} \widetilde{u}_i \widetilde{u}_j}. \tag{5.23}$$

The main observation presented in this chapter is that two separate parts can be identified in ξ_{ij} for compressible flow,

$$\xi_{ij} \;=\; \overline{\rho} \eta_{ij} + \overline{\rho' \widetilde{u}_i \widetilde{u}_j}, \tag{5.24}$$

where $\eta_{ij} = \widetilde{u_i u_j} - \widetilde{u}_i \widetilde{u}_j$. The first part, $\overline{\rho} \eta_{ij}$, was shown to be associated primarily with small-scale variations in velocity. For example, η_{ij} corresponds to the computational turbulent stress tensor for incompressible flow [84, 83] in case the Mach number tends to zero. The second term, $\overline{\rho' \widetilde{u}_i \widetilde{u}_j}$, is associated with small-scale variations in the density. This contribution is negligibly small in the incompressible limit, and becomes dynamically important at sufficiently high Mach number. This

was quantified in an *a priori* investigation based on DNS-data of turbulent mixing at various Mach numbers. The density variation part is negligibly small in the incompressible limit ($M = 0.2$), but in case of supersonic flow ($M = 1.2$) these dynamic effects were considerably larger and achieve levels of up to 20% of those of the velocity variation part for this particular flow.

The decomposition of ξ_{ij} suggests the use of separate models for variations in velocity u_i'' and density ρ'. For the velocity variations one of the well known SGS-models such as the Smagorinsky, gradient or Leray model can be used [48]. In this chapter we modeled the small-scale density variations using the approximate deconvolution method [116]. Results of an *a priori* investigation showed that the ADM-approximations reproduce the unfiltered density already at modest-order ($N = 2$ or $N = 3$). *A priori* investigations are well known to be limited, e.g., since important effects such as interaction and accumulation of different modeling and numerical error-components can not be quantified [90]. *A posteriori* investigations are needed to complement the present *a priori* analysis.

Chapter 6

Variational Multi-scale approach to LES for compressible flow

In this chapter[1] an alternative formulation of LES is derived using the Variational Multi-scale approach to LES (VMS-LES). This alternative approach was recently introduced in [24, 69] for incompressible adopting Fourier-spectral basis-functions. In this chapter we will present a VMS-LES formulation for compressible flow using general basis-functions.

6.1 Introduction

6.1.1 Motivation and Goals

Due to the wide range of dynamically relevant flow scales present in a typical turbulent flow it is not possible to compute most realistic turbulent flows by means of a Direct Numerical Simulation (DNS) within the foreseeable future. Multiple simulation techniques based on a coarsened flow description have been proposed to overcome this problem of which Large-Eddy Simulation (LES) is one of the most promising. In an LES the spectrum of flow scales is divided into a resolved and unresolved part. Only the resolved scales are computed while the dynamic effects of the unresolved scales on the resolved scales are replaced by Sub-Grid Scale (SGS) models [48, 91]. By only computing the resolved scales an LES requires significantly less computational resources than a DNS.

---

[1]This chapter is largely based on Van der Bos, Van der Vegt and Geurts [127].

Traditionally LES techniques have been developed using the filtering approach [48, 91]. A low-pass filter operator with a filter-width Δ is used to identify which scales are resolved and which not. It is then believed that a grid can be used with a grid-spacing h on the order of the filter-width Δ. In a recent paper by Hughes *et al.* [69], and later in a different form by Collis [24], the Variational Multi-Scale approach to LES (VMS-LES) was introduced. In fact, VMS-LES as discussed in [24, 69] contributes to two different topics which are of interest to LES. First, by considering an *a priori* scale separation of the solution space $\mathcal{U}$ in terms of resolved $\overline{\mathcal{U}}$ and unresolved $\mathcal{U}'$ scales, i.e.

$$\mathcal{U} = \overline{\mathcal{U}} \oplus \mathcal{U}', \tag{6.1}$$

an alternative approach to LES is obtained. Here the solution space $\mathcal{U}$ contains all admissible solutions $\mathbf{U} = [\rho, \rho u_i, E]$ for the Navier-Stokes equations (2.1)-(2.3) and the scale separation considered in VMS-LES is such that $\mathbf{U} = \overline{\mathbf{U}} + \mathbf{U}'$, where $\overline{\mathbf{U}} \in \overline{\mathcal{U}}$ and $\mathbf{U}' \in \mathcal{U}'$. Among others VMS-LES differs from the traditional filtering approach in the sense that it explicitly uses projection rather than low-pass integral filters traditionally employed in LES.

The second contribution of VMS-LES to turbulence simulation, is a promising approach to SGS-modeling by considering an additional *a priori* scale separation of the resolved flow scales into large- and small-resolved scales. An approach which resembles the application of high-pass filters [108, 134] and dynamic modeling in the traditional filtering approach to LES [39, 40]. In this chapter we will only use the separation in terms of resolved and unresolved scales. We will extend this methodology to compressible flows and adapt the formulation such that it becomes applicable to a wide range of discretization methods.

The influence of the underlying discretization on the resulting VMS-LES formulation is a less emphasized aspect of VMS-LES as presented in [24, 69]. This is mainly reflected in the specific choice of the resolved flow scales in [24, 69],

$$\overline{\mathcal{U}} := \mathcal{U}_h. \tag{6.2}$$

Here $\mathcal{U}_h$ denotes the finite dimensional computational solution space which is determined by the method of discretization and the computational mesh. In [24, 69] Fourier-spectral methods are used for which $\mathcal{U}_h$ is spanned by a finite number of Fourier-spectral basis-functions $e^{i\mathbf{k}\cdot\mathbf{x}}$. As is well known, discretizations based on Fourier-spectral methods are in general impractical to use for complex flow-domains. In order for VMS-LES to be applicable to complex flow domains other discretization methods should also be considered and the VMS-LES formulation should be adjusted accordingly. We will do so in this chapter and frequently use DG-FEM as an illustrative example [25, 75, 130].

6.1.2 VMS-LES for compressible flow

The discussion in this chapter leading to a VMS-LES formulation for compressible flows follows along the same lines as the derivation for incompressible flows given by Collis in [24]. This contrasts recent work by Koobus and Farhat [77]. They introduce VMS-LES for compressible flows based on the formulation of Hughes *et al.* [69], which does not explicitly account for the dynamic effects of the unresolved flow scales. But maybe more importantly, the formulation presented in [77] does not resemble what is known as the Favre-filtered Navier-Stokes equations.

Favre- or density weighted filtering (averaging) has originally been introduced by Favre [31, 32, 33] and used in LES of compressible flow by Vreman *et al.* [137, 141], Lele [79], Moin *et al.* [95] and Erlebacher *et al.* [30]. One of the main reasons for adopting a Favre averaging or filtering procedure is the reduction in the number of SGS-terms. For example no SGS-term is encountered in the continuity equation when such a procedure is used. The compressible VMS-LES formulation presented in this chapter is analogous to the Favre-filtered Navier-Stokes equations.

6.1.3 VMS-LES formulation and discretization

The method of discretization and the grid adopted in a simulation form an integral part in VMS-LES as reflected by (6.2). The choice of setting the resolved scales equal to the computational solution space is convenient and is also adopted in this chapter. For example there is no need of specifying an external filtering operator to determine which scales are resolved and which not. Instead one can directly use the projection onto the grid.

There is also a drawback to the fact that VMS-LES is strongly interwoven with the discretization. When a different method of discretization is used, a different VMS-LES formulation emerges. In this chapter we will compare the VMS-LES formulation using a Fourier-spectral discretization with the VMS-LES formulation when using a more generally applicable numerical method such as DG-FEM.

The VMS-LES formulations in [24, 69] are based on a Fourier-spectral discretization. The computational solution space then contains all Fourier-modes $e^{i\mathbf{k}\cdot\mathbf{x}}$ with $|\mathbf{k}| < k_c$, where k_c denotes the cut-off wave number. VMS-LES formulations based on Fourier-spectral methods have the advantage that the associated projection $\mathcal{P} : \mathcal{U} \to \overline{\mathcal{U}}$ commutes with differentiation, i.e.,

$$\mathcal{P}[\partial_i \mathbf{U}] = \partial_i \mathcal{P}[\mathbf{U}], \quad \forall \mathbf{U} \in \mathcal{U}, \tag{6.3}$$

and no so-called commutator error is encountered [51, 52, 54]. In the first part of this chapter leading to the VMS-LES formulation for compressible flows we will assume commuting projections.

In the second part of this chapter we will focus on discretization methods other than Fourier-spectral methods and use DG-FEM as an illustrative example. Such methods can conveniently be used in complex flow domains. The main difference between a VMS-LES formulation based on a Fourier-spectral discretization and methods like DG-FEM can be isolated to the fact that projection generally does not commute with differentiation. There are $\mathbf{U} \in \mathcal{U}$ for which,

$$\mathcal{P}[\partial_i \mathbf{U}] \; \neq \; \partial_i \mathcal{P}[\mathbf{U}]. \tag{6.4}$$

In the final part of this chapter we will consider those properties which are satisfied by a DG-FEM and adjust the VMS-LES formulation accordingly. A number of additional contributions emerge which, as we will show, have a one to one correspondence with the commutator error $\mathcal{C}_i$ (2.29) encountered in LES [51, 52, 54, 122, 123].

The organization of this chapter is as follows. In section 6.2 we repeat some of the essential details of the DG-FEM, outline the VMS approach to LES and discuss the differences between a commuting and non-commuting projection. In section 6.3 the VMS-LES formulation for compressible flow is given assuming a commuting projection. The VMS-LES formulation using non-commuting projections follows in section 6.4. Finally, in section 6.5 some concluding remarks are collected.

6.2 Mathematical Model

In this section we first briefly recall some aspects of the DG-FEM introduced in chapter 2. Then we outline VMS-LES and further elaborate on the relation between the spatial discretization and the resulting VMS-LES formulation. Finally, we discuss the commutation properties of the projection operator $\mathcal{P} : \mathcal{U} \to \overline{\mathcal{U}}$ with respect to differentiation.

6.2.1 Outline of the DG-FEM

DG-FEM is used as a characteristic numerical method for illustrating the general VMS-LES formulation that is developed in this chapter. A DG-FEM discretization has been introduced in section 2 and those aspects essential to the VMS-LES formulation developed in this chapter are briefly recalled. Specifically, we will divide the spatial domain Ω into elements $K \subset \Omega$, define the computational solution space $\mathcal{U}_h$ and introduce the operator B_h for the weak formulation of the compressible Navier-Stokes equations. These form central elements in the subsequent VMS-LES formulation.

In DG-FEM the domain Ω is divided into non-overlapping elements K with a

typical diameter h, resulting in a tessellation $\mathcal{T}_h$,

$$\mathcal{T}_h \;=\; \left\{ K \subset \mathbb{R}^3 \,\middle|\, K_i \cap K_j = \emptyset \text{ if } i \neq j, \; \bigcup_{i=1}^{N_K} K_i = \Omega \right\}. \tag{6.5}$$

Here N_K denotes the number of elements. The computational solution space $\mathcal{U}_h$ is spanned by element-wise continuous basis functions ϕ_k. These basis functions are constructed such that they are linearly independent and on each element $K \in \mathcal{T}_h$ they span the local finite dimensional solution space $P(K)$. Typical local solution spaces $P(K)$ that are considered in DG-FEM are polynomial spaces which include polynomials up to a certain degree, see section 2.3 or [119, 130]. The resulting computational solution space is then given by,

$$\mathcal{U}_h \;=\; \left\{ \mathbf{U} \in (L_2(\Omega))^5 \,\middle|\, \mathbf{U}\big|_K \in [P(K)]^5, \forall K \in \mathcal{T}_h \right\}, \tag{6.6}$$

and the total number of basis functions used is denoted by N_ϕ.

The operator B_h used to define the weak formulation for the Navier-Stokes equations is arrived at by multiplying (2.10) with test-functions $\mathbf{W} \in \mathcal{U}_h$, integrate by parts over each element $K \in \mathcal{T}_h$ and finally sum over all elements,

$$
\begin{aligned}
B_h(\mathbf{W}, \mathbf{V}) \;=\; \sum_{K \in \mathcal{T}_h} & \left(W_\alpha \middle| \partial_t V_\alpha \right)_K - \left(\partial_j W_\alpha \middle| F_{\alpha j}^c(\mathbf{V}) - F_{\alpha j}^v(\mathbf{V}) \right)_K \\
& + \left(W_\alpha n_j \middle| F_{\alpha j}^c(\mathbf{V}) - F_{\alpha j}^v(\mathbf{V}) \right)_{\partial K}.
\end{aligned}
\tag{6.7}
$$

Here $\left(\cdot \middle| \cdot \right)$ denotes the L_2-innerproduct, $\left(f \middle| g \right)_\Omega = \int_\Omega f(\mathbf{x}) g(\mathbf{x}) \, d\mathbf{x}$, and $\mathbf{n}$ is the unit outward normal vector at the element boundary ∂K. Throughout this chapter integrals are written in terms of these inner-products as a short-hand notation.

The distinctive aspect of DG-FEM is that it allows the basis functions to be discontinuous across element faces, hence for $\mathbf{V} \in \mathcal{V}_h$, $\mathbf{y} \in \partial K$, $K \in \mathcal{T}_h$, generally

$$\mathbf{V}_-(\mathbf{y}) \neq \mathbf{V}_+(\mathbf{y}), \tag{6.8}$$

where $\mathbf{V}_\pm(\mathbf{y}) = \lim_{\varepsilon \downarrow 0} \mathbf{V}(\mathbf{y} \pm \varepsilon \mathbf{n})$ denote the traces of $\mathbf{U}$ at the element boundary ∂K. In order to deal with the jumps at the element boundaries ∂K and also for numerical stability it is necessary to introduce numerical fluxes [8, 9, 25, 75, 119]. However, to simplify the presentation in this chapter we restrict ourselves to the terms in (6.7).

6.2.2   Outline of the VMS approach to LES

The specification of the VMS approach to LES proceeds in a few steps. Central in VMS-LES is a splitting of the solution space of all admissible solutions of (2.1)-(2.3) $\mathcal{U}$ into a finite dimensional space of resolved flow scales $\overline{\mathcal{U}}$ and a space of

unresolved flow scales $\mathcal{U}'$,

$$\mathcal{U} \;=\; \overline{\mathcal{U}} \oplus \mathcal{U}'. \tag{6.9}$$

In this chapter we assume that the space of resolved conserved variables can be determined by a projection $\mathcal{P} : \mathcal{U} \to \overline{\mathcal{U}}$ and each $\mathbf{U} \in \mathcal{U}$ can be written as $\mathbf{U} = \overline{\mathbf{U}} + \mathbf{U}'$ with $\overline{\mathbf{U}} \in \overline{\mathcal{U}}$ and $\mathbf{U}' \in \mathcal{U}'$. In the next step we rewrite the operator B_h as defined in (6.7) into a so-called "large-eddy template" [48],

$$B_h(\mathbf{W}_h, \overline{\mathbf{U}} + \mathbf{U}') \;=\; B_h(\mathbf{W}_h, \overline{\mathbf{U}}) + B_h^{\mathrm{SGS}}(\mathbf{W}_h, \overline{\mathbf{U}}, \mathbf{U}'), \tag{6.10}$$

with $\mathbf{W}_h \in \mathcal{U}_h$. In this large-eddy template we distinguish a large-scale part $B_h(\mathbf{W}_h, \overline{\mathbf{U}})$ and the SGS-terms B_h^{SGS}. The SGS-terms are dependent on both resolved and unresolved variables and describe the dynamical effects of the unresolved scales on the resolved scales. In principle one could also determine the large eddy template immediately from a discrete Navier-Stokes operator such as B_h^{DG} (2.74) and identify the SGS-terms as they occur in the discretization. This would, however, add to the technical complexity of the current chapter and is not considered here.

In a DNS the computational solution space contains all dynamically relevant flow scales up to the Kolmogorov length-scale η and the dynamical effects of the SGS-terms are negligibly small. At the typical resolution considered in LES the dynamical effects of the SGS-terms can not be neglected. Rather than neglecting the SGS-terms one needs to incorporate them by introducing SGS-models $M_h(\mathbf{W}_h, \overline{\mathbf{U}})$ which only depend on the resolved scales in order to close the equations. For a specific model M_h this results in the following set of LES-equations,

$$0 \;=\; B_h(\mathbf{W}_h, \overline{\mathbf{U}}) + M_h(\mathbf{W}_h, \overline{\mathbf{U}}). \tag{6.11}$$

In this chapter we will describe the VMS-LES formulation in terms of a large-eddy template (6.10) for the compressible Navier-Stokes equations and we will not touch upon possible models as encountered in (6.11).

A distinctive aspect of the VMS approach to LES is that the discretization forms an integral part of the method. Specifically this is reflected in two aspects. Firstly by the choice of the resolved scales,

$$\overline{\mathcal{U}} := \mathcal{U}_h, \tag{6.12}$$

which lets these resolved scales be determined by the discretization. The second way the VMS-LES formulation is affected by the discretization comes from the fact that the equations are immediately evaluated at the level of the "computational model" [45, 124], i.e., the equations are evaluated *after* the application of the discretization step, see the discussion in the previous chapter. This contrary to most traditional filtering approaches to LES. In these approaches the filtered

equations are evaluated at the level of the "partial differential equation", i.e. *before* the application of the discretization step. The discretization step should, however, not be neglected as has already been noticed by a number of authors, see [21, 83, 106, 115] and results in a modification of the closure problem (see the discussion in the previous chapter). The VMS approach to LES has the advantage of immediately including this discretization step and consequently the SGS-terms in the VMS-LES formulation resemble the modified closure problem. This observation immediately explains why, in the incompressible case, the Leonard term [113] is absent in the SGS-stress in VMS-LES [24].

Due to the choice of the space of resolved scales and the specific construction of the computational solution space $\mathcal{U}_h$ we can now proceed with the introduction of the projection $\mathcal{P} : \mathcal{U} \to \overline{\mathcal{U}}$ as an L_2-projection onto the basis functions ϕ_k, $k = 0, \ldots, N_\phi - 1$ (2.22). This projection plays an important role in the discussion in this chapter. Recall that for a field f we can define $\mathcal{P}$ as,

$$\mathcal{P}[f](\mathbf{x}) = \sum_{k=0}^{N_\phi-1} \left\{ \sum_{l=0}^{N_\phi-1} \left(f\big|\phi_l\right)_\Omega \mathbb{M}_{lk}^{-1} \right\} \phi_k(\mathbf{x}). \tag{6.13}$$

Here $\mathbb{M}_{lk} = \left(\phi_l\big|\phi_k\right)_\Omega$ is an $N_\phi \times N_\phi$, symmetric, positive definite matrix. This matrix is often referred to as the mass matrix and in case orthogonal basis functions are used this matrix reduces to a diagonal matrix.

Some properties of this projection that will be used in the sequel are:

1. $\mathcal{P}$ is assumed to be mean-preserving, i.e. $P(1) = 1$.

2. $\mathcal{P}$ is a linear operator such that for $c_1, c_2 \in \mathbb{R}$ and $\mathbf{U}_1, \mathbf{U}_2 \in \mathcal{U}$,

$$\mathcal{P}[c_1\mathbf{U}_1 + c_2\mathbf{U}_2] = c_1\mathcal{P}[\mathbf{U}_1] + c_2\mathcal{P}[\mathbf{U}_2]. \tag{6.14}$$

3. $\mathcal{P}$ is projective, i.e. $\overline{\overline{\mathbf{U}}} = \overline{\mathbf{U}}$. This can be easily checked by considering,

$$\overline{\overline{\mathbf{U}}}(\mathbf{x}) = \sum_{k,l=0}^{N_\phi-1} \left(\overline{\mathbf{U}}\big|\phi_l\right)_\Omega \mathbb{M}_{lk}^{-1} \phi_k(\mathbf{x}), \tag{6.15}$$

$$= \sum_{k,l=0}^{N_\phi-1} \left\{ \sum_{m,n=0}^{N_\phi-1} \left(\mathbf{U}\big|\phi_n\right)_\Omega \mathbb{M}_{nm}^{-1} \left(\phi_m\big|\phi_l\right)_\Omega \right\} \mathbb{M}_{lk}^{-1} \phi_k(\mathbf{x}), \tag{6.16}$$

$$= \sum_{k,l=0}^{N_\phi-1} \left\{ \sum_{m,n=0}^{N_\phi-1} \left(\mathbf{U}\big|\phi_n\right)_\Omega \mathbb{M}_{nm}^{-1} \mathbb{M}_{ml} \right\} \mathbb{M}_{lk}^{-1} \phi_k(\mathbf{x}), \tag{6.17}$$

$$= \sum_{k,l=0}^{N_\phi-1} \left\{ \sum_{n=0}^{N_\phi-1} \left(\mathbf{U}\big|\phi_n\right)_\Omega \delta_{nl} \right\} \mathbb{M}_{lk}^{-1} \phi_k(\mathbf{x}) = \overline{\mathbf{U}}(\mathbf{x}). \tag{6.18}$$

4. $\mathcal{P}$ is self-adjoint with respect to the L_2-innerproduct $\left(\, \cdot \, \middle| \, \cdot \, \right)_\Omega$, i.e.

$$\left(\overline{\mathbf{U}} \middle| \mathbf{W} \right)_\Omega \;\; = \;\; \left(\mathbf{U} \middle| \overline{\mathbf{W}} \right)_\Omega, \tag{6.19}$$

which is a consequence of $\mathcal{P}$ being projective [147].

6.2.3 Commuting and non-commuting projections

In earlier papers on VMS-LES, Fourier-spectral discretizations were used [24, 69]. In this chapter we also consider discretization methods, such as DG-FEM, that can be more conveniently used in complex flow domains. As was motivated in the previous subsection the method of discretization determines the projection of $\mathcal{P}$ and hence ultimately the VMS-LES formulation.

The main difference between a VMS-LES formulation based on, e.g., DG-FEM compared to a formulation based on a Fourier-spectral discretization can be expressed in terms of the projection $\mathcal{P}$. Whereas the projection operator commutes with differentiation when a Fourier-spectral method is used it does not necessarily commute with differentiation when other discretization methods are considered, i.e.,

$$\mathcal{P}[\partial_i \mathbf{U}] \neq \partial_i \mathcal{P}[\mathbf{U}]. \tag{6.20}$$

In the traditional filtering approach a similar problem exists. Recalling from earlier chapters, so-called commutator errors emerge in the filtered equations when [51, 54],

$$\mathcal{L}[\partial_i \mathbf{U}] \neq \partial_i \mathcal{L}[\mathbf{U}]. \tag{6.21}$$

We will show that in VMS-LES similar SGS-terms emerge when the projection $\mathcal{P}$ does not commute with differentiation.

Important for our further discussion is that a commuting projection implies that both the spaces of resolved and unresolved scales are "closed with respect to differentiation". We consider the space of resolved scales to be closed with respect to differentiation if[2],

$$\partial_i \overline{\mathbf{U}} \;\; \in \;\; (\overline{\mathcal{U}})^3, \;\; \forall \overline{\mathbf{U}} \in \overline{\mathcal{U}}. \tag{6.22}$$

Similarly, the space of unresolved scales is closed with respect to differentiation if,

$$\partial_i \mathbf{U}' \;\; \in \;\; (\mathcal{U}')^3, \;\; \forall \mathbf{U}' \in \mathcal{U}'. \tag{6.23}$$

In fact one can verify that the projection operator $\mathcal{P}$ commutes with differentiation if and only if *both* spaces $\overline{\mathcal{U}}$ and $\mathcal{U}'$ are closed with respect to differentiation.

---

[2]By the Einstein notation, $\partial_i = [\partial_1, \partial_2, \partial_3]$, hence $\partial_i \overline{\mathbf{U}} = \nabla \overline{\mathbf{U}}$

The proof that both $\overline{\mathcal{U}}$ and $\mathcal{U}'$ must be closed with respect to differentiation when $\mathcal{P}$ commutes follows directly from,

$$\partial_i \overline{\mathbf{U}} \;=\; \partial_i \mathcal{P}[\mathbf{U}] \;=\; \mathcal{P}(\partial_i \mathbf{U}) \in \overline{\mathcal{U}}, \tag{6.24}$$

$$\partial_i \mathbf{U}' \;=\; \partial_i \{(Id - \mathcal{P})[\mathbf{U}]\} \;=\; (Id - \mathcal{P})[\partial_i \mathbf{U}] \in \mathcal{U}'. \tag{6.25}$$

Here Id denotes the identity operator. In order to show that $\mathcal{P}$ commutes with differentiation when both $\overline{\mathcal{U}}$ and $\mathcal{U}'$ are closed we need to show that when either $\overline{\mathcal{U}}$ or $\mathcal{U}'$ is not closed then $\mathcal{P}$ does not commute. In case $\overline{\mathcal{U}}$ is not closed then $\partial_j \overline{U}_\alpha = A_{\alpha j} + B_{\alpha j}$ where $A_{\alpha j} \in (\overline{\mathcal{U}})^3$ and $B_{\alpha j} \in (\mathcal{U}')^3$. Consequently, $\mathcal{P}[\partial_j \overline{U}_\alpha] = A_{\alpha j}$ whereas $\partial_j \mathcal{P}[\overline{U}_\alpha] \;=\; \partial_j \overline{U}_\alpha \;=\; A_{\alpha j} + B_{\alpha j}$. Similarly when $\mathcal{U}'$ is not closed we have $\partial_j U'_\alpha = C_{\alpha j} + D_{\alpha j}$ where $C_{\alpha j} \in (\overline{\mathcal{U}})^3$ and $D_{\alpha j} \in (\mathcal{U}')^3$. This results in a non-commuting projection because $\mathcal{P}[\partial_j U'_\alpha] = C_{\alpha j}$ whereas $\partial_j \mathcal{P}[U'_\alpha] \;=\; 0$.

An important consequence of the statement made above, is that in case a discretization is used which results in a non-commuting projection, then (6.22) and/or (6.23) do not hold. Based on this observation the remainder of this chapter can be divided into two parts. In section 6.3 we specify the VMS-LES formulation where we conveniently assume a commuting projection. Subsequently, in section 6.4 we consider projections $\mathcal{P}$ which do not commute with differentiation. Specifically, we will assume that the space of resolved scales is closed with respect to differentiation while the space of unresolved scales is not. These assumptions apply among others to projections which emerge when DG-FEM is used.

6.3   VMS-LES formulation for compressible flow using Fourier-spectral methods

As outlined in the previous section, in the VMS-LES a splitting of the space of conserved variables $\mathcal{U}$ in terms of resolved and unresolved scales is considered. A subtle problem which seriously complicates the formulation for compressible flow is that the VMS-LES formulation cannot be expressed in terms of the conserved variables ρ, ρu_i and $E = \rho e$ [77]. Instead, in this chapter we express the formulation in terms of the density ρ, together with the velocity u_i and total energy $e = E/\rho$ which is defined as [4],

$$e \;=\; \frac{1}{(\gamma - 1)} \frac{p}{\rho} + \tfrac{1}{2} u_k u_k. \tag{6.26}$$

These variables are decomposed into a resolved and unresolved part. The distinctive difference between the VMS-LES formulation presented in this chapter and the one presented in [77] lies in the construction of resolved part of the velocity and total energy.

In subsection 6.3.1 the large-eddy template for the compressible Navier-Stokes equations is sketched and the construction of the resolved velocity and total energy is explained. The resulting SGS-terms are shown in subsection 6.3.2 and briefly discussed in subsection 6.3.3.

6.3.1   Large eddy template for the compressible Navier Stokes equations

For their VMS-LES formulation of incompressible flow, Hughes *et al.* [69] and Collis [24] exploited a series expansion of the Navier-Stokes operator B_h with respect to the conserved variables $\mathbf{U}$. If there is a finite number of non-zero variations $B_{h,k}(\overline{\mathbf{W}}, \overline{\mathbf{U}}, \mathbf{U}')$ we may write,

$$B_h(\overline{\mathbf{W}}, \mathbf{U}) \;=\; B_h(\overline{\mathbf{W}}, \overline{\mathbf{U}} + \mathbf{U}') \;=\; B_h(\overline{\mathbf{W}}, \overline{\mathbf{U}}) + \sum_{k=1}^{N} B_{h,k}(\overline{\mathbf{W}}, \overline{\mathbf{U}}, \mathbf{U}'), \quad (6.27)$$

where $B_{h,k}$ is the k-th variation of B_h which is given by,

$$B_{h,k}(\overline{\mathbf{W}}, \overline{\mathbf{U}}, \mathbf{U}') \;=\; \lim_{\varepsilon \to 0} \left(\frac{1}{k!} \frac{d^k}{d\varepsilon^k} B_h(\overline{\mathbf{W}}, \overline{\mathbf{U}} + \varepsilon \mathbf{U}') \right). \quad (6.28)$$

Comparison of (6.27) with the large-eddy template (6.10) reveals that the variations $B_{h,k}(\overline{\mathbf{W}}, \overline{\mathbf{U}}, \mathbf{U}')$, $k = 1, \ldots, N$ contain all the SGS-terms of VMS-LES.

For the incompressible Navier-Stokes equations $B_{h,k} = 0$ for $k > 2$ [24, 69]. If exactly the same procedure would be followed for the compressible Navier-Stokes operator using conservative variables (6.7) an *infinite* number of non-zero variations of B_h will be found. The fact that an infinite number of variations is found is best illustrated by the convective flux in the momentum equation $\partial_j \rho u_i u_j$. In terms of the conserved variables the convective flux is given by $\partial_j U_i U_j / U_0$ and its variations are given by,

$$\lim_{\varepsilon \to 0} \frac{1}{k!} \frac{d^k}{d\varepsilon^k} \frac{(\overline{U}_i + \varepsilon U_i')(\overline{U}_j + \varepsilon U_j')}{(\overline{U}_0 + \varepsilon U_0')}. \quad (6.29)$$

In general these variations will be nonzero for all $k \geq 1$ due to the division by the density ($U_0 = \rho$). As a result, the above described methodology can no longer be used.

A possible way to arrive at a *finite* number of non-zero variations is to first consider the Navier-Stokes operator B_h in terms of ρ, the velocity u_i and total energy e and expand the Navier-Stokes operator with respect to these variables, which shows to have only four variations.

The Navier-Stokes operator expressed in terms of the vector $\mathbf{V} = [\rho, u_i, e]$ is defined through,

$$\mathcal{B}_h(\mathbf{W}, \mathbf{V}) = B_h(\mathbf{W}, \mathbf{U}(\mathbf{V})) = B_h(\mathbf{W}, \mathbf{U}). \tag{6.30}$$

Next write $\mathbf{V}$ as $\widetilde{\mathbf{V}} + \mathbf{V}''$, where $\widetilde{\mathbf{V}} = [\overline{\rho}, \widetilde{u}_i, \widetilde{e}]$ is the resolved and $\mathbf{V}'' = [\rho', u_i'', e'']$ the unresolved part. Further we define $\overline{\rho} = \mathcal{P}[\rho]$ and require that $\widetilde{u}_i$ and $\widetilde{e}$ satisfy,

$$\overline{\overline{\rho}\,\widetilde{u}_i} = \overline{\rho u_i}, \qquad \overline{\overline{\rho}\,\widetilde{e}} = \overline{\rho e}, \tag{6.31}$$

where $\overline{\rho u_i} = \mathcal{P}[\rho u_i]$ and $\overline{\rho e} = \mathcal{P}[\rho e]$ are the resolved conserved momentum and energy density, respectively. Definition (6.31) is of particular importance as we will observe that additional SGS-terms emerge when $\widetilde{u}_i$ and $\widetilde{e}$ do not satisfy (6.31).

One can readily verify that when $\widetilde{u}_i$ and $\widetilde{e}$ are defined according to (2.27) $\widetilde{u}_i$ and $\widetilde{e}$ satisfy (6.31). However, than $\widetilde{u}_i$ and $\widetilde{e}$ cannot be expressed in terms of a finite number of basis-functions, i.e.,

$$\widetilde{u}_i(\mathbf{x}) = \sum_{l=0}^{N_\phi - 1} \hat{b}_{il} \phi_l(\mathbf{x}), \qquad \widetilde{e}(\mathbf{x}) = \sum_{l=0}^{N_\phi - 1} \hat{b}_{4l} \phi_l(\mathbf{x}). \tag{6.32}$$

In the subsequent part we will determine $\hat{b}_{il}$ and $\hat{b}_{4l}$ such that $\widetilde{u}_i$ and $\widetilde{e}$ can be expressed in terms of basis-functions and satisfy (6.31) as well. In fact, a generalization of Favre-averaging to general projections is arrived at.

First we will show that Favre averaging is a special case of (6.31). Momentarily restricting the discussion to the velocity field, if we replace the projection operator $\overline{\cdot}$ with the averaging operator over an element K, $\langle \cdot \rangle_K$, in (6.31), we get,

$$\langle \langle \rho \rangle_K \widetilde{u}_i \rangle_K = \langle \rho u_i \rangle_K. \tag{6.33}$$

Averaging can be considered as a special case of (6.31) because we are allowed to place the $\langle \rho \rangle_K$-term, which is a scalar variable, outside the averaging brackets: $\langle \langle \rho \rangle_K \widetilde{u}_i \rangle_K = \langle \rho \rangle_K \langle \widetilde{u}_i \rangle_K$. Then dividing by the averaged density allows us to define the resolved velocity field as,

$$\langle \widetilde{u}_i \rangle_K = \frac{\langle \rho u_i \rangle_K}{\langle \rho \rangle_K}, \tag{6.34}$$

which corresponds to the well known definition of Favre averaging [31, 32, 33].

For general projections it is not possible to place the projected density $\overline{\rho}(\mathbf{x})$ outside the projection operator, i.e.

$$\overline{\overline{\rho}\,\widetilde{u}_i} \neq \overline{\rho}\,\overline{\widetilde{u}}_i. \tag{6.35}$$

and as a result

$$\overline{\rho u_i} \neq \overline{\rho}\,\overline{\widetilde{u}}_i. \tag{6.36}$$

Equality in these expressions would allow us to define the resolved velocity field $\widetilde{u}_i$ by $\overline{\rho u_i}/\overline{\rho}$. That (6.35) and (6.36) cannot be an equality for general projection operators is clearly illustrated using polynomial basis functions. Consider the one-dimensional case on a reference element $\hat{K} = [-1, 1]$ using first order polynomials. Then the resolved density is given by $\overline{\rho} = \hat{\rho}_0 + \hat{\rho}_1 x$, the resolved momentum by $\overline{\rho u_i} = \hat{a}_0 + \hat{a}_1 x$ and the resolved velocity by $\widetilde{u} = \hat{b}_0 + \hat{b}_1 x$ where $\hat{b}_0$ and $\hat{b}_1$ are unknowns. Inserting this into the right hand side of (6.35) or (6.36) gives,

$$(\hat{\rho}_0 + \hat{\rho}_1 x)(\hat{b}_0 + \hat{b}_1 x) \;=\; \hat{\rho}_0 \hat{b}_0 + (\hat{\rho}_0 \hat{b}_1 + \hat{\rho}_1 \hat{b}_0)x + \hat{\rho}_1 \hat{b}_1 x^2, \qquad (6.37)$$

which is a second order polynomial. However the left hand sides of (6.35) and (6.36) result in the first order polynomials $\hat{\beta}_0 + \hat{\beta}_1 x$ and $\hat{a}_0 + \hat{a}_1 x$, respectively, where the coefficients $\hat{\beta}_0$ and $\hat{\beta}_1$ are given by,

$$\hat{\beta}_0 \;=\; \frac{1}{2}\Big(\hat{\rho}_0 \hat{b}_0 + (\hat{\rho}_0 \hat{b}_1 + \hat{\rho}_1 \hat{b}_0)x + \hat{\rho}_1 \hat{b}_1 x^2 \Big| 1\Big)_{\hat{K}},$$
$$\hat{\beta}_1 \;=\; \frac{3}{2}\Big(\hat{\rho}_0 \hat{b}_0 + (\hat{\rho}_0 \hat{b}_1 + \hat{\rho}_1 \hat{b}_0)x + \hat{\rho}_1 \hat{b}_1 x^2 \Big| x\Big)_{\hat{K}}.$$

Because of this mismatch in polynomial order one cannot define $\hat{b}_0, \hat{b}_1 \in \mathbb{R}$ for which equality holds in (6.35) and (6.36) for all $x \in \hat{K}$.

Returning to the three-dimensional case and assuming p-th order polynomial basis functions, the terms on the left-hand-sides of (6.35) and (6.36) have polynomial order p, while the term on the right-hand-sides results in polynomials of order $p \times p$. Equality can only be achieved when both sides are of equal polynomial order which is the case when $p = 0$ or $p = \infty$. The former case corresponds to elements-wise averaging which has just been described above as a special case. For the latter case we would have to consider a computational solution space $\mathcal{U}_h$ of infinite dimension which is not allowed in the VMS approach to LES. Therefore it is not possible to determine $\hat{b}_{il}$, $l = 0, \ldots, N_\phi - 1$ directly from $\overline{\rho u_i}/\overline{\rho}$ when $p > 0$. Next, we will show, however, that it is possible to uniquely determine the coefficients $\hat{b}_{il}$, $l = 0, \ldots, N_\phi - 1$ using (6.31). By directly determining the coefficient $\hat{b}_{il}$ using this definition we do not encounter the mismatch in polynomial order as encountered in (6.36).

First we introduce the following short hand notation for the resolved momentum contribution in terms of the basis functions ϕ_k,

$$\overline{\rho u_i} \;=\; \sum_{k=0}^{N_\phi - 1} \hat{a}_{ik} \phi_k, \qquad (6.38)$$

where the expansion coefficients $\hat{a}_{ik}$ are given by $\hat{a}_{ik} = \sum_{l=0}^{N_\phi - 1} \left(\rho u_i \big| \phi_l\right)_\Omega \mathbb{M}_{lk}^{-1}$, $k = 0, \ldots, N_\phi - 1$. The expansion coefficients for the resolved velocity contribution,

$\hat{b}_{il}$, $l = 0 \ldots N_\phi - 1$, are determined by inserting the expansions of $\overline{\rho u_i}$ and $\widetilde{u}_i$ into (6.31),

$$\overline{\overline{\rho} \sum_{l=0}^{N_\phi-1} \hat{b}_{il}\phi_l} \;=\; \sum_{k=0}^{N_\phi-1} \hat{a}_{ik}\phi_k, \tag{6.39}$$

which is equivalent to,

$$\sum_{l=0}^{N_\phi-1} \hat{b}_{il} \; \overline{\overline{\rho}\phi_l} \;=\; \sum_{k=0}^{N_\phi-1} \hat{a}_{ik}\phi_k. \tag{6.40}$$

If we replace $\overline{\overline{\rho}\phi_l} \in \overline{\mathcal{U}}$ with it's expansion in terms of the basis functions ϕ_k we get,

$$\sum_{l=0}^{N_\phi-1} \hat{b}_{il} \; \sum_{k=0}^{N_\phi-1} \left\{ \sum_{m=0}^{N_\phi-1} \widehat{\mathbb{M}}_{lm}\mathbb{M}_{mk}^{-1} \right\} \phi_k \;=\; \sum_{k=0}^{N_\phi-1} \hat{a}_{ik}\phi_k. \tag{6.41}$$

where $\widehat{\mathbb{M}}_{lm} = \left(\overline{\rho}\phi_l \big| \phi_m\right)_\Omega$ is the weighted mass matrix with the resolved density as weight. This matrix is positive definite as long as the resolved density is strictly positive.

Next, we introduce the matrix $\mathbb{F} = \widehat{\mathbb{M}}\,\mathbb{M}^{-1}$ which can be used to simplify (6.41),

$$\sum_{l=0}^{N_\phi-1} \hat{b}_{il} \; \sum_{k=0}^{N_\phi-1} \mathbb{F}_{lk}\phi_k \;=\; \sum_{k=0}^{N_\phi-1} \hat{a}_{ik}\phi_k. \tag{6.42}$$

Because $\widehat{\mathbb{M}}$ is positive definite, its inverse exists and the coefficients $\hat{b}_{il}$ can be determined by,

$$\hat{b}_{il} \;=\; \sum_{k=0}^{N_\phi-1} \hat{a}_{ik}\mathbb{F}_{kl}^{-1}, \quad l = 0, \ldots, N_\phi - 1, \tag{6.43}$$

where $\mathbb{F}^{-1} = \mathbb{M}\widehat{\mathbb{M}}^{-1}$. Comparison with (6.34) reveals that the division by the averaged density is replaced by multiplication with the inverse of the matrix $\mathbb{F}$.

If we now expand the Navier-Stokes operator $\mathcal{B}_h(\overline{\mathbf{W}}, \mathbf{V})$ as $\mathcal{B}_h(\overline{\mathbf{W}}, \widetilde{\mathbf{V}} + \mathbf{V}'')$, where $\widetilde{\mathbf{V}} = [\overline{\rho}, \widetilde{u}_i, \widetilde{e}]$ and $\mathbf{V}'' = [\rho', u_i'', e'']$, a finite series expansion is found. Only four non-zero variations,

$$\mathcal{B}_{h,k}(\mathbf{W}, \widetilde{\mathbf{V}}, \mathbf{V}'') \;=\; \lim_{\varepsilon \to 0} \left(\frac{1}{k!} \frac{d^k}{d\varepsilon^k} \mathcal{B}_h(\mathbf{W}, \widetilde{\mathbf{V}} + \varepsilon\mathbf{V}'') \right), \tag{6.44}$$

exist. For example consider the term $\rho\, u_j u_k u_k$ which shows up in the energy equation (combine equations (2.3) and (2.4)). The variations for this term are

given by,

$$
\lim_{\varepsilon \to 0} \frac{1}{k!} \frac{d^k}{d\varepsilon^k} \left(\overline{\rho} + \varepsilon \rho' \right)(\widetilde{u}_j + \varepsilon u_j'')(\widetilde{u}_l + \varepsilon u_l'')(\widetilde{u}_l + \varepsilon u_l'')
$$

$$
= \lim_{\varepsilon \to 0} \frac{1}{k!} \frac{d^k}{d\varepsilon^k} \left\{ \overline{\rho} \widetilde{u}_j \widetilde{u}_l \widetilde{u}_l + \varepsilon(\rho' \widetilde{u}_j \widetilde{u}_l \widetilde{u}_l + 2\overline{\rho} \widetilde{u}_j \widetilde{u}_l u_l'' + \overline{\rho} u_j'' \widetilde{u}_l \widetilde{u}_l) \right.
$$

$$
+ \varepsilon^2 (2\,\rho' \widetilde{u}_j \widetilde{u}_l u_l'' + \rho' u_j'' \widetilde{u}_l \widetilde{u}_l + \overline{\rho} \widetilde{u}_j u_l'' u_l'' + 2\,\overline{\rho} u_j'' \widetilde{u}_l u_l'')
$$

$$
\left. + \varepsilon^3 (\rho' \widetilde{u}_j u_l'' u_l'' + 2\rho' u_j'' \widetilde{u}_l u_l'' + \overline{\rho} u_j'' u_l'' u_l'') + \varepsilon^4 \rho' u_j'' u_l'' u_l'' \right\}, \quad (6.45)
$$

and are zero for $k > 4$.

The resulting large eddy template is given by,

$$
0 \;=\; B_h(\overline{\mathbf{W}}, \mathbf{U}) \;=\; B_h(\overline{\mathbf{W}}, \overline{\mathbf{U}}) + \sum_{k=1}^{4} \mathcal{B}_{h,k}(\overline{\mathbf{W}}, \widetilde{\mathbf{V}}, \mathbf{V}''), \quad (6.46)
$$

where we have used that the resolved velocity field $\widetilde{u}_i$ and $\widetilde{e}$ can be expressed in terms of the resolved conserved variables such that,

$$
\mathcal{B}_h(\overline{\mathbf{W}}, \widetilde{\mathbf{V}}) \;=\; \mathcal{B}_h(\overline{\mathbf{W}}, \widetilde{\mathbf{V}}(\overline{\mathbf{U}})) \;=\; B_h(\overline{\mathbf{W}}, \overline{\mathbf{U}}). \quad (6.47)
$$

In (6.46) we can identify a large-scale part $B_h(\overline{\mathbf{W}}, \overline{\mathbf{U}})$ and a SGS-part which is formed by the four variations $\mathcal{B}_{h,k}(\overline{\mathbf{W}}, \widetilde{\mathbf{V}}, \mathbf{V}'')$, $k = 1, 2, 3, 4$.

In the following subsection we will identify all SGS-terms assuming a commuting projection. The case of non-commuting projections is given in section 6.4.

6.3.2   SGS-terms in compressible VMS

The VMS-LES formulation for the compressible Navier-Stokes equations contains a large number of SGS-terms. In order to facilitate the presentation, the compressible Navier-Stokes operator B_h is split into several parts, related to the continuity, momentum and energy equation and are denoted by B_h^{cont}, B_h^{mom} and B_h^{energy}, respectively. The parts corresponding to the continuity and momentum equation are respectively given by

$$
B_h^{\text{cont}}(\overline{\mathbf{W}}, \mathbf{U}) \;=\; \sum_{K \in \mathcal{T}_h} \left(\overline{W}_0 \Big| \partial_t \rho \right)_K + \left(\overline{W}_0 \Big| \partial_j \rho u_j \right)_K, \quad (6.48)
$$

and

$$
B_h^{\text{mom}}(\overline{\mathbf{W}}, \mathbf{U}) \;=\; \sum_{K \in \mathcal{T}_h} \left(\overline{W}_i \Big| \partial_t \rho u_i \right)_K
$$

$$
- \left(\overline{W}_i \Big| \partial_j [\rho u_i u_j + (\gamma - 1)(\rho e - \tfrac{1}{2} \rho u_k u_k)\delta_{ij} + \sigma_{ij}] \right)_K. \quad (6.49)
$$

Their VMS-LES formulations will be given in this subsection. The VMS-LES formulation for the energy equation is given in appendix A.

Since the projection operator is self-adjoint we may write the continuity equation as,

$$B_h^{\text{cont}}(\overline{\mathbf{W}}, \mathbf{U}) \;=\; \sum_{K \in \mathcal{T}_h} \left(\overline{W}_0 \middle| \overline{\partial_t \rho}\right)_K + \left(\overline{W}_0 \middle| \overline{\partial_j \rho u_j}\right)_K. \tag{6.50}$$

Next we use that the projection operator commutes with differentiation $\overline{\partial_t \rho} = \partial_t \overline{\rho}$ and $\overline{\partial_j \rho u_i} = \partial_j \overline{\rho u_i}$. Hence

$$B_h^{\text{cont}}(\overline{\mathbf{W}}, \mathbf{U}) \;=\; \sum_{K \in \mathcal{T}_h} \left(\overline{W}_0 \middle| \partial_t \overline{\rho}\right)_K + \left(\overline{W}_0 \middle| \partial_j \overline{\rho u_j}\right)_K. \tag{6.51}$$

For the continuity equation, the right-hand-side of (6.51) is fully expressed in terms of resolved conserved variables $\overline{\rho}$ and $\overline{\rho u_i}$ and we arrive at the following large-eddy template for this equation:

$$B_h^{\text{cont}}(\overline{\mathbf{W}}, \mathbf{U}) \;=\; B_h^{\text{cont}}(\overline{\mathbf{W}}, \overline{\mathbf{U}}), \tag{6.52}$$

which does not contain any SGS-terms.

Applying the same steps as for the continuity equation above to the momentum equation gives,

$$\begin{aligned}
B_h^{\text{mom}}(\overline{\mathbf{W}}, \mathbf{U}) \;=\; & \sum_{K \in \mathcal{T}_h} \left(\overline{W}_i \middle| \overline{\partial_t \rho u_i}\right)_K \\
& - \left(\overline{W}_i \middle| \partial_j [\overline{\rho u_i u_j} + (\gamma - 1)(\overline{\rho e} - \tfrac{1}{2}\overline{\rho u_k u_k})\delta_{ij} + \overline{\sigma}_{ij}]\right)_K.
\end{aligned} \tag{6.53}$$

The momentum equation is non-linear with respect to the vector of conserved variables and needs to be expanded in terms of variations in order to identify its SGS-terms. The momentum equation has three non-zero variations $\mathcal{B}_{h,k}$, such that,

$$B_h^{\text{mom}}(\overline{\mathbf{W}}, \mathbf{U}) \;=\; B_h^{\text{mom}}(\overline{\mathbf{W}}, \overline{\mathbf{U}}) + \sum_{k=1}^{3} \mathcal{B}_{h,k}^{\text{mom}}(\overline{\mathbf{W}}, \widetilde{\mathbf{V}}, \mathbf{V}''). \tag{6.54}$$

The SGS-terms appearing in this equation, $\mathcal{B}_{h,k}^{\text{mom}}(\overline{\mathbf{W}}, \widetilde{\mathbf{V}}, \mathbf{V}'')$, $k = 1, 2, 3$, are re-

spectively given by,

$$
\begin{aligned}
\mathcal{B}_{h,1}^{\mathrm{mom}}&(\overline{\mathbf{W}}, \widetilde{\mathbf{V}}, \mathbf{V}'') \\
&= \sum_{K \in \mathcal{T}_h} \left(\overline{W}_i \Big| \partial_t \overline{\rho} u_i'' + \partial_t \overline{\rho' \widetilde{u}_i} \right)_K \\
&\quad + \left(\overline{W}_i \Big| \partial_j \Big[\overline{\rho' \widetilde{u}_i \widetilde{u}_j} + \overline{\rho} \widetilde{u}_i u_j'' + \overline{\rho} u_i'' \widetilde{u}_j \right. \\
&\qquad\qquad \left. + (\gamma - 1)(\overline{\rho} e'' + \overline{\rho' \widetilde{e}} - \tfrac{1}{2} \overline{\rho' \widetilde{u}_k \widetilde{u}_k} - \overline{\rho} \widetilde{u}_k u_k'')\delta_{ij} - \bar{\dot{\sigma}}_{ij} \Big] \Big)_K,
\end{aligned}
\tag{6.55}
$$

$$
\begin{aligned}
\mathcal{B}_{h,2}^{\mathrm{mom}}&(\overline{\mathbf{W}}, \widetilde{\mathbf{V}}, \mathbf{V}'') \\
&= \sum_{K \in \mathcal{T}_h} \left(\overline{W}_i \Big| \partial_t \overline{\rho' u_i''} \right)_K \\
&\quad + \left(\overline{W}_i \Big| \partial_j \Big[\overline{\rho' \widetilde{u}_i u_j''} + \overline{\rho' u_i'' \widetilde{u}_j} + \overline{\rho} u_i'' u_j'' \right. \\
&\qquad\qquad \left. + (\gamma - 1)(\overline{\rho' e''} - \overline{\rho' \widetilde{u}_k u_k''} - \tfrac{1}{2} \overline{\rho} u_k'' u_k'')\delta_{ij} \Big] \Big)_K,
\end{aligned}
\tag{6.56}
$$

and

$$
\begin{aligned}
\mathcal{B}_{h,3}^{\mathrm{mom}}&(\overline{\mathbf{W}}, \widetilde{\mathbf{V}}, \mathbf{V}'') \\
&= \sum_{K \in \mathcal{T}_h} \left(\overline{W}_i \Big| \partial_j \Big[\overline{\rho' u_i'' u_j''} - \tfrac{1}{2}(\gamma - 1)\overline{\rho' u_k'' u_k''}\delta_{ij} \Big] \right)_K.
\end{aligned}
\tag{6.57}
$$

The term $\dot{\sigma}_{ij}$ in (6.55) denotes the first variation of the viscous flux and is given by,

$$
\dot{\sigma}_{ij} = \frac{1}{Re}(\partial_j u_i'' + \partial_i u_j'' - \tfrac{2}{3}\delta_{ij}\partial_k u_k'').
\tag{6.58}
$$

Furthermore, one can verify that the terms $\overline{\rho' u_i''}$ and $\overline{\rho' e''}$ in (6.56) are canceled out by $\overline{\rho} u_i'' + \overline{\rho' \widetilde{u}_i}$ and $\overline{\rho} e'' + \overline{\rho' \widetilde{e}}$ in (6.55), respectively, if $\widetilde{u}_i$ and $\widetilde{e}$ satisfy (6.31). This is because,

$$
\overline{\rho} u_i'' + \overline{\rho' \widetilde{u}_i} = \overline{\rho(u_i - \widetilde{u}_i)} + \overline{\rho' \widetilde{u}_i},
\tag{6.59}
$$

and by (6.31) we can replace the $\overline{\overline{\rho} \widetilde{u}_i}$ contribution with $\overline{\rho u_i}$ such that,

$$
\overline{\rho} u_i'' + \overline{\rho' \widetilde{u}_i} = \overline{\overline{\rho} u_i} - \overline{\rho u_i} + \overline{\rho' \widetilde{u}_i} = -\overline{\rho' u_i} + \overline{\rho' \widetilde{u}_i} = -\overline{\rho' u_i''}.
\tag{6.60}
$$

Similarly one can show that $\overline{\rho} e'' + \overline{\rho' \widetilde{e}} = -\overline{\rho' e''}$. This shows why it is essential for $\widetilde{u}_i$ and $\widetilde{e}$ to satisfy (6.31). If this would not be the case the terms $\overline{\rho' u_i''}$ and $\overline{\rho' e''}$ in (6.56) would not cancel out by $\overline{\rho} u_i'' + \overline{\rho' \widetilde{u}_i}$ and $\overline{\rho} e'' + \overline{\rho' \widetilde{e}}$ in (6.55), respectively.

Inserting these variation $\mathcal{B}_{h,k}$ into (6.54) gives, after some manipulations,

$$
\begin{aligned}
B_h^{\mathrm{mom}}(\overline{\mathbf{W}}, \mathbf{U}) \;=\;\; & B_h^{\mathrm{mom}}(\overline{\mathbf{W}}, \overline{\mathbf{U}}) \\
& + \sum_{K \in \mathcal{T}_h} -\Big(\partial_j \overline{W}_i \big| \overline{\rho \widetilde{u}_i u_j''} + \overline{\rho u_i'' \widetilde{u}_j} - (\gamma - 1)\overline{\rho \widetilde{u}_k u_k''}\delta_{ij}\Big)_K \\
& + \Big(\overline{W}_i n_j \big| \overline{\rho \widetilde{u}_i u_j''} + \overline{\rho u_i'' \widetilde{u}_j} - (\gamma - 1)\overline{\rho \widetilde{u}_k u_k''}\delta_{ij}\Big)_{\partial K} \\
& - \Big(\partial_j \overline{W}_i \big| \overline{\rho u_i'' u_j''} - \tfrac{1}{2}(\gamma - 1)\overline{\rho u_k'' u_k''}\delta_{ij}\Big)_K \\
& + \Big(\overline{W}_i n_j \big| \overline{\rho u_i'' u_j''} - \tfrac{1}{2}(\gamma - 1)\overline{\rho u_k'' u_k''}\delta_{ij}\Big)_{\partial K} \\
& - \Big(\partial_j \overline{W}_i \big| \overline{\rho' \widetilde{u}_i \widetilde{u}_j} - \tfrac{1}{2}(\gamma - 1)\overline{\rho' \widetilde{u}_k \widetilde{u}_k}\delta_{ij}\Big)_K \\
& + \Big(\overline{W}_i n_j \big| \overline{\rho' \widetilde{u}_i \widetilde{u}_j} - \tfrac{1}{2}(\gamma - 1)\overline{\rho' \widetilde{u}_k \widetilde{u}_k}\delta_{ij}\Big)_{\partial K} \\
& - \Big(\partial_j \overline{W}_i \big| -\overline{\dot{\sigma}}_{ij}\Big)_K + \Big(W_i n_j \big| -\overline{\dot{\sigma}}_{ij}\Big)_{\partial K} \qquad (6.61)
\end{aligned}
$$

In (6.61) a number of SGS-terms is encountered which can be divided into several groups,

1. the cross terms $\overline{\rho \widetilde{u}_i u_j''} + \overline{\rho u_i'' \widetilde{u}_j}$ and the Reynolds terms $\rho u_i'' u_j''$ originating from the convective flux $\rho u_i u_j$ and the pressure flux $(\gamma - 1)\tfrac{1}{2}\rho u_k u_k\,\delta_{ij}$,

2. the density fluctuations in $\overline{\rho' \widetilde{u}_i \widetilde{u}_j}$,

3. the first variation of the viscous flux $\overline{\dot{\sigma}}_{ij}$,

The cross terms and Reynolds stress are similar to the cross terms and Reynolds stress encountered in incompressible flow [24, 69]. The other SGS-terms are typical for compressible flows.

6.3.3   Comparison with the SGS-stress for compressible flow

Studies regarding LES of compressible flow using the traditional filtering approach have shown that the main SGS-term, even up to quite high Mach numbers, is the divergence of the SGS-stress tensor $\partial_j \overline{\rho} \tau_{ij}$ [137, 141]. The SGS-stress tensor for compressible flow is given by,

$$
\overline{\rho} \tau_{ij} \;=\; \overline{\rho u_i u_j} - \overline{\rho} \widetilde{u}_i \widetilde{u}_j. \qquad (6.62)
$$

The SGS-term requires modeling and a wide array of models exists for this stress [141]. Although models have been proposed for other SGS-terms appearing in the

Favre-filtered Navier-Stokes equations, in most cases the dynamical effects of these SGS-terms can be neglected [137].

Next, we will establish which of the SGS-terms in (6.61) correspond to the divergence of the SGS-stress $\partial_j \overline{\rho} \tau_{ij}$. For this we multiply the divergence of the SGS-stress given by (6.62) with test-functions $\overline{\mathbf{W}} \in \overline{\mathcal{U}}$ and integrate over the domain Ω. This results in the following expression,

$$\left(\overline{W}_i \middle| \partial_j \overline{\rho} \tau_{ij} \right)_\Omega \;=\; \sum_{K \in \mathcal{T}_h} \left(\overline{W}_i \middle| \partial_j \overline{\rho u_i u_j} - \partial_j \overline{\rho} \widetilde{u}_i \widetilde{u}_j \right)_K. \tag{6.63}$$

For a self-adjoint, commuting projection, this is equivalent to,

$$\left(\overline{W}_i \middle| \partial_j \overline{\rho} \tau_{ij} \right)_\Omega \;=\; \sum_{K \in \mathcal{T}_h} \left(\overline{W}_i \middle| \partial_j \overline{\rho u_i u_j} - \partial_j \overline{\overline{\rho} \widetilde{u}_i \widetilde{u}_j} \right)_K. \tag{6.64}$$

After integration by parts we find,

$$\left(\overline{W}_i \middle| \partial_j \overline{\rho} \tau_{ij} \right)_\Omega \;=\; \sum_{K \in \mathcal{T}_h} -\left(\partial_j \overline{W}_i \middle| \overline{\rho u_i u_j} - \overline{\overline{\rho} \widetilde{u}_i \widetilde{u}_j} \right)_K$$
$$+ \left(\overline{W}_i n_j \middle| \overline{\rho u_i u_j} - \overline{\overline{\rho} \widetilde{u}_i \widetilde{u}_j} \right)_{\partial K}. \tag{6.65}$$

Since $\overline{\rho} = \rho - \rho'$ and $u_i = \widetilde{u}_i + u_i''$ (6.65) becomes,

$$\left(\overline{W}_i \middle| \partial_j \overline{\rho} \tau_{ij} \right)_\Omega \;=\; \sum_{K \in \mathcal{T}_h} -\left(\partial_j \overline{W}_i \middle| \overline{\rho \widetilde{u}_i u_j''} + \overline{\rho u_i'' \widetilde{u}_j} + \overline{\rho u_i'' u_j''} + \overline{\rho' \widetilde{u}_i \widetilde{u}_j} \right)_K$$
$$+ \left(\overline{W}_i n_j \middle| \overline{\rho \widetilde{u}_i u_j''} + \overline{\rho u_i'' \widetilde{u}_j} + \overline{\rho u_i'' u_j''} + \overline{\rho' \widetilde{u}_i \widetilde{u}_j} \right)_{\partial K}. \tag{6.66}$$

Observe that these SGS-terms correspond to the non-linear terms in the large-eddy template of the momentum equation (6.61) which originate from the convective flux, i.e., the cross terms, the Reynolds stress and a contribution with a fluctuating density.

6.4 Extension to non-commuting projection operators

In the previous section a VMS-LES formulation was given for the compressible Navier-Stokes equations when a commuting projection operator is assumed. For the application of VMS-LES to complex flow geometries it will generally not be possible to make such an assumption. Numerical methods other than Fourier-spectral methods have to be used resulting in a non-commuting projection. In this section non-commuting projections are considered and only the space of resolved conserved variables $\overline{\mathcal{U}}$ is assumed to be closed with respect to differentiation. With respect to differentiation in time we will assume a commuting projection and hence $\partial_t P(\mathbf{U}) = P(\partial_t \mathbf{U}) \; \forall \mathbf{U} \in \mathcal{U}$.

6.4.1 SGS-terms in VMS-LES when using non-commuting projection operators

In order to arrive at the VMS-LES formulation a slightly different approach has to be taken than in the previous section. We start with the continuity equation as formulated in (6.48) and apply partial integration,

$$B_h^{\text{cont}}(\overline{\mathbf{W}}, \mathbf{U}) \;=\; \sum_{K \in \mathcal{T}_h} \left(\overline{W}_0 \Big| \partial_t \rho \right)_K - \left(\partial_j \overline{W}_0 \Big| \rho u_j \right)_K + \left(\overline{W}_0 n_j \Big| \rho u_j \right)_{\partial K}. \quad (6.67)$$

Now use can be made of the assumption that the space of resolved scales is closed with respect to differentiation. This implies that on the interior of an element $\partial_j \overline{W}_0 = \overline{\partial_j \overline{W}_0}$. Inserting this into (6.67) gives,

$$B_h^{\text{cont}}(\overline{\mathbf{W}}, \mathbf{U}) \;=\; \sum_{K \in \mathcal{T}_h} \left(\overline{W}_0 \Big| \partial_t \rho \right)_K - \left(\overline{\partial_j \overline{W}_0} \Big| \rho u_j \right)_K + \left(\overline{W}_0 n_j \Big| \rho u_j \right)_{\partial K}. \quad (6.68)$$

Then using that a projection operator is self-adjoint and the assumption that $\mathcal{P}$ commutes with differentiation in time allows us to rewrite (6.68) as,

$$\begin{aligned}
B_h^{\text{cont}}(\overline{\mathbf{W}}, \mathbf{U}) \;=\; & \sum_{K \in \mathcal{T}_h} \left(\overline{W}_0 \Big| \partial_t \overline{\rho} \right)_K - \left(\partial_j \overline{W}_0 \Big| \overline{\rho u_j} \right)_K \\
& + \left(\overline{W}_0 n_j \Big| \overline{\rho u_j} + (\rho u_j)' \right)_{\partial K},
\end{aligned} \quad (6.69)$$

where we decomposed ρu_j as $\overline{\rho u_j} + (\rho u_j)'$. This results into,

$$B_h^{\text{cont}}(\overline{\mathbf{W}}, \mathbf{U}) \;=\; B_h^{\text{cont}}(\overline{\mathbf{W}}, \overline{\mathbf{U}}) + \sum_{K \in \mathcal{T}_h} \left(\overline{W}_0 n_j \Big| (\rho u_j)' \right)_{\partial K}. \quad (6.70)$$

Contrary to the case of commuting projections we encounter now a SGS-term: the trace of the unresolved scales at the element boundary.

Next, we apply similar steps to the momentum equation. We start with integration by parts of (6.49), which results in,

$$\begin{aligned}
& B_h^{\text{mom}}(\overline{\mathbf{W}}, \mathbf{U}) \\
& = \sum_{K \in \mathcal{T}_h} \left(\overline{W}_i \Big| \partial_t \rho u_i \right)_K - \left(\partial_j \overline{W}_i \Big| \rho u_i u_j + (\gamma - 1)(\rho e - \tfrac{1}{2}\rho u_k u_k)\delta_{ij} + \sigma_{ij} \right)_K \\
& \quad + \left(\overline{W}_i n_j \Big| \rho u_i u_j + (\gamma - 1)(\rho e - \tfrac{1}{2}\rho u_k u_k)\delta_{ij} + \sigma_{ij} \right)_{\partial K}.
\end{aligned} \quad (6.71)$$

Then using that the space of resolved conserved variables is closed with respect to differentiation, hence $\partial_j \overline{W}_i = \overline{\partial_j \overline{W}_i}$, the fact that the projection operator $\mathcal{P}$ is

self-adjoint and commutes with differentiation in time gives,

$$
\begin{aligned}
B_h^{\mathrm{mom}}&(\overline{\mathbf{W}}, \mathbf{U}) \\
&= \sum_{K \in \mathcal{T}_h} \left(\overline{W}_i \big| \partial_t \overline{\rho u_i} \right)_K - \left(\partial_j \overline{W}_i \big| \overline{\rho u_i u_j} + (\gamma - 1)(\overline{\rho e} - \tfrac{1}{2}\overline{\rho u_k u_k})\delta_{ij} + \sigma_{ij} \right)_K \\
&\quad + \left(\overline{W}_i n_j \big| \overline{\rho u_i u_j} + (\gamma - 1)(\overline{\rho e} - \tfrac{1}{2}\overline{\rho u_k u_k})\delta_{ij} + \overline{\sigma}_{ij} \right)_{\partial K} \\
&\quad + \left(\overline{W}_i n_j \big| (\rho u_i u_j)' + (\gamma - 1)((\rho e)' - \tfrac{1}{2}(\rho u_k u_k)')\delta_{ij} + \sigma'_{ij} \right)_{\partial K}. \quad (6.72)
\end{aligned}
$$

In the next step we take variations and after a rather lengthy calculation we arrive at,

$$
\begin{aligned}
B_h^{\mathrm{mom}}&(\overline{\mathbf{W}}, \mathbf{U}) \\
&= B_h^{\mathrm{mom}}(\overline{\mathbf{W}}, \overline{\mathbf{U}}) \\
&\quad + \sum_{K \in \mathcal{T}_h} -\left(\partial_j \overline{W}_i \big| \overline{\rho \widetilde{u}_i u''_j} + \overline{\rho u''_i \widetilde{u}_j} - (\gamma - 1)\overline{\rho \widetilde{u}_k u''_k}\delta_{ij} \right)_K \\
&\qquad + \left(\overline{W}_i n_j \big| \overline{\rho \widetilde{u}_i u''_j} + \overline{\rho u''_i \widetilde{u}_j} - (\gamma - 1)\overline{\rho \widetilde{u}_k u''_k}\delta_{ij} \right)_{\partial K} \\
&\qquad - \left(\partial_j \overline{W}_i \big| \overline{\rho u''_i u''_j} - \tfrac{1}{2}(\gamma - 1)\overline{\rho u''_k u''_k}\delta_{ij} \right)_K \\
&\qquad + \left(\overline{W}_i n_j \big| \overline{\rho u''_i u''_j} - \tfrac{1}{2}(\gamma - 1)\overline{\rho u''_k u''_k}\delta_{ij} \right)_{\partial K} \\
&\qquad - \left(\partial_j \overline{W}_i \big| \overline{\rho' \widetilde{u}_i \widetilde{u}_j} - \tfrac{1}{2}(\gamma - 1)\overline{\rho' \widetilde{u}_k \widetilde{u}_k}\delta_{ij} \right)_K \\
&\qquad + \left(\overline{W}_i n_j \big| \overline{\rho' \widetilde{u}_i \widetilde{u}_j} - \tfrac{1}{2}(\gamma - 1)\overline{\rho' \widetilde{u}_k \widetilde{u}_k}\delta_{ij} \right)_{\partial K} \\
&\qquad - \left(\partial_j \overline{W}_i \big| - \overline{\overline{\sigma}}_{ij} \right)_K + \left(W_i n_j \big| - \overline{\overline{\sigma}}_{ij} \right)_{\partial K} \\
&\qquad + \left(\overline{W}_i n_j \big| (\rho u_i u_j)' + (\gamma - 1)((\rho e)' - \tfrac{1}{2}(\rho u_k u_k)')\delta_{ij} + \sigma'_{ij} \right)_{\partial K}. \quad (6.73)
\end{aligned}
$$

Compared to (6.61) additional SGS-terms emerge which all have been gathered on the last line in (6.73). Similar to the continuity equation all these additional SGS-terms are traces of the unresolved parts of the convective flux F^c_{ij} and the viscous flux F^v_{ij} at the element boundary. Next, we will show that these terms correspond to the commutator error $\mathcal{C}_j$ encountered in the traditional filtering approach to LES.

6.4.2   Comparison with the commutator error in LES

The use of a non-commuting projection immediately calls for a comparison with the commutator error encountered in LES. For a field f, the commutator error

SGS-term in LES is given by [51, 52, 54, 122],

$$\mathcal{C}_j(f) = \overline{\partial_j f} - \partial_j \overline{f} \tag{6.74}$$

For convolution filters such as the top-hat and Gaussian filters [48] the commutator error is typically encountered when the filter-width is non-uniform, but a non-uniform filter-width is not the only source of commutator errors. For example a filter which is not of convolution type or of which the filter-kernel is not a symmetric function, also contribute to commutator errors [47, 51]. Moreover, the projection used in this chapter cannot be rewritten in terms of a convolution, see (2.19) [134].

Formally every term in the matrices $F_{\alpha j}^v$ and $F_{\alpha j}^c$ as defined in (2.11) induces a commutator error. In this chapter we only discuss the commutator error encountered in the continuity equation $\mathcal{C}_j(\rho u_j)$ as an illustrative example. This commutator error is analyzed in a similar way as done for the SGS-stress previously.

After multiplication with test-functions $\overline{\mathbf{W}} \in \overline{\mathcal{U}}$ and integrating over the domain Ω the commutator error $\mathcal{C}_j(\rho u_j)$ is given by,

$$\left(\overline{W}_0 \Big| \mathcal{C}_j(\rho u_j)\right)_\Omega = \sum_{K \in \mathcal{T}_h} \left(\overline{W}_0 \Big| \mathcal{C}_j(\rho u_j)\right)_K \tag{6.75}$$

$$= \sum_{K \in \mathcal{T}_h} \left(\overline{W}_0 \Big| \overline{\partial_j \rho u_j} - \partial_j \overline{\rho u_j}\right)_K, \tag{6.76}$$

$$= \sum_{K \in \mathcal{T}_h} \left(\overline{W}_0 \Big| \partial_j \rho u_j\right)_K - \left(\overline{W}_0 \Big| \partial_j \overline{\rho u_j}\right)_K. \tag{6.77}$$

In the next step the variables ρu_j are decomposed as $\rho u_j = \overline{\rho u_j} + (\rho u_j)'$. Then (6.77) reduces to,

$$\left(\overline{W}_0 \Big| \mathcal{C}_j(\rho u_j)\right)_\Omega = \sum_{K \in \mathcal{T}_h} \left(\overline{W}_0 \Big| \partial_j (\rho u_j)'\right)_K \tag{6.78}$$

$$= \sum_{K \in \mathcal{T}_h} -\left(\partial_j \overline{W}_0 \Big| (\rho u_j)'\right)_K + \left(\overline{W}_0 n_j \Big| (\rho u_j)'\right)_{\partial K}. \tag{6.79}$$

Next we use the assumption that the space of resolved scales is closed with respect to differentiation, hence $\partial_j \overline{W}_0 = \overline{\partial_j \overline{W}_0}$, which yields,

$$\left(\overline{W}_0 \Big| \mathcal{C}_j(\rho u_j)\right)_\Omega = \sum_{K \in \mathcal{T}_h} -\left(\overline{\partial_j \overline{W}_0} \Big| (\rho u_j)'\right)_K + \left(\overline{W}_0 n_j \Big| (\rho u_j)'\right)_{\partial K}, \tag{6.80}$$

$$= \sum_{K \in \mathcal{T}_h} -\left(\partial_j \overline{W}_0 \Big| \overline{(\rho u_j)'}\right)_K + \left(\overline{W}_0 n_j \Big| (\rho u_j)'\right)_{\partial K}, \tag{6.81}$$

$$= \sum_{K \in \mathcal{T}_h} \left(\overline{W}_0 n_j \Big| (\rho u_j)'\right)_{\partial K}. \tag{6.82}$$

This expression for the commutator error $\mathcal{C}_j(\rho u_j)$ corresponds to the SGS-terms in the continuity equation (6.70). Consequently the SGS-term appearing in (6.70) can be identified as a commutator error.

6.5 Conclusions

In this chapter the Variational Multi-Scale approach to LES (VMS-LES) is considered as an alternative approach to LES. VMS-LES has been recently introduced in [24, 69] and considers a scale separation of the space of conserved variables $\overline{\mathcal{U}}$ into a finite dimensional space of resolved scales $\overline{\mathcal{U}}$ and the space of unresolved scales $\mathcal{U}'$. Contrary to the traditional filtering approach to LES a projection rather than a low pass filter is used to determine which scales are resolved and which not.

In this chapter we have extended VMS-LES to compressible flow and adapted the formulation such that it can be used for a wide range of discretization methods. The VMS-LES formulation for compressible flow has been constructed such that it resembles the Favre filtered Navier-Stokes equations. In the traditional filtering approach these equations are used in the simulation of compressible flow.

VMS-LES is strongly interwoven with the underlying discretization because typically the computational solution space $\mathcal{U}_h$ is used to define the space of resolved scales, i.e. $\overline{\mathcal{U}} = \mathcal{U}_h$. This aspect of the VMS approach to LES has been extensively discussed in this chapter. In [24, 69] only Fourier spectral discretizations were used which result in a commuting projection $\mathcal{P}: \mathcal{U} \to \overline{\mathcal{U}}$. As is well known Fourier spectral methods are generally impractical to be used in complex geometries. In this chapter we have considered the use of other discretization methods and used DG-FEM as an illustrative example. Such methods result in a projection which no longer commutes with differentiation. In the resulting VMS-LES formulation additional terms emerge which correspond to the commutator error encountered in traditional LES.

Chapter 7

Effect of numerical viscosity in LES of turbulent flow

In this chapter we present results of LES for homogeneous turbulent flow using DG-FEM. In particular, we investigate the effect of numerical viscosity introduced by the discretization to the LES SGS-modeling, using a data-base approach recently introduced in [92, 93].

7.1 Introduction

One of the distinctive aspects of a DG-FEM is that solutions are allowed to be double valued across an element interface as illustrated in figure 2.1 and, as discussed in section 2.3, numerical fluxes are used to deal with these discontinuities. Traditionally, upwind type fluxes or (approximate) Riemann solvers are used [121], that are excellent in capturing shocks, but have a considerable viscous contribution [80]. Numerical viscosity is required for the stabilization of any numerical scheme, e.g., to prevent the occurrence of spurious oscillations around sharp discontinuities in a flow [20, 80]. However, at coarse grid resolution the numerical viscosity can have a considerable contribution to the total dissipation rate of resolved kinetic energy (numerical dissipation). This may present problems when using DG-FEM in an LES. SGS-models, like Smagorinsky's model (2.32) considered here, are introduced for similar reasons. They are introduced to dissipate kinetic energy (SGS-dissipation) thus stabilizing an under-resolved simulation of turbulent flow in an attempt to model the action of the unresolved scales on the resolved scales [20, 112]. Hence, in actual LES at coarse grid resolution dissipative effects of both numerics and SGS-modeling influence the accuracy with which the

smoothed flow is predicted.

In an LES one primarily tries to capture large-scale flow-quantities such as the resolved kinetic energy. For decaying homogeneous turbulent flow Smagorinsky's SGS-model is well capable of capturing the evolution in time of resolved kinetic energy, however, this model requires a well chosen value of the Smagorinsky constant c_s in order to do so. Analytical estimates exist which show that the Smagorinsky constant should be around 0.17 for isotropic turbulence in order to accurately capture the dissipation rate of resolved kinetic energy [81, 102, 109]. Additionally, a number of numerical studies exist in which suggestions are made for the Smagorinsky-constant. These studies typically suggest $0.1 < c_s < 0.2$ [92, 102]. However, none of these studies take into account the effect of the numerical viscosity introduced by the numerical discretization. In case numerical methods are used with a larger viscous contribution it is unclear whether possibly different values of c_s should be used to achieve optimal accuracy.

In this chapter the effect of the numerical viscosity on resolution dependent "optimal" SGS-constants c_s^* for the Smagorinsky SGS-model (2.32) is studied. These optimal Smagorinsky constants c_s^* are determined using a data-base approach recently introduced in [92, 93] and correspond to the Smagorinsky constant c_s for which an *a-posteriori* error for the resolved kinetic energy is minimal. We will determine optimal Smagorinsky constants for second and third order accurate DG-FEM as presented in section 2.3. Use is made of a modified flux formulation in which a numerical viscosity parameter γ_c is introduced that gives explicit control over the numerical viscosity. We are particularly interested in the dependence of c_s^* on the numerical viscosity parameter γ_c.

The numerical viscosity parameter resembles the upwinding parameter γ_u often found in simulations of the one-dimensional wave-equation, $\partial_t u + \partial_x u = 0$ [3, 68]. Then the following flux formulation is used,

$$\hat{f}(u) = \{\!\{u\}\!\} + \gamma_u [\![u]\!], \tag{7.1}$$

where $[\![\cdot]\!]$ and $\{\!\{\cdot\}\!\}$ are the (one-dimensional) jump and averaging operators (2.45), respectively. In case $\gamma_u = 0$ (7.1) corresponds to a dispersive, central flux, while $\gamma_u = 1$ corresponds to a dissipative, upwind flux [80].

In figure 7.1 the effect of this upwinding parameter γ_u is illustrated by considering a step-function, initially located at $x = 0.5$, over an interval in time $t \in [0, 0.1]$. In particular, in figure 7.1 the discontinuity at $t = 0.1$ is shown (figure 7.1(a)) as well as the location of the discontinuity as a function of time (figure 7.1(b)) and the kinetic energy $\mathcal{E}(t)$ in the domain $[0, 1]$ as a function of time (figure 7.1(c)),

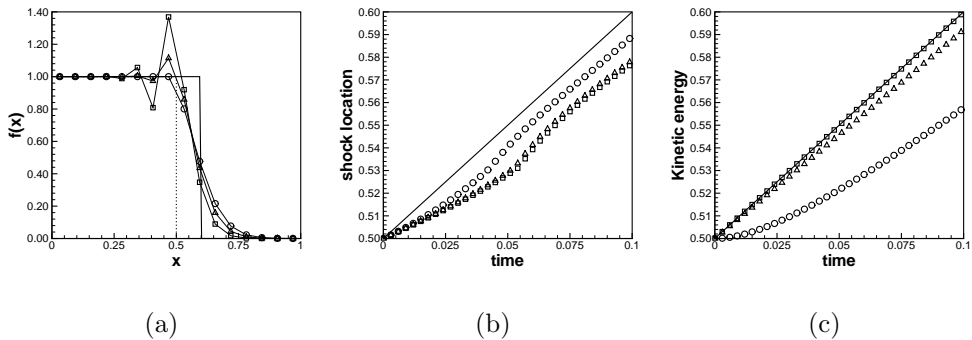$$\mathcal{E}(t) = \int_0^1 u(x, t)^2 \, dx. \tag{7.2}$$

(a) (b) (c)

Figure 7.1: a) Evolution of a discontinuity initially located at $x = 0.5$ (dotted) by the wave-equation $\partial_t u + \partial_x u = 0$ over a time interval $[0, 0.1]$: exact wave at $t = 0.1$ (solid) and the numerical predictions using first order DG-FEM and (7.1) as numerical flux: $\gamma_u = 1$ ($\circ$), $\gamma_u = 0.5$ ($\triangle$) and $\gamma_u = 0.01$ ($\square$). b) location ($u(x) = 0.5$) of the discontinuity c) Evolution of the kinetic energy $\mathcal{E}(t)$ (7.2). For these simulations 16 elements are used with only an element mean ($p = 0$), the time step is 0.001.

Because the step function is moving into the interval $[0, 1]$ the kinetic $\mathcal{E}(t)$ is a strictly increasing function for the analytics solution; $\mathcal{E}(t) = \frac{1}{2} + t$.

As can be seen in figures 7.1(a) and 7.1(b) the flux (7.1) with $\gamma_u = 1$ is best in capturing the discontinuity. However, its large viscous contribution can be observed in figure 7.1(c). The opposite is observed when $\gamma_u \approx 0$. Then the simulation accurately captures the evolution of the kinetic energy, but is less effective in capturing the discontinuity. Also, spurious oscillations are observed which eventually will lead to a break down of the simulation. For three-dimensional turbulent flow analogous effects are expected when the numerical viscosity parameter γ_c is used as a generalization of the upwinding parameter γ_u. Adopting $\gamma_c \approx 0$ will lead to a reduction of the numerical dissipation, but may lead to numerical instability, while adopting $\gamma_c = 1$ results in a stable simulation, although, a considerable contribution to the dissipation rate of kinetic energy is to be expected.

We will study how γ_c affects the optimal choice of Smagorinsky constants. To determine optimal Smagorinsky constants c_s^* a large number of LES of decaying homogeneous turbulent flow has been performed at various Reynolds numbers adopting a wide range of grid-resolutions. The results of these simulations are a-posteriori compared against filtered DNS-data and are gathered in an error-landscape or "accuracy chart" [92, 93]. By also varying parameters affecting the SGS-dissipation c_s and the numerical dissipation γ_c it is possible to determine the "optimal" Smagorinsky constant for a given resolution and numerical viscosity pa-

rameter γ_c. Next to the already observed dependence of this optimal SGS-constant on the resolution [92] it will be shown that the optimal SGS-constant c_s^* is dependent on the amount of numerical viscosity introduced by the discretization. For a fixed resolution a lower value of c_s^* is found if more numerical viscosity is introduced. For second order DG-FEM the effect of the numerical viscosity is so large if $\gamma_c = 1$ that the analysis suggests to abandon SGS-modeling and "let the numerical dissipation do the work" [59]. However, it will be shown that the best possible prediction for the decay of resolved kinetic energy at fixed resolution is arrived at by adopting $\gamma_c \approx 0$ in which case the decay of resolved kinetic energy is governed by the dissipation through the SGS-model instead of dissipation through the numerical viscosity.

The outline of this chapter is the following. In section 7.2 we identify the main sources of dissipation and relate to existing literature. In section 7.3 details are given of the Runge-Kutta DG-FEM (RKDG-FEM) code used in this chapter. Then in section 7.4 LES results are *a-posteriori* compared against filtered DNS-data and the effect of the numerical viscosity is qualitatively shown. In section 7.5 the database approach used to determine optimal Smagorinsky constants is introduced and the dependence of the optimal constants c_s^* on the numerical viscosity parameter γ_c is quantified. Finally in section 7.6 the results are summarized and discussed.

7.2　Evolution of the resolved kinetic energy in LES

Following [92] we will focus on the evolution of the resolved kinetic energy $\widetilde{E}$ in an unforced simulation of homogeneous turbulent flow in a periodic domain $\Omega = [0,1]^3$. In principle the analysis presented in this chapter can also be applied to other quantities such as the skewness or Taylor length-scale, but this is not considered here. For compressible flow the resolved kinetic energy is given by,

$$\widetilde{E} = \int_\Omega \overline{\rho}\,\widetilde{u}_k\widetilde{u}_k\,d\mathbf{x}. \tag{7.3}$$

In an unforced simulation of homogeneous turbulent flow the decay of resolved kinetic energy $\varepsilon = -d\widetilde{E}/dt$ is mainly affected by: *i)* the resolved molecular dissipation ε_μ, *ii)* the SGS-dissipation $\varepsilon_{\mathrm{SGS}}$ and *iii)* the numerical dissipation $\varepsilon_{\mathrm{num}}$. Hence the dissipation rate of resolved kinetic is given by,

$$\varepsilon = \varepsilon_\mu + \varepsilon_{\mathrm{SGS}} + \varepsilon_{\mathrm{num}}. \tag{7.4}$$

The resolved molecular dissipation ε_μ and the dissipation through the Smagorinsky

SGS-model $\varepsilon_{\mathrm{SGS}}$ are respectively given by,

$$\varepsilon_\mu \;\; = \;\; \int_\Omega \mu(\widetilde{T})\widetilde{S}_{ij}\partial_j\widetilde{u}_i\,d\mathbf{x}, \tag{7.5}$$

$$\varepsilon_{\mathrm{SGS}} \;\; = \;\; \int_\Omega \mu_e\widetilde{S}_{ij}\partial_j\widetilde{u}_i\,d\mathbf{x} \;\; = \;\; \int_\Omega \overline{\rho}(c_s h)^2|\widetilde{S}|\widetilde{S}_{ij}\partial_j\widetilde{u}_i\,d\mathbf{x}. \tag{7.6}$$

Here $\mu(\widetilde{T})$ is the dynamic viscosity and μ_e is the eddy-viscosity (2.32) in which it is chosen to set the filter-width equal to the typical element size h. From (7.5) and (7.6) one can observe that both the resolved molecular dissipation and the SGS-dissipation are dependent on the resolved rate-of-strain tensor $\widetilde{S}_{ij}$. At a fixed Reynolds number and resolution, independent control of the SGS-dissipation over the molecular dissipation is possible through the Smagorinsky constant c_s.

The dissipative component of numerical fluxes can be identified by rewriting the flux function (see section 2.3) as,

$$\widehat{F}^c_{\alpha j}(\mathbf{U}^L, \mathbf{U}^R) \;\; = \;\; \{\!\{F^c_{\alpha j}(\mathbf{U})\}\!\} + \gamma_c\widehat{D}_{\alpha j}. \tag{7.7}$$

In this formulation of the numerical flux we, analogous to (7.1), distinguish between a central flux $\{\!\{F^c_{\alpha j}\}\!\}$ and the term $\gamma_c\widehat{D}_{\alpha j}$ which constitutes the dissipative component of the modified numerical flux. In the dissipative component the numerical viscosity parameter γ_c is introduced in order to have explicit control over the numerical viscosity. As a convention we adopt that $\gamma_c = 0$ results in a central flux $\widehat{F}^c_{\alpha j} = \{\!\{F^c_{\alpha j}\}\!\}$, while choosing $\gamma_c = 1$ results in the recovery of the original flux definition. The central flux is known to be unstable in DG-FEM [130] such that choosing $\gamma_c \approx 0$ may lead to numerical instability. In case the original flux definition is used the simulation is sufficiently stable but may produce a large contribution to the dissipation rate of kinetic energy.

The viscous contribution of a numerical flux $\widehat{F}^c_{\alpha j}$ to the dissipation rate of kinetic energy typically scales with the size of the jump $[\![U_\alpha]\!]_j$ at an element interface. This is most easily observed for Lax-Friedrich's flux. The modified version of this flux is given by,

$$\widehat{F}^c_{\alpha j}(\mathbf{U}^L, \mathbf{U}^R) \;\; = \;\; \{\!\{F_{\alpha j}(\mathbf{U})\}\!\} + \tfrac{1}{2}\gamma_c\lambda[\![U_\alpha]\!]_j, \tag{7.8}$$

where λ is the maximal eigenvalue of the Euler-flux Jacobian. The dissipative contribution of this flux is given by $\gamma_c\lambda[\![U_\alpha]\!]_j/2$. Hence, the larger the jump at an interface, the larger the regularizing behavior of the numerical flux. Only in case $[\![U_\alpha]\!]_j \approx 0$ the numerical dissipation is negligible. This, however, is only achieved at high resolution.

The three sources of dissipation are affected the flow conditions and by three different parameters: the resolution $N > 0$, the Smagorinsky constant $c_s \geq 0$ and
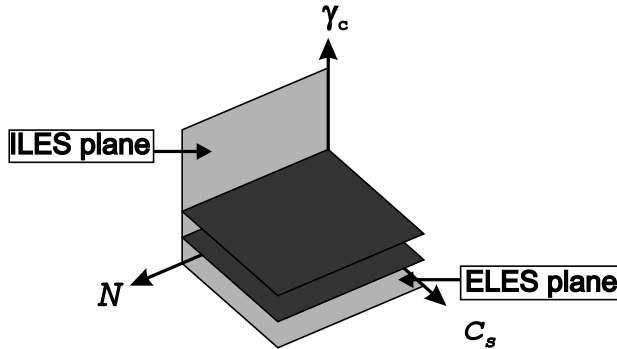
Figure 7.2: Axes for the three dimensional accuracy charts. The plane where $c_s = 0$ is referred to as the ILES plane while the plane with $\gamma_c = 0$ is referred to as the ELES plane.

the numerical dissipation parameter γ_c. Of these three parameters the Smagorinsky constant and the numerical dissipation parameter can be used to independently control the SGS-dissipation and numerical dissipation, respectively. Throughout this study the effect of other numerical parameters is neglected and left out of the discussion. In figure 7.2 we graphically displayed the parameter space spanned by these parameters. Two planes in this parameter space have a special interpretation and are shortly discussed next.

First of all at the plane where $\gamma_c \approx 0$ the numerical dissipation through the convective flux is small. We will refer to this plane as the Explicit-LES (ELES) plane. Here, next to the molecular dissipation, only the dissipation through the *explicit* SGS-model is of importance. Meyers *et al.* [92] studied optimal Smagorinsky constants in this plane using a fourth other central finite volume scheme. It was shown that the optimal Smagorinsky constant is dependent on the resolution. At higher resolution a lower value of the optimal Smagorinsky constant is suggested by [92].

The other plane in figure 7.2 which has a special interpretation is the plane for which $c_s = 0$. Here the numerical dissipation acts as an *implicit* model [2, 59] and no explicit SGS-model is used. Therefore this plane is referred to as the Implicit LES (ILES) plane [2]. In the present study $\gamma_c \widehat{D}_{\alpha j}$ constitutes the implicit model. The best known example of an LES approach exploiting the implicit model is the Monotonically Integrated LES (MILES) technique as proposed by Boris *et al.* [12, 57, 58]. In recent years, many other numerical dissipation or stabilization operators based on numerical arguments have been dubbed a SGS-model. Examples can be found in articles by Margolin and Rider [85, 86], Hoffman and Johnson [66], Adams, Hickel and Fransz [2] and in Braack and Burman [14].

In the remainder of this chapter we will explore the full parameter space spanned

by N, c_s and γ_c. Next to the dependence of c_s^* on the resolution we will study the effect of γ_c on the optimal Smagorinsky constant. First, however, details are given of the Runge-Kutta DG-FEM (RKDG-FEM) code used.

7.3 Code description and validation

For the results presented in this chapter a RKDG-FEM code based on the discretization described in section 2.3 is used. In this section additional details will be given concerning the grid and the actual implementation of the discretization as well as results of a code validation.

The code can handle different polynomial orders $p \geq 1$ and together with sufficiently high order numerical evaluation of the integrals and explicit Runge-Kutta time stepping this results in a $p+1$-th order RKDG-FEM discretization. In detail, all integrals are evaluated using $p + 1$-th order Gaussian integration and for time integration use is made of a $p+1$-th order, explicit Runge-Kutta scheme, satisfying the Strong Stability Preserving (SSP) criterion, see [34, 35, 56, 110, 114] for details. Dynamic time stepping is used and the time step restrictions are based on a stability analysis using the advection-diffusion equation. Further, the stabilization term for the viscous flux, $\eta_v + n_f$ in (2.74), is set to 6 [5, 15] and for the convective treatment the modified HLLC-flux (2.62) including the numerical viscosity parameter is used.

We consider homogeneous turbulent flow in a periodic domain $\Omega = [0, 1]^3$ over a time-interval $[0, 1]$. A uniform grid is adopted for which the domain Ω is divided into N^3 hexahedronal elements K with a length $h = 1/N$. The resulting tessellation $\mathcal{T}_h$ is given by,

$$\mathcal{T}_h = \left\{ K_{ijk} = ((i-1)h, ih) \times ((j-1)h, jh) \times ((k-1)h, kh) \Big| 1 \leq i, j, k \leq N \right\}. \quad (7.9)$$

The polynomial basis-functions of maximal order p are constructed as described in section 2.3. Because a uniform grid is used, the mapping $G^K : \hat{K} \to K$ reduces to an affine transformation and the basis-functions $\phi_i^K(\mathbf{x})$, $K \in \mathcal{T}_h$, $i = 0 \ldots N_p - 1$ remain mutually orthogonal.

In order to validate the code, a number of simulations using various resolutions N, $Re_\lambda = 50$, $M = 0.2$ and $Pr = 1.0$ are performed. Here Re_λ denotes the Taylor-Reynolds number [102]. For these simulation the HLLC-flux is used with $\gamma_c = 1$ and the results are compared against the results of a Fourier-Spectral simulation using 384^3 modes [78]. The initial conditions are determined by projecting the incompressible and isothermal velocity field at $t = 0$ to the basis-functions ϕ_i^K, $K \in \mathcal{T}_h$, $i = 0, \ldots, N_p - 1$ [78, 92]. In this chapter use is made of the following
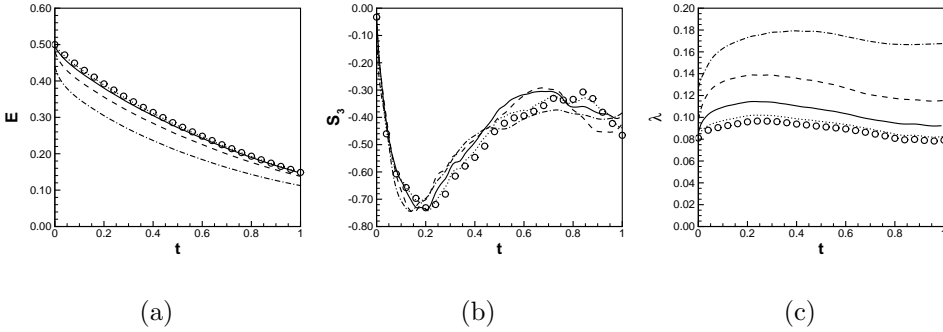
Figure 7.3: Code validation at $Re_\lambda = 50$ using second order accurate RKDG-FEM with 16^3 (dash-dot), 32^3 (dashed), 64^3 (solid) and 128^3 (dotted) elements a) Kinetic energy, b) skewness S_3, c) Taylor length-scale λ. The circles indicate the results of the reference DNS.
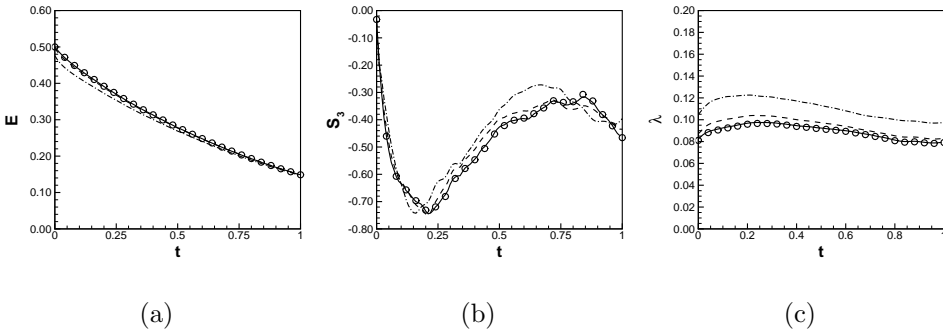

Figure 7.4: Code validation at $Re_\lambda = 50$ using third order accurate DG-FEM with 16^3 (dash-dot), 32^3 (dashed) and 64^3 (solid) elements a) Kinetic energy, b) skewness S_3, c) Taylor length-scale λ. The circles indicate the results of the reference DNS.

face-based projection,

$$\mathcal{P}_{\partial K}[f](\mathbf{x}) \;=\; \sum_{K \in \mathcal{T}_h} \sum_{i,j=0}^{N_p-1} \mathbb{M}_{ij}^{-1}(\partial K) \int_{\partial K} f(\mathbf{y})\phi_i^K(\mathbf{y})\,d\mathbf{y}\,\phi_j^K(\mathbf{x}). \qquad (7.10)$$

Here the mass-matrix $\mathbb{M}_{ij}(\partial K)$ is given by $\mathbb{M}_{ij}(\partial K) = \int_{\partial K} \phi_i^K(\mathbf{y})\phi_j^K(\mathbf{y})\,d\mathbf{y}$. This projection differs from the projection $\mathcal{P}$ defined in (2.22). For the face-based projection $\mathcal{P}_{\partial K}$ the integrals are evaluated only over the faces of an element. The face-based projection results in a considerably more regularized flow-field compared to the element-based projection.

A number of reasons exist why the face-based projection (7.10) instead of the element-based projection (2.22) is used within the present analysis. However, the main reason for adopting the face-based projection is that the analysis using the element-based projection suggested the use of Smagorinsky constants that would render the simulation to become unstable. We will come back to this issue at the end of section 7.5. The main conclusions, however, do not change when adopting either the face-based or the element-based projection. In both cases it is shown that c_s^* is affected in by the amount of numerical dissipation introduced by the discretization and lower values of c_s are suggest with increasing numerical viscosity.

Results of the code validation are shown in figures 7.3 and 7.4 for second and third order accurate RKDG-FEM, respectively. In these figures the decay of kinetic energy is shown,

$$E(t) = \tfrac{1}{2} \int_\Omega \rho u_i u_i \, d\mathbf{x}, \qquad (7.11)$$

as well as the evolution in time of the skewness S_3 and Taylor length-scale λ,

$$S_3 \;=\; \frac{\langle (\partial_1 u_1)^3 \rangle_\Omega}{\langle (\partial_1 u_1)^2 \rangle_\Omega^{3/2}}, \qquad \lambda \;=\; \sqrt{\frac{\langle u_1^2 \rangle_\Omega}{\langle (\partial_1 u_1)^2 \rangle_\Omega}}. \qquad (7.12)$$

Here $\langle \cdot \rangle_\Omega$ denotes averaging over the domain Ω.

For third order DG-FEM the kinetic energy E is captured at low resolution (32^3 elements) while at least 64^3 elements are needed to capture the skewness S_3 and Taylor length scale λ. When using second order DG-FEM as shown in figure 7.3 considerably more elements are needed to capture the kinetic energy, skewness and Taylor length scale. The kinetic energy requires 128^3 elements, while for the skewness and Taylor length-scale more than 128^3 are required.

Next we will turn to LES results using DG-FEM. These results are *a-posteriori* compared with filtered DNS-data.

7.4 Effect of numerical viscosity on the decay of resolved kinetic energy

In this section we will present results of LES using different values of γ_c and c_s and these results are *a-posteriori* compared against DNS-data. This allows us to illustrate the effect of numerical viscosity in a LES on the evolution of the resolved kinetic energy (7.3). Moreover, it allows us to qualitatively show that depending on γ_c different Smagorinsky constants should be used in order to capture the decay of resolved kinetic energy.
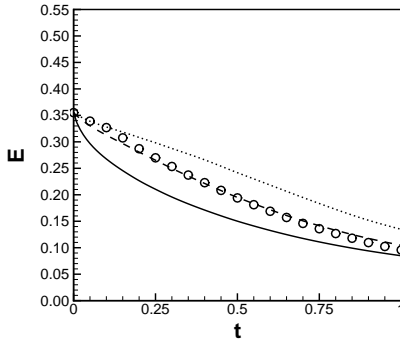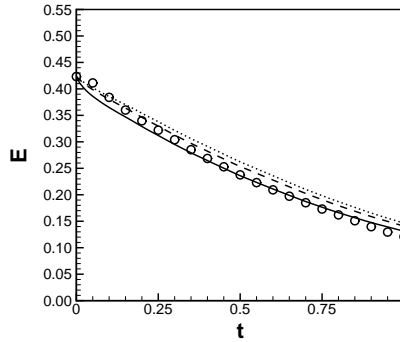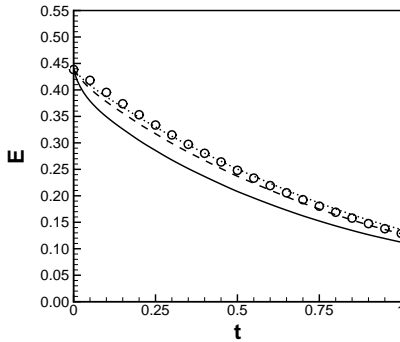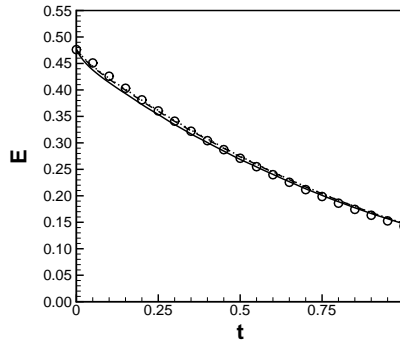
(a) 8^3 elements, second order

(b) 8^3 elements, third order

(c) 16^3 elements, second order

(d) 16^3 elements, third order

Figure 7.5: The decay of resolved kinetic energy at $Re_\lambda = 50$ using second and third order accurate DG-FEM, 8^3 or 16^3 elements and $\gamma_c = 1.00$ (solid), $\gamma_c = 0.10$ (dashed) and $\gamma_c = 0.01$ (dotted). No SGS-model is used for these simulations. The symbols indicate the filtered-DNS solutions.

In figures 7.5 and 7.6 the decay of the resolved kinetic energy $\widetilde{E}$ is shown at $Re_\lambda = 50$ and $Re_\lambda = 100$, respectively, using a coarse grid ($N = 8$ and $N = 16$) and both second and third order accurate DG-FEM. In each of the figures the results are shown of three simulations using $\gamma_c = 1.00$, $\gamma_c = 0.10$ and $\gamma_c = 0.01$, respectively. From the reference DNS [78] twenty DNS fields are available with a time spacing of 0.05. These fields are projected using (7.10) in the same way as used for the initial condition and the resulting values of $\widetilde{E}$ are indicated in figures 7.5 and 7.6. We emphasize that in these figures no use was made of an explicit SGS-model ($c_s = 0.0$) such that solely the effect the implicit model $\gamma_c \widehat{D}_{\alpha j}$
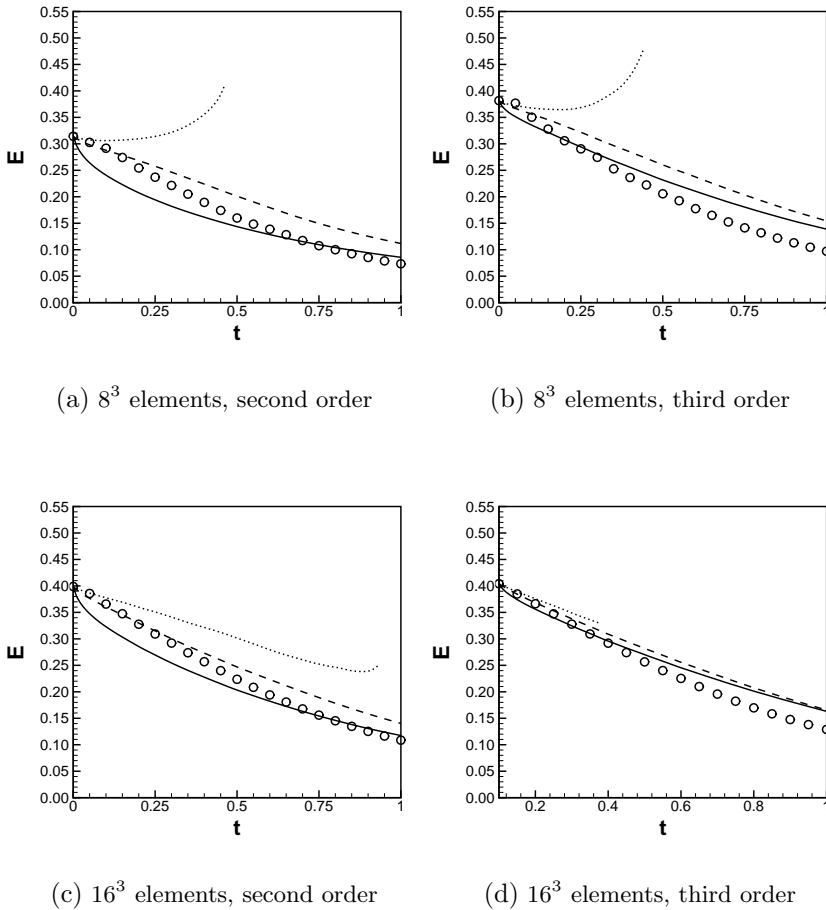
(a) 8^3 elements, second order

(b) 8^3 elements, third order

(c) 16^3 elements, second order

(d) 16^3 elements, third order

Figure 7.6: The decay of resolved kinetic energy at $Re_\lambda = 100$ using second and third order accurate DG-FEM, 8^3 or 16^3 elements and $\gamma_c = 1.00$ (solid), $\gamma_c = 0.10$ (dashed) and $\gamma_c = 0.01$ (dotted). No SGS-model is used for these simulations. The symbols indicate the filtered-DNS solutions.

is observed.

A number of observations can be made. First of all, it can be observed that in case γ_c is chosen very small ($\gamma_c = 0.01$) this may lead to numerical instability. In fact all simulations shown in figure 7.6 ($Re_\lambda = 100$) using $\gamma_c = 0.01$ resulted in a numerically unstable simulation. In these cases the flow is not well enough smoothed through any dissipation and eventually the simulation breaks down. On the other hand in most of the cases in which the HLLC flux is used with $\gamma_c = 1.0$ the decay of resolved kinetic energy is already under-predicted and there seems no
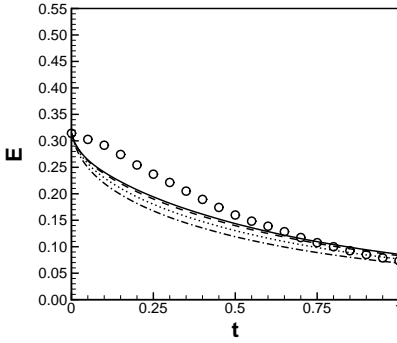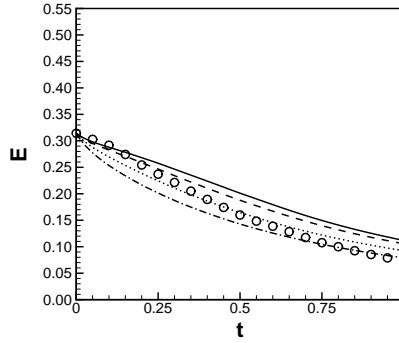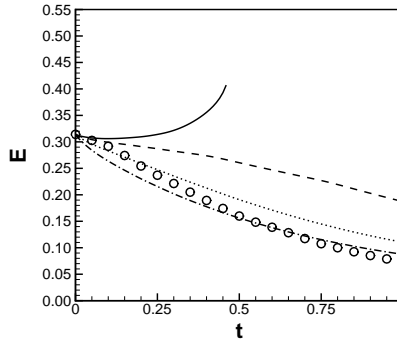
(a) $\gamma_c = 1.00$

(b) $\gamma_c = 0.10$

(c) $\gamma_c = 0.01$

Figure 7.7: The decay of resolved kinetic energy at $Re_\lambda = 100$ using second order accurate DG-FEM with an explicit SGS-model and 8^3 elements: filtered DNS (circles), $c_s = 0.00$ (solid), $c_s = 0.04$ (dashed), $c_s = 0.08$ (dotted) and $c_s = 0.12$ (dash-dot). a) $\gamma_c = 1.00$, b) $\gamma_c = 0.10$ and c) $\gamma_c = 0.01$.

need to use an SGS-model.

In figures 7.7 and 7.8 results are shown of $\widetilde{E}(t)$ for various values of c_s and γ_c using second and third order accurate DG-FEM, respectively. The Reynolds number in these figures is $Re_\lambda = 100$. Now with the additional dissipation through the SGS-model the simulations at minimal numerical dissipation as shown in figures 7.7(c) and 7.8(c) no longer break down. The decay of resolved kinetic energy highly depends on the choice of the Smagorinsky constant c_s.

For second order accurate DG-FEM (figure 7.7) we observe that in case $\gamma_c = 1.0$

(a) $\gamma_c = 1.00$
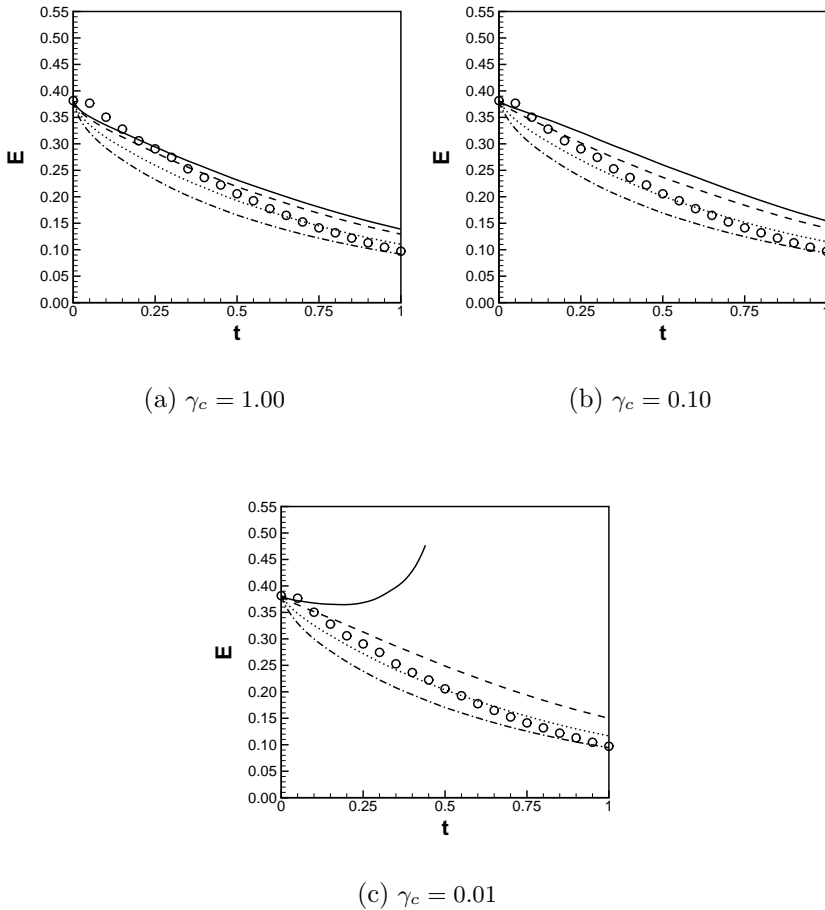
(b) $\gamma_c = 0.10$

(c) $\gamma_c = 0.01$

Figure 7.8: The decay of resolved kinetic energy at $Re_\lambda = 100$ using third order accurate DG-FEM with an explicit SGS-model and 8^3 elements: filtered DNS (circles), $c_s = 0.00$ (solid), $c_s = 0.04$ (dashed), $c_s = 0.08$ (dotted) and $c_s = 0.12$ (dash-dot). a) $\gamma_c = 1.00$, b) $\gamma_c = 0.10$ and c) $\gamma_c = 0.01$.

the numerical dissipation is so large that $c_s = 0$ yields the best approximation. On the other hand, in case $\gamma_c \approx 0$, $c_s \sim 0.10$ should be chosen while slightly lower values of c_s should be used in the intermediate case $\gamma_c = 0.10$. For third order accurate DG-FEM (figure 7.8) similar observation are made. Lower values of c_s should be adopted with increasing γ_c, however, the differences between the various optimal choices of c_s are small.

Summarizing, these results indicate that SGS-parameters should be modified at different levels of numerical dissipation in order to capture the resolved kinetic

energy as accurately as possible. However, deciding which Smagorinsky-constant is "optimal" based on these graphs is difficult. Moreover, it does not allow for general, widely applicable suggestions for the Smagorinsky constant as many more combinations of N, γ_c and c_s are possible than the ones shown in this section. Therefore, in the next section a database approach is used to determine the optimal Smagorinsky constant for a wide range of resolutions N and numerical viscosity parameters γ_c.

7.5   Accuracy charts approach

The discussion at the beginning of this chapter resulted in the identification of three different parameters affecting the dissipation rate of kinetic energy. These are, the resolution N, the numerical viscosity parameter γ_c controlling the numerical dissipation and the Smagorinsky constant c_s. In this section, using a database approach, the effect of these parameters on the decay of resolved kinetic energy is investigated and we determine the optimal Smagorinsky constant for given resolution N and numerical viscosity parameter γ_c. In the absence of numerical viscosity earlier investigations have already shown that the choice which c_s is optimal is dependent on the resolution N [92], while the results in the previous section suggest that the "optimal" choice for the Smagorinsky constant is also dependent on the amount of dissipation introduced by the discretization.

For the database approach a large number of simulations was performed. Essential to the approach adopted in this section is that all data available from the simulations is significantly reduced by considering a single *a-posteriori* error measure per simulation, i.e., the quality of one simulation is expressed by a single value. The particular error measure adopted in this study is based on the L_2-error of the resolved kinetic energy $\widetilde{E}$ over a time-interval $[0, 1]$ and is defined as,

$$
\delta_{\mathrm{L2}}[\widetilde{E}] \;=\; \frac{\left\{ \int_{t_0}^{t_1} \left(\widetilde{E}_{\mathrm{LES}}(t) - \widetilde{E}_{\mathrm{DNS}}(t) \right)^2 dt \right\}^{\frac{1}{2}}}{\left\{ \int_{t_0}^{t_1} \widetilde{E}_{\mathrm{DNS}}^2(t)\, dt \right\}^{\frac{1}{2}}}. \tag{7.13}
$$

Here a tilde denotes that we are evaluating LES-data and compare it with the filtered DNS-data.

After having determined $\delta_{\mathrm{L2}}[\widetilde{E}]$ for each simulation the results can be put into a single plot. Such a three-dimensional "error landscape" or "accuracy chart" is shown in figure 7.9. In figure 7.9 the contours indicate $\delta_{\mathrm{L2}}[\widetilde{E}]$, the black dots denote the individual LES that were performed and the red octahedrons correspond to the Smagorinsky constant where the error is minimal for a given resolution N and
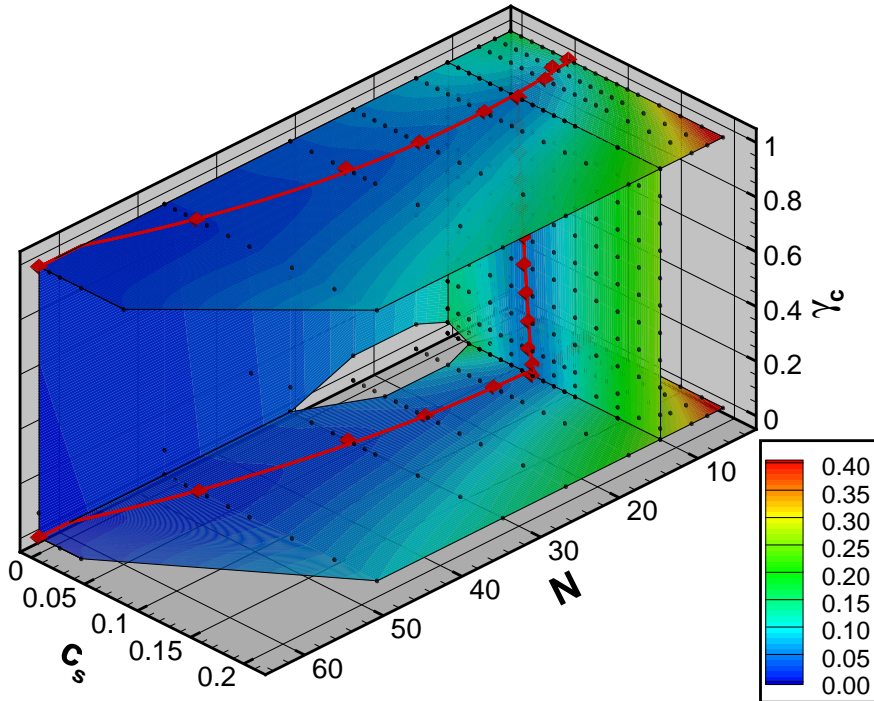
Figure 7.9: Three dimensional error landscape of $\delta_{\mathrm{L2}}[\widetilde{E}]$. The slices shown correspond to the planes where $c_s = 0.0$, $\gamma_c = 1.0$, $\gamma_c = 0.01$ and $N = 12$. Further the black dots correspond to individual LES-simulation and the red symbols indicate the optimal Smagorinsky constant c_s^* for a given combination of N and γ_c. The realization shown is for third order accurate DG-FEM at $Re_\lambda = 100$.

numerical viscosity parameter γ_c. In order to accurately determine the optimal Smagorinsky constants for a given combination of N and γ_c the errors in between the simulations are interpolated using a fourth order polynomial interpolation.

Some individual (N, c_s)-slices at fixed $\gamma_c > 0$ and $Re_\lambda = 100$ are shown in figures 7.10 and 7.11. In figure 7.10 we use second order DG-FEM, while in figure 7.11 third order accurate DG-FEM has been used. The dashed lines indicate the optimality curves which are determined using a second order accurate interpolation of the individual optimal Smagorinsky constants c_s^*. These curves clearly show the dependence of optimal Smagorinsky constants on both the numerical viscosity as well as the resolution.

The dependence on the resolution implies that less SGS-dissipation is required at high resolution in order to capture $\widetilde{E}(t)$. In all figures a critical resolution can be identified above which $c_s^* = 0$. Regarding the dependence on the numerical viscosity parameter γ_c it can be observed that lower values of the Smagorinsky constant are
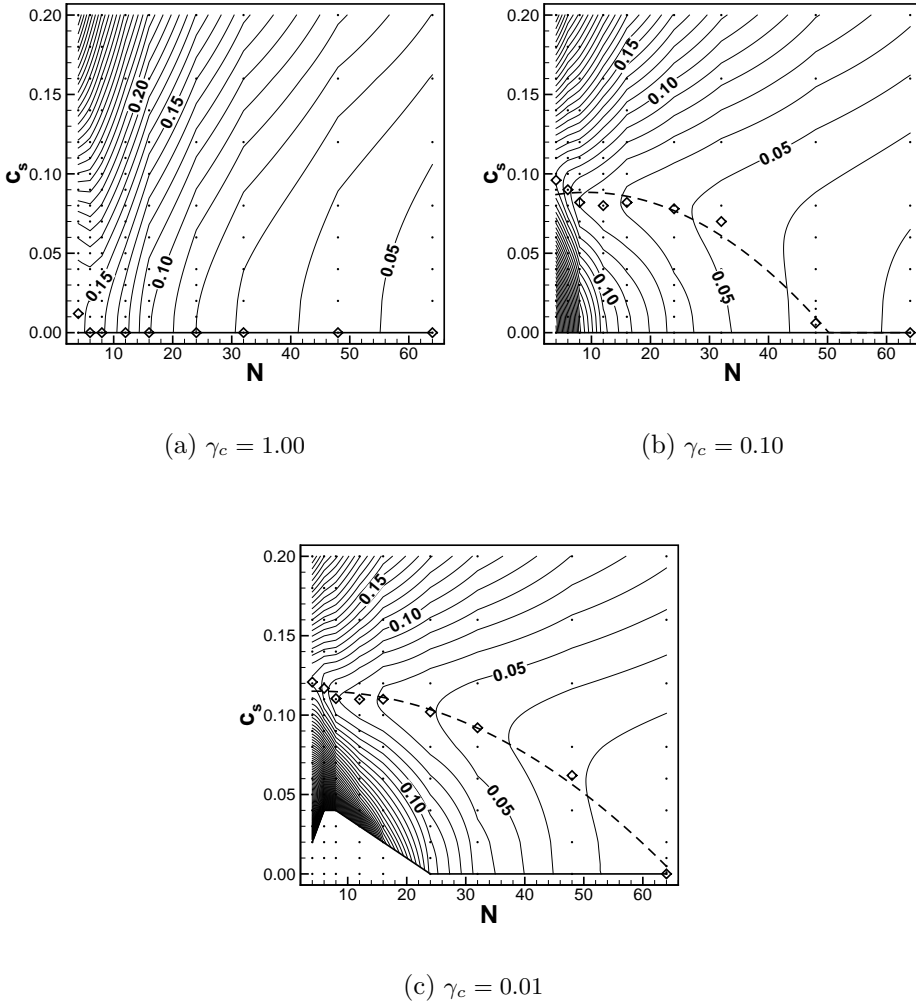
(a) $\gamma_c = 1.00$

(b) $\gamma_c = 0.10$

(c) $\gamma_c = 0.01$

Figure 7.10: Two dimensional error landscape of $\delta_{\mathrm{L2}}[\widetilde{E}]$ for second order accurate DG-FEM using a) $\gamma_c = 1.0$, b) $\gamma_c = 0.10$ and c) $\gamma_c = 0.01$ at $Re_\lambda = 100$. The black points correspond to individual LES-simulation, the diamonds indicate the optimal Smagorinsky constant c_s^* for a given resolution N and the black line is a polynomial fit of the optimal Smagorinsky constants. The contour increment is 0.01.

required in case more numerical dissipation is introduced by the discretization. Moreover, in case of second order DG-FEM adopting the HLLC-flux with $\gamma_c = 1.0$ the optimal Smagorinsky constant $c_s^* \equiv 0.0$ and the analysis suggests to abandon explicit SGS-modeling altogether.
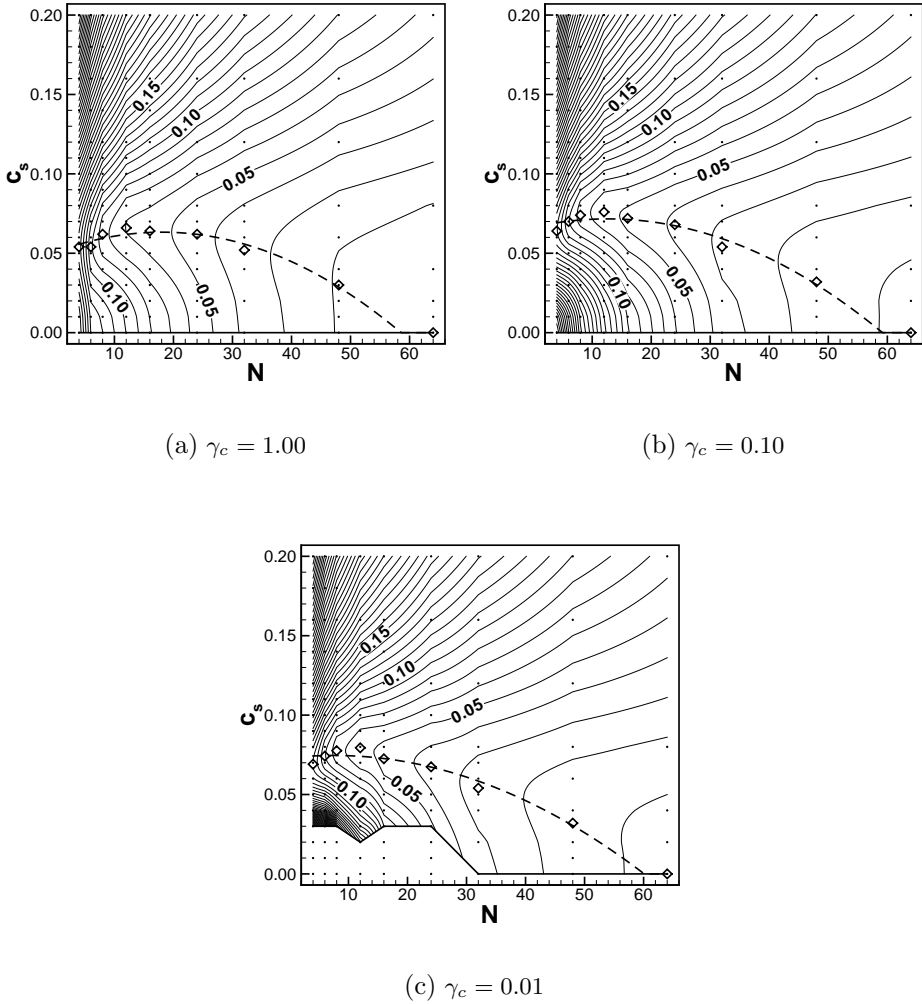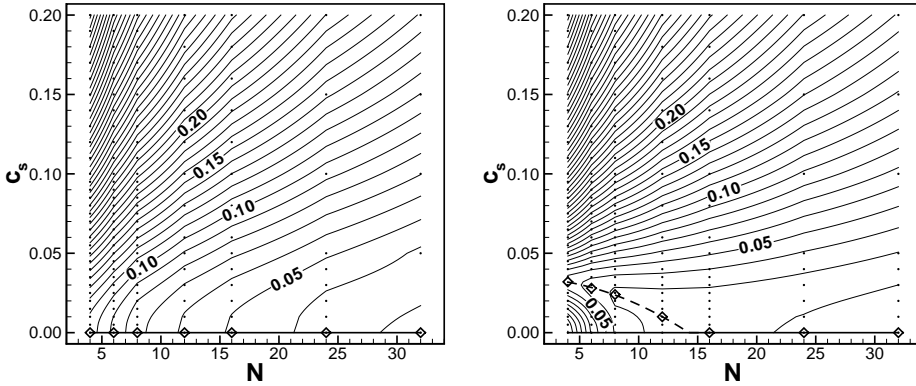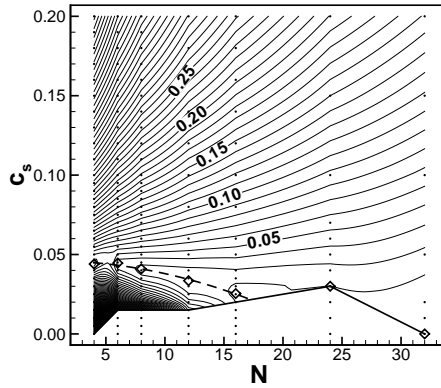
(a) $\gamma_c = 1.00$

(b) $\gamma_c = 0.10$

(c) $\gamma_c = 0.01$

Figure 7.11: Two dimensional error landscape of $\delta_{\mathrm{L2}}[\widetilde{E}]$ for third order accurate DG-FEM. Further details are the same as in figure 7.10.

For the cases with $\gamma_c = 0.01$ in figures 7.10(c) and 7.11(c) "instability" regions can be identified and are illustrative for the alternative role of the Smagorinsky model, that of a stabilization operator. The instability regions are the regions in the lower left corners of these figures below the solid line and correspond to simulations that did not properly complete the simulation until $t = 1$. It can be observed that in the absence of numerical dissipation above a critical c_s the simulations do not become unstable.

(a) $\gamma_c = 1.00$

(b) $\gamma_c = 0.10$

(c) $\gamma_c = 0.01$

Figure 7.12: Two dimensional error landscape of $\delta_{L2}[\widetilde{E}]$ for third order accurate DG-FEM when instead of the face-based projection (7.10) the element-based projection (2.22) is used. Further details are the same as in figure 7.10.

In figure 7.12 the resulting accuracy charts are shown for third order DG-FEM when instead of the face-based projection the element based projection is used. Specifically, the element-based projection is used to determine the initial condition as well as the filtered DNS-data which again is used to determine $\widetilde{E}_{DNS}$ in (7.13). In figure 7.12 similar behavior is observed as in figures 7.11 and 7.10, lower values of c_s are suggested with increasing γ_c. However, in figure 7.12(c) ($\gamma_c = 0.01$) we observe that the optimality curve tends to enter the instability regions for $N > 16$, i.e.
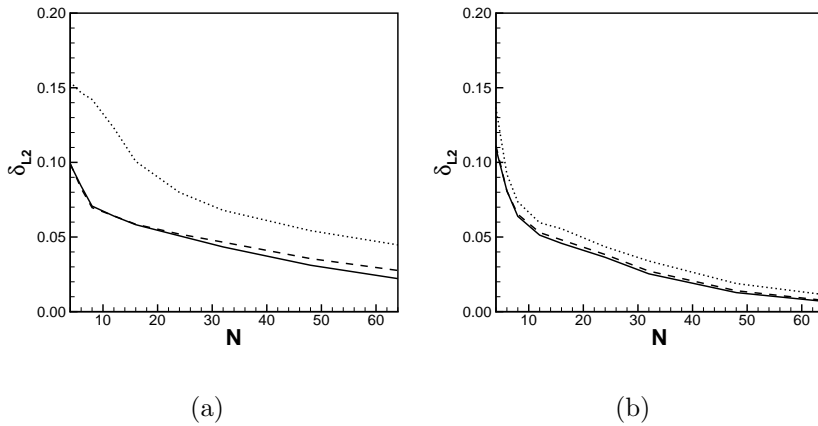
Figure 7.13: Error $\delta_{L2}[\widetilde{E}]$ along the optimal curve using a) second order accurate DG-FEM and b) third order accurate DG-FEM and $\gamma_c = 1.00$ (dotted), $\gamma_c = 0.10$ (dashed) and $\gamma_c = 0.01$ (solid).

the analysis suggests the use of an unstable Smagorinsky constant for resolutions $N > 16$. This seems odd for common practice and has been the main reason of adopting the face-based projection throughout the present analysis.

A natural question that now arises is which of the two dissipations, numerical or SGS-dissipation is preferable in an attempt to minimize $\delta_{L2}[\widetilde{E}]$. Is it preferable to use numerical-dissipation through the HLLC-flux or SGS-dissipation through the Smagorinsky SGS-model, or possibly a combination of the two? In figure 7.13 the error $\delta_{L2}[\widetilde{E}]$ along the optimality curve $c_s^*(N)$ is shown for second order and third order accurate DG-FEM. The results in this figure show which minimal value of $\delta_{L2}[\widetilde{E}]$ can be attained, using Smagorinsky's SGS-model, for a given resolution N and numerical viscosity γ_c.

In figure 7.13 we first of all observe that with increasing resolution the error decreases. This is an expected result but one should also consider the additional computational cost associated with an increase in resolution. Doubling N results in a simulation which is approximately 2^4 times more expensive. Regarding the choice between the two types of dissipation we observe that the error is lowest when $\gamma_c \to 0$. The differences with the other values of γ_c are more pronounced for second order DG-FEM. Hence, for this particular flow one should preferably use the central flux or the modified HLLC-flux with a small viscous contribution and use the SGS-model to stabilize the flow. This allows for a best possible prediction of $\widetilde{E}(t)$.

7.6   Summary

In this chapter the effect of numerical viscosity on optimal Smagorinsky constants has been investigated. It was shown that smaller Smagorinsky constants need to be used if more numerical viscosity is introduced by the discretization. Numerical viscosity is typically introduced for stability reasons and to deal with flow discontinuities. A large contribution of the numerical viscosity to the dissipation rate of the resolved kinetic energy will require the use of different SGS-parameters when one tries to optimally capture the resolved kinetic energy given a particular grid resolution.

Optimal Smagorinsky constants have been determined using a database approach [92, 93] for which a large database of LES-data has been created. The results from these simulations are *a-posteriori* compared with DNS-data and optimal Smagorinsky constants c_s^* are identified. Optimal Smagorinsky constants c_s^* correspond to the value of c_s for which the *a-posteriori* error measure $\delta_{\mathrm{L2}}[\widetilde{E}]$ is minimal for a given resolution N and numerical viscosity parameter γ_c. The dependence of the optimal Smagorinsky coefficients on both the resolution as well as the numerical viscosity was shown. The dependence of optimal Smagorinsky coefficients on the resolution suggests the use of smaller Smagorinsky constants at higher resolutions. The dependence of optimal Smagorinsky coefficients on the numerical viscosity also suggests the use of smaller values of c_s when more numerical dissipation is introduced by the discretization. Moreover in case of second order accurate DG-FEM the numerical dissipation can be so dominant that the analysis suggests to abandon SGS-modeling at all for the particular flow under consideration in our analysis. Finally, we were able to show that given a fixed resolution the most optimal approximation of $\widetilde{E}(t)$ was observed when $\gamma_c \approx 0$ and a SGS-model is used to dissipate kinetic energy instead of the numerical viscosity.

Chapter 8

Conclusions and Outlook of LES for complex vortex dominated flows

In section 1.3 the main motivation of this thesis was stated: the application of LES to complex flow. Throughout this thesis we specifically focused our efforts on two specific topics associated with the application of LES to complex flows:

i) The use of LES in combination with a non-uniform grid and/or filter-width.

ii) The use of LES in combination with a discretization based on DG-FEM.

The main findings are summarized in the first part of this chapter. The second part of this chapter consists a feasibility study into applying LES to a turbulent flow over a delta-wing at $Re_c = 100,000$ using DG-FEM.

8.1 Conclusions

Commutator errors

Preferably, in a numerical simulation of complex, turbulent flow a non-uniform grid is adopted. Such a grid allows one to resolve with greater accuracy those parts of the domain in which the flow is really turbulent. In an LES of such a flow one should at the same time adopt a filter-width which is non-uniform; $\Delta(\mathbf{x}, t)$. This, for example, to maintain an approximately constant filter-width over grid

ratio Δ/h. It is well known that with the introduction of a non-uniform filter-width additional SGS-terms emerge. These SGS-terms are generally referred to as commutator errors [46, 51, 54]. For a field f commutator errors are given by,

$$\mathcal{C}_j(f) \;=\; \overline{\partial_j f} - \partial_j \overline{f}. \tag{8.1}$$

Commutator errors $\mathcal{C}_j$ originate from the fact for a non-uniform filter-width filtering $\overline{\cdot}$ and differentiation ∂_j cannot be interchanged.

The commutator error problem has been investigated in chapters 3 and 4. In chapter 3 we investigated the commutator error based on the relation [46, 51, 54];

$$\mathcal{C}_j \sim (\partial_j \Delta)\Delta^{N-1}, \tag{8.2}$$

where N denotes the order of a filter (3.11). This relation suggests that the size of the commutator error is dependent on *i)* the gradient of the filter-width $\partial_j \Delta$ *ii)* the filter-width and *iii)* the order N of the filter. Using *a priori* analysis we have verified the dependence on $\partial_j \Delta$ and showed that for standard, second order filters, such as the top-hat and Gaussian filter, as well as for skewed, first order filters, commutator effects can become dynamically important if filter-width non-uniformities are large.

Higher order filters

The scaling of the commutator error with the order of the filter suggests that commutator errors can be made arbitrary small and safely neglected if an appropriate higher order filter is used. This observation has been made in a number of publications [54, 133] and has led to a considerable interest into the construction of suitable higher order filters [64, 87, 133]. However, in chapter 3 it was shown that this observation is incomplete.

Commutator errors become dynamically less important if higher order filters are used. However, commutator errors cannot be neglected merely by adopting an appropriate higher order filter. This is because the SGS-stress τ_{ij} also scales with the order of the filter as $\tau_{ij} \sim \Delta^N$. Hence the relevant SGS-flux $\partial_j \tau_{ij}$ shows similar scaling behavior as the commutator error: $O((\partial_j \Delta)\Delta^{N-1})$, with a sub-dominant scaling of $O(\Delta^N)$ in case $\partial_j \Delta = 0$. In chapter 3 the scaling with the order of the filter for both the SGS-flux $\partial_j \tau_{ij}$ and the commutator error $\mathcal{C}_j(u_i u_j)$ was shown analytically and subsequently verified *a-priori* using DNS-data of turbulent mixing flow. Because both the SGS-stress and the commutator error scale with the order of the filter, the only independent control over the commutator error is through $\partial_j \Delta$.

Lagrangian interpretation of commutator errors

A new approach towards commutator errors and possible modeling of commutator effects was presented in chapter 4. In this chapter the Lagrangian behavior of the commutator error was introduced. This Lagrangian behavior suggests that commutator error effects only occur if $u_j \partial_j \Delta \neq 0$, i.e., commutator effects can be expected only if the local flow is directed towards the filter-width non-uniformity. Moreover, we motivated that resolved kinetic energy is either created or dissipated through the commutator error if along a flow-path the filter-width is increased or decreased, respectively. Subsequently, a model for the transport of resolved kinetic energy by the commutator error was formulated.

In the formulation of this model for the transport of resolved kinetic energy considerable effort was put in extending the Lagrangian model for skewed (a-symmetric) filters. In case skewed filters are used the commutator error displays both diffusive and dispersive behavior. This is opposed to symmetric filters in which case only diffusive effects arise. The proposed model was verified using DNS-data of temporal mixing. An almost perfect correlation between the model and the actual transport of resolved kinetic energy through the commutator error was observed. The Lagrangian interpretation of the commutator error suggests to model commutator errors using the material derivative of the filter-width $D_t \Delta = (\partial_t + u_j \partial_j)\Delta$ and a subsequent model for the commutator error $\mathcal{C}_j(u_i u_j)$ was formulated (4.26).

Modeling the commutator error

At the end of chapter 4 three different models for the commutator error $\mathcal{C}_j(u_i u_j)$ have been investigated: the similarity, the gradient and the Lagrangian commutator error model. The first two models resemble the similarity and gradient model for the SGS-stress, while the third model directly follows from the Lagrangian behavior of the commutator error. Results of *a-priori* testing of these models showed that the similarity and gradient commutator error model correlate well with the actual commutator error $\mathcal{C}_j(u_i u_j)$. This is more or less expected as high correlation is also observed for similarity type models for the SGS-stress. The correlation of the Lagrangian model is somewhat lower in case of symmetric filters, but high correlation is observed in case skewed filters are used. However, high correlation *a-priori* does not necessarily imply that a model accurately captures the proper dynamics in an LES. Therefore future *a-posteriori* investigations in which the effectiveness of these commutator error models is investigated are highly needed to provide decisive answers.

Computational stress tensor for compressible flow

In chapter 5 the computational turbulent stress tensor ξ_{ij} for *compressible* flow was studied,

$$\xi_{ij} = \overline{\rho u_i u_j} - \overline{\overline{\rho}\widetilde{u}_i\widetilde{u}_j}. \tag{8.3}$$

The computational turbulent stress tensor ξ_{ij} differs from the SGS-stress $\overline{\rho}\tau_{ij}$ (2.31) because of the additional filter is applied to the resolved convective flux $\overline{\rho}\widetilde{u}_i\widetilde{u}_j$. This additional filter arises from the filtering effect of the coarse grid discretization [83, 106]. The main observation made in this chapter is that the computational SGS-stress for compressible flow ξ_{ij} can be decomposed into two different parts,

$$\xi_{ij} = \overline{\rho}(\widetilde{\widetilde{u_iu_j}} - \widetilde{\widetilde{u}_i\widetilde{u}_j}) + \overline{\rho'\widetilde{u}_i\widetilde{u}_j}. \tag{8.4}$$

The first part is primarily associated with the fluctuating velocity $u_i'' = u_i - \widetilde{u}_i$, while the second part is associated with the fluctuating density $\rho' = \rho - \overline{\rho}$.

In the incompressible limit the density fluctuating part $\overline{\rho'\widetilde{u}_i\widetilde{u}_j}$ is negligible as $\rho' \approx 0$ in this limit. However, density fluctuations become more apparent with increasing Mach number and the part associated with the fluctuating density becomes dynamically important with increasing Mach number. Using DNS-data of turbulent flow at various Mach numbers [144] we could observe this dependence of the density fluctuating part on the Mach number. The velocity fluctuating part was almost unaffected by a change in Mach number. It was observed that for supersonic flow $(M = 1.2)$ the relative magnitude of the density fluctuating part could be up to 25% of that of the velocity fluctuating part.

Variational Multi-scale approach to LES

In chapter 6 an alternative formulation of LES based on the variational multi-scale approach to LES (VMS-LES) was introduced. This approach to LES exploits the weak formulation of discretizations such as DG-FEM as well as the inherent projection onto the basis-functions used in this type of discretizations. VMS-LES was originally introduced in [24, 69] for incompressible flow using Fourier-spectral basis-functions. In chapter 6 a VMS-LES formulation for compressible flow was given using general basis-functions. The resulting VMS-LES formulation for compressible flow was shown to resemble the well known compressible LES-formulations [88, 99, 137]. The use of general basis-functions resulted in additional SGS-terms which were shown to be directly related to the commutator error $\mathcal{C}_j$.
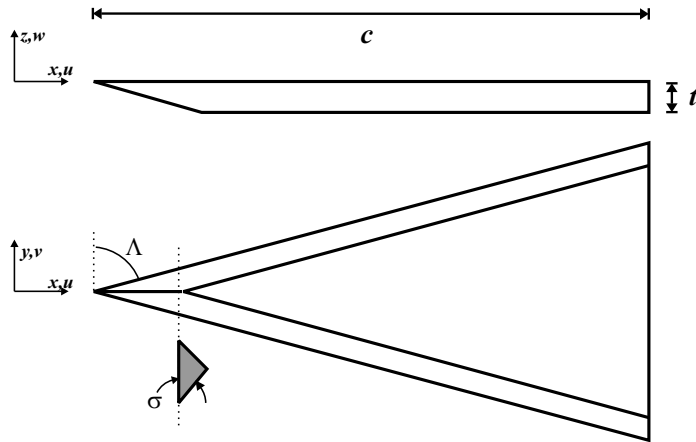
Figure 8.1: Geometry of the delta-wing. For the particular wing considered here $\Lambda = 75°$, $\sigma = 30°$ and $t/c = 0.024$.

Effect of numerical viscosity in LES

In chapter 7 the effect of numerical viscosity in an LES was studied. For stability reasons numerical methods such as DG-FEM incorporate viscous or stabilization terms. These terms can affect the effectiveness of the SGS-modeling in an LES [2]. In particular, in chapter 7 we investigated how the numerical viscosity of a DG-FEM affects the effectiveness of the Smagorinsky SGS-model. A database was created containing a large number of LES using different resolutions, numerical viscosities and Smagorinsky coefficients c_s. We could *a-posteriori* determine optimal Smagorinsky coefficients c_s^* and show that with increasing numerical viscosity other, smaller Smagorinsky coefficients yield a better prediction for the decay of resolved kinetic energy for a given resolution. Moreover, in some cases the numerical viscosity could be so dominant that the analysis suggests to abandon SGS-modeling altogether. Finally, it was shown that the best prediction was possible in case of minimal numerical viscosity in which case the kinetic energy is dissipated through the molecular dissipation and the SGS-model.

8.2   Outlook of LES for complex vortex dominated flows

In this section results are shown of LES for the flow over a delta-wing at high Reynolds number. Based on the experience gained with these simulations we assess the feasibility of LES for such flows. In particular, in this section results are presented of the flow over an 75°-swept delta-wing as illustrated in figure 8.1 at an
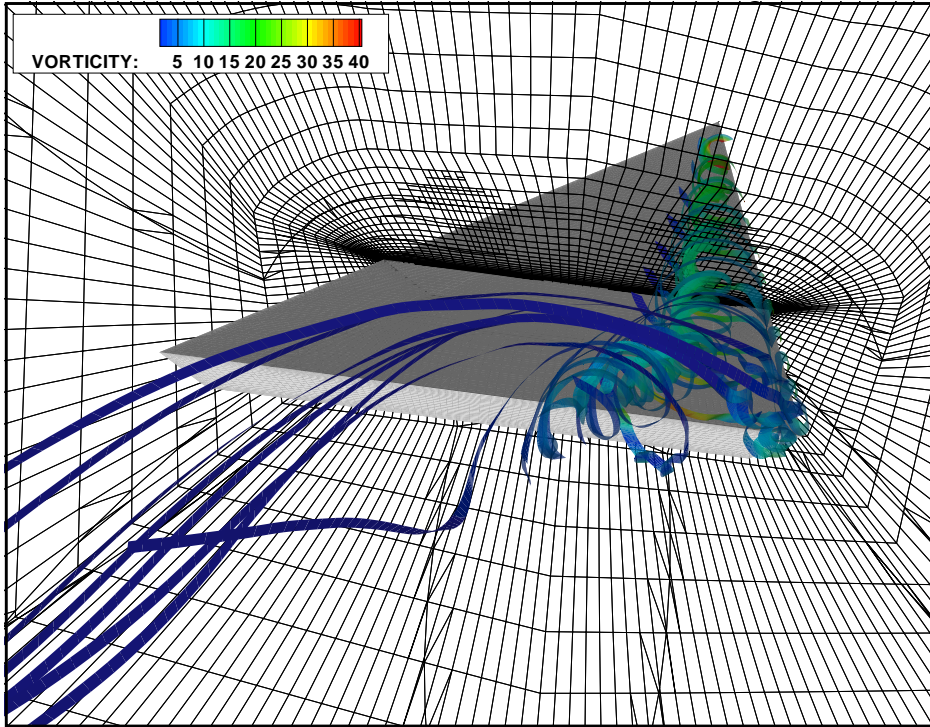
Figure 8.2: Snapshot of the flow over a delta-wing at $Re_c = 100,000$. The slice indicates the refined grid at $x/c = 0.6$ and the coloring of the streamlines indicates the vorticity.

angle of attack of $12.5°$ with $Re_c = 100,000$, $M = 0.3$ and $Pr = 0.72$ [104, 105]. Here Re_c denotes the Reynolds number based on the chord length of the wing [97, 105]. A Smagorinsky SGS-model is used for which the Smagorinsky constant is set to $c_s = 0.075$. The simulations are performed using the program HEXADAP that employs the fully implicit Space-Time DG-FEM (STDG-FEM), see [75, 130] for details. HEXADAP is the second order accurate flow solver developed by the Netherlands Aerospace Institute. An illustration of the resulting flow is given in figure 8.2. We emphasize that the main goal of the present study is to discuss the *technical* feasibility of LES using DG-FEM. Hence, we will not provide extensive comparison with for example experimental results and also we do not touch upon the (in)accuracy of the SGS-modeling for this flow.

Next we will briefly introduce the STDG-FEM algorithm and in particular discuss the pseudo-time stepping procedure (paragraph 8.2.1) [74, 76]. The efficiency of the pseudo-time stepping procedure is of great importance for the total performance of the STDG-FEM algorithm. Subsequently results are presented of simulations of the flow over the delta-wing (paragraph 8.2.2). At the end of this section we will

discuss the main findings (paragraph 8.2.3).

8.2.1 Efficient pseudo-time stepping in Space-Time DG-FEM

Below we will discuss one important component of the STDG-FEM algorithm; the pseudo-time stepping algorithm. STDG-FEM solves the equations directly in four dimensions at once with time as the fourth dimensions and for each time step $[t_n, t_{n+1}]$ a system of non-linear algebraic equations needs to be solved for the expansion coefficient $\hat{\mathbf{U}}^{n+1}$, see [75, 128, 130],

$$\mathcal{L}(\hat{\mathbf{U}}^{n+1}; \hat{\mathbf{U}}^n) \; = \; 0. \tag{8.5}$$

Here $\hat{\mathbf{U}}^n$ and $\hat{\mathbf{U}}^{n+1}$ denote the vector expansion coefficients for the space-time slabs $\Omega \times [t_{n-1}, t_n]$ and $\Omega \times [t_n, t_{n+1}]$, respectively. In (8.5) the expansion coefficients $\hat{\mathbf{U}}^n$ are known and the expansion coefficients $\hat{\mathbf{U}}^{n+1}$ are the unknowns. The full definition of (8.5) can be found in [75]. Notice that (8.5) resembles (2.77) with the exception that in STDG-FEM the part associated with the evolution in time is included in the residuals.

The performance of the STDG-FEM algorithm is largely determined by its ability to efficiently determine $\hat{\mathbf{U}}^{n+1}$. Several strategies are available and we iteratively solve (8.5) in pseudo-time $\tau > 0$,

$$\frac{d\hat{\mathbf{U}}(\tau)}{d\tau} + \frac{1}{\Delta t}\mathcal{L}(\hat{\mathbf{U}}(\tau); \hat{\mathbf{U}}^n) \; = \; 0, \tag{8.6}$$

where in the steady state $\hat{\mathbf{U}}^{n+1} = \hat{\mathbf{U}}$. For the pseudo-time stepping explicit, low-storage Runge Kutta time stepping methods are used. Alternatively, one could solve (8.5) using Newton iterations. However, this requires the storage and computation of a Jacobian matrix which is problematic for large-scale problems. In the steady state $\mathcal{L} = 0$, however, in practice it is not required to reach the steady state exactly and one proceeds to the next implicit time step $[t_{n+1}, t_{n+2}]$ after a predetermined number of pseudo-time steps or as soon as the residuals are sufficiently reduced.

The performance of the total algorithm is greatly affected by its ability to reduce these residuals and the use of suitable Runge-Kutta pseudo-time stepping methods is of critical importance. For the simulations presented in this section use is made of an alternating EXI&EXV scheme. This scheme combines two Runge-Kutta methods, the EXI- and the EXV-scheme. The EXI (EXplicit-Inviscid) scheme is a five stage Runge-Kutta method with a Melson correction [89] which has been optimized for the Euler equations [130]. Due to its time step restrictions, the performance of the EXI scheme for the Navier-Stokes equations is poor. The
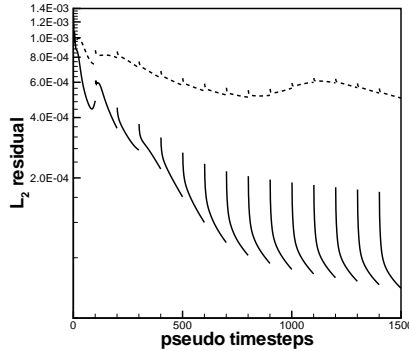
Figure 8.3: L_2-norm of the residual $\mathcal{L}$ when using the EXI scheme (dashed) and the alternating EXI&EXV scheme (solid) for pseudo-time stepping. Several implicit time steps $\Delta t = 0.001$ are shown using 100 pseudo-time steps each and the grid contains approximately 3.5×10^5 elements.

EXV (EXplicit-Viscous) scheme is a four stage method introduced in [76] and specifically constructed to allow large time steps for parabolic problems [74, 76]. In the alternating EXI&EXV scheme we switch between EXI and EXV based on the cell Reynolds number, see [73, 74] for details. The EXI scheme is used for those elements in which convective time step restrictions are most restrictive, while the EXV scheme is used for those elements where viscous time step restrictions are most restrictive. The ability of the pseudo-time stepping algorithm to reduce the residuals was considerably improved with the use of the alternating EXI&EXV scheme.

The effectiveness with which the alternating EXI&EXV scheme can reduce the residuals in comparison with the EXI scheme is illustrated in figure 8.3. In this figure the L_2-norm ε_0 of the residuals $\mathcal{L}$ is shown as a function of the number of pseudo-time steps. In particular ε_0 is shown for a number of implicit physical time steps $\Delta t = 0.001$ each using 100 pseudo-time steps to solve the non-linear algebraic system (8.5) for a grid that contains approximately 3.5×10^5 elements. In figure 8.3 it can be observed that the EXI scheme is only marginally capable of reducing the residuals in 100 pseudo-time steps. The alternating EXI&EXV scheme is considerably more effective in reducing the residuals, greatly increasing the performance of the STDG-FEM algorithm.

Next results are presented of two large-scale simulations of the flow over a delta-wing at $Re_c = 100,000$.

	Simulation A	Simulation B
Reynolds number Re_c	100,000	
Mach number M	0.3	
Smagorinsky constant c_s	0.075	
Time step Δt	0.05	
Pseudo time stepping method	EXI&EXV	
Number of pseudo time steps per time step Δt	100	
Minimal element length	0.005	0.001
Maximum number of elements	3.9×10^5	1.9×10^6
Wall clock hours per time step Δt	4	15

Table 8.1: Simulation details for the high resolution simulations. The wall clock hours are based on four processors on a SGI-Altix 3700 system.

8.2.2   Large-Eddy simulations of the flow over a delta-wing

Two LES of the flow over a delta-wing have been performed and results of these simulations are discussed below. In particular we assess the resolution requirements needed to capture the main vortical flow features above the wing. These provide guidelines along which we assess the feasibility of LES using DG-FEM for this particular flow in subsection 8.2.3.

Two simulations have been carried out and in both simulations the grid is refined based on the vorticity and the grid quality. However, the two simulations differ in terms of the typical element-size h. For the first simulation the smallest elements have a typical element-size of $h_{\min} = 0.005$, while for the second simulation $h_{\min} = 0.001$. We will refer to the simulations as simulation A and simulation B, respectively. The main details of both simulations are gathered in table 8.1 and in figure 8.4 an overview is given of both the grid and the vortical structures in this flow. In this figure one can clearly observe the refinement of the grid near the vortex core.

The complexity of the flow over a delta-wing is mainly due many the different flow regimes that are observed in this flow. Above the wing surface we can distinguish between: *i)* the boundary layer near the wing surface, *ii)* the primary vortices coming from the leading edge, *iii)* the secondary vortices which are formed near the leading edge in between the boundary layer and the leading edge vortex [97]. For a thorough review see [63, 97, 105]. In figure 8.4 an illustration is given of the adapted grid for both simulations and it is indicated which flow phenomena are captured in each simulation.

The secondary vortex near the leading edge is believed to play an important role in the breakdown of the primary vortex [105]. Hence, capturing this secondary vortex
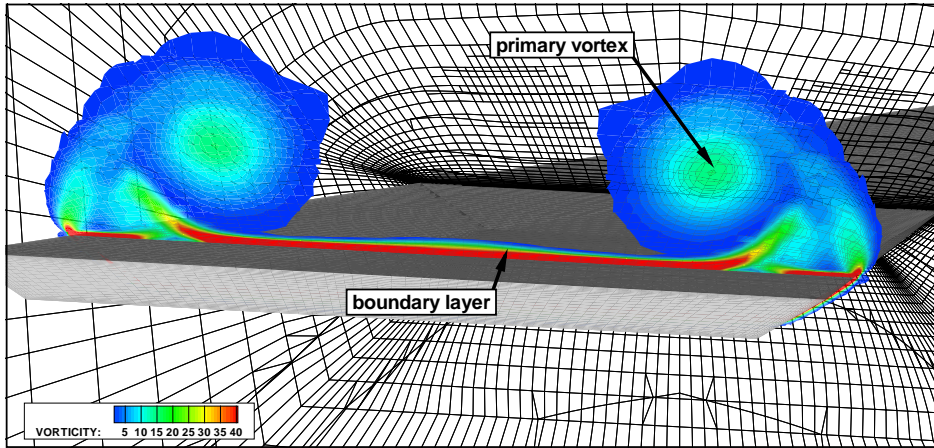
(a)
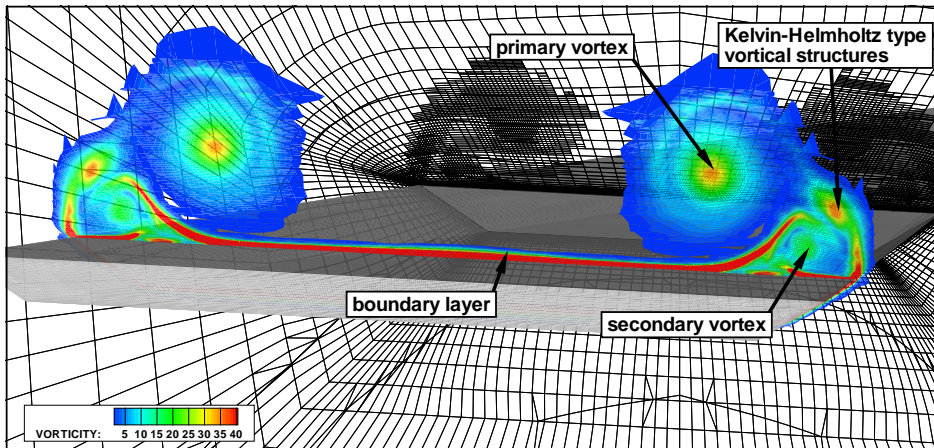
(b)

Figure 8.4: Snapshots of the delta-wing facing the trailing edge with a) $h_{\min} = 0.005$ (Simulation A) and b) $h_{\min} = 0.001$ (Simulation B). Two slices are shown one illustrating the adapted grid and one showing the contours of the vorticity magnitude. The grid-slice corresponds to $x/c = 0.6$ while the contour-slice correspond to $x/c = 0.9$. The labels point to the main flow features captured in these simulations.

is critical. As can be observed in figure 8.4(a) no secondary vortex is observed near the leading edge in simulation A. The minimal grid-distance in simulation B is chosen such that it should be able to capture the secondary vortex and in figure 8.4(b) we clearly observe this secondary vortex. However, the actual breakdown of the vortex is not observed. This can be due to the inaccurate SGS-modeling, insufficient resolution, insufficient pseudo-time steps per implicit time step etc.

Answers to these questions can only be given based on multiple realizations of this flow. This can only be achieved if a simulation can be performed within a workable turn-around time. Based on experiences gained through these two simulations we will next assess what is required before a workable turn-around time is possible.

8.2.3 Discussion of feasibility of large-scale LES of a flow over a 3D delta-wing

Of the two simulations discussed above only simulation B was able to capture the essential flow-features above the delta-wing. Hence we will base our discussion regarding the feasibility of LES using DG-FEM for this particular flow solely on observations made from simulation B. In fact we will determine a turn-around time for this simulation and then discuss which speedup is required to achieve a workable turn-around time.

Presently for a proper assessment of the accuracy of a flow simulation multiple simulations are required adopting various grid resolutions, adaptation criteria and SGS-model coefficients. For unsteady flow, as considered here, results need to be averaged over long time-intervals to get proper statistics. Around 100 time steps appear to be required which corresponds to 10 individual vortex sheddings. Hence including a transition period to steady state at least 250 time steps are required. Based on the wall clock hours per time step as given in table 8.1 such a simulation would have a minimal turn around time of about 5 months on an SGI-Altix 3700 system using four processors.

One weekend (60 hours) is considered to be a workable turn-around time. Hence a speedup by a factor of about 60 is required. This can be achieved in a number of ways. First of all use can be made of more powerful computers. Secondly, we expect that within the near future considerable improvements can be made in the pseudo-time stepping algorithm using, e.g., multi-grid procedures [73, 132].

When using more powerful computers to gain a factor of 60 in performance, presently, one relies on the use of multiple processors [120]. Earlier studies have shown that the parallel speedup of HEXADAP was reasonable [13]. Gaining a factor of 60, however, would require the use of 250-300 processors. This is possible, however it is not certain whether a reasonable speedup is achieved when using such

a large amount of processors. Hence we will also have to rely on improvements in the algorithm.

The performance of the STDG-FEM algorithm is largely determined by the ability of the algorithm to effectively reduce the residuals by means of pseudo-time stepping. Already considerable improvements are made by using the alternating EXI&EXV scheme instead of the EXI scheme. Another improvement appear to results from the use of multi-grid techniques. These have recently become available for STDG-FEM [73, 132]. An expected speedup up to a factor of 4 may be possible and is expected in the near future. In the most optimistic case this would require the use of 60-80 processors on a similar system as the SGI Altix 3700. This is clearly feasible considering present day computing equipment. Still, however, considerable effort needs to be put into validating and improving the SGS-modeling before LES of this type of flows using DG-FEM with locally refined meshes can be performed with sufficient confidence.

Appendix A

Large-eddy template for the Energy equation

The part of the Navier-Stokes operator corresponding to the energy equation is given by,

$$
\begin{aligned}
B_h^{\text{energy}}(\overline{\mathbf{W}}, \mathbf{U}) \;=\; & \left(\overline{W}_4 \Big| \partial_t \rho e\right)_K \\
& -\left(\partial_j \overline{W}_4 \Big| \gamma \rho u_j e - \tfrac{1}{2}(\gamma-1)\rho u_j u_k u_k - u_i \sigma_{ij} + q_j\right)_K \\
& -\left(\overline{W}_4 n_j \Big| \gamma \rho u_j e - \tfrac{1}{2}(\gamma-1)\rho u_j u_k u_k - u_i \sigma_{ij} + q_j\right)_{\partial K}, \quad \text{(A.1)}
\end{aligned}
$$

which is equivalent to,

$$
\begin{aligned}
B_h^{\text{energy}}(\overline{\mathbf{W}}, \mathbf{U}) \;=\; & \left(\overline{W}_4 \Big| \partial_t \overline{\rho e}\right)_K \\
& -\left(\partial_j \overline{W}_4 \Big| \gamma \overline{\rho u_j e} - \tfrac{1}{2}(\gamma-1)\overline{\rho u_j u_k u_k} - \overline{u_i \sigma_{ij}} + \overline{q}_j\right)_K \\
& -\left(\overline{W}_4 n_j \Big| \gamma \rho u_j e - \tfrac{1}{2}(\gamma-1)\rho u_j u_k u_k - u_i \sigma_{ij} + q_j\right)_{\partial K}. \quad \text{(A.2)}
\end{aligned}
$$

The energy is equation is non-linear, but can be written in terms of three variations when expressed in terms of the variables $\mathbf{V} = [\rho, u_i, e]$, i.e.

$$
\begin{aligned}
B_h^{\text{energy}}(\overline{\mathbf{W}}, \mathbf{U}) \;=\; & \mathcal{B}_h^{\text{energy}}(\overline{\mathbf{W}}, \mathbf{V}) & \text{(A.3)} \\
\;=\; & \mathcal{B}_h^{\text{energy}}(\overline{\mathbf{W}}, \widetilde{\mathbf{V}}) + \sum_{k=1}^{3} \mathcal{B}_{h,k}^{\text{energy}}(\overline{\mathbf{W}}, \widetilde{\mathbf{V}}, \mathbf{V}''). & \text{(A.4)}
\end{aligned}
$$

163

The resulting expression is given by,

$$
\begin{aligned}
B_h^{\text{energy}}&(\overline{\mathbf{W}}, \mathbf{U}) \\
&= \left(\overline{W}_4 \Big| \partial_t \overline{\rho e}\right)_K \\
&\quad - \Big(\partial_j \overline{W}_4 \Big| \gamma(\overline{\rho \widetilde{u}_j \widetilde{e}} + \overline{\rho \widetilde{u}_j e''} + \overline{\rho u''_j \widetilde{e}} + \overline{\rho u''_j e''}) \\
&\qquad\quad - \tfrac{1}{2}(\gamma-1)(\overline{\rho \widetilde{u}_j \widetilde{u}_k \widetilde{u}_k} + 2\overline{\rho \widetilde{u}_j \widetilde{u}_k u''_k} + \overline{\rho u''_j \widetilde{u}_k \widetilde{u}_k} \\
&\qquad\qquad\qquad + \overline{\rho \widetilde{u}_j u''_k u''_k} + 2\overline{\rho u''_j u''_k \widetilde{u}_k} + \overline{\rho u''_j u''_k u''_k}) \\
&\qquad\quad - \overline{\widetilde{u}_i \breve{\sigma}_{ij}} - \overline{\widetilde{u}_i \dot{\sigma}_{ij}} - \overline{u''_i \breve{\sigma}_{ij}} - \overline{u''_i \dot{\sigma}_{ij}} + \overline{\breve{q}}_j + \overline{\dot{q}}_j + \overline{\ddot{q}}_j\Big)_K \\
&\quad - \Big(\overline{W}_4 n_j \Big| \gamma(\rho \widetilde{u}_j \widetilde{e} + \rho \widetilde{u}_j e'' + \rho u''_j \widetilde{e} + \rho u''_j e'') \\
&\qquad\quad - \tfrac{1}{2}(\gamma-1)(\rho \widetilde{u}_j \widetilde{u}_k \widetilde{u}_k + 2\rho \widetilde{u}_j \widetilde{u}_k u''_k + \rho u''_j \widetilde{u}_k \widetilde{u}_k \\
&\qquad\qquad\qquad + \rho \widetilde{u}_j u''_k u''_k + 2\rho u''_j u''_k \widetilde{u}_k + \rho u''_j u''_k u''_k) \\
&\qquad\quad \widetilde{u}_i \breve{\sigma}_{ij} + \widetilde{u}_i \dot{\sigma}_{ij} + u''_i \breve{\sigma}_{ij} + u''_i \dot{\sigma}_{ij} + \breve{q}_j + \dot{q}_j + \ddot{q}_j\Big)_{\partial K}, \qquad \text{(A.5)}
\end{aligned}
$$

where $\breve{\sigma}_{ij}$ and $\breve{q}_j$ are the viscous and heat flux evaluated using resolved variables $\widetilde{\mathbf{U}}$, $\dot{\sigma}_{ij}$ is the first variation of the viscous flux, which is defined in (6.58), and finally $\dot{q}_j$ and $\ddot{q}_j$ are the first and second variation of the heat flux, respectively,

$$
\dot{q}_j = \frac{\gamma}{RePr}\partial_j(e'' - \widetilde{u}_k u''_k), \quad \ddot{q}_j = -\frac{\gamma}{RePr}\partial_j \tfrac{1}{2}u''_k u''_k. \qquad \text{(A.6)}
$$

In order to express B^{energy} in terms of the resolved variables, i.e. $B_h^{\text{energy}}(\overline{\mathbf{W}}, \overline{\mathbf{U}})$ we have to decompose the density ρ into $\overline{\rho} + \rho'$ for all the non-linear terms $\rho \widetilde{u}_j \widetilde{e}$ and $\rho \widetilde{u}_j \widetilde{u}_k \widetilde{u}_k$. Then we arrive at,

$$
\begin{aligned}
B_h^{\text{energy}}&(\overline{\mathbf{W}}, \mathbf{U}) \\
&= B_h^{\text{energy}}(\overline{\mathbf{W}}, \overline{\mathbf{U}}) \\
&\quad - \Big(\partial_j \overline{W}_4 \Big| \gamma(\overline{\rho' \widetilde{u}_j \widetilde{e}} + \overline{\rho \widetilde{u}_j e''} + \overline{\rho u''_j \widetilde{e}} + \overline{\rho u''_j e''}) \\
&\qquad\quad - \tfrac{1}{2}(\gamma-1)(\overline{\rho' \widetilde{u}_j \widetilde{u}_k \widetilde{u}_k} + 2\overline{\rho \widetilde{u}_j \widetilde{u}_k u''_k} + \overline{\rho u''_j \widetilde{u}_k \widetilde{u}_k} \\
&\qquad\qquad\qquad + \overline{\rho \widetilde{u}_j u''_k u''_k} + 2\overline{\rho u''_j u''_k \widetilde{u}_k} + \overline{\rho u''_j u''_k u''_k}) \\
&\qquad\quad - \overline{\widetilde{u}_i \dot{\sigma}_{ij}} - \overline{u''_i \breve{\sigma}_{ij}} - \overline{u''_i \dot{\sigma}_{ij}} + \overline{\dot{q}}_j + \overline{\ddot{q}}_j\Big)_K \\
&\quad - \Big(\overline{W}_4 n_j \Big| \gamma(\rho' \widetilde{u}_j \widetilde{e} + \rho \widetilde{u}_j e'' + \rho u''_j \widetilde{e} + \rho u''_j e'') \\
&\qquad\quad - \tfrac{1}{2}(\gamma-1)(\rho' \widetilde{u}_j \widetilde{u}_k \widetilde{u}_k + 2\rho \widetilde{u}_j \widetilde{u}_k u''_k + \rho u''_j \widetilde{u}_k \widetilde{u}_k \\
&\qquad\qquad\qquad + \rho \widetilde{u}_j u''_k u''_k + 2\rho u''_j u''_k \widetilde{u}_k + \rho u''_j u''_k u''_k) \\
&\qquad\quad + \widetilde{u}_i \dot{\sigma}_{ij} + u''_i \breve{\sigma}_{ij} + u''_i \dot{\sigma}_{ij} + \breve{q}_j + \dot{q}_j + \ddot{q}_j\Big)_{\partial K}. \qquad \text{(A.7)}
\end{aligned}
$$

Bibliography

[1] M. Abramovitz and I. A. Stegun. *Handbook of Math Functions with Formulas, Graphs and Mathematical Table.* Dover Publications, New York, 1965.

[2] N. A. Adams, S. Hickel, and S. Franz. Implicit subgrid-scale modeling by adaptive deconvolution. *J. Comput. Phys.*, 200:412–431, 2004.

[3] M. Ainsworth. Dispersive and dissipative behavior of high order discontinuous Galerkin finite element methods. *J. Comput. Phys.*, 198:106–130, 2004.

[4] J. D. Anderson. *Fundamentals of aerodynamics.* McGraw-Hill, New York, 1991.

[5] D. Arnold, F. Brezzi, B. Cockburn, and D. Marini. Unified analysis of discontinuous Galerkin methods for elliptic problems. *SIAM J. Numer. Anal.*, 39:1749–1779, 2002.

[6] D. N. Arnold. An interior penalty finite element method with discontinuous elements. *SIAM J. on Num. Anal.*, 19(4):742–760, 1982.

[7] J. Bardina, J. H. Ferziger, and W. C. Reynolds. Improved turbulence models based on LES of homogeneous incompressible turbulent flows. Technical report No. TF-19, Department of Mechanical Engineering, Stanford University, Stanford, 1984.

[8] F. Bassi, A. Crivellini, S. Rebay, and M. Savini. Discontinuous Galerkin solution of the Reynolds-averaged Navier-Stokes and k-ω turbulence model equations. *Comput. Methods in Appl. Mech. Eng.*, 34:507–540, 2004.

[9] F. Bassi and S. Rebay. A high-order accurate discontinuous finite element method for the numerical solution of the compressible Navier-Stokes equations. *J. Comput. Phys.*, 131:267–279, 1997.

[10] F. Bassi, S. Rebay, G. Mariotti, S. Pedinotti, and M. Savini. A high-order accurate discontinuous finite element method for inviscid and viscous turbomachinery flows. In R. Decuypere and G. Dibelius, editors, *Proceedings of 2nd European Conference on Turbomachinery, Fluid Dynamics and Thermodynamics*, Antwerpen, Belgium, 1997.

[11] P. Batten, N. Clarke, C. Lambert, and D. M. Causon. On the choice of wavespeeds for the HLLC Riemann solver. *SIAM J. of Sci. Comput.*, 18(6):1553–1570, 1997.

[12] J. P. Boris, F. F. Grinstein, E. S Oran, and R. L. Kolbe. New insights into large-eddy simulation. *Fluid Dyn. Res.*, 10:199–228, 1992.

[13] E. G. Bouwman. Rotor blade modeling. Master's thesis, University of Twente, 2002.

[14] M. Braack and E. Burman. Local projection stabilization for the Oseen problem and its interpretation as a variational multiscale method. *SIAM J. on Num. Anal.*, 43(6):2544–2566, 2006.

[15] F. Brezzi, G. Manzini, D. Marini, P. Pietra, and A. Russo. Discontinuous finite elements for diffusion problems. In *Atti Convegno in onore di F. Brioschi*, pages 197–217, Milan, Italy, 1999.

[16] F. Brezzi, G. Manzini, D. Marini, P. Pietra, and A. Russo. Discontinuous Galerkin approximations for elliptic problems. *Numer. Methods Partial Diff. Eqn.*, 16(4):365–378, 2000.

[17] C. Brun and R. Friedrich. Modeling the SGS tensor T_{ij}: An issue in the dynamic approach. *Phys. Fluids*, 13(8):2373–2385, 2001.

[18] R. Bustinza and G. N. Gatica. An local discontinuous Galerkin method for nonlinear diffusion problems with mixed boundary conditions. *SIAM J. of Sci. Comput.*, 26(1):152–177, 2004.

[19] R. Bustinza, G. N. Gatica, and B. Cockburn. An a posteriori error estimate for the local discontinuous Galerkin method applied to linear and nonlinear diffusion problems. *J. of Sci. Comput.*, 22/23:147–185, 2005.

[20] S. Camarri, M. V. Salvetti, B. Koobus, and A. Dervieux. A low-diffusion MUSCL scheme for LES on unstructured grids. *Comp. & Fluids*, 33:1101–1129, 2004.

[21] D. Carati, G. S. Winckelmans, and H. Jeanmart. On the modeling of the subgrid-scale and filtered-scale stress tensors in large-eddy simulation. *J. Fluid Mech.*, 441:119–138, 2001.

[22] F. K. Chow and P. Moin. A further study of numerical errors in large-eddy simulations. *J. Comput. Phys.*, 184(2):366–380, 2003.

[23] R. A. Clark, J. H. Ferziger, and W. C. Reynolds. Evaluation of subgrid-scale models using an accurately simulated turbulent flow. *J. Fluid Mech.*, 91:1–16, 1979.

[24] S. S. Collis. Monitoring unresolved scales in multiscale turbulence modeling. *Phys. Fluids*, 13(6):1800–1806, 2001.

[25] S. S. Collis. Discontinuous Galerkin methods for turbulence simulation. *CTR: Proc. summer program 2002*, pages 155–167, 2002.

[26] I. Daubechies. *Ten lectures on Wavelets*. SIAM, Philadelphia, 1992.

[27] J. J. W. Van der Vegt and J. J. Sudirham. A Space-Time Galerkin method for the time-dependent Oseen equations. *Submitted to Appl. Num. Math.*, 2006.

[28] J. J. W. Van der Vegt and S. K. Tomar. Discontinuous Galerkin Methods for Linear Free-Surface Gravity Waves. *J. of Sci. Comput.*, 22/23:531–567, 2005.

[29] A. Dunca, V. John, and W. J. Layton. The commutation error of the space averaged Navier-Stokes equation on a bounded domain. *J. Math. Fluid Mech.*, pages 53–78, 2004.

[30] G. Erlebacher, M. Hussaini, C. Speziale, and T. Zang. Toward the large-eddy simulation of compressible turbulent flows. *J. Fluid Mech.*, 238:155–185, 1992.

[31] A. Favre. Équation des gaz turbulents compressible. I. Formes générales. *J. Mécanique*, 4:361–390, 1965.

[32] A. Favre. Équation des gaz turbulents compressible. II. Méthode des vitesses moyennes; méthode des vitesses macroscopiques pondérées par la masse volumique. *J. Mécanique*, 4:391–421, 1965.

[33] A. Favre. Turbulence: space-time statistical properties and behavior in supersonic flows. *Phys. Fluids*, 26(10):2851–2863, 1983.

[34] L. Ferracina and M. N. Spijker. An extension and analysis of the Shu-Osher representation of Runge-Kutta methos. *Math. of Comp.*, 74(249):201–219, 2004.

[35] L. Ferracina and M. N. Spijker. Stepsize restrictions for the total-variation-diminishing property in general Runge-Kutta methos. *SIAM J. on Num. Anal.*, 42(3):1073–1093, 2004.

[36] C. Foias, O. Manley, R. M. S. Rosa, and R. Temam. *Navier-Stokes equations and turbulence*, volume 83 of *Encyclopedia of Mathematics and its Applications*. Cambridge University Press, New York, 2001.

[37] J. Franke and W. Frank. Temporal Commutation Errors in Large-Eddy Simulation. *Zeitschrift für angewandt mathematik und mechanik*, supplement 3:S467–S468, 2001.

[38] C. Fureby and G. Tabor. Mathematical and Physical Constraints of Large-Eddy Simulation. *Theoret. Comput. Fluid Dyn.*, 9:85–102, 1997.

[39] M. Germano. Turbulence: the filtering approach. *Phys. Fluids A*, 238:325–336, 1992.

[40] M. Germano, U. Piomelli, P. Moin, and W. H. Cabot. A dynamic subgrid-scale model. *Phys. Fluids A*, 3(7):1760–1765, 1991.

[41] B. J. Geurts. Inverse Modeling for Large-Eddy Simulation. *Phys. Fluids*, 9(12):3585–3587, 1997.

[42] B. J. Geurts and J. Fröhlich. A framework for predicting accuracy limitations in large-eddy simulation. *Phys. Fluids*, 14:L41–L44, 2002.

[43] B. J. Geurts and D. D. Holm. Regularization modeling for large-eddy simulation. *Phys. Fluids*, 15(1):L13–L16, 2003.

[44] B. J. Geurts and D. D. Holm. Commutator errors in large-eddy simulation. *J. Phys. A: Math. Gen.*, 39:1–17, 2006.

[45] B. J. Geurts and F. van der Bos. Numerically induced high-pass dynamics in large-eddy simulation. *Phys. Fluids*, 17(125103), 2005.

[46] B.J. Geurts. Balancing errors in LES. In P.R. Voke, N.D. Sandham, and L. Kleiser, editors, *Direct and Large-Eddy Simulation III*, pages 1–12, Cambridge, 1999. Kluwer Academic Publishers.

[47] B.J. Geurts. How can we make Large Eddy Simulation to fulfill its promise? In R. Friedrich and W. Rodi, editors, *Advances in LES of complex flows*, pages 13–32. Kluwer Academic Publishers, Dordrecht, 2002.

[48] B.J. Geurts. *Elements of Direct and Large-Eddy Simulation*. R.T. Edwards, Inc., Philadelphia, 2003.

[49] B.J. Geurts and D.D. Holm. Alpha-modeling strategy for LES of turbulent mixing. In D. Drikakis and B.J.Geurts, editors, *Turbulent low computations*, chapter 7. Kluwer Academic Publishers, 2002.

[50] B.J. Geurts, A.W. Vreman, and J.G.M. Kuerten. Comparison of DNS and LES of transitional and turbulent compressible flow: flat plate and mixing layer. In *74th Fluid Dynamics Panel and Symposium on Application of DNS and LES to transition and turbulence*, page 551, 1994.

[51] B.J. Geurts, A.W. Vreman, J.G.M. Kuerten, and R. van Buuren. Noncommuting filters and dynamic modeling for LES of turbulent compressible flow in 3D shear layers. In J.P. Chollet, P.R. Voke, and L. Kleiser, editors, *Direct and Large-Eddy simulation II*, pages 47–56, Dordrecht, 1997. Kluwer Academic Publishers.

[52] S. Ghosal. Mathematical and Physical Constraints on Large-Eddy Simulation. *AIAA Journal*, 37(4):425–433, 1999.

[53] S. Ghosal. Analysis and control of errors in the numerical simulation of turbulence. In D. Drikakis and B.J.Geurts, editors, *Turbulent flow computations*, chapter 4, pages 101–140. Kluwer Academic Publishers, 2002.

[54] S. Ghosal and P. Moin. The Basic Equations for the Large Eddy Simulation of Turbulent Flows in Complex Geometry. *J. Comput. Phys.*, 118:24–37, 1995.

[55] R. E. Gordnier and M. R. Visbal. Compact difference scheme applied to simulation of low-sweep delta wing flow. *AAIA J.*, 8:1744–1752, 2005.

[56] S. Gottlieb, C. W. Shu, and E. Tadmor. Strong-Stability-Preserving high-order time discretization methods. *SIAM Rev.*, 43:89–122, 2001.

[57] F. F. Grinstein and C. Fureby. Recent progress on MILES for high reynolds number flows. *J. Fluids Eng.*, 124:848–861, 2002.

[58] F. F. Grinstein, C. Fureby, and C. R. DeVore. On MILES based on flux-limiting algorithms. *Int. J. for Num. Meth. in Fluids*, 47:1043–1051, 2005.

[59] J. L. Guermond and S. Prudhomme. On the construction of suitable solutions to the Navier Stokes equations and questions regarding the definition of large eddy simulation. *Physics D*, 207:64–78, 2005.

[60] J. Gullbrand. Explicit filtering and subgrid-scale models in turbulent channel flow. *CTR: Annual research briefs*, page 31, 2001.

[61] J. Gullbrand. Dynamic modeling of large-eddy simulation of turbulent channel flow: Investigation of two-dimensional versus three-dimensional test filtering. *Int. J. of Num meth. for Heat & Fluid flow*, 14(4):467–492, 2004.

[62] J. Gullbrand and F. K. Chow. The effect of numerical errors and turbulence models in large-eddy simulation of turbulent channel flow, with and without explicit filtering. *J. Fluid Mech.*, 495:323–341, 2003.

[63] I. Gursul, M. R. Allan, and K. J. Badcock. Opportunities for the intergrated use of measurements and computation for the understanding of delta wing aerodynamics. *Aerosp. Sc. and Techn.*, 9:181–189, 2005.

[64] A. Haselbacher and O. V. Vasilyev. Commutative discrete filtering on unstructured grids based on least-squares techniques. *J. Comput. Phys.*, 187(1):197–211, 2003.

[65] G. Hauke and T. J. R. Hughes. A comparative study of different sets of variables for solving compressible and incompressible flows. *Comput. Methods in Appl. Mech. Eng.*, 153:1–44, 1998.

[66] J. Hoffman and C. Johnson. A new approach to computational turbulence modeling. *Comput. Methods in Appl. Mech. Eng.*, 2006. in press.

[67] K. Horiuti. Rotational transformation and geometrical correlation of SGS models. *ERCOFTAC Bulletin*, 48:25–28, 2001.

[68] F. Q. Hu and H. L. Atkins. Eigensolution analysis of the Discontinuous Galerkin method with non-uniform grids. *J. Comput. Phys.*, 182:516–545, 2002.

[69] T. J. R. Hughes, L. Mazzei, and K. E. Jansen. Large eddy simulation and the variational multiscale method. *Computing and visualization in science*, 3:47–59, 2001.

[70] T. J. R. Hughes, L. Mazzei, and A. A. Oberai. The multiscale formulation of large eddy simulation: Decay of homogeneous isotropic turbulence. *Phys. Fluids*, 13(2):505–512, 2001.

[71] T. J. R. Hughes, A. A. Oberai, and L. Mazzei. Large eddy simulation of turbulent channel flows by the variational multiscale method. *Phys. Fluids*, 13(6):1784–1799, 2001.

[72] M. Iovieno and D. Tordella. Variable scale filtered Navier-Stokes equations: A new procedure to deal with the associated commutation error. *Phys. Fluids*, 15(7):1926–1936, 2003.

[73] C. M. Klaij. *Space-Time DG-FEM for complex flows.* Phd. thesis, University of Twente Enschede, 2006.

[74] C. M. Klaij, J. J. W. van der Vegt, and H. van der Ven. Pseudo-time stepping methods for space-time discontinuous Galerkin discretizations of the compressible Navier-Stokes equations. *In press J. Comput. Phys.*, 2006.

[75] C. M. Klaij, J. J. W. van der Vegt, and H. van der Ven. Space-time discontinuous Galerkin method for the compressible Navier-Stokes equations. *In press J. Comput. Phys.*, 2006.

[76] W. L. Kleb, W. A. Wood, and B. van Leer. Efficient multi-stage time marching for viscous flows via local preconditioning. In *AIAA 14th Computational Fluid Dynamics Conference*, pages 8–34, 1999.

[77] B. Koobus and C. Farhat. A variational multiscale method for large eddy simulation of compressible turbulent flow on unstructured meshed - application to vortex shedding. *Comput. Methods in Appl. Mech. Eng.*, 193:1367–1383, 2004.

[78] A. K. Kuczaj and B. J. Geurts. Mixing in manipulated turbulence. *J. of Turbulence*, 2006. to appear.

[79] S. K. Lele. Compressibility effects on turbulence. *Annu. Rev. Fluid Mech.*, 26:211–254, 1994.

[80] R.J. LeVeque. *Numerical methods for conservation laws.* Birkhäuser Verlag, Basel, Switzerland, 1992.

[81] D. K. Lilly. The representation of small-scale turbulence in numerical simulation experiments. In H. H. Goldstine, editor, *Proc. IBM scientific computing Symp. on Environmental Sciences*, pages 195–210, Yorktown Heights, NY, 1967.

[82] S. Liu, C. Meneveau, and J. Katz. On the properties of similarity subgrid-scale models as deduced from measurements in a turbulent jet. *J. Fluid Mech.*, 275:83–119, 1994.

[83] T. S. Lund. The use of explicit filters in Large Eddy simulation. *Computers & mathematics with application*, 46:603–616, 2003.

[84] T. S. Lund and H. J. Kaltenbach. Experiments with explicit filtering for LES using a finite-difference methods. *CTR: Annual research briefs*, pages 91–105, 1995.

[85] L. G. Margolin and W. J. Rider. A rationale for implicit turbulence modeling. *Int. J. for Num. Meth. in Fluids*, 39:821–841, 2002.

[86] L. G. Margolin and W. J. Rider. The design and construction of implicit LES models. *Int. J. for Num. Meth. in Fluids*, 47:1173–1179, 2005.

[87] A. L. Marsden, O. V. Vasilyev, and P. Moin. Construction of commutative filters for LES on unstructured meshes. *CTR: Annual research briefs*, page 179, 2000.

[88] M. P. Martin, U. Piomelli, and G. V. Candler. Subgrid-scale models for compressible large-eddy simulations. *Theor. and Comp. Fluid Dyn.*, 13:361–376, 2000.

[89] N. D. Melson, M. D. Sanetrik, and H. L. Atkins. Time-accurate Navier-Stokes calculations with multigrid acceleration. In *Proc. 6th Copper Mountain conference on multigrid methods*, 1993.

[90] C. Meneveau. Statistics of turbulence subgrid-scale stresses: Necessary conditions and experimental tests. *Phys. Fluids*, 6:815–833, 1994.

[91] C. Meneveau and J. Katz. Scale-invariance and turbulence models for large-eddy simulation. *Annu. Rev. Fluid Mech.*, 32:1–32, 2000.

[92] J. Meyers, B. J. Geurts, and M. Baelmans. Database-analysis of errors in large-eddy simulations. *Phys. Fluids*, 15:2740–2755, 2003.

[93] J. Meyers, B. J. Geurts, and M. Baelmans. Optimality of the dynamic procedure for large-eddy simulation. *Phys. Fluids*, 17(045108), 2005.

[94] P. Moin and J. Kim. Tackling turbulence with supercomputers. *Sc. American*, 276(1):46–52, 1997.

[95] P. Moin, K. Squires, W. Cabot, and S. Lee. A dynamic subgrid-scale model for compressible turbulence and scalar transport. *Phys. Fluids A*, 3(11):2746–2757, 1991.

[96] B. Mols. Bellen blazen in bits en bytes. *Natuur & Techniek*, 10:53, 2000.

[97] S. Morton, J. Forsyth, A. Mitchel, and D. Hajek. Detached-Eddy Simulation and Reynolds Averaged Navier Stokes simulation of Delta Wing vortical flowfields. *J. of Fluid Engineering-Transactions of the ASME*, 124(4):924–932, 2002.

[98] F. T. M. Nieuwstadt. *Turbulentie*. Epsilon Uitgaven, Utrecht, The Netherlands, 1998.

[99] U. Piomelli. Large-eddy simulation: achievements and challenges. *Prog. in Aerosp. Sc.*, 35:335–362, 1999.

[100] M. Polner. *Galerkin least-squares stabilization operators for the Navier-Stokes equations. A unified approach.* Phd. thesis, University of Twente Enschede, 2005.

[101] S. B. Pope. Ten questions concerning the large-eddy simulation of turbulent flows. *New J. of Phys.*, 6(35):1–23, 2004.

[102] S.B. Pope. *Turbulent Flows.* Cambridge University Press, Cambridge, UK, 2000.

[103] S. Ramakrishnan and S. S. Collis. The local variational multi-scale method for turbulence simulation. Technical Report SAND2005-2733, Sandia National Laboratories, Springfield VA, USA, 2005.

[104] A. J. Riley. *Vortical flow over delta wings.* Phd-thesis, University of Bristol, 1996.

[105] A. J. Riley and M. V. Lowson. Development of a three dimensional free shear layer. *J. Fluid Mech.*, 369:49–89, 1998.

[106] R. S. Rogallo and P. Moin. Numerical simulation of turbulent flow. *Ann. Rev. Fluid Mech.*, 16:99–137, 1984.

[107] P. Sagaut. *Large eddy simulation for incompressible flows; an introduction.* Scientific Computation. Springer Verlag, 2001.

[108] U. Schumann. Subgrid scale model for finite difference simulations of turbulents flow in plane channels and annuli. *J. Comput. Phys.*, 18:376–404, 1975.

[109] U. Schumann. Direct and large eddy simulation of turbulence - summary of the state-of-the-art 1991. In *Introduction to the modeling of turbulence*, Von Karman Institute, Brussels, 1991.

[110] C. W. Shu. A survey of strong stability preserving high order time discretizations. In D. Estep and S. Tavener, editors, *Collected Lectures on the Preservation of Stability Under Discretization*, chapter 4, pages 51–65. SIAM, 2002.

[111] J. Smagorinsky. General circulation experiments with the primitive equations. *Mon. Weather Rev.*, 91:99–164, 1963.

[112] J. Smagorinsky. Some historical remarks on the use of nonlinear viscosities. In *Large Eddy Simulation of Complex Engineering and Geophysical Flows*, pages 3–36. Cambridge University Press, 1993.

[113] C. G. Speziale. Galilean invariance of subgrid-scale stress models in the large-eddy simulation of turbulence. *J. Fluid Mech.*, 156:55–62, 1985.

[114] R. J. Spiteri and S. J. Ruuth. A new class of optimal high-order strong-stability-preserving time discretization methods. *SIAM J. Numer. Anal.*, 40(2):469–491, 2002.

[115] G. De Stefano and O. V. Vasilyev. "Perfect" modeling framework for dynamic SGS model testing in large-eddy simulation. *Theor. and Comp. fluid Dyn.*, 18(1):27–41, 2004.

[116] S. Stolz and N. A. Adams. An approximate deconvolution procedure for large eddy simulation. *Phys. Fluids*, 11(7):1699–1701, 1999.

[117] S. Stolz, N. A. Adams, and L. Kleiser. The approximate deconvolution model for large-eddy simulation of compressible flows and its application to shock-turbulent-boundary-layer interaction. *Phys. Fluids*, 13(10):2985–3001, 2001.

[118] S. Stolz, N. A. Adams, and L. Kleiser. An approximate deconvolution model for large eddy simulation with application to incompressible wall-bounded flows. *Phys. Fluids*, 13(4):997–1015, 2001.

[119] J. J. Sudirham. *Space-time discontinuous Galerkin methods for convection-diffusion problems : application to wet-chemical etching*. Phd. thesis, University of Twente Enschede, 2005.

[120] *27th Edition of TOP500 List of World's Fastest Supercomputers Released: DOE/LLNL BlueGene/L and IBM gain Top Positions*. www.top500.org, June 2006. Press Release.

[121] E.F. Toro. *Riemann solvers and numerical methods for fluid dynamics. A practical introduction*. Springer Verlag, 1997.

[122] F. van der Bos and B. J. Geurts. Commutator-errors in the filtering approach to large-eddy simulation. *Phys. Fluids*, 17(035108), 2005.

[123] F. van der Bos and B. J. Geurts. Lagrangian dynamics of commutator-errors in large-eddy simulation. *Phys. Fluids*, 17(075101), 2005.

[124] F. van der Bos and B. J. Geurts. Computational turbulent stress closure for large-eddy simulation of compressible flow. *J. of Turbulence*, 7(9):1–16, 2006.

[125] F. van der Bos and B.J. Geurts. Dynamics of commutator-errors in LES with non-uniform filter-width. In R. Friedrich, B.J. Geurts, and O. Metais, editors, *Direct and Large-Eddy simulation V*, pages 155–162, Dordrecht, 2004. Kluwer Academic Publishers.

[126] F. van der Bos, B. Tao, C. Meneveau, and J. Katz. Effects of small-scale turbulent motions on the filtered velocity gradient tensor as deduced from holographic particle image velocimetry measurements. *Phys. Fluids*, 14(7), 2002.

[127] F. van der Bos, J.J.W. van der Vegt, and B.J. Geurts. Variational multi-scale formulation for compressible flows in discontinuous Galerkin context. *Comput. Methods in Appl. Mech. Eng.*, 2005. submitted.

[128] J. J. W. van der Vegt, C. M. Klaij, H. van der Ven, and F. van der Bos. Space-time Discontinuous Galerkin method for the Compressible Navier-Stokes equations on Deforming Meshes. In P. Wesseling, E. O nate, and J. Périaux, editors, *Proceedings European Conference on Computational Fluid Dynamics ECCOMAS CFD 2006, TU Delft, The Netherlands, September 5-8, 2006*, 2006.

[129] J. J. W. van der Vegt and H. van der Ven. Discontinuous Galerkin finite element method with anisotropic local grid refinement for inviscid compressible flows. *J. Comput. Phys.*, 141(1):46–77, 1998.

[130] J. J. W. van der Vegt and H. van der Ven. Space-time discontinuous Galerkin finite element method with dynamic grid motion for compressible flow: Part I General formulation. *J. Comput. Phys.*, 182(2):546–585, 2002.

[131] H. van der Ven. A family of large eddy simulations LES filters with nonuniform filter widths. *Phys. Fluids*, 7(5):1171–1172, 1995.

[132] M. H. van Raalte and C. M. Klaij. Runge-Kutta multigrid analysis for space-time discontinuous Galerkin discretization of an advection-diffusion equation. *Submitted to SIAM J. Sci. Comput.*, 2006.

[133] O. V. Vasilyev, T. S. Lund, and P. Moin. A General Class of Commutative Filters for LES in Complex Geometries. *J. Comput. Phys.*, 146:82–104, 1998.

[134] A. W. Vreman. The filtering analog of the variational multiscale method in large-eddy simulation. *Phys. Fluids*, 15(8):L61–L64, 2003.

[135] A. W. Vreman. The adjoint filter operator in large-eddy simulation for turbulent flow. *Phys. Fluids*, 16:2012–2022, 2004.

[136] A. W. Vreman. An eddy-viscosity subgrid-scale model for turbulent shear flow: Algebraic theory and applications. *Phys. Fluids*, 16:3670–3681, 2004.

[137] A. W. Vreman, B. J. Geurts, and H. Kuerten. A priori tests of Large Eddy simulation of the compressible plane mixing layer. *J. Eng. Math.*, 29:299–327, 1995.

[138] A. W. Vreman, B. J. Geurts, and H. Kuerten. Shocks in direct numerical simulation of the confined three-dimensional mixing layer. *Phys. Fluids*, 7:2105, 1995.

[139] A. W. Vreman, B. J. Geurts, and H. Kuerten. Subgrid-Modeling in LES of Compressible Flow. *Appl. Sc. Res.*, 54:191–203, 1995.

[140] A. W. Vreman, B. J. Geurts, and H. Kuerten. Comparison of numerical schemes in large-eddy simulation of the temporal mixing layer. *Int. J. for Num. Meth. in Fluids*, 22(4):297–311, 1996.

[141] A. W. Vreman, B. J. Geurts, and H. Kuerten. Large-eddy simulation of the turbulent mixing layer. *J. Fluid Mech.*, 339:357–390, 1997.

[142] A. W. Vreman, B. J. Geurts, and J. G. M. Kuerten. Realizability Conditions for the turbulent stress tensor in Large Eddy Simulation. *J. Fluid Mech.*, 278:351–362, 1994.

[143] A. W. Vreman, N. D. Sandham, and K. H. Luo. Compressible mixing layer growth rate and turbulent characteristics. *J. Fluid Mech.*, 320:235–258, 1996.

[144] A.W. Vreman. *Direct and Large-Eddy Simulation of the Compressible Turbulent Mixing Layer*. Phd. thesis, University of Twente Enschede, 1995.

[145] S. Weinberg. *Gravitation and Cosmology: principles and applications of the general theory of relativity*. John Wiley & Sons, New York, 1972.

[146] G. S. Winckelmans, A. A. Wray, O. V. Vasilyev, and H. Jeanmart. Explicit filtering large-eddy simulation using the tensor-diffusivity model supplemented by a dynamic Smagorinsky term. *Phys. Fluids*, 13(5):1385–1403, 2001.

[147] E. Zeidler. *Applied Functional analysis: Applications to mathematical physics*, volume 108 of *Applied mathematical sciences*. Springer-Verlag, New York, 1995.

Samenvatting

Dit proefschrift levert een bijdrage aan de toepassing van Large-Eddy Simulatie (LES) op niet-uniforme en vervormende grids. Deze uitbreiding maakt het mogelijk om complexe, turbulente stromingen, zoals die voorkomen in industriële toepassingen, het weer en de luchtvaart, op een efficiënte manier te simuleren middels LES. In een LES worden alleen stromingsverschijnselen (eddies) met een typische lengte groter dan de filterbreedte Δ gesimuleerd. De effecten van kleinschalige stromingsverschijnselen worden gemodelleerd door middel van Sub-Grid-Scale (SGS)-modellen. Doordat alleen de grootschalige eddies mee worden genomen in de simulatie, vereist een LES veel minder computercapaciteit dan een Directe Numerieke Simulatie (DNS), waarin alle stromingsverschijnselen worden meegenomen. Voor de simulaties, waarvan resultaten worden gepresenteerd in dit proefschrift, is gebruik gemaakt van de Discontinue Galerkin Eindige Elementen Methode (DG-EEM). Dit type discretisatie kan op een efficiënte manier omgaan met niet-uniforme en vervormende grids.

Het onderzoek wat gepresenteerd wordt in dit proefschrift kan opgedeeld worden in vier verschillende onderwerpen. Deze worden hieronder samengevat.

- Het eerste onderwerp is de commuteer fout die ontstaat wanneer in een LES gebruik wordt gemaakt van een niet uniforme filterbreedte $\Delta(\mathbf{x}, t)$. Een filterbreedte, die afhankelijk is van ruimte en tijd, wordt bij voorkeur gebruikt in LES van complexe, turbulente stromingen. We hebben de relatieve grootte van de commuteer fout bepaald en vergeleken met de turbulente SGS-termen en het Lagrangiaanse gedrag van de commuteer fout bestudeerd.

  De grootte van de commuteer fout is afhankelijk van de filterbreedte Δ, de gradiënt van de filterbreedte $\partial_j \Delta$ en de orde van de filter operator. De grootte van de commuteer fout is analytisch bepaald en *a-priori* geverifieerd, waarbij gebruik is gemaakt van turbulente data verkregen door middel van DNS. Wanneer de filterbreedte voldoende niet uniform is, dan kan de commuteer fout niet verwaarloosd worden. De grootte van de commuteer fout kan ook beïnvloed worden door middel van de orde van de filter operator. Dit kan

177

echter niet onafhankelijk van de turbulente spannings tensor. Beide termen worden op eenzelfde manier beïnvloed wanneer de orde van de filter wordt verhoogd of verlaagd.

Het Lagrangiaanse gedrag van de commuteer fout houdt in dat dynamische effecten van de commuteer fout alleen een rol spelen wanneer het locale stromingsveld wijst in de richting van de niet-uniforme filterbreedte. Dit gedrag is *a-priori* onderzocht voor de transport van kinetische energie. Een bijna perfecte correlatie wordt waargenomen tussen de Lagrangiaanse parameterisatie en het transport van de kinetische energie door de commuteer fout. Daarnaast introduceren we een model gebaseerd op dit Lagrangiaanse gedrag, dat wordt vergeleken met andere modellen voor de commuteer fout.

• Het tweede onderwerp dat wordt behandeld is de numerieke turbulente spannings tensor voor compressibele stromingen. De numerieke turbulente spannings tensor onstaat wanneer het filterende effect van de discretisatie op het LES-grid wordt meegenomen in de LES-vergelijkingen. We laten zien dat de numerieke turbulente spannings tensor voor compressibele stromingen opgedeeld kan worden in twee stukken. Eén deel wat voornamelijk beïnvloed wordt door het kleinschalige snelheidsveld en een ander deel dat voornamelijk beïnvloed wordt door dichtheids fluctuaties. Voor supersone stromingen laten we *a-priori* zien dat het deel wat afhankelijk is van de fluctuerende dichtheid een niet te verwaarlozen bijdrage geeft aan de totale numerieke turbulente spannings tensor.

• Het derde onderwerp wat wordt behandelt is een alternatieve formulering van de LES-vergelijkingen gebaseerd op de Variational-Multi-Scale benadering van LES (VMS-LES). We breiden deze methode uit naar compressibele stromingen en maken daarbij gebruik van algemene basis-functies. Polynomiale basis-functies die typisch worden gebruikt in DG-EEM dienen hierbij als voorbeeld. Eerdere VMS-LES formuleringen zijn toepasbaar voor incompressibele stromingen en maken gebruik van basis-functies die gebruikt worden in spectrale methoden. We tonen aan dat de VMS-LES formulering voor compressibele stromingen overeenkomt met de Favre-gefilterde Navier-Stokes vergelijkingen. Het gebruik van niet spectrale basis-functies leidt tot extra SGS-termen die overeenkomen met de commuteer fout.

• Als vierde wordt het effect van numerieke dissipatie op de LES modellering bestudeerd. Hierbij wordt gebruik gemaakt van een database van LES waaruit "optimale" Smagorinsky constanten worden bepaald. Deze optimale coëfficiënten komen overeen met de Smagorinsky constante waarvoor een *a-postiori* fout voor de kinetische energie minimaal is, gegeven de resolutie van het grid en de numerieke dissipatie. Aangetoond wordt dat, afhanke-

lijk van de hoeveelheid numerieke dissipatie, andere Smagorinsky constanten gebruikt moeten worden voor een optimale benadering van de kinetische energie. De meest optimale benadering van de kinetische energie kan worden behaald wanneer deze voornamelijk gedissipeerd wordt door de moleculaire viscositeit en het SGS-model.

Als laatste tonen we resultaten van LES gebruikmakend van DG-EEM op niet uniforme en vervormende grids voor de stroming over een delta vleugel bij $Re_c = 100.000$. Met deze simulaties beoordelen we de haalbaarheid van LES op niet-uniforme en vervormende grids gebruikmakend van DG-EEM. De resultaten laten zien dat dit *technisch* mogelijk is. Echter gegeven hedendaagse computercapaciteiten is een goede beoordeling van de SGS-modellering niet mogelijk. Hiervoor dienen eerst de prestaties van de DG-EEM te worden verbeterd.

Summary

This thesis contributes to the development of the Large-Eddy Simulation (LES) technique on non-uniform and adaptive grids. This extension allows to efficiently simulate complex, turbulent flow problems as typically encountered in industry, weather prediction and aerodynamics. In an LES only flow features with a typical length-scale larger than the filter-width Δ are computed. The effect of the small or unresolved flow features is incorporated through Sub-Grid-Scale (SGS)-models. By only computing the larger flow features the computing requirements for a LES are considerably reduced compared to those of a Direct Numerical Simulation (DNS) in which all flow features are computed. For the actual simulations presented in this thesis use is made of the Discontinuous Galerkin Finite Element Method (DG-FEM). This type of discretization can efficiently deal with non-uniform and adaptive grids.

The research in this thesis can be divided into four different topics which are summarized below.

- The first topic is the commutator error that arises when a non-uniform filter-width $\Delta(\mathbf{x}, t)$ depending on space and time is used. Such a non-uniform filter-width is preferably used in LES of turbulent flow in complex domains. Specifically we studied the relative magnitude of the commutator error compared to the turbulent terms and its Lagrangian behavior.
  The magnitude of the commutator error is dependent on the filter-width Δ, the gradient of the filter-width $\partial_j \Delta$ and the order of the filter operator. This is shown analytically and verified *a-priori* using turbulent data acquired by means of DNS. It is observed that when the filter-width non-uniformities $\partial \Delta / \partial x_j$ are large that then the commutator error can no longer be neglected compared to other SGS-terms. Controlling the magnitude of the commutator error through the order of the filter is also possible. However higher-order filters do not allow independent control of the relative magnitude of the commutator error compared to the SGS-stress as both terms decrease in a similar way with increasing order of the filter.

The Lagrangian interpretation of the commutator error suggests that significant dynamics effects due to the commutator arise only if the local flow-field is in the direction of the filter-width non-uniformity. *A-priori* verification is given of this behavior in terms of the transport of resolved kinetic energy. An almost prefect correlation is achieved between the proposed Lagrangian parameterization and the actual transport of resolved kinetic energy through the commutator error. Finally, a model based on the Lagrangian behavior is formulated and compared with other commutator error models.

- The second topic concerns the computational turbulent stress tensor for compressible flow. The computational turbulent stress tensor arises when the filtering effect associated with the coarse-grid discretization is incorporated into the large-eddy equations. It is shown that the computational turbulent stress tensor for compressible flow can be decomposed into two parts, one part associated with fluctuating velocity and another associated with the fluctuating density. At supersonic Mach number it is *a-priori* shown that the density fluctuating part contributes considerably to the computational turbulent stress tensor and separate modeling of the fluctuating density is required.

- The third topic involves an alternative formulation of the large-eddy equations based on the Variational-Multi Scale approach to LES (VMS-LES). We extend earlier VMS-LES formulations to compressible flow and general basis-functions. The polynomial basis-functions typically encountered in DG-FEM are used as an illustrative example. Earlier VMS-LES formulations were restricted to incompressible flow and Fourier-spectral basis-functions. The compressible VMS-LES formulation resembles the Favre-filtered Navier-Stokes equations. The use of basis-functions other than Fourier-spectral basis-functions is shown to lead to additional SGS-terms in the VMS-LES formulation which resemble the commutator error SGS-terms.

- The fourth topic is a study into the effect of numerical dissipation on LES. Using a data-base approach "optimal" Smagorinsky constants are determined. These optimal coefficients correspond to minimal *a-posteriori* errors for the resolved kinetic energy at given resolution and numerical dissipation. Depending on the amount of numerical dissipation introduced by the discretization different Smagorinsky constants lead to an optimal prediction of the decay of resolved kinetic energy. The most accurate prediction of the resolved kinetic energy could be arrived at in case the kinetic energy is mainly dissipated through the resolved molecular viscous flux and the SGS-model.

Finally, results are included of a LES using DG-FEM on a non-uniform and adaptive grid of the flow over a delta wing with a sharp leading edge at $Re_c = 100.000$.

These results are included to assess the feasibility of LES on locally refined meshes using DG-FEM and show that it is *technically* possible for this type of flow. However, proper assessment of e.g. the SGS-modeling is not possible. The first bottleneck that needs to be confronted concerns a performance issue of DG-FEM on presently available computing infrastructure.

List of publications

- C. M. Klaij, J. J. W. van der Vegt, H. van der Ven and F. van der Bos, *Space-time discontinuous Galerkin method for the compressible Navier-Stokes equations on deforming meshes*, In P. Wesseling, E. Oñate and J. P''eriaux, editors, Proceedings ECCOMAS CFD 2006, Delft, The Netherlands, 2006.

- F. van der Bos, J.J.W. van der Vegt and B.J. Geurts, A Variational Multi-Scale Formulation for Compressible Flows in Discontinuous Galerkin Context, submitted to *Computer Methods in Applied Mechanics and Engineering.*

- F. van der Bos and B.J. Geurts, Computational turbulent stress closure for large-eddy simulation of compressible flow, *Journal of Turbulence* 7(9), 1-16, (2006).

- F. van der Bos and B.J. Geurts, Commutator errors in the filtering approach to large-eddy simulation, *Physics of Fluids* 17 (035108), 1-18, (2005).

- F. van der Bos and B.J. Geurts, Lagrangian dynamics of commutator errors in large-eddy simulation, *Physics of Fluids* 17 (075101), 1-15, (2005).

- B.J. Geurts and F. van der Bos, Numerically induced high-pass dynamics in large-eddy simulation, *Physics of Fluids* 17 (125103), 1-12, (2005).

- F. van der Bos and B.J. Geurts, *Dynamics of commutator-errors in LES with non-uniform filter-width.* In R. Friedrich, B.J. Geurts and O. Metais, editors, Proceedings Direct and Large-Eddy simulation V, pages 155-162, Kluwer Academic Publishers, Dordrecht, 2004.

- F. van der Bos and B.J. Geurts, Energy dynamics modeling of commutator errors, *Bull. American Physical Society* 48 (10), page 119, (2003).

- F. van der Bos, Bo Tao, C. Meneveau and J. Katz, Effects of small-scale turbulent motions on the filtered velocity gradient tensor as deduced from holo-

graphic particle image velocimetry measurements, *Physics of Fluids* 14(7), pages 2456-2474, (2002).

- F. van der Bos and B.J. Geurts, Commutator errors in LES of a turbulent mixing layer, *Bull. American Physical Society* 47 (10), page 140, (2002).

Curriculum Vitae

The author of this thesis was born on September 13th 1978 in Joure. He finished his secondary education at the "Bornego College" Heerenveen in 1996.

From September 1996 until May 2002 he studied Applied Mathematics at the University of Twente. His practical training was performed at the department of Mechanical Engineering of the Johns Hopkins University, Baltimore, USA. Under supervision of Prof. Charles Meneveau he analyzed various models used in the Large-Eddy Simulation (LES) of turbulent flow in the context of the restricted Euler equations. The research for his master thesis "*An investigation into Large-Eddy simulation of turbulence with non-uniform filter width*" was performed at the group Numerical Analysis and Computational Mechanics under supervision of Prof. Bernard Geurts.

In June 2002 he started his Ph.D.-research in the same group at the University of Twente under supervision of Prof. Bernard Geurts and Prof. Jaap van der Vegt. In this research he used the large-eddy simulation technique on non-uniform and adaptive grids extending LES to complex, turbulent flows. Use was made of a discretization based on the Discontinuous-Galerkin Finite Element Method (DG-FEM) and simulations were performed of the flow over a delta-wing. His Ph.D.-project was performed in cooperation with the Netherlands Aerospace Institute and the author was responsible for the implementation of turbulence models into the DG-FEM based flow solver HEXADAP used by the Dutch Aerospace Institute.